frontiers | Research Topics

Probing out-of-equilibrium soft matter

Edited by
Roberto Cerbino, Alberto Fernandez-Nieves, Emanuela Del Gado, Irmgard Bischofberger, Ramon Castañeda-Priego and Luca Cipelletti

Published in
Frontiers in Physics

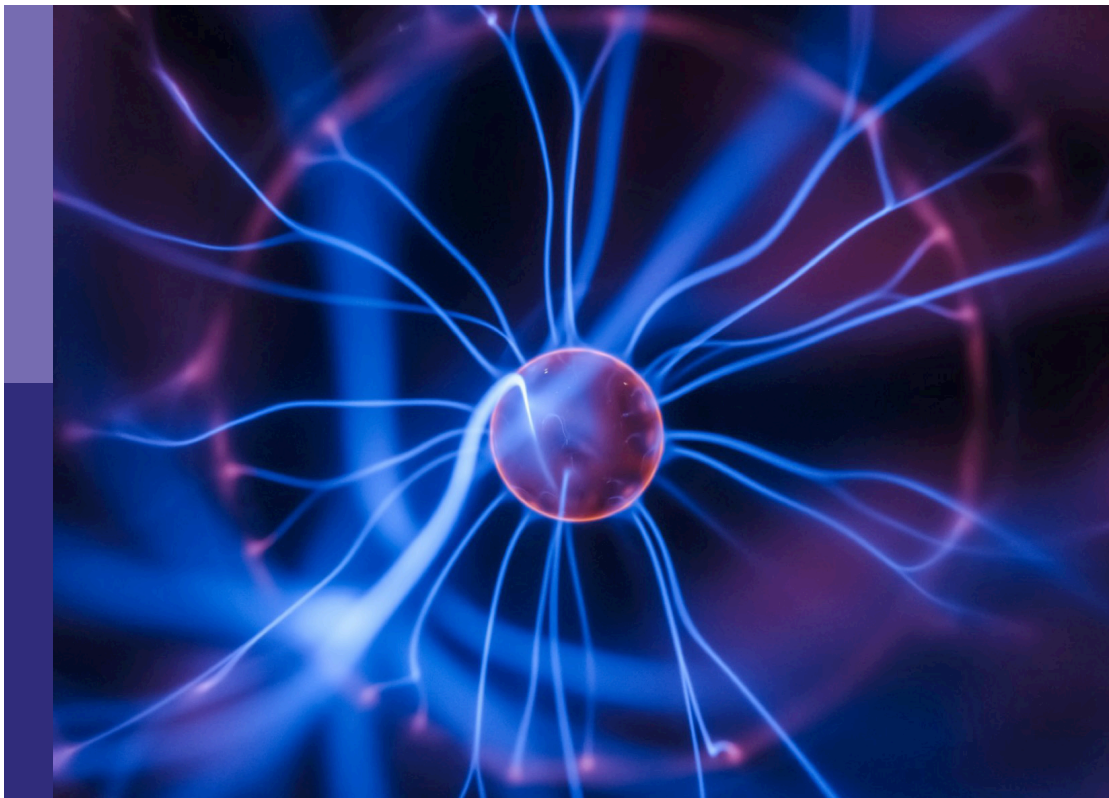

ISSN 1664-8714
ISBN 978-2-83252-035-2
DOI 10.3389/978-2-83252-035-2

About Frontiers

Frontiers is more than just an open access publisher of scholarly articles: it is a pioneering approach to the world of academia, radically improving the way scholarly research is managed. The grand vision of Frontiers is a world where all people have an equal opportunity to seek, share and generate knowledge. Frontiers provides immediate and permanent online open access to all its publications, but this alone is not enough to realize our grand goals.

Frontiers journal series

The Frontiers journal series is a multi-tier and interdisciplinary set of open-access, online journals, promising a paradigm shift from the current review, selection and dissemination processes in academic publishing. All Frontiers journals are driven by researchers for researchers; therefore, they constitute a service to the scholarly community. At the same time, the *Frontiers journal series* operates on a revolutionary invention, the tiered publishing system, initially addressing specific communities of scholars, and gradually climbing up to broader public understanding, thus serving the interests of the lay society, too.

Dedication to quality

Each Frontiers article is a landmark of the highest quality, thanks to genuinely collaborative interactions between authors and review editors, who include some of the world's best academicians. Research must be certified by peers before entering a stream of knowledge that may eventually reach the public - and shape society; therefore, Frontiers only applies the most rigorous and unbiased reviews. Frontiers revolutionizes research publishing by freely delivering the most outstanding research, evaluated with no bias from both the academic and social point of view. By applying the most advanced information technologies, Frontiers is catapulting scholarly publishing into a new generation.

What are Frontiers Research Topics?

Frontiers Research Topics are very popular trademarks of the *Frontiers journals series*: they are collections of at least ten articles, all centered on a particular subject. With their unique mix of varied contributions from Original Research to Review Articles, Frontiers Research Topics unify the most influential researchers, the latest key findings and historical advances in a hot research area.

Find out more on how to host your own Frontiers Research Topic or contribute to one as an author by contacting the Frontiers editorial office: frontiersin.org/about/contact

Probing out-of-equilibrium soft matter

Topic editors

Roberto Cerbino — University of Vienna, Austria
Alberto Fernandez-Nieves — Catalan Institution for Research and Advanced Studies (ICREA), Spain
Emanuela Del Gado — Georgetown University, United States
Irmgard Bischofberger — Massachusetts Institute of Technology, United States
Ramon Castañeda-Priego — University of Guanajuato, Mexico
Luca Cipelletti — Université de Montpellier, France

Citation

Cerbino, R., Fernandez-Nieves, A., Gado, E. D., Bischofberger, I., Castañeda-Priego, R., Cipelletti, L., eds. (2023). *Probing out-of-equilibrium soft matter*. Lausanne: Frontiers Media SA. doi: 10.3389/978-2-83252-035-2

Table of contents

frontiers | Frontiers in Physics

TYPE Editorial
PUBLISHED 14 March 2023
DOI 10.3389/fphy.2023.1173632

OPEN ACCESS

EDITED AND REVIEWED BY
Jasper Van Der Gucht,
Wageningen University and Research,
Netherlands

*CORRESPONDENCE
Irmgard Bischofberger,
irmgard@mit.edu
Ramón Castañeda-Priego,
ramoncp@fisica.ugto.mx
Roberto Cerbino,
cerbino@gmail.com
Luca Cipelletti,
luca.cipelletti@umontpellier.fr
Emanuela Del Gado,
ed610@georgetown.edu
Alberto Fernandez-Nieves,
alberto.fernandez@physics.gatech.edu

SPECIALTY SECTION
This article was submitted to
Soft Matter Physics,
a section of the journal
Frontiers in Physics

RECEIVED 24 February 2023
ACCEPTED 06 March 2023
PUBLISHED 14 March 2023

CITATION
Bischofberger I, Castañeda-Priego R, Cerbino R, Cipelletti L, Gado ED and Fernandez-Nieves A (2023), Editorial: Probing out-of-equilibrium soft matter. *Front. Phys.* 11:1173632. doi: 10.3389/fphy.2023.1173632

Editorial: Probing out-of-equilibrium soft matter

Irmgard Bischofberger[1]*, Ramón Castañeda-Priego[2]*, Roberto Cerbino[3]*, Luca Cipelletti[4,5]*, Emanuela Del Gado[6]* and Alberto Fernandez-Nieves[7]*

[1]Department of Mechanical Engineering, Massachusetts Institute of Technology, Cambridge, MA, United States, [2]Sciences and Engineering Division, University of Guanajuato, León, Mexico, [3]Faculty of Physics, University of Vienna, Vienna, Austria, [4]L2C, University of Montpellier, Montpellier, France, [5]Institut Universitaire de France, Paris, France, [6]Department of Physics, Institute for Soft Matter Synthesis and Metrology, Georgetown University, Washington, DC, United States, [7]Department of Condensed Matter Physics, ICREA-Institucio Catalana de Recerca i Estudis Avancats, Institute for Complex Systems (UBICS), University of Barcelona, Barcelona, Spain

KEYWORDS

soft matter, biophysics, non-equilibrium, structure, dynamics, rheology, microrheology

Editorial on the Research Topic
Probing out-of-equilibrium soft matter

This Research Topic originates from the symposium *Probing Out-of-Equilibrium Soft Matter* that was held on October 22–23, 2021 at the University of Fribourg (Switzerland) to celebrate and honor the career of Véronique Trappe (https://orcid.org/0000-0002-0301-258X). The symposium assembled leading scientists in the rapidly growing field of non-equilibrium soft matter physics, a field to which V. Trappe has made key contributions that have changed the view of many [1–6]. While the equilibrium behaviour of soft matter is amply studied and understood, novel tools are needed to capture the complexity of out-of-equilibrium soft materials. A particular challenge is getting access to and understanding the fast processes occurring at the nano- and micro-scale of the elementary constituents, while simultaneously capturing the slower evolution of bulk properties in non-equilibrium conditions. To take on this task, new theoretical, numerical and experimental methodologies need to be developed that enable the investigation of the structure, dynamics, thermodynamics, and rheology of out-of-equilibrium soft matter. Adopting a comprehensive view that covers fundamental topics as well as research focusing on processes and issues faced in applications, this Research Topic aims to showcase some of the latest advancements and innovations in the field.

Living and active materials are intrinsically non-equilibrium systems due to metabolic activity and/or energy consumption. Using newly developed fabrication and image processing tools, Chang et al. probe the effect of surface curvature on the proliferation of Madin-Darby Canine Kidney (MDCK) epithelial cells. They show that proliferation is insensitive to changes in curvature, and that the main mechanism of cell proliferation control is contact inhibition. Sheung et al. use a combination of light sheet microscopy, particle tracking, and differential dynamic microscopy to elucidate anomalous and advective transport in actomyosin-microtubule biomimetic composites. A complex interplay between increasing activity and confinement as the

actomyosin fraction increases governs the transport properties of these active cytoskeletal systems.

Three studies address shear-driven patterning in soft materials. Applying shear flow during the temperature-induced gelation of a colloid-polymer mixture which contains thermosensitive microgel particles, Rel et al. show that they can tune the morphology of mesoscopic colloidal clusters. Gels comprised of fibrous, elongated colloid-dense clusters, log-like flocs that are aligned along the vorticity direction or isotropic clusters can be produced by controlling the shear. Villa et al. adapt a previously designed shear cell [7] to perform stress-controlled rheo-microscopy experiments on commercial microscopes. This flexible rheo-microscopy setup, compatible with different imaging methods, allows to perform quantitative rheology by assessing the microscopic dynamics with particle tracking and differential dynamic microscopy analysis. Lastly, Miller et al. introduce a novel approach to assess dynamic ordering in sheared dense suspensions using a combined rheometer and laser scanning confocal microscope. The spatiotemporal dynamics obtained with high spatial and temporal resolution reveals distinct regimes of ordering depending on the particle concentration and the applied stress, which reflect shear-thickening and transiently shear-jammed states.

Colloidal suspensions are also the focus of Carpineti et al., who study the transient patterns that emerge during Rayleigh-Bénard convection with thermophilic particles. The gravitationally destabilizing temperature gradient induces rotating patterns in the form of traveling waves that eventually disappear as the stabilizing effect of thermophoresis returns the system to a conductive state. Probing the crystallization kinetics of charged temperature-sensitive microgels in deionized conditions, Bocanegra-Flores et al. discover that due to their microgels' low polydispersity and electrostatic charge a liquid-crystal transition occurs for volume fractions of the order of 0.01–0.05, a factor of ten lower than in neutral microgels.

Soft Matter research is increasingly impacted by current developments in Machine Learning (ML) techniques. Methods including computer vision, feature engineering, and classification tasks have been applied to characterize colloidal systems. In particular, ML methods have proven useful to identify correlations in non-equilibrium systems such as glasses. Oyama et al. discuss how deep neural networks can predict the characteristic local meso-structures of glasses solely from instantaneous particle configurations, without any information about the particle dynamics. Finally, the nature of the non-equilibrium states also depends on how rapidly a material is quenched to a specific condition. Rouzaire and Levis discuss the dynamics of the short range noisy Kuramoto model, where spins are able to rotate with an intrinsic frequency taken from a quenched Gaussian distribution. By connecting synchronisation with the so-called topological Berezenskii-Kosterlitz-Thouless phase transition, the authors investigate the dynamics of vortices and other topological defects, shedding light on their long-time super-diffusive behaviour.

The articles of this Research Topic are representative, while non-exhaustive, of a variety of out-of-equilibrium phenomena in Soft Matter that are rapidly emerging among the most fascinating topics in modern multidisciplinary science. Symposia and workshops such as the one that inspired this Research Topic will continue to play an important role in promoting and deepening interactions between researchers with diverse backgrounds. The ability to discuss openly and in depth, so distinctive of Véronique Trappe's way of conducting research, will be key to continue progress in the field.

Author contributions

All authors listed have made a substantial, direct, and intellectual contribution to the work and approved it for publication.

Funding

The organization of the workshop was possible thanks to funding from the following contributors: Swiss National Science Foundation, University of Fribourg, NCCR Bioinspired Materials Fribourg, Frontiers, Michelin, Villars, Fri-Mousse.

Acknowledgments

The authors thank the participants of the symposium and the contributors to this Research Topic. AF-N acknowledges support from MCIN/AEI/10.13039/501100011033/FEDER, UE (Grant No. PID2021-122369NB-100). LC gratefully acknowledges support from the Institut Universitaire de France.

Conflict of interest

The authors declare that the research was conducted in the absence of any commercial or financial relationships that could be construed as a potential conflict of interest.

Publisher's note

References

1. Trappe V, Prasad V, Cipelletti L, Segre P, Weitz DA. Jamming phase diagram for attractive particles. *Nature* (2001) 411:772–5. doi:10.1038/35081021

2. Cipelletti L, Bissig H, Trappe V, Ballesta P, Mazoyer S. Time-resolved correlation: A new tool for studying temporally heterogeneous dynamics. *J Condens Matter Phys* (2003) 15:S257–62. doi:10.1088/0953-8984/15/1/334

3. Trappe V, Sandkühler P. Colloidal gels—Low-density disordered solid-like states. *Curr Opin Colloid Interf Sci.* (2004) 8:494–500. doi:10.1016/j.cocis.2004.01.002

4. Cerbino R, Trappe V. Differential dynamic microscopy: Probing wave vector dependent dynamics with a microscope. *Phys Rev Lett* (2008) 100:188102. doi:10.1103/physrevlett.100.188102

5. Bischofberger I, Calzolari DC, De Los Rios P, Jelezarov I, Trappe V. Hydrophobic hydration of poly-N-isopropyl acrylamide: A matter of the mean energetic state of water. *Sci Rep* (2014) 4:4377. doi:10.1038/srep04377

6. Caggioni M, Trappe V, Spicer PT. Variations of the herschel–bulkley exponent reflecting contributions of the viscous continuous phase to the shear rate-dependent stress of soft glassy materials. *J Rheol* (2020) 64:413–22. doi:10.1122/1.5120633

7. Aime S, Ramos L, Fromental JM, Prevot G, Jelinek R, Cipelletti L. A stress-controlled shear cell for small-angle light scattering and microscopy. *Rev Sci Instrum* (2016) 87:123907. doi:10.1063/1.4972253

frontiers | Frontiers in Physics

BRIEF RESEARCH REPORT
published: 14 July 2022
doi: 10.3389/fphy.2022.953067

Transient Localized Rotating Structures in a Suspension of Highly Thermophilic Nanoparticles

*Marina Carpineti, Stefano Castellini, Andrea Pogliani and Alberto Vailati**

Dipartimento di Fisica "A. Pontremoli", Università degli Studi di Milano, Milano, Italy

A thermophilic suspension of nanoparticles heated from below exhibits a complex stability diagram determined by the competition between the stabilizing flux of nanoparticles induced by thermophoresis and the destabilizing flux determined by thermal convection. We investigate Rayleigh-Bénard convection in a suspension of highly thermophilic nanoparticles with large negative separation ratio $\psi = -3.5$ heated from below. We show that transient localized states appear in the range of Rayleigh numbers $2200 < \mathrm{Ra} < 3000$. These states rotate rapidly around their axis and gradually shrink in size until the system returns in a purely conductive state. We discuss how these states are originated by the travelling waves arising from the competition between Rayleigh-Bénard convection and the solutal stabilisation of the sample.

Keywords: thermophilic nanoparticles, Rayleigh-Bénard convection, travelling waves, localized structures, convectons

OPEN ACCESS

Edited by:
Ramon Castañeda-Priego, University of Guanajuato, Mexico

Reviewed by:
Alokmay Datta, University of Calcutta, India
Sutapa Roy, Indian Institute of Technology Gandhinagar, India

****Correspondence:***
Alberto Vailati
alberto.vailati@unimi.it

Specialty section:
This article was submitted to Soft Matter Physics, a section of the journal Frontiers in Physics

Received: *25 May 2022*
Accepted: *22 June 2022*
Published: *14 July 2022*

Citation:
Carpineti M, Castellini S, Pogliani A and Vailati A (2022) Transient Localized Rotating Structures in a Suspension of Highly Thermophilic Nanoparticles. Front. Phys. 10:953067. doi: 10.3389/fphy.2022.953067

1 INTRODUCTION

In the presence of a density stratification, a layer of fluid exhibits a rich phenomenology determined by the action of gravity that can lead to oscillations and wave propagation [1, 2]. A typical case is represented by a single component fluid heated from below, where the stratification is determined by the thermal dilation of the fluid, which can transfer heat either in a conductive or in a convective regime. The stability of the system is parametrized by the dimensionless Rayleigh number $\mathrm{Ra}=\frac{\alpha g \Delta T h^3}{\nu \kappa}$, which quantifies the applied thermal stress. Here α is the thermal expansion coefficient, g the acceleration of gravity, ΔT the temperature difference, h the thickness of the layer, ν the kinematic viscosity, and κ the thermal diffusivity. The transfer of heat is parametrized by the Nusselt number Nu, which represents the ratio between the heat transferred by the fluid and the one transferred by conduction only. For a layer of fluid of infinite aspect ratio $r = \Phi/h$, where Φ is the diameter of the layer of fluid, the transfer of heat is conductive ($\mathrm{Nu} = 1$) when the Rayleigh number is below the threshold value $\mathrm{Ra}_c = 1708$, while it occurs by convection ($\mathrm{Nu} > 1$) above the threshold (**Figure 1**). The addition of a second component to the fluid dramatically alters the stability of the layer. More in detail, the temperature gradient imposed to the fluid gives rise to a non-equilibrium mass flux determined by the Ludwig-Soret effect: $j = -\rho D\,[\nabla c - c\,(1-c) S_T \nabla T]$, where ρ is the density of the sample, D the diffusion coefficient, c the weight fraction concentration, and S_T the Soret coefficient. As a result, the density profile inside the sample becomes affected both by the vertical temperature and concentration profiles of the fluid. The case of a suspension of thermophilic particles heated from below is particularly interesting, because in this case the stabilizing flux of nanoparticles induced by thermophoresis competes with the destabilizing flux determined by thermal convection. The relative weight of these two contributions is expressed by the separation ratio $\psi = \Delta\rho_s/\Delta\rho_T$, which represents the ratio between the density differences $\Delta\rho_s$

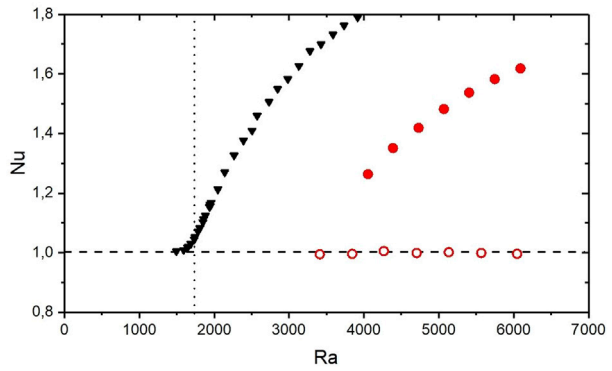

FIGURE 1 | Stability diagram. Nusselt number as a function of Rayleigh number for a single component fluid (liquid Helium, triangles) and LUDOX™ colloidal silica nanoparticles in water at a concentration of 4.0% w/w (circles). The colloidal sample exhibits bistability, represented by the co-existence of a stable convective branch (full circles) and a stable conductive branch (open circles). The dashed horizontal line represents the purely conductive regime (Nu = 1), while the vertical dotted line is the threshold $Ra_c = 1708$ for Rayleigh-Bénard convection in a single component fluid. Transient rotating structures are observed in the range of Rayleigh numbers $2000 < Ra < 4000$.

and $\Delta\rho_T$ determined by solutal and thermal expansion, respectively. In the case of a separation ratio in the range $-1 < \psi < 0$ this competition determines the onset of travelling waves, accompanied by the presence of localized pulses of convection, localized states and convectons [3–14]. The case $\psi < -1$ is particularly interesting, because in this case the stabilizing effect determined by the Soret flux dominates, and the transfer of heat occurs in the conductive regime, irrespectively of the magnitude of the imposed temperature gradient. However, experiments performed on suspensions of strongly thermophilic nanoparticles with $\psi = -3.5$ and $\psi = -7.5$ have shown that the behaviour of the system is strongly affected by the initial conditions [15, 16]. When the temperature gradient is imposed gradually, nanoparticles migrate towards the bottom of the fluid and give rise to a density profile that completely stabilizes the layer of fluid against Rayleigh-Bénard convection. Under this condition, the transfer of heat occurs by conduction. Conversely, when the temperature gradient is imposed rapidly and the particles are initially dispersed uniformly, convective motions set in and, provided that the Rayleigh number is large enough, keep the particles dispersed and convection lasts indefinitely. The theoretical investigation of the stability of a strongly thermophilic colloidal suspension with large negative separation ratio has shown that the competition between Rayleigh-Bénard convection and the stabilizing effect determined by the Soret effect leads to a transient oscillatory instability [17]. The analysis of the role of the settling of the nanoparticles showed that the presence of a sedimentation profile leads to the oscillatory onset of convection [18] and to the development of travelling waves [19, 20]. Under these conditions, an additional parameter affecting the stability of the system is represented by the sedimentation length $l_g = k_B T/(\Delta\rho V g)$, which characterizes the typical length scale of variation of the concentration profile (here $\Delta\rho$ is the density mismatch between the particle and the carrier fluid, and V is the volume of the particle). The investigation of experimental conditions where the settling of particles is not strong and the sedimentation length l_g is comparable or larger than the sample thickness showed that a decrease of l_g is accompanied by a decrease of the convection threshold and of the frequency of neutral oscillations [21]. The analysis of the interplay between the combined effects of sedimentation, thermophoresis with negative separation ratio and convection led to the discovery of a new travelling wave solution, characterized by an anharmonic distribution of the vertical velocity across the sample layer [22]. Two dimensional simulations performed under conditions mirroring those adopted in experiments on a Hyflon MFA colloidal suspension [15], characterized by $\psi = -7.5$, showed recently that including the effect of gravitational sedimentation allows to achieve a quantitative estimate of the lifetime of the oscillatory flow as a function of Rayleigh number [20].

In this work we focus on the investigation of transient Rayleigh-Bénard convection in a suspension of highly thermophilic nanoparticles with large negative separation ratio $\psi = -3.5$ heated from below, under experimental conditions similar to those employed in theoretical studies [20–22]. We show that transient localized states appear in the range of Rayleigh numbers $2200 < Ra < 3000$ after the sudden imposition of a thermal gradient to a suspension of uniformly distributed nanoparticles. These states rotate rapidly around their axis, and gradually shrink in size, until they disappear and the system returns in a purely conductive state. We provide a quantitative characterization of the wave number and angular velocity of the localized states and we discuss our results in comparison with previous theoretical models and simulations summarized above.

The study of spatially localized states is of great interest in the field of pattern formation, as they appear in a great variety of physical and biological systems [23, 24]. In the case of localized stationary convective states, they take the name of *convectons*, and there is a growing number of works studying them from a theoretical, computational and experimental point of view [10, 23, 25–27].

2 METHODS

2.1 The Sample

The sample chosen for the experiment is a colloidal suspension made by distilled water and LUDOX™ TMA, a commercial colloid made of silica nanoparticle with an average diameter of 22 nm. In this work we have used concentrations of 4.0% w/w. The thermophysical properties are detailed in **Table 1**. This sample has been selected as a model system for the investigation of thermophoresis at the mesoscopic scale in the absence of gravity within the framework of the Giant Fluctuations and TechNES space projects of the European Space Agency [28, 29]. Within these projects, a series of experiments will be performed on the International Space Station to investigate the non-equilibrium fluctuations determined by the thermophoretic

TABLE 1 | LUDOX^{TM} TMA thermo-physical properties.

Quantity	Diameter (nm)	D	D_T	α	ν	β	S_T
Value	22	2.2e-7cm^2/s	1.52e-3cm^2/s	2.97e-4K^{-1}	8.18e-3cm^2/s	0.57	−4.7e-2K^{-1}

process. Preliminary studies performed on Earth under isothermal conditions showed the presence of a peculiar relaxation dynamics of non-equilibrium concentration fluctuations, characterized by anomalous diffusion at large wave vectors [30]. For these reasons, it is very important to achieve a full understanding of the stability of this colloidal suspension in the presence of gravity.

2.2 Experimental System

The central element of the apparatus is a thermal gradient cell, consisting in a layer of fluid confined by two sapphire plates through which a thermal gradient can be applied. The heating elements are two ring-shaped Thermo Electric Devices (TED) thermally coupled to the sapphire plates. The other side of both the TED elements is in contact with a thermal reservoir, consisting of two annular aluminium chambers, inside which there is a steady flow of water at constant temperature. The purpose of this reservoir is to remove the excess heat. The cell is mounted on an optical bench in the configuration where the sample layer is horizontal, and is illuminated by a superluminous diode (Superlum SLD-261) with central wavelength 670 nm. The limited temporal coherence of the source avoids interference determined by multiple reflections of the beam on the surfaces of the cell windows. The sensor employed is a monochrome CCD Camera (JAI CV-M300) with a resolution of 576 × 768 pixels and a depth of 8 bit, operating at a frame rate of 10 images per second. An achromatic doublet with focal length of 30 cm, placed between the sample cell and the camera images a plane at distance $z = -90.6 \pm 0.5$ cm from the sample in a shadowgraph configuration that allows to visualize the self-organized structures generated by the convective motions. The camera is controlled remotely by a computer through a National Instrument PCI-1407 frame-grabber.

3 RESULTS

Heat conduction in fluids is greatly affected by the presence of colloidal particles that exhibit a thermophilic behaviour. In particular, the presence of even a small amount of thermophilic particles has a stabilizing effect when the suspension is heated from below and, as a result, the sample can transfer heat either in a conductive or in a convective regime, depending on the initial condition (**Figure 1**) [15, 16]. The conductive regime can be accessed by imposing slowly a temperature difference to the sample heating from below, so that the thermophilic particles accumulate at the bottom of the cell and stabilize the sample against Rayleigh-Bénard convection. The convective regime can be accessed by first heating the sample from above to determine the accumulation of nanoparticles at the top of the cell, and then suddenly reversing the temperature gradient by heating from below. Under these conditions a Rayleigh-Bénard instability starts and the accumulation of the thermophilic particles at the bottom of the cell is prevented by the convective flow that keeps the particles mixed. Conversely, if the temperature gradient is reversed by slowly heating from below thermophoresis determines the rapid formation of a stable boundary layer at the bottom of the cell and the system ends up in the conductive regime.

The bistable heat transfer is currently a well established feature of strongly thermophilic nanoparticles [15, 16], but bistability is apparent only for Rayleigh numbers Ra > 4000. Below this value of the Rayleigh number and above the threshold for Rayleigh-Bénard convection $\mathrm{Ra}_c = 1708$ the system exhibits transient convective behaviour when heated from below, but eventually the stabilization determined by the particles dominates and the system enters into a purely conductive regime.

In order to study the transient convective regime in this range of Rayleigh numbers we have performed experiments according to the following procedure: i) The sample is heated from *above* for 1 h, applying a temperature difference $\Delta T = 10.5K$. This ensures that, because of the strong thermophilic behaviour of LUDOX^{TM} TMA, the colloidal particles diffuse towards the upper plate, and the sample enters a regime of solutal convection [31–33]. The time needed to enter this solutal convective regime has been determined empirically. Physically, it corresponds to the diffusive time $\tau_\delta = \delta^2/D$ needed for the formation of a thin—unstable—boundary layer of thickness δ at the top of the cell, and is affected by the size of the nanoparticles through their diffusion coefficient D. ii) The temperature gradient is abruptly reverted to a negative value. In our tests we used temperature differences of $\Delta T = -3.00$ K, − 3.38 K, − 3.75 K, − 4.13 K. iii) shadowgraph images of the sample are recorded with a frame rate of, approximatively, 10 images/second.

Under these conditions, when the sample is first heated from above at the beginning of the experiment, solutal convection destabilizes the suspension (**Figure 2A**) so that, when the gradient is inverted, a convective instability develops in the sample, even when the sample is below the threshold needed for the development of stationary Rayleigh-Bénard convection in the nanofluid (**Figure 2**). At the beginning, the convective patterns are the usual convective rolls that characterize Rayleigh-Bénard convection, spanning all the area of the cell. After some time, the patterns begin to rotate around the vertical axis (clockwise or anticlockwise, indifferently). Subsequently, convection begins to die out starting from the borders of the cell, giving rise to the formation of a single rotating localized pattern. Eventually, the rotating pattern shrinks in size, until it disappears completely and the sample reaches the stationary conductive state. The duration of the entire phenomenon, measured from the inversion of the gradient, is of the order of

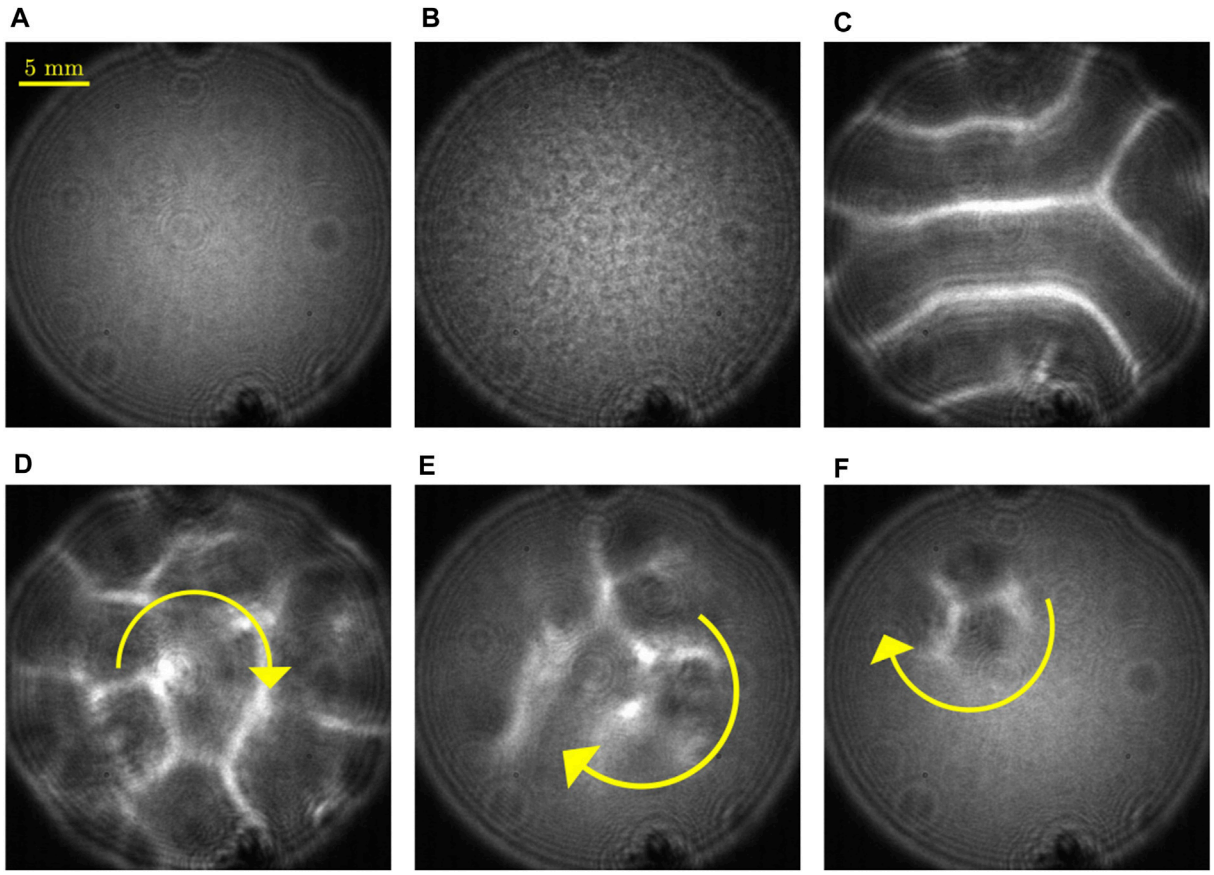

FIGURE 2 | Image sequence representing the evolution of the convective instability in a 3.1 mm thick layer of LUDOX^{TM} TMA 4% w/w. **(A)** at the beginning, heating from above with a temperature difference of 10.5K, no macroscopic motions are present; **(B)** after a time of the order of tens of minutes solutal convection develops in the cell; **(C)** after 1 h, the temperature difference is inverted and set to -4.13 K. In, approximatively 3 min thermal convective rolls appear in the sample; **(D)** the rolls, after a time that depends on the Rayleigh number, start to rotate; **(E)** they die out starting from the borders; **(F)** they gradually shrink in size, until they finally disappear.

1–3 h. The same phenomenology is observed for all temperature differences studied.

By looking at sequences of images, we measured some characteristic parameters of the localized states as a function of Rayleigh number. The interesting quantities are the wave vector k of the patterns and their angular velocity ω, and the typical timescales t_{ap} needed for the appearance of the convective structure, t_{rot} needed for the rotation of the pattern to start, and t_{ex} needed for the patterns to disappear. The results are summarized in **Figure 3**.

The characteristic wave vector k is compatible with the value 3.117 predicted for Rayleigh-Bénard convection close to the threshold. The angular velocity of the patterns has been determined from the visual observation of a large number of complete revolutions of the localized pattern (typically 10–20 revolutions). In selecting the maximum number of revolutions to consider for a reliable determination of the angular velocity we relied on the fact that the structure of the rotating pattern needed to be preserved, so that the motion of the spatial features of the patterns could be followed during their rotation. This method proved to be more effective and immune to errors than the automatic processing of the angular correlations.

The rotation of the patterns is very slow, a complete revolution taking a time in the range 500–800 s. The time t_{ap} needed for the appearance of the structures is of the order of 200 s, and slightly decreases as the Rayleigh number increases. The behaviour of the time t_{rot} needed for the rotation to start is of major interest, because it exhibits a variation of a factor 10 when the Rayleigh number is increased from 2180 to 3000, indicating that the range explored is extremely important and revealing. Indeed, in this range, as already noted, there is a competition between the Rayleigh-Bénard thermal convection and the stabilizing effect of the colloidal particles. This competition leads to the formation of travelling waves patterns, which, in a circular cell, become rotating patterns, due to the confinement determined by the lateral boundary. However, in the regime of subcritical Rayleigh numbers explored by us Rayleigh-Bénard convection prevails, and the stabilizing effect due to the accumulation of the colloid on the bottom of the cell is hampered by the continuous remixing of the particles. Under these conditions, the sedimentation of the particles is slowed down, and so are the appearance of travelling waves and the beginning of the rotation. The time needed for convection to disappear also exhibits a marked dependence on the Rayleigh number, and is in qualitative agreement with the

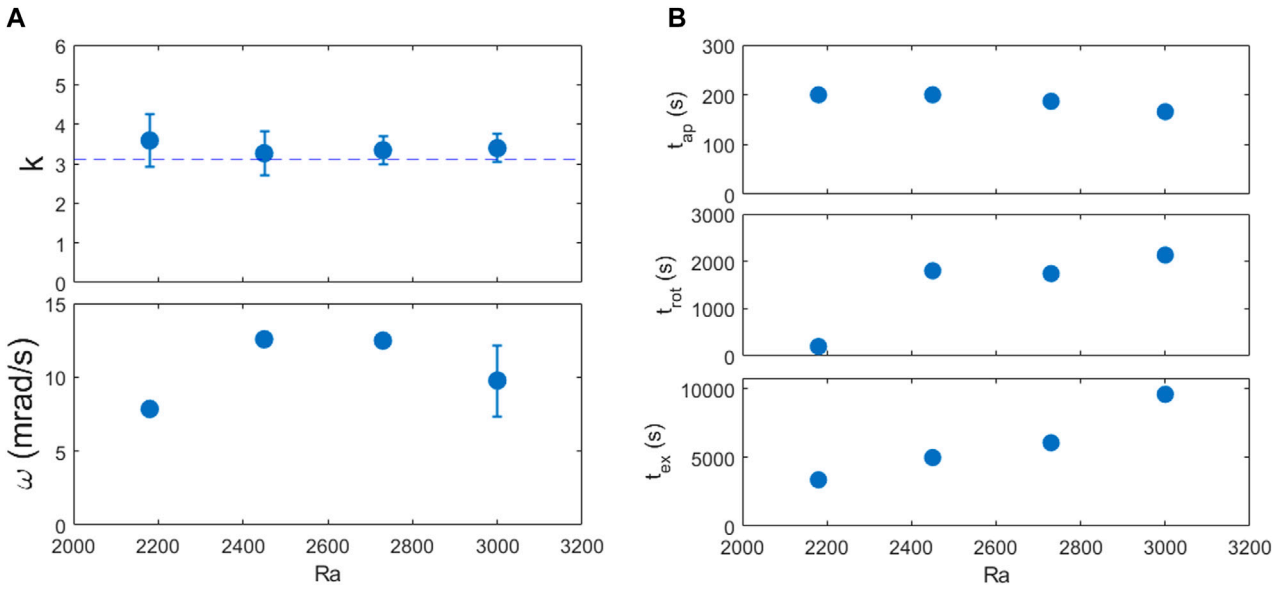

FIGURE 3 | (A): dimensionless wave number k (top) and angular velocity ω of the patterns (bottom) as a function of Rayleigh number. The dashed line marks the theoretical wave number $k_c = 3.117$ of Rayleigh-Bénard convection close to the onset. **(B)**: time needed for the appearance of the convective pattern, t_{ap} (top), time for the beginning of the rotation of the pattern, t_{rot} (middle), and time of extinction of the convective instability, t_{ex} (bottom), plotted as a function of the Rayleigh number. Time $t = 0$ corresponds to the instant when the gradient gets reversed.

results of simulations on suspensions of thermophilic nanoparticles with large negative separation ratio heated from below [20].

4 DISCUSSION

Our system is different from most of those that, to our knowledge, have been previously characterized experimentally or theoretically and by means of simulations. In fact, a large number of studies has been devoted to the investigation of water-ethanol mixtures heated form below. Depending on the concentration of ethanol, this system can exhibit a negative separation ratio $\psi > -1$, leading to the oscillatory onset of a convective instability when the fluid is heated from below. Water-ethanol mixtures exhibit a multistable heat transfer at sufficiently small supercritical Rayleigh numbers [3, 5, 6, 8, 11, 12, 14], where depending on the initial condition and on the history of the system the transfer of heat can either occur by conduction or by steady overturning convection, similarly to the bistable behaviour reported by us. The investigation of transient behaviour during the onset of convection shows the development of localized pulses of travelling-wave convection in 1D [9, 23] and 2D geometries [10]. Under supercritical conditions, localized rotating structures develop, and gradually expand until they reach the boundaries of the cell [10, 27]. Conversely, bringing back the system in a subcritical condition after the onset of convection determines the formation of rotating structures that gradually shrink in time until they disappear [13, 34].

All these works deal with binary fluids with a negative separation ratio $-1 < \psi < 0$, a condition where the thermal contribution to the density variation is larger than the solutal one. At variance, our system is a colloidal suspension of nanoparticles and has a separation ratio $\psi = -3.5$, so that the solutal contribution to the density profile largely dominates the thermal one. Indeed, many of the solutions studied in the cited works are travelling waves that don't die out, whereas the instability that we observed in the end disappears, notwithstanding the fact that the system is under supercritical conditions, due to the stabilization determined by the highly thermophilic particles.

The case of thermal convection in a suspension of thermophilic nanoparticles with a large negative separation ratio $\psi = -10$ has been investigated theoretically by Ryskin and Pleiner [17]. They studied the linear and nonlinear behaviour starting from a suspension with an initially uniform distribution of nanoparticles. They found that at small supercritical Rayleigh numbers $\mathrm{Ra} < 1840$ the fluid exhibits a transient oscillatory instability, while at higher Rayleigh numbers the system exhibits bistability, characterized by the presence of a stationary instability and of a stable conductive state. The phenomenology reported is qualitatively very similar to the one reported by us, but the threshold for the transition from a transient oscillatory instability to a stationary one is much larger in our experiments.

Cherepanov and Smorodin have performed a detailed theoretical investigation of the stability of a colloidal suspension heated from below and with negative separation ratio $\psi = -0.8$, taking into account not only the Soret effect but also the effect of sedimentation induced by gravity [21,22]. The sedimentation length l_g becomes in this case an important parameter: for $l_g \ll h$ the colloid gets almost entirely accumulated at the bottom boundary, and the system behaves as a single component fluid. When $l_g \geq h$, the

threshold for Rayleigh-Benard convection gradually increases to values of the order of several time the threshold for a single component fluid. While the parameters adopted in these studies partially mirror the ones of our sample, the separation ratio $\psi = -0.8$ adopted by Cherepanov and Smorodin corresponds to the condition where the Rayleigh-Bénard convection dominates over the solutal stabilization. By contrast, in the case investigated by us the sedimentation length is moderately high, $l_s/h = 20$, but the strong negative separation ratio $\psi = -3.5$ determines an accumulation of particles at the bottom boundary dominated by the Soret effect and affected only marginally by sedimentation.

Recent experimental studies have outlined the potentiality of the bistability of nanofluids with large negative separation ratio, like the one we studied in this work, to actively control heat transfer by switching between the conductive regime and the convective one (and vice-versa) exploiting the thermophilic behaviour of the nanoparticles [15, 16]. Cherepanov and Smorodin performed 2-dimensional simulations of thermophilic nanofluids with a separation ratio $\psi = -7.5$ heated from below mirroring the one used in these experiments. This study has been able to reproduce accurately the following quantitative aspects observed in experiments performed on a Hyflon MFA suspension of nanoparticles at a concentration of 4.0% w/w [15]: i) The presence of transient and stationary travelling wave regimes separated by a threshold Rayleigh number $Ra^* \approx 3400$; ii) the modifications determined by the presence of nanoparticles on the bifurcation diagram of the Nusselt number as a function of Rayleigh Number; iii) the diagram of the lifetime of travelling waves in the transient regime as a function of Rayleigh number.

Simulations along the same lines of the ones performed by Cherepanov and Smorodin on suspensions of Hyflon MFA nanoparticles should be able to describe effectively the experimental results provided by us in this publication, in particular the bifurcation diagram (**Figure 1**), and the lifetime of transient convection (**Figure 3**) in a suspension of Ludox nanoparticles.

DATA AVAILABILITY STATEMENT

The raw data supporting the conclusion of this article will be made available by the authors, without undue reservation.

AUTHOR CONTRIBUTIONS

AV conceived the study and wrote the paper. AP performed measurements. MC and AV coordinated research. All the authors analysed results and contributed to the manuscript.

FUNDING

Work partially supported by the European Space Agency, CORA-MAP TechNES Contract No. 4000128933/19/NL/PG.

ACKNOWLEDGMENTS

We thank M. Allevi, M. Bernardin, R. Cerbino, F. Comitani, and G. Donzelli for early discussion.

REFERENCES

1. Lighthill MJ. Waves in Fluids. *Comm Pure Appl Math* (2010) 20:267–93. doi:10.1002/cpa.3160200204
2. Carpineti M, Croccolo F, Vailati A. Levitation, Oscillations, and Wave Propagation in a Stratified Fluid. *Eur J Phys* (2021) 42:055011. doi:10.1088/1361-6404/ac0fba
3. Walden R, Kolodner P, Passner A, Surko CM. Traveling Waves and Chaos in Convection in Binary Fluid Mixtures. *Phys Rev Lett* (1985) 55:496–9. doi:10.1103/physrevlett.55.496
4. Kolodner P, Passner A, Surko CM, Walden RW. Onset of Oscillatory Convection in a Binary Fluid Mixture. *Phys Rev Lett* (1986) 56:2621–4. doi:10.1103/physrevlett.56.2621
5. Moses E, Fineberg J, Steinberg V. Multistability and Confined Traveling-Wave Patterns in a Convecting Binary Mixture. *Phys Rev A* (1987) 35:2757–60. doi:10.1103/physreva.35.2757
6. Heinrichs R, Ahlers G, Cannell DS. Traveling Waves and Spatial Variation in the Convection of a Binary Mixture. *Phys Rev A* (1987) 35:2761–4. doi:10.1103/physreva.35.2761
7. Kolodner P, Bensimon D, Surko CM. Traveling-wave Convection in an Annulus. *Phys Rev Lett* (1988) 60:1723–6. doi:10.1103/physrevlett.60.1723
8. Niemela JJ, Ahlers G, Cannell DS. Localized Traveling-Wave States in Binary-Fluid Convection. *Phys Rev Lett* (1990) 64:1365–8. doi:10.1103/physrevlett.64.1365
9. Kolodner P, Glazier JA, Williams H. Dispersive Chaos in One-Dimensional Traveling-Wave Convection. *Phys Rev Lett* (1990) 65:1579–82. doi:10.1103/PhysRevLett.65.1579
10. Lerman K, Bodenschatz E, Cannell DS, Ahlers G. Transient Localized States in 2d Binary Liquid Convection. *Phys Rev Lett* (1993) 70:3572–5. doi:10.1103/physrevlett.70.3572
11. Lerman K, Ahlers G, Cannell DS. Different Convection Dynamics in Mixtures with the Same Separation Ratio. *Phys Rev E* (1996) 53:R2041–R2044. doi:10.1103/physreve.53.r2041
12. Porta AL, Surko CM. Dynamics of Two-Dimensional Traveling-Wave Convection Patterns. *Phys Rev E* (1996) 53:5916–34.
13. Lerman K, Cannell DS, Ahlers G. Analysis of Transients for Binary Mixture Convection in Cylindrical Geometry. *Phys Rev E* (1999) 59:2975–85. doi:10.1103/physreve.59.2975
14. Aegertner CM, Surko CM. Effect of Lateral Boundaries on Traveling-Wave Dynamics in Binary Fluid Convection. *Phys Rev E* (2001) 63:046301.
15. Donzelli G, Cerbino R, Vailati A. Bistable Heat Transfer in a Nanofluid. *Phys Rev Lett* (2009) 102:104503. doi:10.1103/physrevlett.102.104503
16. Bernardin M, Comitani F, Vailati A. Tunable Heat Transfer with Smart Nanofluids. *Phys Rev E Stat Nonlin Soft Matter Phys* (2012) 85:066321. doi:10.1103/PhysRevE.85.066321
17. Ryskin A, Pleiner H. Thermal Convection in Colloidal Suspensions with Negative Separation Ratio. *Phys Rev E Stat Nonlin Soft Matter Phys* (2005) 71:056303. doi:10.1103/PhysRevE.71.056303

18. Shliomis MI, Smorodin BL. Onset of Convection in Colloids Stratified by Gravity. *Phys Rev E Stat Nonlin Soft Matter Phys* (2005) 71:036312. doi:10.1103/PhysRevE.71.036312
19. Smorodin BL, Cherepanov IN, Myznikova BI, Shliomis MI. Traveling-wave Convection in Colloids Stratified by Gravity. *Phys Rev E Stat Nonlin Soft Matter Phys* (2011) 84:026305. doi:10.1103/PhysRevE.84.026305
20. Cherepanov I, Smorodin B. Traveling Waves of a Colloidal Suspension in a Closed Cell. *Eur Phys J E* (2022) 45. doi:10.1140/epje/s10189-022-00192-4
21. Cherepanov IN, Smorodin BL. Influence of Sedimentation Length on the Convective Stability of a Colloidal Suspension. *J Exp Theor Phys* (2017) 125:1199–207. doi:10.1134/s1063776117120020
22. Cherepanov IN, Smorodin BL. Convection of strong Stratified Colloidal Suspension. *Microgravity Sci Technol* (2019) 31:517–25. doi:10.1007/s12217-019-09726-6
23. Batiste O, Knobloch E, Alonso A, Mercader I. Spatially Localized Binary-Fluid Convection. *J Fluid Mech* (2006) 560:149–58. doi:10.1017/s0022112006000759
24. Knobloch E. Spatially Localized Structures in Dissipative Systems: Open Problems. *Nonlinearity* (2008) 21:T45–T60. doi:10.1088/0951-7715/21/4/t02
25. Batiste O, Knobloch E. Simulations of Localized States of Stationary Convection in 3he-4he Mixtures. *Phys Rev E* (2005) 95:244501. doi:10.1103/PhysRevLett.95.244501
26. Batiste O, Knobloch E. Simulations of Oscillatory Convection in 3he-4he Mixtures in Moderate Aspect Ratio Containers. *Phys Fluids* (2005) 17:064102. doi:10.1063/1.1920349
27. Mercader I, Alonso A, Batiste O. Spatiotemporal Dynamics Near the Onset of Convection for Binary Mixtures in Cylindrical Containers. *Phys Rev E Stat Nonlin Soft Matter Phys* (2008) 77:036313. doi:10.1103/PhysRevE.77.036313
28. Baaske P, Bataller H, Braibanti M, Carpineti M, Cerbino R, Croccolo F, et al. The NEUF-DIX Space Project - Non-EquilibriUm Fluctuations during DIffusion in compleX Liquids. *Eur Phys J E* (2016) 39. doi:10.1140/epje/i2016-16119-1
29. Vailati A, Baaske P, Bataller H, Bolis S, Braibanti M, Carpineti M, et al. Giant Fluctuations Induced by thermal Diffusion in Complex Liquids. *Microgravity Sci Technol* (2020) 32:873–87. doi:10.1007/s12217-020-09815-x
30. Giavazzi F, Savorana G, Vailati A, Cerbino R. Structure and Dynamics of Concentration Fluctuations in a Non-equilibrium Dense Colloidal Suspension. *Soft Matter* (2016) 12:6588–600. doi:10.1039/c6sm00935b
31. Cerbino R, Vailati A, Giglio M. Soret Driven Convection in a Colloidal Solution Heated from above at Very Large Solutal Rayleigh Number. *Phys Rev E Stat Nonlin Soft Matter Phys* (2002) 66:055301. doi:10.1103/PhysRevE.66.055301
32. Mazzoni S, Giavazzi F, Cerbino R, Giglio M, Vailati A. Mutual Voronoi Tessellation in Spoke Pattern Convection. *Phys Rev Lett* (2008) 100:188104. doi:10.1103/physrevlett.100.188104
33. Giavazzi F, Vailati A. Scaling of the Spatial Power Spectrum of Excitations at the Onset of Solutal Convection in a Nanofluid Far from Equilibrium. *Phys Rev E Stat Nonlin Soft Matter Phys* (2009) 80:015303. doi:10.1103/PhysRevE.80.015303
34. Alonso A, Mercader I, Batiste O. Pattern Selection Near the Onset of Convection in Binary Mixtures in Cylindrical Cells. *Fluid Dyn Res* (2014) 46:1–18. doi:10.1088/0169-5983/46/4/041418

Conflict of Interest: The authors declare that the research was conducted in the absence of any commercial or financial relationships that could be construed as a potential conflict of interest.

frontiers | Frontiers in Physics

TYPE Original Research
PUBLISHED 31 August 2022
DOI 10.3389/fphy.2022.976515

OPEN ACCESS

EDITED BY
Roberto Cerbino,
University of Vienna, Austria

REVIEWED BY
Nuno A. M. Araújo,
University of Lisbon, Portugal
Nicoletta Gnan,
National Research Council (CNR), Italy

*CORRESPONDENCE
Ylann Rouzaire,
rouzaire.ylann@gmail.com

SPECIALTY SECTION
This article was submitted to Soft Matter Physics,
a section of the journal
Frontiers in Physics

RECEIVED 23 June 2022
ACCEPTED 01 August 2022
PUBLISHED 31 August 2022

CITATION
Rouzaire Y and Levis D (2022), Dynamics of topological defects in the noisy Kuramoto model in two dimensions. *Front. Phys.* 10:976515.
doi: 10.3389/fphy.2022.976515

Dynamics of topological defects in the noisy Kuramoto model in two dimensions

Ylann Rouzaire [1,2,3]* and Demian Levis [1,2]

[1]Departament de Física de la Materia Condensada, Universitat de Barcelona, Barcelona, Spain, [2]UBICS University of Barcelona Institute of Complex Systems, Barcelona, Spain, [3]CECAM, Centre Européen de Calcul Atomique et Moléculaire, Ecole Polytechnique Fédérale de Lausanne (EPFL), Lausanne, Switzerland

We consider the two-dimensional (2D) noisy Kuramoto model of synchronization with short-range coupling and a Gaussian distribution of intrinsic frequencies, and investigate its ordering dynamics following a quench. We consider both underdamped (inertial) and over-damped dynamics, and show that the long-term properties of this intrinsically out-of-equilibrium system do not depend on the inertia of individual oscillators. The model does not exhibit any phase transition as its correlation length remains finite, scaling as the inverse of the standard deviation of the distribution of intrinsic frequencies. The quench dynamics proceeds via domain growth, with a characteristic length that initially follows the growth law of the 2D XY model, although is not given by the mean separation between defects. Topological defects are generically free, breaking the Berezinskii-Kosterlitz-Thouless scenario of the 2D XY model. Vortices perform a random walk reminiscent of the self-avoiding random walk, advected by the dynamic network of boundaries between synchronised domains; featuring long-time super-diffusion, with the anomalous exponent $\alpha = 3/2$.

KEYWORDS

topological defects, synchronisation, active matter, langevin dynamics, anomalous diffusion, out-of-equilibrium systems

1 Introduction

Back in the XVII-th century, Huygens realised that two pendulum clocks, when sitting on the same board, start, after some transient time, to beat at the same frequency in phase or in anti-phase [1]. Such spontaneous temporal coordination of coupled oscillatory objects is referred to as synchronization. Since then, the study of synchronization in large populations of oscillators has remained a recurrent problem across different sciences, ranging from physics to biology, computational social sciences or engineering [2, 3].

Much progress in the understanding of synchronisation has been achieved through the detailed analysis of simplified model systems. In this context, the Kuramoto model of phase coupled oscillators has (and still does) played a central role [4, 5]. The original version of the model [4], considering only all-to-all interactions, shows that global phase

synchronisation can be achieved for large enough coupling, relative to the dispersion of the oscillators' intrinsic frequencies.

Persistent oscillations, obviously need a constant energy supply, which at the microscopic scale is dissipated into the environment, which also provides a source of noise. Thus, to describe oscillator systems at the micro-scale, such as genetic oscillators [6], noise should be taken into account, as well as shorter-range interactions, leading to finite-dimensional noisy extensions of the Kuramoto model [7]. The situation in this case, which is the object of the present study, is quite more involved than the original Kuramoto model and the literature far more scarce [8–10].

The problem of synchronisation in physical sciences has more recently experienced a resurge of interest in the context of active matter. Active matter stands for a class of soft matter systems, composed of coupled interacting agents that convert energy from their surrounding into some kind of persistent motion [11], such as biological units oscillating at a given rate. Such injection of energy at the level of each single constituent, drives active systems out-of-equilibrium. At the collective level, interactions between active agents result in the emergence of a variety of collective states. In particular, a broad class of active systems can spontaneously self-organise into synchronised states characterised by the coherent motion of self-propelled individuals, a phenomenon called flocking (a term borrowed from the spectacular example of the murmuration of starling birds) [12]. The interpretation of flocking in terms of synchronisation of active oscillators has been pointed out in a number of recent works [13–15].

Closer to the standard synchronisation set-up of oscillators lying on a static substrate, synchronised states have been studied in numerous active matter systems in the absence of self-propulsion. A salient example are active filament carpets, such as cilia or flagella attached on a surface. Cilia, for instance, perform a beating cycle (usually modelled as a phase oscillator) generating a net hydrodynamic flow (at low Reynolds number) that affects the motion of their neighbours [16–18]. Such filaments, thought as coupled oscillators, might then synchronise, to optimise a biological function such as propelling microorganisms. Chiral colloidal fluids composed of spinning colloidal magnets constitute another promising novel venue to investigate synchronisation at the micro-scale [19–22]. In these systems, an external oscillatory field drives the colloidal magnets, making them rotate around their body axis at a given frequency imposed by the field.

Here we investigate the collective dynamics of Kuramoto oscillators, with short range coupling, in two dimensions (2D), in contact with a thermal bath and with a Gaussian distribution of intrinsic frequencies. In the absence of driving, or intrinsic oscillations, the system is equivalent to the 2D XY model, which exhibits a topological Berezinskii-Kosterlitz-Thouless (BKT) transition driven by the unbinding of topological defects [23–25]. As such, it provides a natural playground to study the role played by topological defects in systems of coupled oscillators. The dynamics of topological defects in out-of-equilibrium systems has been extensively investigated over the last decade in soft active systems [11], where it has been found that, in many instances, defects self-propel, or super-diffuse [10, 21, 26, 27]. A recent study of this model shows that defects become free upon self-spinning, although two regimes remain clearly distinct, a vortex-rich and a vortex-poor one [10]. Here we focus our attention on the dynamics of the system following a quench, from a random initial state, where many defects proliferate, to the low temperature (noise) regime where defects are scarce. The coarsening dynamics following an infinitely rapid quench has been extensively studied in model statistical physics systems [28], but has received little attention in the context of synchronisation [29]. Of particular interest for us, the study of the coarsening dynamics of the 2D XY model has shown that topological defects, here vortices, diffuse, interact and annihilate, in a way that sheds light on the mechanisms underlying the non-equilibrium relaxation of the system [30–34]. In this contribution, we aim at characterising the dynamics of the noisy Kuramoto model in 2D, to examine the random motion of vortices and discuss the fundamental differences displayed by the system as compared to its equilibrium limit.

We first introduce the model and its governing Langevin equation in Section 2. The main results are presented in Section 3: in section 3.1, we first focus on the overdamped regime and study the coarsening dynamics of the system following different quench protocols, focusing our analysis on the evolution of different correlation lengths and density of topological defects. We then study the relaxation dynamics in the underdamped regime in section 3.2 to show that the inertia of individual spins (or oscillators) does not influence the overall large-scale dynamics of the system. Section 4 is devoted to the defects's dynamics. We first discuss the breakdown of the Berezenskii-Kosterlitz-Thouless scenario in section 4.1, by investigating the effective interactions between defects. In section 4.2, we then describe the spontaneous creation process of vortices and the complex dynamics they exhibit. We argue that even though the trajectories of defects are very much reminiscent of genuine self-avoiding random walks, the full displacement statistics indicate that they are not strictly equivalent.

2 The model

We consider a set of N phase oscillators sitting on the nodes of a $L \times L$ square lattice with periodic boundary conditions (PBC). The evolution of their phase θ_i is described by the Kuramoto model. The governing equations of motion are given by the following set of coupled Langevin equations

$$m\ddot{\theta}_i + \gamma\dot{\theta}_i = \sigma\omega_i + J\sum_{j\in\partial_i}\sin\left(\theta_j - \theta_i\right) + \sqrt{2\gamma k_B T}\,\nu_i \qquad (1)$$

where the sum runs over the four nearest-neighbours of spin i, denoted by ∂_i, ν_i is a Gaussian white noise of unit variance and zero mean and γ the damping coefficient. The system is thus in contact with a thermal bath at temperature T. The driving amplitude ω_i is drawn from a Gaussian distribution with zero mean and unit variance. [Since Eq. 1 is invariant under the transformation $\theta \to \theta - \Omega t$, one can choose a distribution of frequencies with zero-mean without loss of generality.]. The amplitude σ quantifies the dispersion of the intrinsic frequencies.

In the absence of intrinsic persistent oscillations, i.e. $\sigma = 0$, the model Eq. 1 is equivalent to the 2D XY model with non-conserved order parameter dynamics [35]. Indeed, Eq. 1 can be rewritten as

$$m\ddot{\theta}_i = -\gamma\dot{\theta}_i + \sigma\omega_i - \frac{\partial H}{\partial\theta_i} + \sqrt{2\gamma k_B T}\,\nu_i \qquad (2)$$

where

$$H = -J\sum_{\langle i,j\rangle}\mathbf{S}_i\cdot\mathbf{S}_j, \quad \mathbf{S}_i = (\cos\theta_i,\ \sin\theta_i) \qquad (3)$$

is just the classical XY Hamiltonian (here the sum runs over all the links of the lattice, or, equivalently, all nearest neighbours pairs). This system exhibits a BKT transition at a critical temperature $T_{KT} \approx 0.89$ [36, 37]. The distribution of natural frequencies introduces quench disorder in the XY model. The way it is introduced though, is fundamentally different to what is typically done in disordered systems, namely, adding disorder in the interactions or an external random field [38–40]. The distribution of intrinsic frequencies drives the system out-of-equilibrium. Adding a term $\sigma\sum_i\theta_i\omega_i$ in the Hamiltonian $H \to H' = H + \sigma\sum_i\theta_i\omega_i$, would provide the same equation of motion Eq. 1 when writing: $m\ddot{\theta}_i + \gamma\dot{\theta}_i = -\frac{\partial H'}{\partial\theta_i} + \sqrt{2\gamma k_B T}\,\nu_i$. However, H' is now unbounded, as a result of the constant injection of energy into the system needed in order to sustain the intrinsic oscillations. Thus, the system is intrinsically out-of-equilibrium and cannot be mapped to random field or random bond XY models.

In equilibrium conditions ($\sigma = 0$), the nature of the dynamics does not affect the steady-properties of the system, as long as it fulfills detailed balance. Most studies on the dynamics of the 2D XY model have been performed in the overdamped limit, namely

$$\gamma\dot{\theta}_i = \sigma\omega_i - \frac{\partial H}{\partial\theta_i} + \sqrt{2\gamma k_B T}\,\nu_i, \qquad (4)$$

in its Langevin version, or, equivalently, using single-spin flip Monte Carlo dynamics [33, 34, 36, 37, 40].

However, in non-equilibrium conditions, the specific features of the dynamics might affect the resulting large scale behavior at long times. The dynamics of the model introduced by Kuramoto was also originally overdamped. Later on, the model was extended to include inertia [41–43]. Here we study both the model with underdamped and overdamped dynamics following Eqs 2, 4, respectively.

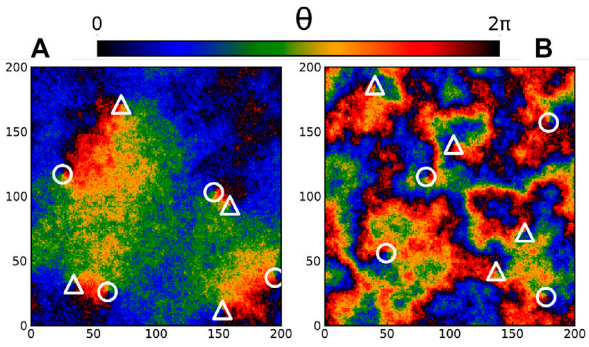

FIGURE 1
Snapshots for $T = 0.2$, **(A)** $\sigma^2 = 0$ and **(B)** $\sigma^2 = 0.1$. The phase of each oscillator is represented by a color scale. Vortices (antivortices) are represented by circles (triangles).

To identify the key control parameters of the present model, we rewrite the equations of motion in their dimensionless form (see Supplementary Material (SM) [44]), expressing time in units of γ/J. This leads to the following set of quantities: 1) the reduced temperature $\tilde{T} = k_B T/J$, 2) the reduced frequency dispersion $\tilde{\sigma} = \sigma/J$ and, for inertial dynamics, 3) the reduced inertia $\tilde{m} = m\,J/\gamma^2$. From now on, we shall make use of these reduced parameters and drop the tilde $\tilde{T}, \tilde{\sigma}, \tilde{m} \to T, \sigma, m$.

We integrate numerically Eqs 2, 4 using a modified velocity Verlet algorithm as in [41] and standard Euler-Mayurama scheme (details provided in the SM [44]). The typical system size used is $L = 200$, if not stated otherwise.

3 Results

3.1 Overdamped dynamics

We first study in this section the dynamics of the model in the overdamped limit, i.e., Eq. 4, following a infinitely rapid quench from an initially disordered state where all the phases are picked from a homogeneous distribution between 0 and 2π.

In order to illustrate the nature of the low temperature state, we show in Figure 1 representative steady state snapshots for **(A)** $T = 0.2$ and $\sigma^2 = 0$ **(B)** $T = 0.2$ and $\sigma^2 = 0.1$. Both snapshots contain the same number of defects: four vortices (circles) and four antivortices (triangles), visually identified as the points where black, red, yellow, green and blue regions meet. This correspond to plaquettes with a winding number $q = \pm 1$, defined by the discrete circulation of the phase differences along a plaquette, namely $\sum_{\square}\Delta\theta_{ij} = 2\pi q$.

At equilibrium, when spins are not forced, one recovers the classical XY model picture, with large regions of spins sharing the

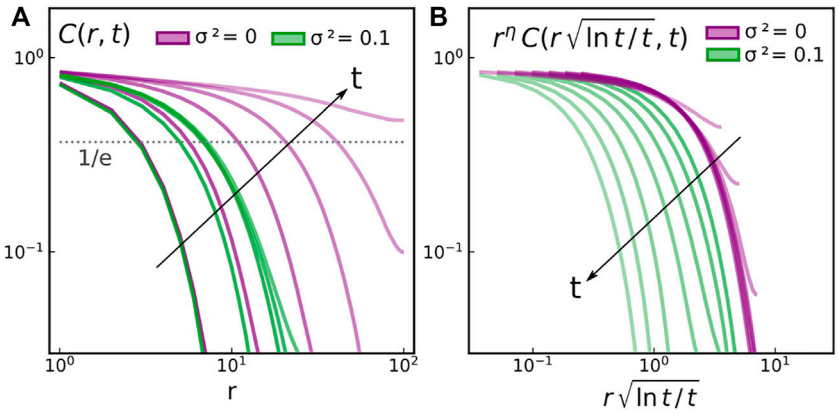

FIGURE 2
Time evolution of **(A)** the space correlation function $C(r, t)$ at different times $t \approx 4, 20, 100, 400, 2000, 10000$ **(B)** the rescaled correlation function ($\eta = T/2\pi$ from the spin-wave theory) against the rescaled time. In both panels, the purple curves correspond to the XY model at $T = 0.4$ and the green curves correspond to a forced system at $T = 0.4$ and $\sigma^2 = 0.1$. Longer times are represented by lighter colors, as the arrows indicate.

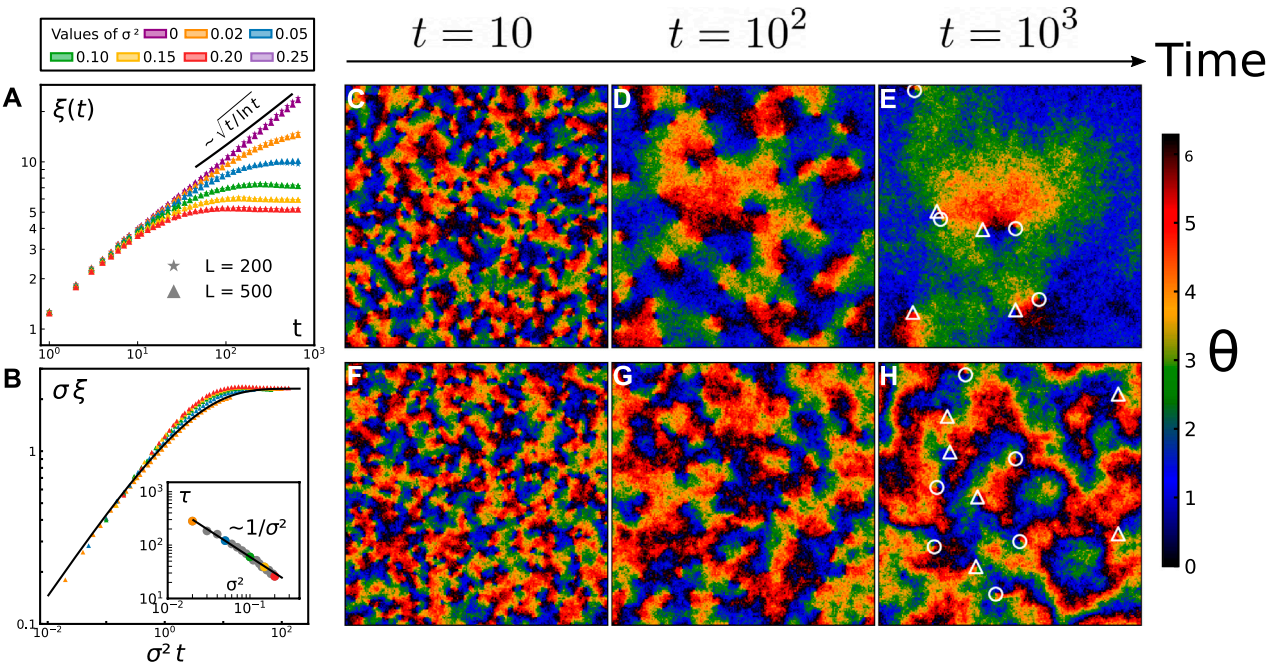

FIGURE 3
Time evolution of the characteristic length scale **(A–B)** illustrated by typical snapshots of a 200 × 200 system **(C–H)**. **(A)** Growth of the typical length scale $\xi(t)$ for $T = 0.4$ and several σ, as indicated in the legend above (same colors as in Figures 2, 4); **(B)** the same data where ξ and t have been rescaled by σ and σ^2, respectively. All curves collapse onto a single master curve $f(x) = a(1 - \exp(-b\sqrt{x}))$ with $a = 2.3$ and $b = 0.65$. **Inset:** variation of the transients time τ defined in Eq. 9 against the self-spinning intensity. **(C–D–E)** Representative configurations at different times showing the evolution of the system after a quench (for $T = 0.2$ and $\sigma^2 = 0$). The phase of each oscillator is represented by a cyclic color scale. In the last panel only, vortices (anti-vortices) are represented by circles (triangles). **(F–G–H)** Representative configurations at different times now for $T = 0.2$ and $\sigma^2 = 0.1$.

same color, ending at topological defects of opposite charge. As the Kosterlitz-Thouless theory [23, 24] predicts, those defects visually come in pairs. From the snapshots one already observes a clear connection between the typical size of correlated domains of mostly parallel spins, and the typical distance between defects. We will come back to this point later on.

On the contrary, upon self-spinning, the first impression is qualitatively different, even though the number of defects is identical in both panels (here 8). The phase field pattern emanating from the vortices does not extend over large distances, and the typical size of oriented domains seem decoupled from the defects' locations, as seen in Figure 1B. Ordered regions are in this case rather localized, and one can no longer pair vortices by visual inspection of the snapshots.

3.1.1 Coarsening dynamics

To gain quantitative insight, we compute the spin-spin correlation function

$$C(r,t) = \langle \cos(\theta(r,t) - \theta(0,t)) \rangle, \tag{5}$$

where the angular brackets denote the average over spins and independent realisations of both thermal noise and quenched frequencies and r is the lattice distance between two oscillators, or spins. For $\sigma = 0$ equilibrium correlations in the low-T regime, $T < T_{KT}$, decay algebraically in space:

$$C_0(r) \sim r^{-\eta(T)}, \ \eta(T) = T/2\pi, \tag{6}$$

a signature of quasi-long-range order. For $\sigma > 0$, it has been shown that steady state correlations decay exponentially in space [10].

$$C_\sigma(r) \sim e^{-r/\xi_\infty}, \tag{7}$$

at any finite temperature, signalling the absence of quasi-long-range order in the system.

We show in Figure 2A the spatial decay of $C(r, t)$ at different times following a quench to $T = 0.4$, for $\sigma^2 = 0$ (in purple) and for $\sigma^2 = 0.1$ (in green). The data is shown in a log-log scale to easily discriminate between algebraic and geometric decays. As time goes on, spatial correlations build up in the system, indicating the growth of ordered structures, to finally collapse on the before mentioned long-time behaviour. To study the coarsening, or phase ordering, dynamics, we define a correlation length $\xi(t)$, extracted from $C(\xi(t), t) = 1/e$ and plot its time evolution in Figure 3A for different values of σ. For $\sigma = 0$, we recover without surprise the well-known scaling $\xi(t) \sim \sqrt{t/\log t}$ [30, 31, 34]. The logarithmic correction takes root in the logarithmic dependence of a defect mobility on its size; note that it is only relevant for large t. Such logarithmic correction to the usual $\sim \sqrt{t}$ growth law in systems with non-conserved order parameter dynamics also appears in all related quantities such as the evolution of the number of vortices n or the mean square displacement (MSD) of a single vortex, as we shall discuss in more detail later on. As shown in Figure 2B the dynamic scaling hypothesis [45] is consistently fulfilled for $\sigma = 0$, as all the curves $C(r, t)$ collapse into a single master curve in the scaling regime, once the space variable has been rescaled by the characteristic growing length.

For $\sigma > 0$, the results qualitatively differ: independently of the system size L, the growing length $\xi(t)$ saturates at a finite value ξ_∞ at long times. Such steady value decreases as σ increases. This is consistent with the limit case $\sigma \to \infty$, corresponding to a system of decoupled oscillators. Interestingly, Figure 3B shows that all curves for $\sigma > 0$ collapse into a single master curve if both distances and time are rescaled. This master curve follows $f(x) = a(1 - \exp(-b\sqrt{x}))$, from which we conclude that

$$\xi(t) = \frac{a}{\sigma}\left(1 - e^{-b\sqrt{\sigma^2 t}}\right), \tag{8}$$

with $a = 2.3$, a constant related to the long time limit of ξ, and $b = 0.65$.

Eq. 8 contains information about both short time and long time dynamics. At short times, one recovers the short-time dynamics of the XY model. Indeed, by expanding $\xi(t)$ to first order in t, one gets $\sigma\,\xi(t) \approx ab\sqrt{t}$; $ab = 1.5$ thus represent the slope of the initial $\sim \sqrt{t}$ coarsening. At long times, in the steady state, the characteristic length boils down to $\lim_{t\to\infty}\xi(t) = \xi_\infty \sim 1/\sigma$, as found in [10] using a simplified 1D argument, which we sum up hereafter. Let's consider, for the sake of clarity, two neighbouring spins i and j at $T = 0$ sitting on the nodes of a 1D chain. One can easily show that their steady-state angle difference is no longer $\Delta\theta = 0$ as in equilibrium, but instead $\Delta\theta = \arcsin(\Delta\omega/2)$, where $\Delta\theta = |\theta_i - \theta_j|$ and $\Delta\omega = |\omega_i - \omega_j|$. If we now consider the phase difference accumulated along n links in the chain, and replace the phase difference between each pair of nearest-neighbour oscillators by its expectation value $\overline{|\Delta\theta|}$, one gets a characteristic length $\propto 1/\overline{|\Delta\theta|} \sim \sigma^{-1}$. Note that in addition to this argument, the same scaling can be tackled and understood from a different angle, involving topological defects; we will come back to this point later on.

At intermediate times, the system crosses over from its short-time dynamics, following the passive XY scaling, to its steady state. We define this transient time $\tau(\sigma)$ as the time for which the equilibrium correlation length is equal to the steady state out-of-equilibrium one:

$$\xi(\sigma = 0, \tau) = \xi(\sigma, t \to \infty). \tag{9}$$

We plot it in the inset of Figure 3B and obtain $\tau \sim 1/\sigma^2$: the wider the frequency distribution is, the faster is the relaxation process. This intuitive tendency is easily captured by a trivial scaling argument: the logarithmic correction is a long term effect, so we drop it and assume for the sake of simplicity that ξ first follows an equilibrium growth $\sqrt{t}$. As it eventually saturates at a steady state value $\xi_\infty \sim 1/\sigma$, the crossover between both regimes thus occurs when

$$\sqrt{\tau} \sim \xi_\infty \sim 1/\sigma \Rightarrow \tau \sim 1/\sigma^2, \tag{10}$$

confirming the scaling naturally contained in Eq. 8.

We complete the picture by reporting the total number of defects $n(t)$ for different driving strengths σ in Figure 4A. At equilibrium (purple), one obtains $n(t) \sim \log t/t$. The similarity of

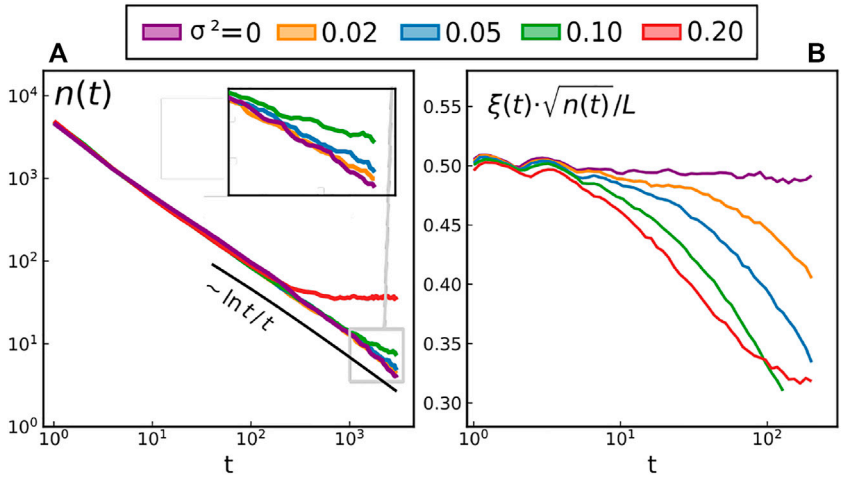

FIGURE 4
Time evolution of **(A)** the total number of defects n for different forcing intensities and $T = 0.4$ **(B)** the quantity $\xi\sqrt{\rho}$ where $\rho = n/L^2$ is the defect density. Note that because the defects are homogeneously distributed, $1/\sqrt{\rho}$ is the average distance between two of them.

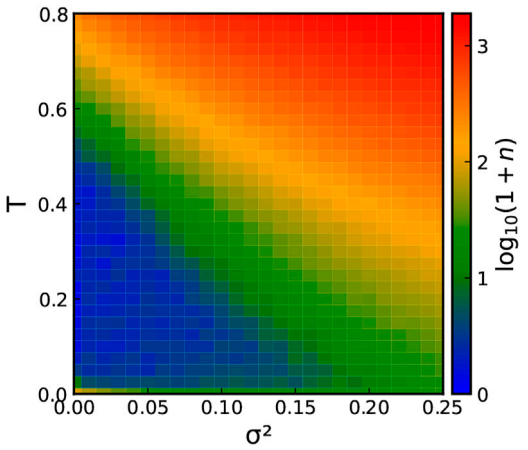

FIGURE 5
Color map of the number of the number of defects n (in log-scale, $\log_{10}(1 + n)$) over the parameter space $\sigma^2 - T$ in the steady state. In the blue region defects are scarce in the system, while in the red one the system is populated by lots of defects (the number growing exponentially fast as one leaves the blue region).

the equilibrium long-term scaling for $\xi(t)$ and for $n(t)$ is not a coincidence. The correlation length ξ is intimately related to the total number of defects n in the equilibrium XY model. Indeed, as a first approximation, ξ is given by the average distance between defects; the system being homogeneous, it follows that $\xi \sim 1/\sqrt{n}$. We indeed recover that at equilibrium, $\xi\sqrt{n}$ is constant over time, cf. Figure 4B. For $\sigma > 0$, $n(t)$ eventually saturates at a finite steady state value, as the number of defects at a given temperature increases with σ. This departure from the XY equilibrium behavior is also clearly reflected by the fact that ξ is no longer given by the typical distance between defects, as shown in Figure 4B. The steady state of the Kuramoto model is characterized by both a finite number of defects and a finite correlation length which are, *a priori*, unrelated. As such, the quench dynamics of the system is no longer fully governed by a single growing length, as its equilibrium counterpart, and the dynamics of the vortices have to be considered in more detail.

3.1.2 Topological defects

As a useful reference for our analysis, we first report a map of the total number of vortices in the steady state over the $\sigma^2 - T$ plane in Figure 5. As T and σ^2 decrease, the dynamics gets slower and slower, up to the $T = 0$ limit case where the self-spinning alone cannot help annihilating pairs of defects: the system initially disordered remains stuck in a metastable state with a lot more vortices than the number of vortices it would exhibit if relaxed from an initially ordered state.

We state once again that the crossover from the defect-rare (blue region) to the defect-rich (red region) regime does not result from an actual phase transition: there is no qualitative change in the correlation length as one moves across the phase space (the system only exhibits short-range order at any $\sigma \neq 0$ for all $T \geq 0$). At contrast with the standard literature of the XY model [23, 46], we do not classify vortices into free and bounded here. Indeed, as mentioned above and discussed in more detail below, the core mechanism responsible for the BKT phase transition, namely the defects' unbinding at *a finite* temperature, breaks down upon self-spinning. In the driven model, topological defects are found to be genuinely free at *any* temperature $T > 0$. In other words, there exists no finite

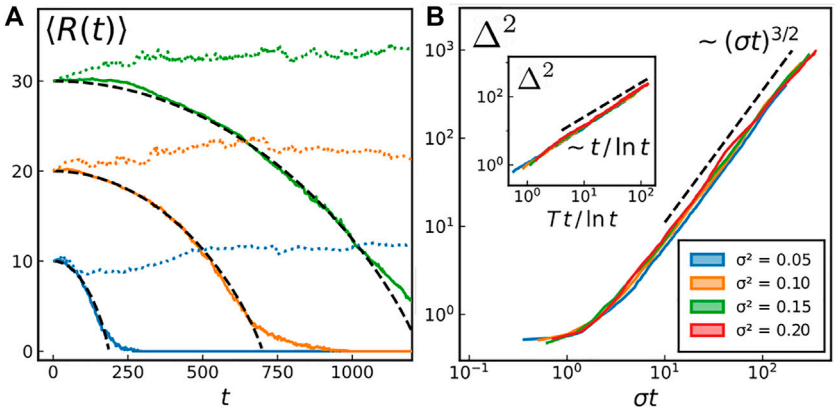

FIGURE 6
(A) Vortex-antivortex separation, averaged over 120 independent runs, for three different initial vortex-antivortex distances R_0 (blue: $R_0 = 10$, orange: $R_0 = 20$ and green: $R_0 = 30$). Full colored lines correspond to $T = 0.1$ and $\sigma^2 = 0$. Dotted colored lines correspond to $T = 0.1$ and $\sigma^2 = 0.1$. Black dashed lines are the predictions for an overdamped dynamics with a Coulomb interaction potential Eq. 11. **(B)** Mean square displacement (MSD) $\Delta^2(t) = \langle(\mathbf{r}(t) - \mathbf{r}(0))^2\rangle$ against time, at $T = 0.05$ for different σ. **Inset**: MSD for the XY model ($\sigma = 0$) for different temperatures ($T = 0.2, 0.3, 0.4, 0.5$ from blue [left] to red [right]).

temperature at which vortices are bounded into pairs. While two XY defects of opposite charge attract each other with a logarithmic potential, we find that the defects, upon self-spinning, generically unbind at any $T \geq 0$ and $\sigma > 0$. We prove it by tracking vortices in time, and considering the average distance between two defects. To do so, we initialize the system in a configuration with a vortex-antivortex pair at a distance R_0, enforcing PBC (cf. SM [44] for details). We then let the system evolve at low-T and low-σ such that there is no (or very few) spontaneous creation of vortices. We monitor the distance $R(t)$ between our two defects and present the results in Figure 6A.

As shown in Figure 6A, the XY model data is in perfect agreement with the overdamped description

$$\dot{R} \log R = V'(R) \tag{11}$$

where $V(R) \propto \log R$, a Coulomb 2D potential [30]. For the Kuramoto model, the vortex-antivortex distance $R(t)$ remains in average equal to their initial distance R_0, proving that there is no distinct effective potential between them. One could naively attribute this feature solely to the non-equilibrium nature of the system. However, deciphering the impact of a non-equilibrium drive on the long-range properties of a system on general grounds is a challenging task and one is usually constrained to rely on specific examples where this question has been addressed. For instance, it has been shown that the general BKT scenario remains valid (at least not so far from equilibrium) for an XY model with exponentially correlated thermal noise [47] and for the 2D solid-hexatic transition of self-propelled disks [48, 49]. In the present model system though, the BKT scenario breaks down.

Another remarkable property of topological defects upon self-spinning is found in the statistics of their displacement: they feature anomalous diffusion, their mean-square displacement $\Delta^2(t) \sim t^{\alpha}$, with $\alpha = 3/2$ (i.e., super-diffusion). Once again we investigate the dynamics of vortices by tracking them. Since, as discussed earlier, defects are free, we can now focus on the motion a single defect. To do so, we prepare an initial configuration hosting a single +1 defect at the center of the simulation box. One can exclusively focus on + 1 vortices without loss of generality because the equation of motion 1) is statistically invariant under a change of variable $\theta \to -\theta$ (as long as the distribution of the $\{\omega_i\}$ is centered) and such a transformation transforms a +1 vortex into a −1 anti-vortex. The dynamics of ±1 defects are thus statistically identical. We then let the system evolve at low-T and low-σ ensuring that 1) new defects are not spontaneously created and 2) the simulation box is large enough such that boundary effects are negligible. The mean square displacement (MSD) thus obtained is shown in Figure 6B. For the XY model (inset of **6B**) and at long times, it follows

$$\Delta^2(t) = \langle(\mathbf{r}(t) - \mathbf{r}(0))^2\rangle \sim t \,/\, \log t, \tag{12}$$

showing the expected correction to the normal diffusion scaling, due to the logarithmic dependence of the defect mobility on its size [30] [$\mathbf{r}(t)$ being the position of the vortex in the lattice at time t.].

Upon self-spinning, the defects become super-diffusive and the MSD (cf. Figure 6B) instead follows

$$\Delta^2(t) \sim (\sigma t)^{3/2}. \tag{13}$$

The σ-dependence of the vortex dynamics enters through a rescaling of time: the typical time associated with its motion

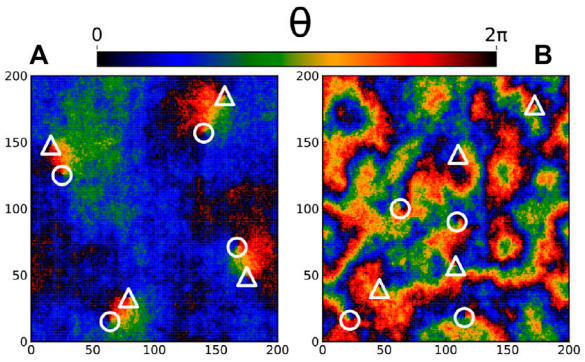

FIGURE 7
Snapshots for $m = 1$, $T = 0.2$, **(A)** $\sigma^2 = 0$ and **(B)** $\sigma^2 = 0.1$. The phase of each oscillator is represented by a color scale. Vortices (antivortices) are represented by circles (triangles).

along a domain is proportional to its typical size $\xi \sim 1/\sigma$. A careful characterisation of the stochastic motion of the defects will be presented in Section 4.2.

3.2 Underdamped dynamics

The nature of the dynamics, being overdamped or underdamped, does not have any impact on the long-time, large-scale properties of a system as long as its dynamics fulfil detailed balance. If this defining feature of equilibrium is satisfied, the steady-states obey Boltzmann statistics. For the Kuramoto model, being out-of-equilibrium, different ways of exploring the configuration space might lead to different steady large scale behaviour [41–43]. We are thus interested in putting into test the robustness of our results to the presence of inertial effects.

We first explore the steady states produced by letting the model Eq. 2, with inertia, relax from an initially disordered state with many vortices, to a state with only a few of them (i.e. the low temperature regime). If we look at typical snapshots of the steady state, Figure 7 (for the same parameter values in Figure 1 but $m = 1$), we observe basically the same features as in the overdamped case: for $\sigma = 0$ we find oppositely charged defects pairs visually connected by a phase field reminiscent of the magnetic field lines generated by a planar magnet, while for $\sigma > 0$ vortices are surrounded by a phase texture that makes difficult pairing them by eye, featuring synchronised domains of different shapes and sizes.

3.2.1 Coarsening dynamics

We now turn into the relaxation dynamics of the model with inertia following a quench from an initially disordered state. We investigate the same dynamical quantities as for the overdamped regime (cf. Figures 2–4), varying the inertia from $m = 10^{-2}$ to 10 and comparing them to their overdamped counterparts (in blue, $m = 0$). The results are reported in Figure 8.

At equilibrium, the results confirm that we do recover the same long term values for ξ and n independently from the inertia m, cf. Figures 8A,C. The results also indicate that, even in the presence of self-spinning, the inertia does not affect significantly the long-time behavior as one recover the same steady state values for values of m covering three orders of magnitude (see Figures 8B,D). The short-time dynamics is however affected by the inertia of individual rotors.

3.2.2 Topological defects

We now turn back to topological defects and shall see that, surprisingly, their MSD is not affected by the inertia of individual oscillators. We resort to the same protocol (track a single defect over time in a big system with free boundaries) and plot the result in Figure 9.

We recover the same (sub)diffusive motion for the XY model and the super-diffusion with the same exponent in the presence of self-spinning.

Overall, our results are robust as they indicate that the long-term properties of the system are not affected by the inertia of the underlying individual oscillators. We emphasis that this result is new and somehow surprising as, beyond the fact that there are no general guidelines for out-of-equilibrium systems, including inertia in a model of coupled oscillators can yield dramatic changes. For instance, in the *globally* coupled Kuramoto model inertia changes the order of the disordered/synchronised transition from second to first order [41–43, 50]. It is therefore remarkable that this does not happen in a model of *locally* coupled oscillators.

And finally, we have seen that a non-equilibrium forcing $\sigma > 0$ dramatically changes the MSD regime from sub-diffusive to super-diffusive.

4 Discussion

4.1 The fate of the BKT transition

The BKT transition scenario usually occurs when topological defects interact with a long-ranged $\sim 1/r$ force, in 2D, establishing quasi-long range order at low temperatures. After a quench across such a phase transition, due to the collective behaviour of topological defects, the typical length scale grows as $\xi \sim \sqrt{t/\log t}$. Such behaviour is driven by the diffusion and annihilation of defects, whose number decreases as $n \sim 1/\xi^2$.

In contrast, in the presence of intrinsic spinning, the field disturbances generated by the defects only expand over relatively short length scales, at any temperature. Consider the equation of

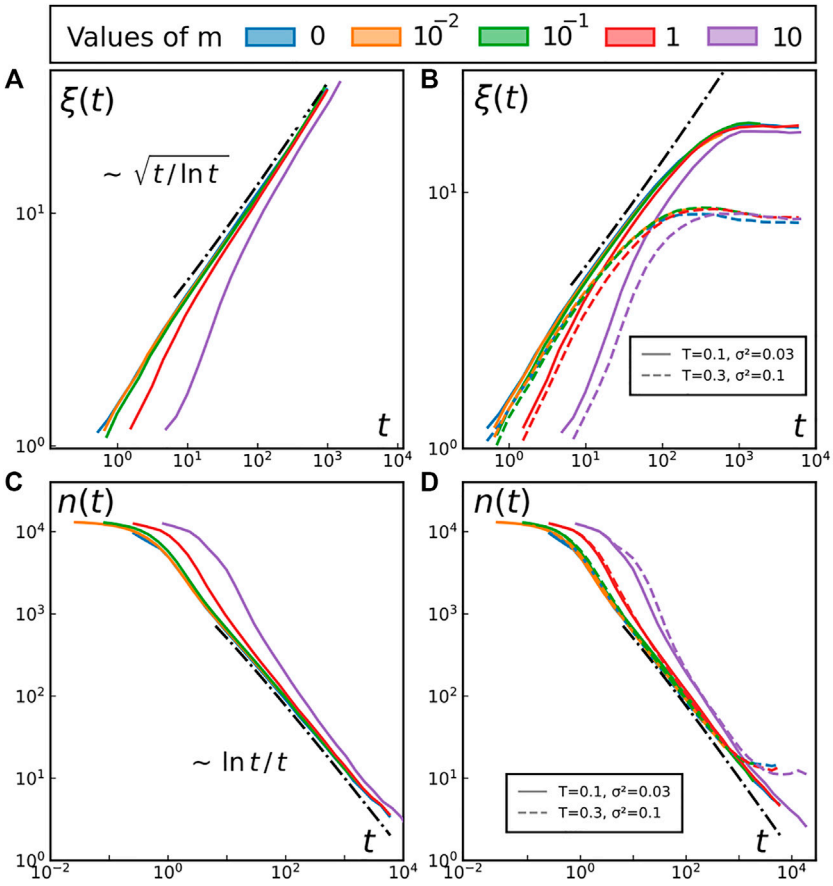

FIGURE 8
Relaxation from an initially disordered state. Different colours represent different inertia m for all four panels, as indicated at the top of the figure. **Top row:** Time evolution of the correlation length $\xi(t)$ for **(A)** the XY model at $T = 0.2$ and for **(B)** the driven system at the different values of T and σ. **Bottom row:** Time evolution of the total number of defects $n(t)$ for **(C)** the XY model at $T = 0.2$ and for **(D)** the driven system at the different values of T and σ. We only display two sets of parameters for readability but we have reached the same conclusions for all the other tested parameters (distributed across the entire phase space). **Left column:** At equilibrium. **Right column:** out-of-equilibrium.

motion Eq. 1 defining the model, at $T = 0$, for a test spin at distance r from a topological defect. The defect generates a field $\theta(x, y) = \arctan(y/x)$ around itself. As a first approximation, we replace the influence of the spin's neighbourhood (∂) by the Coulomb force generated by the defect, namely:

$$\sum_{\partial} \sin(\Delta\theta) \approx \sum_{\partial} |\nabla\theta(x, y)| = c/r.$$

The constant c, homogeneous to a length, depends on various parameters, in particular the defect's charge. One thus gets $\dot{\theta}_i = \sigma\omega_i + c/r$. It now becomes clear that for $r > c/(\sigma\omega)$, $\dot{\theta}$ is dominated by the forcing term. As ω is a random variable with zero mean and unit variance, averaging over the whole system proves that beyond a typical distance $\xi \sim 1/\sigma$, the spins' dynamics is no longer primarily governed by the topological defects' influence but rather by the intrinsic driving frequency. Importantly, this second argument explains the same scaling without resorting to the crude 1D approximation of the first argument.

Indeed, the behaviour of a pair of vortices shows a clear absence of any relevant defect-defect interacting potential: topological defects are genuinely free in the driven system. Once the phase patterns have formed, they screen the expected $\sim \log r$ potential of the XY model, key prerequisite to belong to the BKT universality class.

The measurements of the correlation length $\xi \sim 1/\sigma$ and the absence of relation between ξ and n upon self-spinning strengthen that claim. In our model, it only took an energy injection at the smallest scale, independent from spin to spin, for the BKT scenario of the XY model to collapse. As it shows that long-range influence is lost as soon as the model is made active, the present work conceptually supports the conclusions of Pearce *et al.* [51], where they report the absence of long-range ordering of defects in active nematics. Following up on the recent work of Pokawanvit *et al.* [52], we underline that our system features an incompressible, dense and immobile

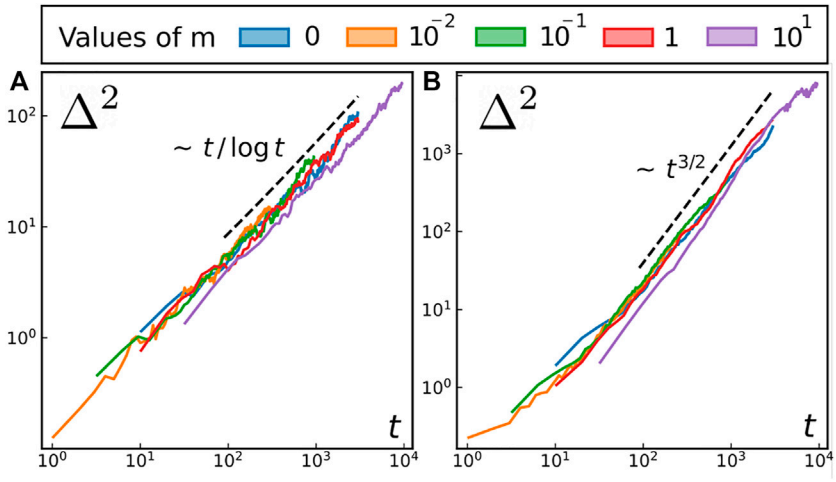

FIGURE 9
Mean Square Displacement (MSD) of individual defects for **(A)** XY model at $T = 0.2$ **(B)** forced model at $T = 0.2$ and $\sigma^2 = 0.03$.

ensemble of particles, which, based on their work, will not give rise to any collective motion of topological defects.

However, this out-of-equilibrium system still inherits some of the coarsening dynamics of the 2D Xy model physics: Figure 3 (and Figures 8B,D for $m \ll 1$) show that the short-time dynamics do follow $\xi \sim \sqrt{t/\log t}$, $n(t) \sim \log\ t/t$ and $\Delta^2 \sim t/\log\ t$. As the establishment of the domain boundaries (on which defects will then surf) take some transient time, the underlying equilibrium XY mechanisms prevail at short times. For example, consider an initially disordered system, at first crowded with defects: the vortex mean free time (time before collision/annihilation) is so small that

They rapidly end up colliding and annihilating, as bounded vortices would have done. We have shown that such transient time τ from equilibrium to active dynamics scales as $1/\sigma^2$.

4.2 Defects' dynamics

This section aims at shedding some light on the underlying mechanisms responsible for the spontaneous creation of domain boundaries and topological defects, and their super-diffusive random motion.

4.2.1 Creation of domain boundaries and defects

Interested by the emergence of the patterns such as those in Figures 1B, 7B, we look at the short time dynamics of the fields $\theta \equiv \theta(x, y)$ and $\dot{\theta} \equiv \dot{\theta}(x, y)$ (x, y being the spatial coordinates of a point in the lattice). We do so by following the evolution of the system from an ordered initial condition (all sites with identical phase). We proceed in such a way in order to isolate the underlying mechanisms at stake and avoid being blurred by the numerous defects inherent to a disordered initial condition. As the time series of θ is noisy for $T > 0$, one has to average in time to obtain a meaningful signal $\dot{\theta}$. Details about the exponential moving average used in that preliminary signal processing step can be found in the SM [44].

After very few time-steps, a clear picture appears: locally synchronised regions develop in the $\dot{\theta}$ field. We recall that since $d = 2$ is the lower critical dimension for frequency locking in the noiseless short range Kuramoto model, we do not expect more than local frequency synchronization. Since the average instantaneous frequency (over the N spins at a given time t) scales as $1/\sqrt{N}$ —as one should expect from a zero-mean distribution of intrinsic frequencies, reciprocal interactions and Gaussian white noise—, some regions rotate clockwise and some others counterclockwise; look for instance at the dark and bright regions of Figure 10A. Naturally, these locally synchronized regions in $\dot{\theta}$ translate into locally aligned domains in the phase field. This is illustrated in Figure 10: the dark region by the left of panel **10A** generates a phase synchronised domain of same shape and at the same position in panel **10D**, now in red.

Progressively, as time goes on, the different domains grow, (cf. Panel **10E**), defining a network of domain boundaries. As they correspond to regions where $|\nabla\theta|$ is large, they can be visually identified by looking for thin elongated regions across which colours change rapidly (though in a smooth way in contrast to, for instance, domain boundaries in the Ising model).

At this stage, the domains are locally ordered, their boundaries concentrate most of the energy of the system and the instantaneous frequencies $\dot{\theta}$ gradually decrease in amplitude

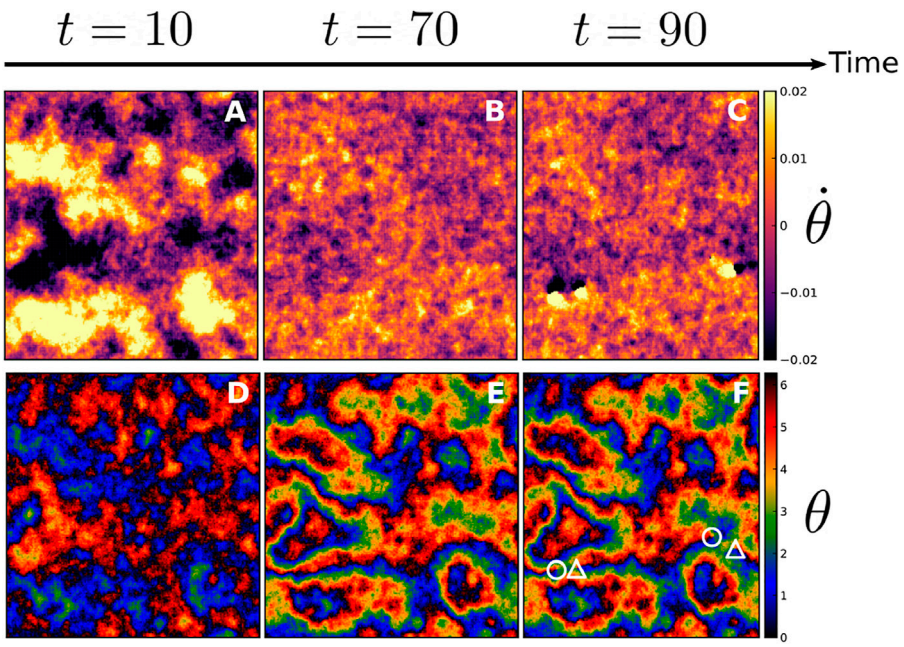

FIGURE 10
Three snapshots over time of the fields $\dot{\theta}(x, y)$ **(A–C)** and $\theta(x, y)$ **(D–F)** for a system initially ordered with $T = 0.05$ and $\sigma^2 = 0.2$. In panel **(C)**, defects are clearly identified thanks to the localized and intense amplitude of the instantaneous frequencies. In panel **(F)**, +1 defects are highlighted by a circle, − 1 defects are highlighted by a triangle.

(compare panels **10A** and **10B**). The system finally reaches its steady state characterised by synchronised domains resulting from the competition between the elastic energy and the driving frequencies $\sigma\omega_i$.

These domain boundaries play a crucial role in the formation of defects. There, the important gradients $|\nabla\theta|$ provide most of the energy needed to create and sustain topological defects. The remaining energy contribution eventually comes from thermal fluctuations, explaining why the temperature threshold necessary to spontaneously generate defects decreases as the forcing increases, see Figure 5. It also explains why one observes defects creation primarily at the domain boundaries, as exemplified in Figure 10F. This creation mechanism contrasts with that of the equilibrium case, entirely due to thermal fluctuations and hence homogeneously distributed in space.

Yet, the creation mechanism is not the only difference between the active and the passive case: a major difference lies in the motion of these topological defects, as we detail in the last part of this article.

4.2.2 Defects super-diffusion

The MSD of individual defects is shown in Figures 6B, 9. As soon as $\sigma \neq 0$, in the time window allowed by our simulations (spanning over 4 decades) the MSD of the defects has an anomalous exponent $\alpha = 3/2$ without any sign of a crossover to a diffusive regime at longer times. We depict in Figure 11A typical vortex trajectories. Since super-diffusion is a frequent phenomenon in active matter (e.g., topological defects in active nematics [11, 53–55] or cells in biophysics experiments [56]), it naturally led to a plethora of random walk models exhibiting transient [57, 58] or long term super-diffusion [59–61].

Among models featuring long-term super-diffusion, the family of Lévy processes is a popular choice, in particular in biology [56, 62]. In Lévy walks (respectively Lévy flights, their discontinuous counterpart), the duration τ of each walk (respectively the size of each jump) is usually sampled from a fat-tailed distribution $f(\tau) \sim \tau^{-(1+\gamma)}$, where $1 < \gamma < 2$ is a common choice for super-diffusing Lévy walks. The resulting MSD follows $\sim t^{3-\gamma}$ (see [63] and references therein for a complete review). The super-diffusion stems from the infinite variance of this distribution, explaining why the resulting trajectories sometimes feature a dramatic jump (as trajectories six and seven depict in Figure 11B. As such jumps cannot occur in our system, Lévy processes do not provide a faithful description of the random motion of vortices in the Kuramoto model. In addition, there is no physical argument to support the specific choice of the exponent $\gamma = 3/2$ (the only one reproducing the anomalous exponent $\alpha = 3/2$ of the vortices).

An important feature of the system to grasp the dynamics of the vortices is the domain structure of the system. Indeed, there is a feedback between the spatio-temporal patterns dynamics and the defects' motion. On one hand, defects have a strong

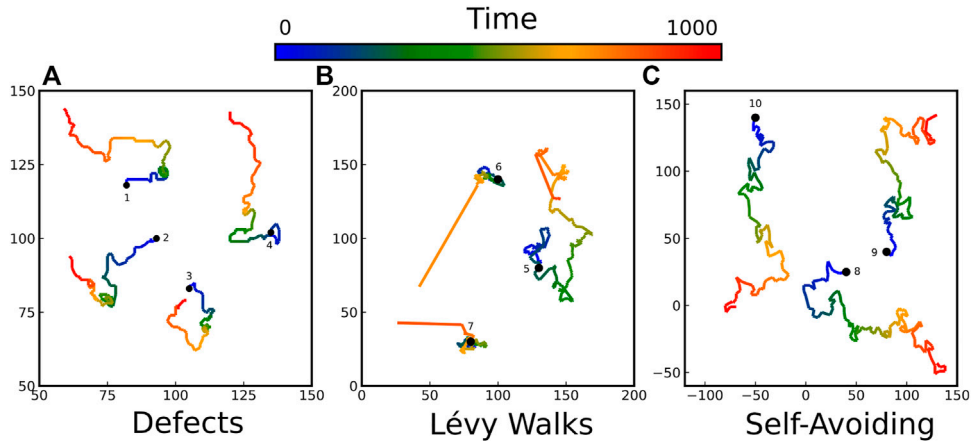

FIGURE 11
Sample trajectories of **(A)** topological defects in the actual spin model **(B)** Lévy walks with exponent $\gamma = 3/2$ **(C)** self-avoiding random walks (SAW). Each path departs from a black circle and lasts for $\Delta t = 10^3$, indicated by the color code.

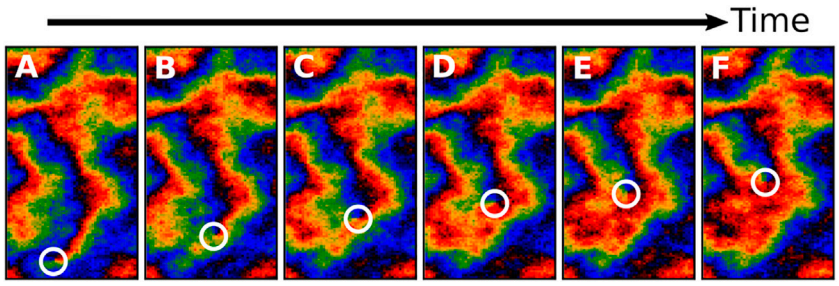

FIGURE 12
Times are T = **(A)** 260 **(B)** 270 **(C)** 280 **(D)** 290 **(E)** 300 **(F)** 308.

preference to move along domain boundaries, where elastic energy is the largest [10, 64]. As a domain boundary separates two neighbouring synchronised regions, it is characterised by an excess elastic energy. They thus provide a preferential direction for the motion of the topological defects, in contrast with the isotropic random motion of a single defect in the equilibrium XY model, for instance. This phenomenon has been observed recently in experimental systems by Kumar *et al.* [65], where they report that defects are 'catapulted' along these boundaries. On the other hand, such excess energy is released during the motion of the defects along domain boundaries. Indeed, the local θ field is strongly and quickly rearranged upon the passage of a topological defect. The field becomes smoother as the domain boundary is removed by the passage of a vortex, dissipating elastic energy. As shown in the successive snapshots of Figure 12, defects act like a zip, bringing together the two domains on each side of the boundary (e.g., in Figure 12A, these are the two red regions, separated by the thin black line), leaving a synchronized region behind (big red region in Figure 12F). This area is no longer favorable to the future passage of a defect (be it itself or another one), as the elastic energy it previously contained has been dissipated. As such, the phase pattern has a strong impact on the motion of the defects and conversely, defects significantly alter the structure of the system as they move.

As vortices remove the domain boundaries as they move, they perform a random walk with memory: it is more likely for a vortex to keep moving along the domain boundary than retrace its steps. The classical framework to treat this kind of motion is the self-avoiding random walk (SAW), which might be at the origin of the anomalous exponent 3/2. In order to explore whether SAW could provide a useful description of our defects motion, we simulate a few of SAW and visually compare the generated trajectories with the ones we recorded for vortices. As shown in Figure 11C, they look qualitatively similar. To be more quantitative, we also computed the MSD and the distribution of displacements $G(x, t)$, defined as the

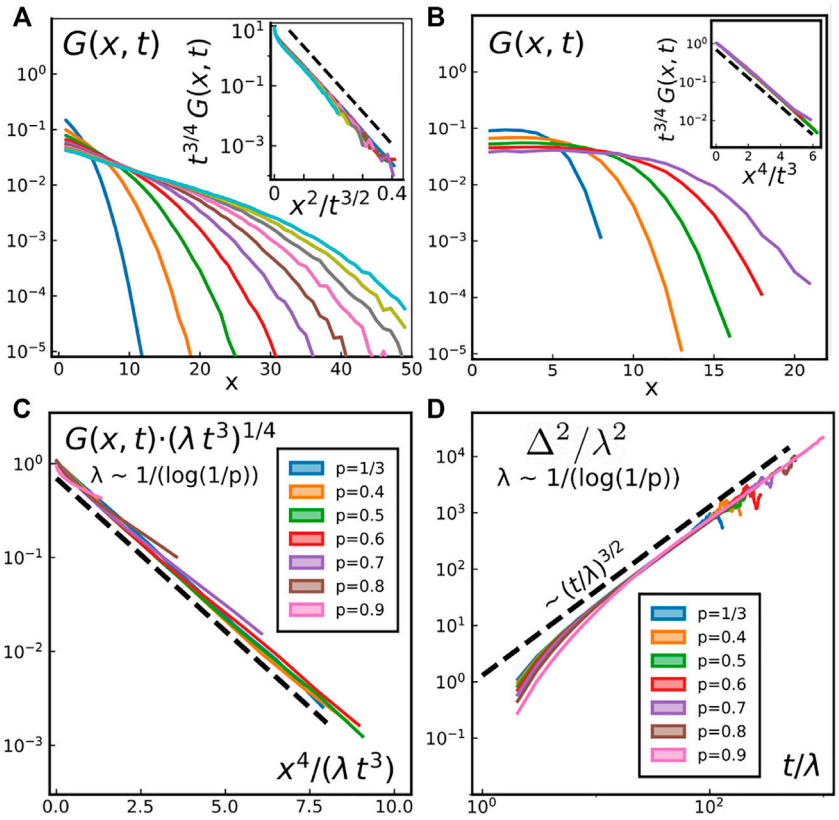

FIGURE 13
Probability densities of displacement $G(x, t)$ (see main text for definition) for different cases. Both insets represent rescaled data in order to highlight the functional form of **(G)**. We considered **(A)** topological defects with $\sigma^2 = 0.025$ and $T = 0.2$, at times (from left to right) $t = 50, 100, 150, \ldots, 500$. Inset: the dashed line follows $f(x) \sim \exp(-60x)$ **(B)** SAW ($\Delta t = 1$) at times (from left to right) $t = 10, 15, 20, 25, 30$. Inset: the dashed line follows $f(x) \sim \exp(-0.85x)$ **(C)** Persistent SAW (see main text for definition) with different persistence probabilities on rescaled axes to highlight that the functional form is identical for all $1/3 \leq p < 1$. The dashed line follows $f(x) \sim \exp(-3x/4)$. **(D)** MSD resulting from $G(x, t)$ of panel **(C)**, for different persistence probabilities p.

probability that a walker initially at $x = 0$ at $t = 0$ is at position x at time $t > 0$. SAW feature a super-diffusion with $\Delta^2(t) \sim t^{\nu}$ with $\nu = \frac{6}{d+2}$ [66], hence providing an explanation of the 3/2 exponent we found for the defects' MSD (here $d = 2$, the number of spatial dimensions). Yet, the description provided by SAW is not complete, as the full distribution of displacements differ significantly. As shown in Figure 13A, for defects,

$$G(x,t) \sim \exp\left(-x^2/t^{3/2}\right) \tag{14}$$

while for SAW, one obtains (cf. Inset of Figure 13B)

$$G(x,t) \sim \exp\left(-x^4/t^3\right). \tag{15}$$

We also investigated the effect of including self-propulsion to mimic the behaviour of vortices on domain boundaries. To do so, we add persistence to the walk, on top of the self-avoiding condition. Instead of continuing straight, turning left or turning right with equal probability 1/3, we set the probability to continue straight to $1/3 \leq p < 1$, and thus turning left or right with probability $(1 - p)/2$. This process introduces a typical length $\lambda \sim 1/\log(1/p)$, as $p^n = e^{-n/\lambda}$. The typical timescale before the trajectory has changed orientation with probability 1/3 also scales as λ. In other words, a persistent SAW, when expressed in terms of the rescaled space x/λ and rescaled time t/λ, is indistinguishable from a non persistent SAW expressed in terms of x and t. This explains why, for all $1/3 \leq p < 1$, the probability density of displacement for a persistent SAW with probability p is given by

$$G(x,t) = \frac{1}{2\,\Gamma(5/4)\,(\lambda\, t^3)^{1/4}}\ \exp\left(-\frac{x^4}{\lambda\, t^3}\right), \tag{16}$$

where $\Gamma(x)$ is the usual Gamma function. Note that the slope of the curves in Figure 13C determines the exact value of the rescaling factor: $\lambda = 4/(3\log(1/p))$.

Overall, a complete, faithful microscopic description of the topological defects' motion in the short-range Kuramoto model remains to be found. Despite the simplicity of their displacements' functional form $G(x, t) \sim \exp(-x^2/t^{3/2})$, it is likely that collective effects drive the defects' motion in a way simple random walk models cannot capture. While vortex superdiffusion and the value

of the anoumalous exponent can be reproduced by a self-avoiding walk picture (considering only a single vortex and omitting the dynamics of the domain boundaries), the particular form of $G(x, t)$ seems to require a more involved treatment, calling for a full many-body description which takes into account the two-way coupling between the domain boundaries' dynamics and the vortex motion.

5 Conclusion

In this article we have studied the dynamics of the short-range noisy Kuramoto model, constructed as a non-equilibrium extension of the 2D XY model, where spins rotate with an intrinsic frequency, taken from a (quenched) Gaussian distribution. Exploiting the connection between the emergence of synchronisation and the topological Berezenskii-Kosterlitz-Thouless phase transition in the 2D XY model, we investigate the dynamics of vortices in detail, contributing to our current understanding of the dynamics of topological defects in non-equilibrium soft condensed matter.

In 2D, the short range noisy Kuramoto does not exhibit any kind of phase transition at any finite temperature, its correlation length is always finite and scales as $\xi \sim \sigma^{-1}$. Instead, there is a crossover between a high temperature region with many topological defects, and a low temperature region with a few, as the number of vortices decreases exponentially fast close to such crossover temperature. We have showed that the relaxation towards the low temperature regime from a disordered initial state proceeds via the growth of a characteristic length scale, setting the typical size of synchronised domains Such growth does not proceed indefinitely, as the correlation length of the system is finite. The number of defects decays in time following the expected behaviour from the 2D XY model, although the mean separation between defects is not given by growing length extracted from the correlation function, meaning that the dynamics cannot be fully described by a single length scale, as for the coarsening of the 2D XY model. Indeed, vortices are free in the non-equilibrium model, advected by the domain boundaries of phase synchronised regions, resulting in super-diffusion with a long-time mean-square displacement $\Delta^2(t) \sim t^{3/2}$. Thus, the mean distance between topological defects does not bare any information regarding the large-scale structure of the system. Interestingly, similar defect's dynamics has been observed in different experimental systems: in active nematics [65], monolayers of self-propelled colloids [64] and spinning colloidal magnets [21].

We have found that our results remain valid both for inertial and over-damped Kuramoto dynamics, showing the robustness of the before-mentioned scenario and the breakdown of BKT physics. We have provided a detailed characterisation of the random walks performed by vortices, and have found that, although their stochastic dynamics shares several similarities to self-avoiding walks, in particular the scaling $\Delta^2(t) \sim t^{3/2}$, their full statistics of displacements are not equivalent. A faithful description of the dynamics of the dynamics of vortices would require a theory capturing the two-way dynamical feedback between the phase field and the vortices, a challenging endeavour that we leave for future work.

Data availability statement

The Julia code used to conduct the research and produce the figures is available on GitHub at https://github.com/yrouzaire/forced_xy.

Author contributions

YR and DL designed research: YR performed the research and analysed the data; YR and DL wrote the paper.

Funding

YR thanks the CECAM (Centre Européen de Calcul Atomique et Moléculaire; Head-director: I. Pagonabarraga) for financial support. DL acknowledges Ministerio de Ciencia, Innovación y Universidades MCIU/AEI/FEDER for financial support under grant agreement RTI2018-099032-J-I00.

Acknowledgments

We warmly thank Elisabeth Agoritsas for helpful discussions.

Conflict of interest

The authors declare that the research was conducted in the absence of any commercial or financial relationships that could be construed as a potential conflict of interest.

Publisher's note

Supplementary Material

The Supplementary Material for this article can be found online at: https://www.frontiersin.org/articles/10.3389/fphy.2022.976515/full#supplementary-material.

References

1. Huygens C. *Letters to de sluse, (letters; no. 1333 of 24 february 1665, no. 1335 of 26 february 1665, no. 1345 of 6 march 1665)*. La Haye: Societe Hollandaise Des Sciences, Martinus Nijhoff (1895).

2. Strogatz SH. *Sync: How order emerges from chaos in the universe, nature, and daily life*. Hachette UK) (2012).

3. Pikovsky A, Rosenblum M, Kurths J. *Synchronization: A universal concept in nonlinear sciences*, 12. Cambridge University Press (2003).

4. Sakaguchi H, Shinomoto S, Kuramoto Y. Local and global self-entrainments in oscillator lattices. *Prog Theor Phys* (1897).

5. Acebrón JA, Bonilla LL, Perez-Vicente CJ, Ritort F, Spigler R. The kuramoto model: A simple paradigm for synchronization phenomena. *Rev Mod Phys* (2005) 77:137–85. doi:10.1103/revmodphys.77.137

6. Mondragón-Palomino O, Danino T, Selimkhanov J, Tsimring L, Hasty J. Entrainment of a population of synthetic genetic oscillators. *Science* (2011) 333: 1315–9. doi:10.1126/science.1205369

7. Arenas A, Díaz-Guilera A, Kurths J, Moreno Y, Zhou C. Synchronization in complex networks. *Phys Rep* (2008) 469:93–153. doi:10.1016/j.physrep.2008.09.002

8. Hong H, Chaté H, Tang LH, Park H. Finite-size scaling, dynamic fluctuations, and hyperscaling relation in the kuramoto model. *Phys Rev E* (2015) 92:022122. doi:10.1103/physreve.92.022122

9. Lee TE, Tam H, Refael G, Rogers JL, Cross M. Vortices and the entrainment transition in the two-dimensional kuramoto model. *Phys Rev E* (2010) 82:036202. doi:10.1103/physreve.82.036202

10. Rouzaire Y, Levis D. Defect superdiffusion and unbinding in a 2D XY model of self-driven rotors. *Phys Rev Lett* (2021) 127:088004. doi:10.1103/physrevlett.127.088004

11. Shankar S, Souslov A, Bowick MJ, Marchetti MC, Vitelli V. Topological active matter. *Nat Rev Phys* (2022) 4:380–98. doi:10.1038/s42254-022-00445-3

12. Ginelli F. The physics of the vicsek model. *Eur Phys J Spec Top* (2016) 225: 2099–117. doi:10.1140/epjst/e2016-60066-8

13. Chepizhko A, Kulinskii V. On the relation between vicsek and kuramoto models of spontaneous synchronization. *Physica A: Stat Mech its Appl* (2010) 389: 5347–52. doi:10.1016/j.physa.2010.08.016

14. Chepizhko O, Saintillan D, Peruani F. Revisiting the emergence of order in active matter. *Soft Matter* (2021) 17:3113–20. doi:10.1039/d0sm01220c

15. Levis D, Pagonabarraga I, Liebchen B. Activity induced synchronization: Mutual flocking and chiral self-sorting. *Phys Rev Res* (2019) 1:023026. doi:10.1103/physrevresearch.1.023026

16. Golestanian R, Yeomans JM, Uchida N. Hydrodynamic synchronization at low Reynolds number. *Soft Matter* (2011) 7:3074–82. doi:10.1039/c0sm01121e

17. Solovev A, Friedrich BM. Synchronization in cilia carpets: Multiple metachronal waves are stable, but one wave dominates. *New J Phys* (2022) 24: 013015. doi:10.1088/1367-2630/ac2ae4

18. Solovev A, Friedrich BM. Synchronization in cilia carpets and the kuramoto model with local coupling: Breakup of global synchronization in the presence of noise. *Chaos* (2022) 32:013124. doi:10.1063/5.0075095

19. Soni V, Bililign ES, Magkiriadou S, Sacanna S, Bartolo D, Shelley MJ, et al. The odd free surface flows of a colloidal chiral fluid. *Nat Phys* (2019) 15:1188–94. doi:10.1038/s41567-019-0603-8

20. Massana-Cid H, Levis D, Hernández RJH, Pagonabarraga I, Tierno P. Arrested phase separation in chiral fluids of colloidal spinners. *Phys Rev Res* (2021) 3:L042021. doi:10.1103/physrevresearch.3.l042021

21. Bililign ES, Usabiaga FB, Ganan YA, Soni V, Magkiriadou S, Shelley MJ, et al. Chiral crystals self-knead into whorls. *arXiv preprint arXiv:2102.03263* (2021).

22. Liebchen B, Levis D. *Chiral active matter* (2022). *arXiv e-print*sarXiv–2207.

23. Kosterlitz JM, Thouless DJ. Ordering, metastability and phase transitions in two-dimensional systems. *J Phys C: Solid State Phys* (1973) 6:1181–203. doi:10.1088/0022-3719/6/7/010

24. Kosterlitz JM. The critical properties of the two-dimensional xy model. *J Phys C: Solid State Phys* (1974) 7:1046–60. doi:10.1088/0022-3719/7/6/005

25. Berezinskii V. Destruction of long-range order in one-dimensional and two-dimensional systems having a continuous symmetry group i. classical systems. *Sov Phys JETP* (1971) 32:493–500.

26. You Z, Pearce DJ, Sengupta A, Giomi L. Geometry and mechanics of microdomains in growing bacterial colonies. *Phys Rev X* (2018) 8:031065. doi:10.1103/physrevx.8.031065

27. Bowick MJ, Fakhri N, Marchetti MC, Ramaswamy S. Symmetry, thermodynamics, and topology in active matter. *Phys Rev X* (2022) 12:010501. doi:10.1103/physrevx.12.010501

28. Bray AJ. Theory of phase-ordering kinetics. *Adv Phys X* (2002) 51:481–587. doi:10.1080/00018730110117433

29. Levis D, Pagonabarraga I, Diaz-Guilera A. Synchronization in dynamical networks of locally coupled self-propelled oscillators. *Phys Rev X* (2017) 7:011028. doi:10.1103/physrevx.7.011028

30. Yurke B, Pargellis A, Kovacs T, Huse D. Coarsening dynamics of the xy model. *Phys Rev E* (1993) 47:1525–30. doi:10.1103/physreve.47.1525

31. Rojas F, Rutenberg A. Dynamical scaling: The two-dimensionalXYmodel following a quench. *Phys Rev E* (1999) 60:212–21. doi:10.1103/physreve.60.212

32. Bray A, Briant A, Jervis D. Breakdown of scaling in the nonequilibrium critical dynamics of the two-DimensionalXYModel. *Phys Rev Lett* (2000) 84:1503–6. doi:10.1103/physrevlett.84.1503

33. Berthier L, Holdsworth PC, Sellitto M. Nonequilibrium critical dynamics of the two-dimensional xy model. *J Phys A: Math Gen* (2001) 34:1805–24. doi:10.1088/0305-4470/34/9/301

34. Jelic A, Cugliandolo L. Quench dynamics of the 2d xy model. *J Stat Mech* (2018) 2011:P02032. doi:10.1088/1742-5468/2011/02/p02032

35. Hohenberg PC, Halperin BI. Theory of dynamic critical phenomena. *Rev Mod Phys* (1977) 49:435–79. doi:10.1103/revmodphys.49.435

36. Weber H, Minnhagen P. Monte Carlo determination of the critical temperature for the two-dimensionalXYmodel. *Phys Rev B* (1988) 37:5986–9. doi:10.1103/physrevb.37.5986

37. Hasenbusch M. The two-dimensional xy model at the transition temperature: A high-precision Monte Carlo study. *J Phys A: Math Gen* (2005) 38:5869–83. doi:10.1088/0305-4470/38/26/003

38. Cardy JL, Ostlund S. Random symmetry-breaking fields and theXYmodel. *Phys Rev B* (1982) 25:6899–909. doi:10.1103/physrevb.25.6899

39. Le Doussal P, Giamarchi T. Replica symmetry breaking instability in the 2DXYModel in a random field. *Phys Rev Lett* (1995) 74:606–9. doi:10.1103/physrevlett.74.606

40. Agrawal R, Kumar M, Puri S. Domain growth and aging in the random field xy model: A Monte Carlo study. *Phys Rev E* (2021) 104:044123. doi:10.1103/physreve.104.044123

41. Komarov M, Gupta S, Pikovsky A. Synchronization transitions in globally coupled rotors in the presence of noise and inertia: Exact results. *EPL* (2014) 106: 40003. doi:10.1209/0295-5075/106/40003

42. Gupta S, Campa A, Ruffo S. Kuramoto model of synchronization: Equilibrium and nonequilibrium aspects. *J Stat Mech* (2014) 2014:R08001. doi:10.1088/1742-5468/14/08/R08001

43. Olmi S, Navas A, Boccaletti S, Torcini A. Hysteretic transitions in the kuramoto model with inertia. *Phys Rev E* (2014) 90:042905. doi:10.1103/PhysRevE.90.042905

44.

45. Bray A. Random walks in logarithmic and power-law potentials, nonuniversal persistence, and vortex dynamics in the two-dimensionalXYmodel. *Phys Rev E* (2000) 62:103–12. doi:10.1103/physreve.62.103

46. Cugliandolo L. *Advanced statistical physics: Phase transitions* (2018).

47. Paoluzzi M, Marconi UMB, Maggi C. Effective equilibrium picture in the xy model with exponentially correlated noise. *Phys Rev E* (2018) 97:022605. doi:10.1103/physreve.97.022605

48. Digregorio P, Levis D, Suma A, Cugliandolo LF, Gonnella G, Pagonabarraga I. Full phase diagram of active brownian disks: From melting to motility-induced phase separation. *Phys Rev Lett* (2018) 121:098003. doi:10.1103/physrevlett.121.098003

49. Digregorio P, Levis D, Cugliandolo LF, Gonnella G, Pagonabarraga I. Unified analysis of topological defects in 2d systems of active and passive disks. *Soft Matter* (2022) 18:566–91. doi:10.1039/d1sm01411k

50. Tanaka HA, Lichtenberg AJ, Oishi S. First order phase transition resulting from finite inertia in coupled oscillator systems. *Phys Rev Lett* (1997) 78:2104–7. doi:10.1103/PhysRevLett.78.2104

51. Pearce D, Nambisan J, Ellis P, Fernandez-Nieves A, Giomi L. Orientational correlations in active and passive nematic defects. *Phys Rev Lett* (2021) 127:197801. doi:10.1103/PhysRevLett.127.197801

52. Pokawanvit S, Chen Z, You Z, Angheluta L, Marchetti MC, Bowick MJ. *Active nematic defects in compressible and incompressible flows* (2022). *arXiv preprint arXiv:2206.13598*.

53. Doostmohammadi A, Ignés-Mullol J, Yeomans JM, Sagués F. *Active Nematics Nat Commun* (2018) 9:1–13.

54. Giomi L, Bowick MJ, Mishra P, Sknepnek R, Marchetti MC. Defect dynamics in active nematics. *Phil Trans R Soc A* (2014) 372:20130365. doi:10.1098/rsta.2013.0365

55. Vliegenthart GA, Ravichandran A, Ripoll M, Auth T, Gompper G. Filamentous active matter: Band formation, bending, buckling, and defects. *Sci Adv* (2020) 6:eaaw9975. doi:10.1126/sciadv.aaw9975

56. Huda S, Weigelin B, Wolf K, Tretiakov KV, Polev K, Wilk G, et al. Lévy-like movement patterns of metastatic cancer cells revealed in microfabricated systems and implicated *in vivo*. *Nat Commun* (2018) 9:4539. doi:10.1038/s41467-018-06563-w

57. Caprini L, Marconi UMB, Wittmann R, Löwen H. Dynamics of active particles with space-dependent swim velocity. *Soft Matter* (2022) 18:1412–22. doi:10.1039/d1sm01648b

58. Villa-Torrealba A, Chávez-Raby C, de Castro P, Soto R. Run-and-tumble bacteria slowly approaching the diffusive regime. *Phys Rev E* (2020) 101:062607. doi:10.1103/PhysRevE.101.062607

59. Fedotov S, Korabel N. Emergence of Lévy walks in systems of interacting individuals. *Phys Rev E* (2017) 95:030107. doi:10.1103/PhysRevE.95.030107

60. Han D, da Silva MAA, Korabel N, Fedotov S. Self-reinforcing directionality generates truncated lévy walks without the power-law assumption. *Phys Rev E* (2021) 103:022132. doi:10.1103/PhysRevE.103.022132

61. Bertoin J. *Lévy processes*, 121. Cambridge university press Cambridge (1996).

62. Ariel G, Beér A, Reynolds A. Chaotic model for lévy walks in swarming bacteria. *Phys Rev Lett* (2017) 118:228102. doi:10.1103/physrevlett.118.228102

63. Zaburdaev V, Denisov S, Klafter J. Lévy walks. *Lévy Walks Rev Mod Phys* (2015) 87:483–530. doi:10.1103/RevModPhys.87.483

64. Chardac A, Hoffmann LA, Poupart Y, Giomi L, Bartolo D. Topology-driven ordering of flocking matter. *Phys Rev X* (2021) 11:031069. doi:10.1103/physrevx.11.031069

65. Kumar N, Zhang R, Redford S, de Pablo JJ, Gardel M. Catapulting of topological defects through elasticity bands in active nematics. *Soft Matter* (2022) 18:5271–81. doi:10.1039/d2sm00414c

66. Barat K, Chakrabarti BK. Statistics of self-avoiding walks on random lattices. *Phys Rep* (1995) 258:377–411. doi:10.1016/0370-1573(95)00009-6

frontiers | Frontiers in Physics

TYPE Original Research
PUBLISHED 08 September 2022
DOI 10.3389/fphy.2022.988903

OPEN ACCESS

EDITED BY
Roberto Cerbino,
University of Vienna, Austria

REVIEWED BY
Marco Laurati,
University of Florence, Italy
Silvia Corezzi,
University of Perugia, Italy

*CORRESPONDENCE
C. Haro-Pérez,
cehp@azc.uam.mx
L. F. Rojas-Ochoa,
luisf.rojas@cinvestav.mx

SPECIALTY SECTION
This article was submitted to Soft Matter Physics,
a section of the journal
Frontiers in Physics

RECEIVED 07 July 2022
ACCEPTED 10 August 2022
PUBLISHED 08 September 2022

CITATION
Bocanegra-Flores J, Haro-Pérez C, Reyes-Contreras D and Rojas-Ochoa LF (2022), Crystallization kinetics of charged PNIPAM microgels dispersions at low volume fractions.
Front. Phys. 10:988903.
doi: 10.3389/fphy.2022.988903

Crystallization kinetics of charged PNIPAM microgels dispersions at low volume fractions

J. Bocanegra-Flores[1], C. Haro-Pérez[2]*, D. Reyes-Contreras[3] and L. F. Rojas-Ochoa[1]*

[1]Departamento de Física, CINVESTAV-IPN, Av. Instituto Politécnico Nacional 2508, Mexico City, Mexico, [2]Departamento de Ciencias Básicas, Universidad Autónoma Metropolitana-Azcapotzalco, Mexico City, Mexico, [3]Facultad de Ciencias, Campus El Cerrillo, Universidad Autónoma del Estado de México, Toluca, Mexico

This work studies the kinetics of crystallization of charged microgels suspensions of Poly-N-Isopropylacrylamide (PNIPAM) at low ionic strength. The liquid-crystal transition is induced by suddenly decreasing the temperature of the microgel dispersion, and the crystallization process is monitored by measuring the temporal evolution of the static structure factor of the dispersion using light scattering. We find that the crystal growth rate, indicated by the temporal evolution of the crystallinity factor, strongly depends on the quenching temperature.

KEYWORDS

colloidal crystallization, microgels, PNIPAM, light scattering, charged colloids

Introduction

Microgels dispersions are unique since they respond to different stimuli, such as temperature, pH, ionic strength, and solvent [1–3]. The size of thermosensitive microgels, such as PNIPAM microgels, can be tuned by changing the temperature. At low temperatures, the microgels are swollen, and the effective particle density is very similar to that of the solvent. As the temperature increases, the microgel size decreases slowly until the Lower Critical Solution Temperature (LCST) is reached, provoking a sudden coil-to-globule transition of the constituent polymer chains that translates into a particle volume phase transition (VPT). For charged microgels, dispersions are colloidally stable even beyond the LCST due to electrostatic stabilization [4]. We can take advantage of this property to study various physical phenomena that occur as a function of temperature in microgel dispersions [2, 3, 5–7]. The temperature affects the particle size, softness, permeability and charge density, implying a temperature-dependent interaction potential [4, 8, 9]. Thanks to this, a microgel dispersion can undergo, for example, a phase transition from liquid to crystal by changing the temperature [4]. Temperature is maybe one of the parameters that experimentalists can better control. Phase transitions such as melting [10] and crystallization [5, 11, 12] are still open questions. For example, crystallization kinetics

in atomic systems is complicated to follow due to the requirement of high temporal and atomic spatial resolutions [13]. However, colloidal systems, composed of particles of larger sizes, such as microgel dispersions, provide the possibility to follow physical phenomena such as crystallization in time. Moreover, the possibility of controlling the particle pair-interaction in colloids makes them very attractive. In particular, the peculiarity of microgel systems allows for tuning the particle interaction potential by changing the temperature and, consequently, inducing crystallization in a controlled way [14, 15]. This characteristic may be of great interest in material science to design, for example, photonic materials made of thermosensitive microgels [5, 16–18]. In case of ionic microgels, the presence of charged groups can also induce interesting responsiveness to other parameters, such as pH and, by controlling its temporal profile, microgel dispersions can be programmed to melt or crystallize [19]. Charged groups are frequently present in PNIPAM microgels due to the use of an ionic initiator or an ionic comonomer [20]. Pure PNIPAM microgels are frequently considered neutral, but their residual charge may significantly affect their colloidal behavior, mainly at low salt concentrations and/or high-volume fractions [19, 21–23]. Here, thanks to the long-range interaction potential among charged PNIPAM microgels at deionized conditions, we study the crystallization of microgel systems at low particle number concentrations and the influence of temperature on the crystallization kinetics in contrast to previous studies, where very high-volume fractions were used [11]. The crystallization process is followed by measuring the sample structure time-evolution by light scattering.

Materials and methods

Microgel synthesis and sample preparation

The PNIPAM microgels under study are synthesized by polymerization precipitation as described in Ref. [24]. First, the monomer (NIPAM), the crosslinker (bisacrylamide, BIS), and the surfactant (sodium dodecyl sulfate, SDS) are dissolved in 450 ml of water in a three-mouth round bottom flask, purged with nitrogen during 30 min and heated to 70°C. Then, in another recipient, the initiator, (potassium persulfate, KPS), is dissolved in 50 ml of water and purged with nitrogen for 30 min. Then, the initiator solution is injected into the monomer solution, and the sample is kept under continuous stirring. After 5 h, the solution is left to cool down to room temperature. Finally, the microgel dispersion is filtered through glass wool, dialyzed for 2 weeks, and centrifuged ten times. In each centrifugation step, the supernatant is removed, and the microgels are redispersed in ultrapure water.

We perform the crystallization study with two types of microgels having different electrostatic charges, and this is achieved by using a different initiator concentration in the microgel synthesis. The quantities of reactants used in each synthesis are shown in Table 1. Once the microgel dispersion is purified, the weight fraction is obtained from weighing a specific volume of microgel dispersion before and after drying. The weight fraction was obtained for six samples, the average value is reported in Table 1, and the error is the sample standard deviation. The resulting weight fractions, shown in Table 1, are 3.17% [(128 ± 3) particles/μm^3] and 1.1% [(19 ± 2) particles/μm^3] for the KPS0.1 and KPS0.6 systems, respectively. The number particle concentration of each microgel stock is obtained by following the procedure described in [4]. First, several samples are prepared by dilution of the stock solution and deionized to maximize particle electrostatic repulsion. At ambient temperature, most of the samples crystallize and show Bragg peaks whose relative positions indicate the appearance of a BCC lattice. Then, from the main peak position, the particle concentration of each sample is obtained by using [25].

$$n = \left(\frac{2\sqrt[3]{2}\mu}{\sqrt{2}\lambda}\right)^3 \sin^3\left(\frac{\theta_{max}}{2}\right) \quad (1)$$

μ is the refractive index of the solvent, λ is the wavelength of the laser used in the light scattering experiments, and θ_{max} is the angular position of the main peak of the structure factor. Finally, the particle number density of the stock solution is obtained by multiplying the concentration of each sample by the dilution factor used to prepare it. In Table 1 we report the average values of the particle number concentration for each stock solution.

Once the stock solution concentration is known, the system was prepared by dilution with ultrapure water to the desired concentration and placed in cylindrical quartz cells with ionic exchanger resins (Amberlite IRN-150) to deionize the sample completely. After that, the cells were sealed to avoid contact with air.

Light scattering experiments

The system crystallization kinetics was followed by measuring the static structure factor of the microgel dispersions by static light scattering. The device used to perform the experiments is a 3D-DLS spectrometer [26–28] (LS Instruments, Switzerland) provided with a laser working at 632.8 nm and two avalanche photodiodes. In this device, it is possible to perform two light scattering experiments simultaneously with the same wavevector. Cross-correlating the scattered signals from both experiments makes possible the suppression of multiple scattering from the total intensity impinging on the detectors. The static structure factor is

TABLE 1 Reactants used in synthesizing 500 ml of PNIPAM microgel dispersion, the weight fraction, and the particle number density of the resulting stock microgel dispersions.

System	NIPAM (g)	BIS (g)	KPS (g)	SDS (g)	W/W (%)	n (pp/μm^3)
KPS0.1	7.87	0.15	0.1	0.15	3.17 ± 0.06	128 ± 3
KPS0.6	7.87	0.15	0.6	0.15	1.10 ± 0.02	19 ± 2

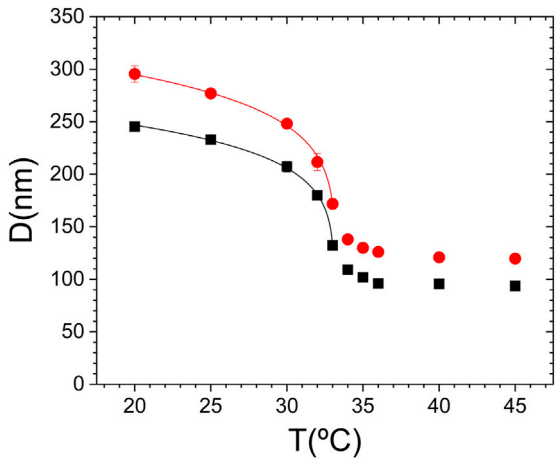

FIGURE 1
Temperature dependence of the hydrodynamic radius for KPS0.1 (black squares) and KPS0.6 (red circles) samples. The continuous lines are fits the critical-like function D_H = A $(T_c\text{-}T)^B$.

obtained by dividing the intensity scattered by the correlated sample by that scattered by a very diluted sample where particle interactions are absent; see further details in Ref. [29].

Before light scattering experiments, the samples were heated up to 45°C. They were kept at this temperature for 10 min to ensure all the samples were in a fluid state. After that, the quenching was performed by introducing the samples into the decalin bath located in the light scattering device at a temperature lower than the microgel volume phase transition temperature (VPTT); a thermostat controls the bath temperature. We measure the sample structure's time evolution after 10 min to follow its crystallization. The sample was steadily rotated during the experiments to obtain the ensemble-averaged intensity since the crystalline samples are non-ergodic. The temperatures used to do the quenching are 20°C, 25°C, and 30°C. At all these temperatures, the microgel dispersions crystallize. The microgel size was obtained by dynamic light scattering using a diluted sample. Here, the sample prepared at a high dilution was equilibrated at the desired temperature, and the free diffusion coefficient, D_0, was obtained from a second cumulant fit to the measured scattered field correlation function [30]. Finally, we calculate the hydrodynamic radius, *a*, by applying the Stokes-Einstein relation, $D_0 = \kappa_B T/(6\pi\eta a)$, where κ_B is the Boltzmann constant, T the temperature, and η the solvent viscosity [31].

Results and discussion

Before the crystallization experiments, the temperature dependence of the microgel size was measured by dynamic (DLS) and static light scattering (SLS). From DLS measurements, we can see that both microgel systems, KPS0.1 and KPS0.6, show the typical thermosensitive behavior of PNIPAM, as shown in Figure 1, where the temperature dependence of the hydrodynamic diameter of both systems is shown. The microgels display a swollen conformation and a larger particle diameter at low temperatures. As the temperature increases, the microgel expels water from inside and thus monotonously decreases its size. PNIPAM is hydrophobic at high temperatures, so microgels size decreases suddenly at temperatures above but close to the LCST. The measured temperature dependent hydrodynamic size is fitted to the critical-like function D_H = A∗(LCST−T)^B to determine the LCST of each microgel, obtaining that the LCST is (33.09 ± 0.02)°C, and (33.19 ± 0.09)°C for KPS0.1 and KPS0.6 system, respectively. The fits are shown in Figure 1 as continuous lines. Besides the similarity of the LCST values obtained for both microgels, they also display similar sizes at all temperatures. However, the most charged microgels display sizes slightly larger, probably due to the higher electrostatic repulsion between the ionized groups in the polymer chains that compose the particles. Note that the microgels are colloidally stable even beyond the LCST due to the electrostatic stabilization provided by the ionic initiator used in the synthesis. The presence of a small fraction of sulphate groups, originated by the KPS initiator, provides the microgel with a negative charge, whose presence has also been confirmed by electrophoretic mobility experiments [32, 33].

Once the thermosensitive behavior and particle dimensions are known, we characterize the microgel dispersion static structure at different particle concentrations at a temperature beyond the VPTT for both systems at deionized conditions. Figure 2A) shows the results for the KPS0.1 system, and Figure 2B) for the KPS0.6,

respectively. In both cases, the samples are in the fluid state for the concentrations shown in the figures.

Figure 2 shows the principal structural peak related to neighboring interparticle correlations and successive damped peaks. Moreover, as expected for charged colloids at low ionic strengths, the primary peak shifts to higher q-values as particle concentration increases following a one-third power law [34, 35], as seen in the insets. Here, the main peak position of the experimental $S(q)$ is plotted as a function of the dilution factor used to prepare the different systems from the stock solution on a log-log scale. We use the same color code in the inset as in the main figure, and blue symbols correspond to additional samples studied to span the concentration interval. The dashed lines are linear fits to the experiments, and their slopes are -0.34 and -0.33, agreeing with the expected −1/3 value. This means that particles arrange to maximize distances due to the electrostatic repulsion among them. Moreover, all structure factors display the typical short-range order present in liquids as confirmed by the agreement between experiments (symbols) and the theoretical $S(q)$'s (lines) obtained from liquid state theory by solving the Ornstein-Zernike equation using the hypernetted chain (HNC) closure relation, and assuming a Yukawa-like particle interaction potential [36],

$$U(r) = \frac{Z_{eff}^2 e^2}{4\pi\varepsilon_0\varepsilon_r}\left(\frac{\exp(\kappa a)}{1+\kappa a}\right)^2 \frac{\exp(-\kappa r)}{r} \tag{2}$$

where, Z_{eff} is an effective charge, e the electron charge, κ the effective inverse Debye screening length, a the particle radius, ε_0 the vacuum dielectric constant, ε_r the relative solvent-vacuum dielectric constant, and r the particle-particle center distance. Since the systems are deionized, we calculate the theoretical $S(q)$'s by fixing the salt concentration to 10^{-7} M and assuming monodisperse systems. The only fitting parameters are the particle effective charge, and the number concentration, n. The n needed to perform all the fits only differs up to 5% from that corresponding to the stock solution divided by the dilution factor, which corroborates the initially estimated particle concentration. We find that the effective particle charge slightly varies with particle concentration in the investigated concentration interval, and its value is around 420 for KPS0.1 system, and 470 for KPS0.6 system. It is convenient to point out that, even though the influence of the electrostatic charge of PNIPAM microgels is often neglected in many studies, accounting for the interparticle electrostatic repulsion could be relevant to avoid misleading interpretations of the results. The use of the ionic initiator in the microgel synthesis, even in small quantities as that used in the KPS0.1 microgel system, provokes the appearance of a residual charge in the PNIPAM polymer chains that is reflected on the measured structure factors.

To carry out the crystallization study, we chose the samples prepared at n = 5.94 particles/μm^3 for the less charged microgel system KPS01 and n = 2.39 particles/μm^3 for the most charged microgels KPS0.6. At these

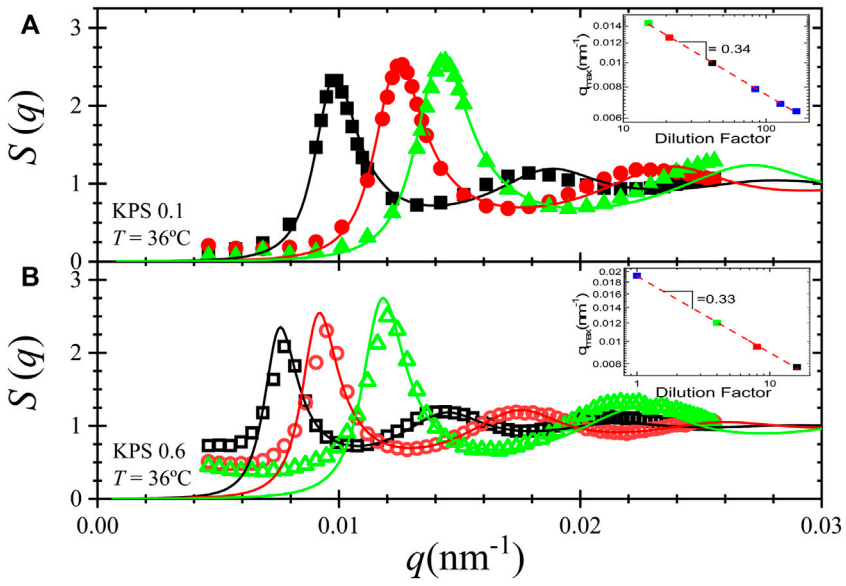

FIGURE 2
Measured static structure factors at 36°C for: **(A)** KPS0.1 system at n = 2.94 particles/μm^3 (black squares), 5.94 particles/μm^3 (red circles), and 8.85 particles/μm^3 (green triangles), **(B)** KPS0.6 system at n = 1.34 particles/μm^3 (black open squares), 2.39 particles/μm^3 (red open circles), and 5.06 particles/μm^3 (green open triangles), along with their HNC calculations (lines). Insets: Main peak position versus dilution factor used to prepare the system from the stock solution. The dashed line is a linear fit in the log-log presentation with a slope of -0.34 for KPS0.1 system and −0.33 for KPS0.6.

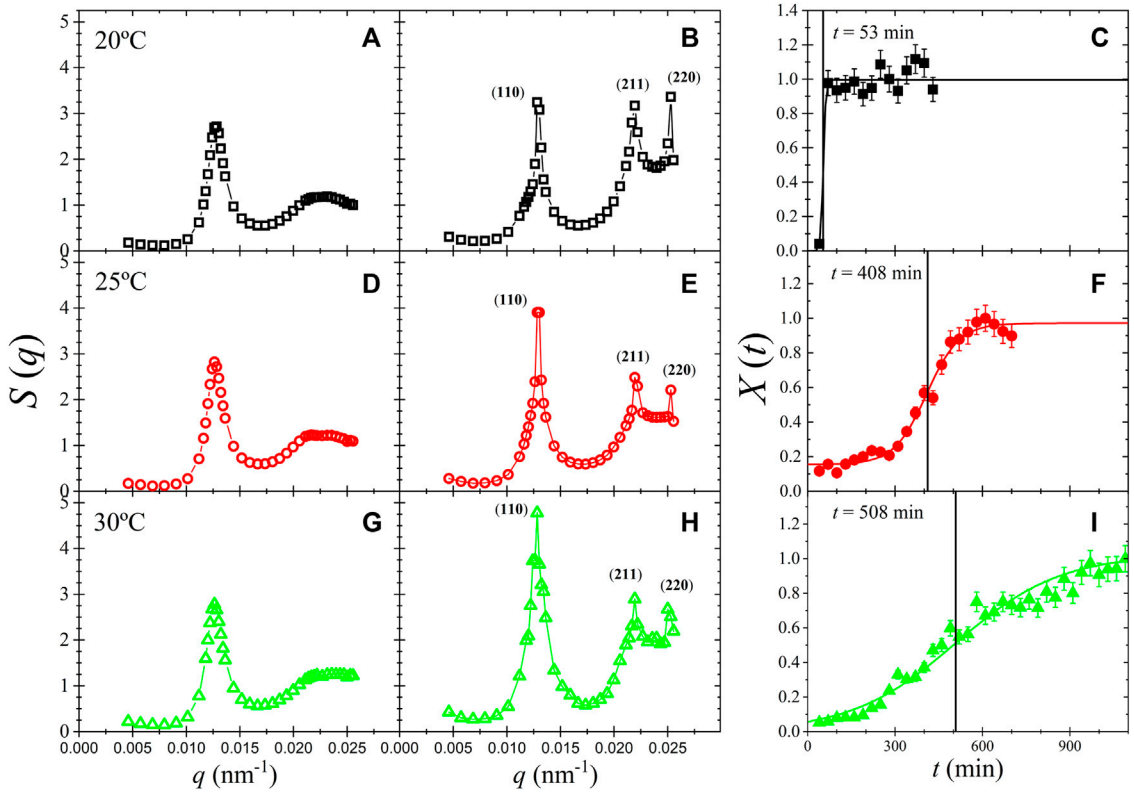

FIGURE 3
(A) Initial measured static structure factor, $S(q)$, right after quenching, **(B)** Final equilibrium static structure, **(C)** time evolution of the degree of crystallinity (symbols) along with a Boltzmann fit (continuous line) at 20°C. **(D)** Initial $S(q)$ right after quenching, **(E)** Final equilibrium static structure, **(F)** time evolution of the degree of crystallinity (symbols) along with a Boltzmann fit (continuous line) at 25°C. **(G)** Initial $S(q)$ right after quenching, **(H)** Final equilibrium static structure, **(I)** time evolution of the degree of crystallinity (symbols) along with a Boltzmann fit (continuous line) at 30°C for sample KPS0.1 at n = 5.94 particles/μm^3.

concentrations, the systems are in the liquid phase at high temperatures, and the crystallization process can be followed in time at lower temperatures. Notice that a more diluted sample was chosen for the more charged system because, at higher concentrations, the samples crystallize so quickly that the crystallization kinetics could not be followed. This fact confirms that the higher the initiator used in the synthesis, the higher the microgel electrostatic charge. Conversely, at lower particle concentrations, either microgel dispersions do not crystallize at low temperatures, or the crystallization is too slow to be followed experimentally. Therefore, after confirming that our sample was in the liquid state at 45°C, we carried out the quenching from 45°C to lower temperatures by placing the sample, previously heated up to 45°C, on the decalin bath of the light scattering device that was at 20°C, 25°C, and 30°C, respectively. Then, the sample was left there for 10 min to assure thermal equilibrium at the desired temperature, and the crystallization of the system was followed by measuring the temporal evolution of the $S(q)$. The initial $S(q)$ measured right after the equilibration time shows a liquid static structure for all the investigated temperatures, as shown in Figure 3 for the KPS0.1 sample. The initial $S(q)$ measured at 20°C, 25°C, and 30°C are plotted in Figures 3A,D,G); respectively. Notice that, right after quenching, the samples show a liquid-like structure, but the main peak height of the $S(q)$ is above 2.85, thus indicating that the sample will eventually crystallize as predicted by the Hansen-Verlet freezing criterion for monodisperse systems [37]. Indeed, the sample static structure evolves to its final equilibrium state, corresponding to a crystalline phase, as shown in Figures 3B,E,H for 20°C, 25°C, and 30°C; respectively. Moreover, the appearance of iridescence highlights the crystallization of the sample. At all temperatures, the microgel dispersion displays a body-centered cubic crystalline (BCC) structure, identified by the Miller indexes corresponding to the Bragg peaks appearing in the structure factor. Previous simulations [38] and experiments [4], performed for systems at low particle concentrations displaying long-range repulsive interparticle interactions, report spontaneous assembling into BCC lattices. To study

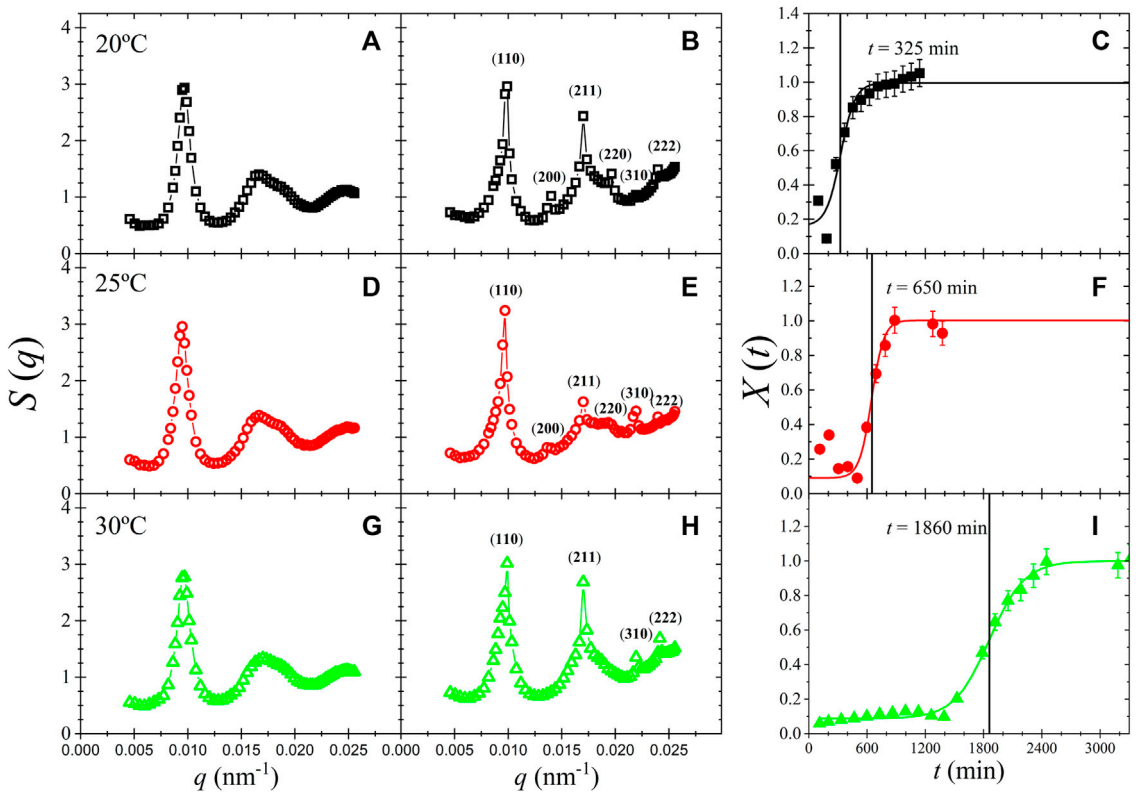

FIGURE 4
(A) Initial measured static structure factor, $S(q)$, right after quenching, **(B)** Final equilibrium static structure, **(C)** time evolution of the degree of crystallinity (symbols) along with a Boltzmann fit (continuous line) at 20°C. **(D)** Initial $S(q)$ right after quenching, **(E)** Final equilibrium static structure, **(F)** time evolution of the degree of crystallinity (symbols) along with a Boltzmann fit (continuous line) at 25°C. **(G)** Initial $S(q)$ right after quenching, **(H)** Final equilibrium static structure, **(I)** time evolution of the degree of crystallinity (symbols) along with a Boltzmann fit (continuous line) at 30°C for sample KPS0.6 at n = 2.4 particles/μm^3.

the crystallization evolution, we determine the time dependence of the sample structure by measuring the $S(q)$ at different times.

Interestingly, the naked eye can observe differences in the crystallization kinetics since the sample quenched to 20°C crystallizes faster than that at 25°C, and the latter is faster than that at 30°C. As the final equilibrium state is deeper into the crystal region and farther from the liquid-crystal transition, the crystallization kinetics is faster. To quantitatively analyze the crystallization kinetics, we calculate the degree of crystallization, $X(t)$, by using

$$X(t) = c\int_{q_1}^{q_2} S_c(q,t)dq, \tag{3}$$

Where c is a normalization constant. The static structure factor of the crystalline phase $S_c(q, t)$ is calculated by subtracting the contribution of the background fluid from the measured static structure factor $S(q, t)$. We estimate the contribution from the background fluid by scaling the initial measurement with a factor, $S_f(q, t = 0) = \alpha(t)S(q, t = 0)$, so that the scattered intensity matches the background of the measurement at time t, $S_c(q, t) = [S(q, t) - \alpha(t)S(q, t = 0)]$ [39]. The time evolution of the resulting degree of crystallization calculated for 20°C, 25°C, and 30°C are shown as symbols in Figures 3C,F,I, respectively. At all temperatures, we can observe three regimes: 1) the first one corresponds to the early states where the crystalline precursor appears, 2) then, the crystallinity increases sharply (crystal growth), and 3) the last region is reached steadily (coarsening) after the crystallization of the whole sample, where $X(t)$ remains almost constant. These crystallinity curves resemble others obtained in crystallization studies performed on different colloidal systems [39]. Based on these results, where a sigmoidal pattern is observed, similarly to other phase-transition phenomena, the degree of crystallization can be reasonably described by a Boltzmann-type function of the form [40].

$$X(t) = \frac{A_1 - A_2}{1 + e^{(t-\tau)/p}} + A_2, \tag{4}$$

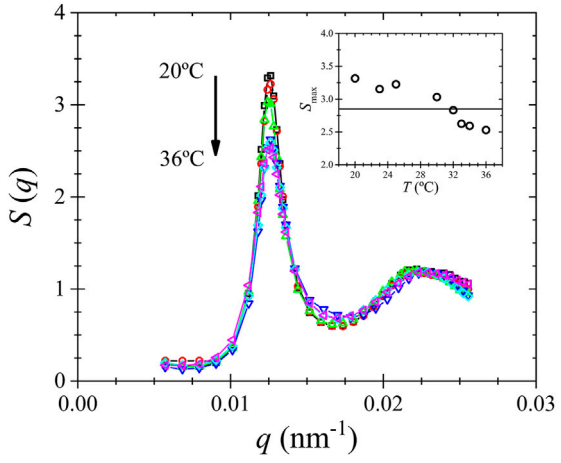

FIGURE 5
Measured static structure factor measured right after quenching at different temperatures for system KPS0.6. The arrow indicates the interval temperature under study, and its direction points to higher temperatures. Inset: Height of the mean peak of the structure factor, S_{max}, as a function of temperature. The horizontal line indicates the Hansen-Verlet criterion, corresponding to $S(q) = 2.85$.

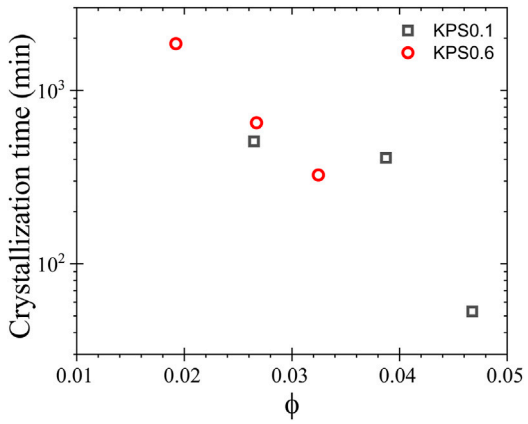

FIGURE 6
Crystallization times as a function of volume fraction occupied by microgels for both systems, KPS 0.1 (black open squares), and KPS 0.6 (red open circles).

where A_1, A_2, and p are constants obtained from the fit, and τ can be identified as a characteristic time for the crystallization of the system, considered as the time where the crystallinity increases faster, as observed in Figures 3C,F,I.

The fits to the $X(t)$, shown as continuous lines in the figure, describe the experiments reasonably well and provide the values of the mean crystallization time τ marked by vertical lines. For the lowest temperature under study, 20°C, the crystallization time obtained is τ = 53 min; then this time increases to τ = 412 min for 25°C and τ = 508 min for 30°C. Note that in the crystallization process, the temperature increase provokes slower.

Kinetics reflected in the increase of the crystallization times and a slowdown of the crystallization rate. Analogously, the same study was carried out for the most charged system, KPS0.6; the results are shown in Figure 4. In this case, the initial $S(q)$ also displays a liquid-like structure with the main peak height higher than 2.85 for all temperatures investigated, as can be seen in Figures 4A,D,G. Similar to the less charged system, the equilibrium state corresponds to a BCC crystal (Figures 4B,E,H).

Additionally, the evolution of the crystallinity factors resembles those obtained for the KPS0.1 system, as shown in Figures 4C,F,I. For the most charged system, the crystallization times are τ = 325 min at 20°C, τ = 650 min at 25°C, and τ = 1860 min at 30°C, represented in the figures by vertical lines. For this system, the crystallization process also slows as the system temperature approximates the temperature where the sample undergoes a liquid-solid transition. The liquid-solid transition temperature of the system is estimated from measurements of the static structure factor at different temperatures, right after thermal equilibrium. The measured static structure factors are shown in Figure 5. Here, we can observe that the sample structure is more correlated at low temperatures, reflected in the height of the principal peak of $S(q)$, S_{max}, than at high temperatures.

The decrease in correlation with temperature has been reported previously for deionized charged microgel dispersions [4, 8, 41], and it is associated with an entry of counterions to the microgel as the particle collapses, which translates into a smaller net particle charge [4]. This entry of counterions compensates for the increased electrostatic energy due to the distance reduction between the particles charged groups during microgel shrunk. For those samples showing a $S_{max} > 2.85$, the measured static structure at initial times corresponds to a metastable state since the sample eventually crystallizes. However, at higher temperatures, around the VPTT and beyond, the initial measured structure corresponds to an equilibrium liquid state. The liquid-solid transition temperature is better observed in the inset of Figure 5, where S_{max} is plotted as a function of temperature. Notice that the liquid-crystal transition temperature, marked with a horizontal line at 2.85, is around 32°C. The similarity between the values found for the VPTT and the liquid-crystal transition temperature is a coincidence since, for more concentrated systems, an increase of the latter is expected [4].

The crystallization occurs when the initial colloidal fluid is quenched to a temperature beyond the fluid-solid transition boundary. Thus, in both cases, KPS0.1 and KPS0.6 display the expected temperature dependence of the crystallization rate. In Figure 6, the crystallization times are shown for both systems as a function of volume fraction. Here we can observe that, on the one hand, crystallization is faster for the lowest temperature studied, 20°C, because the particle's charge, size and volume fraction become larger than at higher temperatures. At this temperature,

particles fill more space and interact more strongly, thus reducing the free energy of the whole system and favoring crystal formation. On the other hand, at higher temperatures close to but smaller than the liquid-crystal temperature, the free energy of the crystal becomes unfavorably for crystallization. Thus, an increment of environment entropy is required to achieve crystallization, resulting in a slower process. Interestingly, the volume fraction dependence of the crystallization time is very similar for both systems and, apparently, independent of the charge of the microgel. However, in order to confirm this behavior, more experiments are needed.

Concluding remarks

In this work, we study the crystallization kinetics of charged PNIPAM microgels dispersions at deionized conditions. We find that the crystallization rate can be tuned by temperature, resulting from the inherent temperature dependence of PNIPAM that affects microgel size, volume fraction, and particle charge. The crystallization study shows that, independently of the microgel charge, the nucleation time increases as the dimension of the microgel decreases with increasing temperature. The temperature increase provokes changes in the dispersion volume fraction, particle diffusion coefficient, and particle electrostatic charge, being a complex problem worthy of being analyzed. Previously, similar studies have been performed, but in neutral microgel suspensions, where the volume fraction of the dispersions under study was higher than 50% [11]. In our case, the system undergoes a liquid-crystal transition at very low volume fractions, ~ 1–5%, thanks to the microgels' low polydispersity and electrostatic charge. Another difference between previous studies and ours is how the initial state is reached. In the first, the initial metastable state is achieved by molten shearing once the system is at the desired temperature. However, in our case, the initial liquid phase that assures no memory effects is reached by heating the sample to 45°C and then quenching to the temperature under study. Working with charged microgels under deionized conditions offers the possibility of studying the phenomena of colloidal crystallization at very low volume fractions, which helps to minimize the inherent experimental difficulties associated with gravity and systems turbidity. We consider that our results encourage further systematic studies as a function of number concentration, temperature, and electrostatic charge in microgels dispersions to describe a complete scenario.

Data availability statement

The original contributions presented in the study are included in the article/supplementary material, further inquiries can be directed to the corresponding authors.

Author contributions

JB-F and DR-C performed the experiments and helped with data analysis. CH-P and LR-O planned the experiments, analyzed data, and wrote the manuscript.

Funding

CH-P and LR-O acknowledge Conacyt (Projects A1-S-16002, A1-S-9197, and INFR-294203) and UAM-Azcapotzalco for financial support.

Conflict of interest

The authors declare that the research was conducted in the absence of any commercial or financial relationships that could be construed as a potential conflict of interest.

Publisher's note

All claims expressed in this article are solely those of the authors and do not necessarily represent those of their affiliated organizations, or those of the publisher, the editors and the reviewers. Any product that may be evaluated in this article, or claim that may be made by its manufacturer, is not guaranteed or endorsed by the publisher.

References

1. Hirotsu Y, Hirokawa T, Tanaka T. Volume-phase transitions of ionized N-isopropylacrylamide gels. *J Chem Phys* (1987) 87:1392–5. doi:10.1063/1.453267

2. Hu Z. Crystallization of microgel spheres. In: A Fernandez-Nieves, HM Wyss, J Mattsson, DA Weitz, editors. *Microgel suspensions: Fundamentals and applications*. Weinheim, Germany: WILEY-VCH Verlag GmbH & Co (2011). p. 207–28.

3. Karg M, Pich A, Hellweg T, Hoare T, Lyon LA, Crassous JJ, et al. Nanogels and microgels: From model colloids to applications, recent developments, and future trends. *Langmuir* (2019) 35:6231–55. doi:10.1021/acs.langmuir.8b04304

4. Braibanti M, Haro-Pérez C, Quesada-Pérez M, Rojas-Ochoa LF, Trappe V. Impact of volume transition on the net charge of poly-N-isopropyl acrylamide microgels. *Phys Rev E* (2016) 94:032601. doi:10.1103/physreve.94.032601

5. Lyon LA, Meng Z, Singh N, Sorrell CD, John ST. Thermoresponsive microgel-based materials. *Chem Soc Rev* (2009) 38:865–74. doi:10.1039/b715522k

6. Alsayed AM, Islam MF, Zhang J, Collings PJ, Yodh AG. Premelting at defects within bulk colloidal crystals. *Science* (2005) 309:1207–10. doi:10.1126/science.1112399

7. Frenzel L, Dartsch M, Balaguer GM, Westermeier F, Grübel G, Lehmkühle F. Glass-liquid and glass-gel transitions of soft-shell particles. *Phys Rev E* (2021) 104: L012602. doi:10.1103/physreve.104.l012602

8. Aguirre-Manzo LA, Ledesma-Motolinía M, Rojas-Ochoa LF, Trappe V, Callejas-Fernández J, Haro-Pérez C, et al. Accounting for effective interactions among charged microgels. *Phys Rev E* (2019) 100:032602. doi:10.1103/physreve.100.032602

9. Ledesma-Motolinía M, Braibanti M, Rojas-Ochoa LF, Haro-Pérez C. Interplay between internal structure and optical properties of thermosensitive nanogels. *Colloids Surf A: Physicochemical Eng Aspects* (2015) 482:724–7. doi:10.1016/j.colsurfa.2015.07.020

10. Tang S, Hu Z, Zhou B, Cheng Z, Wu J, Marquez M. Melting kinetics of thermally responsive microgel crystals. *Macromolecules* (2007) 40:9544–8. doi:10.1021/ma0716682

11. Tang SJ, Hu ZB, Cheng ZD, Wu JZ. Crystallization kinetics of thermosensitive colloids probed by transmission spectroscopy. *Langmuir* (2004) 20:8858–64. doi:10.1021/la049203h

12. Hellweg T, Dewhurst CD, Brückner E, Kratz K, Eimer W. Colloidal crystals made of poly(N-isopropylacrylamide) microgel particles. *Colloid Polym Sci* (2000) 278:972–8. doi:10.1007/s003960000350

13. Niozu A, Kumagai Y, Hiraki TN, Fukuzawa H, Motomura K, Bucher M, et al. Crystallization kinetics of atomic crystals revealed by a single-shot and single-particle X-ray diffraction experiment. *Proc Natl Acad Sci U S A* (2021) 118: e2111747118. doi:10.1073/pnas.2111747118

14. Zhou J, Cai T, Tang S, Marquez M, Hu Z. Growth of columnar hydrogel colloidal crystals in water-organic solvent mixture. *Langmuir* (2006) 22:863–6. doi:10.1021/la0515773

15. Lapkin D, Mukharamova N, Assalauova D, Dubinina S, Stellhorn J, Westermeier F, et al. *In situ* characterization of crystallization and melting of soft, thermoresponsive microgels by small-angle X-ray scattering. *Soft Matter* (2022) 18:1591–602. doi:10.1039/d1sm01537k

16. Rieese CE, Mikhonin AV, Kamenjicki M, Tikhonov A, Asher SA. Nanogel nanosecond photonic crystal optical switching. *J Am Chem Soc* (2004) 126:1493–6. doi:10.1021/ja037118a

17. Das M, Zhang H, Kumacheva E. Microgels: Old materials with new applications. *Annu Rev Mater Res* (2006) 36:117–42. doi:10.1146/annurev.matsci.36.011205.123513

18. Park JG, Rogers WB, Magkiriadou S, Kodger T, Kim SH, Kim YS, et al. Photonic-crystal hydrogels with a rapidly tunable stop band and high reflectivity across the visible. *Opt Mater Express* (2017) 7:253–63. doi:10.1364/ome.7.000253

19. Go D, Rommel D, Chen L, Shi F, Sprakel J, Kuehne A. Programmable phase transitions in a photonic microgel system: Linking soft interactions to a temporal pH gradient. *Langmuir* (2017) 33:2011–6. doi:10.1021/acs.langmuir.6b04433

20. Zhou J, Wei J, Ngai T, Wang L, Zhu D, Shen J. Correlation between dielectric/electric properties and cross-linking/charge density distributions of thermally sensitive spherical PNIPAM microgels. *Macromolecules* (2012) 45:6158–67. doi:10.1021/ma300454h

21. Mohanty PS, Richtering W. Structural ordering and phase behavior of charged microgels. *J Phys Chem B* (2008) 112:14692–7. doi:10.1021/jp808203d

22. Sennato S, Chauveau E, Casciardi S, Bordi F, Truzzolillo D. The double-faced electrostatic behavior of PNIPAm microgels. *Polymers* (2021) 13:1153–79. doi:10.3390/polym13071153

23. Yang Y, Maldonado-Valderrama J, Martín-Molina A. Temperature and electrostatics effects on charged poly(N-isopropylacrylamide) microgels at the interface. *J Mol Liq* (2020) 303:112678. doi:10.1016/j.molliq.2020.112678

24. Senff H, Richtering W, Temperature sensitive microgel suspensions: Colloidal phase behavior and rheology of soft spheres. *J Chem Phys* (1999) 111:1705–11. doi:10.1063/1.479430

25. Liu J, Schöpe HJ, Palberg T. An improved empirical relation to determine the particle number density of fluid-like ordered charge-stabilized suspensions. *Part Part Syst Charact* (2000) 17:206–12. doi:10.1002/1521-4117(200012)17:5/6<206::aid-ppsc206>3.0.co;2-c

26. Schätzel K. Suppression of multiple scattering by photon cross-correlation techniques. *J Mod Opt* (1991) 38:1849–65. doi:10.1080/09500349114551951

27. Aberle LB, Wiegand S, Staude W. Suppression of multiple scattered light by photon cross-correlation in a 3D experiment. *Prog Colloid Polym Sci* (1997) 104: 121–5. doi:10.1007/bf01182426

28. Urban C, Schurtenberger P. Characterization of turbid colloidal suspensions using light scattering techniques combined with cross-correlation methods. *J Colloid Interf Sci* (1998) 207:150–8. doi:10.1006/jcis.1998.5769

29. Ojeda-Mendoza GJ, Moncho-Jordá A, González-Mozuelos P, Haro-Pérez C, Rojas-Ochoa LF. Evidence of electrostatic-enhanced depletion attraction in the structural properties and phase behavior of binary charged colloidal suspensions. *Soft Matter* (2018) 14:1355–64. doi:10.1039/c7sm02220d

30. Koppel DE. Analysis of macromolecular polydispersity in intensity correlation spectroscopy: The method of cumulants. *J Chem Phys* (1972) 57: 4814–20. doi:10.1063/1.1678153

31. Johnson CS, Gabriel DA. *"Dynamic light scattering" in laser light scattering*. New York, United States: Dover Publications (1994). p. 22–35.

32. López-León T, Ortega-Vinuesa JL, Bastos-González D, Elaïsari A. Cationic and anionic poly(N-isopropylacrylamide) based submicron gel particles: Electrokinetic properties and colloidal stability. *J Phys Chem B* (2006) 110: 4629–36. doi:10.1021/jp0540508

33. Tauer K, Gau D, Schulze S, Völkel A, Dimova R. Thermal property changes of poly(N-isopropylacrylamide) microgel particles and block copolymers. *Colloid Polym Sci* (2009) 287:299–312. doi:10.1007/s00396-008-1984-x

34. Nägele G. On the dynamics and structure of charge-stabilized suspensions. *Phys Rep* (1996) 272:215–372. doi:10.1016/0370-1573(95)00078-x

35. Haro-Pérez C, Rojas-Ochoa LF, Castañeda-Priego R, Quesada-Pérez M, Quesada-Pérez M, Callejas-Fernández J, et al. Dynamic arrest in charged colloidal systems exhibiting large-scale structural heterogeneities. *Phys Rev Lett* (2009) 102:018301. doi:10.1103/physrevlett.102.018301

36. Verwey EJW, Overbeek JTG. *Theory of the stability of lyophobic colloids*. New York: Elsevier (1948).

37. Hansen JP, Verlet L. Phase transitions of the Lennard-Jones system. *Phys Rev* (1969) 184:151–61. doi:10.1103/physrev.184.151

38. Gu L, Xu S, Sun Z, Wang JT. Brownian dynamics simulation of the crystallization dynamics of charged colloidal particles. *J Colloid Interf Sci* (2010) 350:409–16. doi:10.1016/j.jcis.2010.07.009

39. Iacopini S, Palberg T, Schöpe HJ. Crystallization kinetics of polydisperse hard-sphere-like microgel colloids: Ripening dominated crystal growth above melting. *J Chem Phys* (2009) 130:084502. doi:10.1063/1.3078310

40. Navarro-Verdugo AL, Goycoolea FM, Romero-Meléndez G, Higuera-Ciapara I, Argüelles-Monal W. A modified Boltzmann sigmoidal model for the phase transition of smart gels. *Soft Matter* (2011) 7:5847–53. doi:10.1039/c1sm05252g

41. Moncho-Jordá A, Quesada-Pérez M. Crossover of the effective charge in ionic thermoresponsive hydrogel particles. *Phys Rev E* (2019) 100:050602. doi:10.1103/physreve.100.050602

frontiers | Frontiers in Physics

TYPE Brief Research Report
PUBLISHED 15 September 2022
DOI 10.3389/fphy.2022.955006

OPEN ACCESS

EDITED BY
Emanuela Del Gado,
Georgetown University, United States

REVIEWED BY
Orhan Özdemir,
Istanbul University-Cerrahpasa, Turkey
Ryan Poling-Skutvik,
University of Rhode Island, United States
Ali Mohraz,
University of California, Irvine,
United States

*CORRESPONDENCE
Ryan McGorty,
rmcgorty@sandiego.edu

SPECIALTY SECTION
This article was submitted to Soft Matter Physics,
a section of the journal
Frontiers in Physics

RECEIVED 27 May 2022
ACCEPTED 22 August 2022
PUBLISHED 15 September 2022

CITATION
Rel R, Terwilliger D and McGorty R (2022), Shear-induced vorticity aligned flocs in a temperature responsive colloid-polymer mixture.
Front. Phys. 10:955006.
doi: 10.3389/fphy.2022.955006

Shear-induced vorticity aligned flocs in a temperature responsive colloid-polymer mixture

Ryle Rel, Dennis Terwilliger and Ryan McGorty*

Department of Physics and Biophysics, University of San Diego, San Diego, CA, United States

Shear driven patterning is seen in many soft matter systems. We use rheology and optical microscopy to probe the structures formed when we shear a colloid-polymer mixture containing temperature-sensitive microgel particles. By increasing the temperature, we can increase the particle attraction and transition from liquid-like to gel-like behavior. And by applying shear flow to the sample as the temperature and, hence, state of the system changes, we can affect the morphology of mesoscopic colloidal clusters. We can produce gels comprised of fibrous, elongated colloid-dense clusters, or we can form more isotropic clusters. The rheology is measured and shear-induced flocculation observed for colloid-polymer systems with different cluster morphologies. At shear rates high enough to produce elongated clusters but low enough to not break clusters apart, we observe log-like flocs that are aligned with the vorticity direction and roll between the parallel plates of our rheometer.

KEYWORDS

colloids, rheology, microgel particles, rheo-optics, shear-induced aggregation

Introduction

Colloidal suspensions find wide use for their rheological properties and their ability to assemble into complex structures [1]. With a multitude of routes for colloidal synthesis, particle sizes large enough for detection with optical methods, and tunable interparticle interactions, the structure and mechanical properties of colloidal assemblies can be readily observed, measured, and modified. Therefore, the assembly of colloidal particles has been probed to, e.g., understand the kinetics of crystal nucleation and growth [2], the mechanisms of gelation [3], and the fabrication of capsules [4]. Likewise, the rheology of colloidal suspensions has been used to, e.g., develop theoretical models for non-linear flow responses [5] and tailor the properties of 3D printer ink [6]. Whether to test fundamental models of matter or to drive applied research towards product development, these two aspects of colloids—elementary building blocks of complex assemblies and rheological modifiers—are often quite entangled [7]. Flow can assist in the assembly of higher order structures, such as colloidal crystals [8, 9], and the details of a sample's microstructure can assist in explaining rheological properties, like shear thinning or thickening in dense suspensions [10] or how a gel yields and flows [11, 12].

In many colloidal systems, researchers have observed anisotropic shear-induced structures which align along the vorticity direction. These structures are of great

interest due to their implications in determining the (potentially directional dependent) rheology of complex fluids and in revealing routes to fabricate anisotropic materials. Such anisotropic shear-induced structures have been studied experimentally through orthogonal superposition rheology [13, 14], rheo-scattering experiments [15, 16], and real space rheo-optical methods [17, 18]. Of the plethora of anisotropic shear-induced structures observed, a subset feature log-rolling flocs, whose formation strongly depends on the degree of confinement. These vorticity-aligned log-rolling flocculated structures have been observed in emulsions [19]; particle-loaded polymer blends [20]; carbon nanotube suspensions [21, 22]; carbon black suspensions [23–25]; mud samples [26]; and other suspensions of attractive particles [27, 28]. A complete understanding of such log-rolling floc formation is crucial for applications where complex fluids might flow through confined geometries (e.g., 3D printing) and for scalable methods of producing anisotropic materials (e.g., films with anisotropic conductivity [29, 30]).

A large advance in the understanding of this type of shear-induced patterning came from the experiments and simulations performed by Varga et al. in 2019 [27]. The authors demonstrated that density fluctuations within a sheared and confined suspension of attractive particles can set up eddies which, due to hydrodynamic coupling between the particle aggregates and the boundaries, promote the stable formation of log-rolling flocs. Further, the authors showed that if the shear forces are sufficiently large, flocs will break apart and stable vorticity-aligned log-rolling structures will not form. Whether the shear force is too large or not depends on the interparticle attraction, a fact which motivates the use of the Mason number, Mn, the ratio of the shear force on a particle to the interparticle force at contact. Stable logs were only observed below a critical Mason number, Mn_c, with Mn_c decreasing with increasing distance between the confining boundaries.

In this work, we explore the log-rolling floc formation in a colloid-polymer system containing thermoresponsive microgel colloidal particles using an optical microscope attachment on a rheometer with a parallel-plate geometry. Using poly(N-isopropylacrylamide) (pNIPAM) microgel particles allows us to vary the interparticle attraction *in situ* by changing the temperature, a property used in many prior investigations of colloidal phase behavior and rheology [31–36].

We find that, for our system, the morphology of colloidal clusters—assemblies of particles on a mesoscopic scale between that of the particle size (~1 μm) and system size (>150 μm)—is an important factor influencing log formation. With our thermoresponsive colloid-polymer system, we can create colloidal gels comprised of elongated, highly anisotropic clusters or more isotropic clusters. Gels consisting of more elongated clusters tend to more readily form log-rolling flocs. Our work highlights the importance of investigating the impact of this mesoscopic cluster scale on shear-induced pattern formation. In many previous studies of colloidal gels, a cluster-centric view has proven fruitful. For example, past work has shown that colloidal clusters may determine the length scale for mechanical energy storage in colloidal gels [37] with inter-cluster bonds or cluster-cluster connections governing the elasticity [38–40]. Here, we show that a perspective which focuses on the mesoscopic cluster scale may also help elucidate macroscopic pattern formation in attractive colloidal suspensions.

Materials and methods

Materials

We synthesized pNIPAM microgel particles in a manner similar to previous syntheses by our group [41, 42] and following the guidance of previously published protocols [43]. We use ammonium persulfate (APS, purity 98%), N-isopropylacrylamide (NIPAM, 97%), and *N,N′*-methylenebisacrylamide (BIS, 99%), all used as received from Sigma Aldrich without purification. We synthesize particles in a 250 mL three necked round bottom flask heated to 80°C and under nitrogen atmosphere. In 200 mL of deionised water, we add 3.38 g of NIPAM and 0.15 g of BIS. Once dissolved, this solution is transferred to the three necked flask. We then add 0.11 g of APS dissolved in 3 ml of deionised water. We let the reaction run for 4 h with constant stirring with a magnetic stir bar and continuous bubbling of nitrogen through the solution. We concentrate the pNIPAM particle solution through centrifugation. We centrifuge the suspension at 30,000 *g* for 90 min. The supernatant is removed and fresh deionized water is added.

We estimate the pNIPAM particle volume fraction by measuring the viscosity of different particle dilutions using a Cannon-Ubbelohde dilution viscometer. According to the Einstein-Bachelor relation, the viscosity of a suspension of spherical particles relative to that of the suspending medium is $\eta/\eta_0 = 1 + 2.5\phi$ where ϕ is the effective particle volume fraction [44]. We found the volume fraction of our stock solution of concentrated pNIPAM particles to be $\phi \approx 0.6$.

We determine the size of our pNIPAM particles around the lower critical solution temperature (LCST) using dynamic light scattering (DLS) measurements taken with a Malvern Zetasizer NanoZS using a 632.8 nm laser with a detection angle of 173°. Above the LCST at 34°C, the diameter is 480 ± 30 nm (mean and standard deviation of four runs on the Zetasizer) and we used a particle concentration of $\phi < 0.01$ such that we do not see signs of aggregation in our DLS measurements. Below the LCST at 29°C, the diameter is 840 ± 80 nm. At lower temperatures, the size measurements from the Zetasizer are less consistent perhaps due to large polydispersity though follow up measurements are necessary to quantify this. However, from optical microscopy

of the particles at room temperature, we believe that their size at room temperature is approximately 800 nm.

We use xanthan polymer, Ticaxan® Xanthan VI from TIC Gums, to act as a depletant. Xanthan has been used in previous colloid-polymer samples to generate fluid-fluid phase separation or gelation [41, 42, 45]. As reported by the manufacturer, the molecular weight is in the range of 4–12 × 10^6 g mol^{-1}. We prepare a stock solution of xanthan with a concentration of 0.2% by weight with 0.1 M NaCl (Sigma Aldrich, >99%) and 2 mM NaN_3 (Sigma Aldrich, >99.5%).

We made samples to investigate shear-induced pattern formation by combining in equal parts our concentrated pNIPAM stock solution and the 0.2% xanthan solution. This results in a sample with a pNIPAM microgel particle volume fraction of 0.3.

Rheology

Rheological measurements are performed on a Discovery Hybrid Rheometer (DHR-3) from TA Instruments. For all data included here, we use a parallel plate geometry with a 40-mm-diameter upper plate and a bottom 1-mm-thick glass plate. The upper plate is made of stainless steel with a mirror finish to allow for better image quality when using the attached microscope. We use TA Instruments' Upper Heated Plate accessory to vary the sample temperature between 23°C and 34°C.

We load ~210 µL of our colloid-polymer mixture onto the rheometer by pipetting the solution onto the center of the bottom glass plate. The upper plate is slowly lowered while rotating at 0.2 rad/s. The upper plate is lowered until the sample completely fills the gap which usually results in a gap height of between 150 and 160 µm. To prevent sample evaporation, we seal the edge of the sample with mineral oil.

Before experimental runs, we try to erase the sample's shear and loading history by performing a conditioning step where the sample is sheared at 1,000 s^{-1} for 120 s, sheared at −1,000 s^{-1} for 120 s, and then allowed to equilibrate at rest for 180 s. This preshearing procedure is similar to ones used in other studies of shear-induced structuring [24, 25, 27, 28]. For the majority of experiments we discuss here, we then proceed to heat the sample from room temperature to 34°C at a rate of 0.5°C/min while steadily shearing the sample at a rate, $\dot{\gamma}_{T\uparrow}$, between 0 and 15 s^{-1}. After the sample reaches 34°C, we usually measure the frequency dependent viscoelastic moduli. We logarithmically sweep the frequency from 100 to 0.1 rad/s with five points per decade and with a strain amplitude of 3%. This is followed by a constant shear rate step where the sample is sheared at a rate $\dot{\gamma}_{hold}$ for 30 min and kept at 34°C. Typically, we use the same shear rate during this step as was used during the heating stage, i.e., $\dot{\gamma}_{T\uparrow} = \dot{\gamma}_{hold}$. For our samples, if vorticity-aligned log-rolling flocs form, it is at this step in which they appear. This step with constant shear rate is then followed by another oscillatory test using the same parameters as the previous one. The sample is then returned to 23°C at a rate of 2°C/min while being sheared with rate $\dot{\gamma}_{T\downarrow}$. The steps described above are then repeated. This whole procedure where the sample goes from room temperature to 34°C, is held at 34°C for 30 min at a constant shear rate, and is then brought back to 23°C typically takes ~75 min. This is usually repeated up to ~10 times with different shear rates over the course of a day or overnight. Between each run we perform the conditioning step described above (returning the sample to room temperature, shearing at 1,000 s^{-1} for 120 s, and then at −1,000 s^{-1} for 120 s) which allows us to conduct multiple runs of the same sample without noticeable effects from the previous run. See the Supplementary Material for a table of the parameters used in our rheological procedures.

Our rheometer is equipped to counter-rotate the bottom glass plate which results in a stagnation plane between the parallel plates. For most of our experimental runs, we do not enable this counterrotation. However, we occasionally use this feature to observe the formation of vorticity-aligned flocs without having such flocs leave the imaging field of view. When this counterrotation is used, we indicate so in the caption.

Microscopy

We use the modular microscopy accessory from TA Instruments to image the shear-induced flocculation. For images included here, we use Nikon objectives with either 2×, 10×, or 40× magnification (2× 0.1 NA Plan Apo; 10× 0.3 NA Plan Fluor; 40× 0.45 NA ELWD SPlan Fluor). Epi-illumination is provided by a 470-nm LED (M470L3, Thorlabs). Images are recorded on an Allied Vision Manta G-033 CCD camera with a resolution of 656 × 492 pixels at a maximum frame rate of 88 frames per second. We use the software Micro-Manager to record image sequences [46].

For macroscopic imaging where we can capture one-quarter of the 40-mm-diameter geometry, we use a macro lens attached to a 1,920 × 1,200 pixel CCD camera (Imaging Source, DMK 33UX174). Images are typically recorded at five frames per second. We illuminate the sample with a dual gooseneck LED light (AmScope, LED-14M).

Results and discussion

We prepare aqueous solutions of pNIPAM microgel particles and xanthan which exhibit temperature-dependent structural and mechanical properties. This colloid-polymer mixture shows gel-like behavior at room temperature as observed with optical microscopy (Figure 1A) and rheology (Figure 1B; Supplementary Figure S1). This behavior is due to the depletion attraction between the pNIPAM particles mediated by the xanthan polymers.

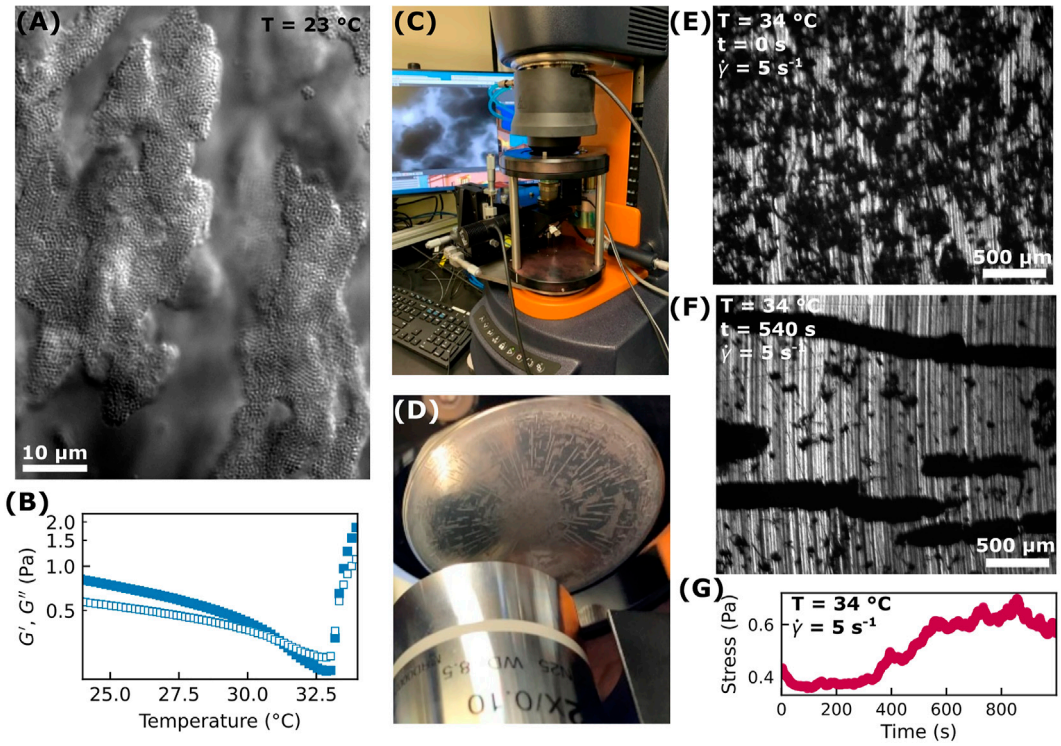

FIGURE 1
(A) At room temperature, the colloid-polymer mixture forms a weak gel as observed with a brightfield microscope using a 60× objective lens. **(B)** As measured with a DHR-3 instrument using a parallel-plate geometry, the storage (G', solid symbols) and loss (G'', open symbols) moduli vary with temperature. The moduli were obtained using a frequency of $\omega = 10$ rad/s with an amplitude of $\gamma_0 = 3\%$. **(C)** The DHR-3 used for collecting rheology and rheo-microscopy data is shown. The instrument is outfitted with a temperature-controlled upper plate and a bottom glass plate under which a microscope is placed. **(D)** A view from underneath the parallel-plate geometry shows a 2× microscope objective placed below the bottom glass plate. The sample shows shear-induced patterning as thin white structures oriented radially outward (in the vorticity direction) can be observed. **(E)** An image of the colloid-polymer mixture in the parallel-plate geometry after the sample was heated from 23°C to 34°C at a rate of 0.5°C/min. During this temperature ramp, the sample was sheared at a constant rate of $\dot{\gamma}_{T\uparrow} = 5\,s^{-1}$. This image was taken immediately after the sample first reached 34°C. **(F)** For the same sample shown in **(E)**, we continue applying a constant shear at a rate $\dot{\gamma}_{hold} = 5\,s^{-1}$ while the temperature was held at 34°C. This image shows vorticity-aligned flocs have formed at $t = 540$ s into this step of constant applied shear rate and constant temperature. The vertical axis of the image is along the flow direction and the horizontal axis is along the vorticity direction. **(G)** During this period of constant shear described in **(F)**, we measure the stress over time. Increases in the stress coincide with the formation of vorticity-aligned log-like flocs as seen by the uptick in stress at around 500 s which coincides with when the logs seen in **(F)** begin to form.

When sheared at room temperature (23°C) between parallel plates (40 mm diameter, ~150 μm gap size), we observe colloid-rich domains aligning along the flow direction. At room temperature, we never observe vorticity-aligned flocs for any of the shear rates we used, 0.5 s^{-1}–15 s^{-1}. This may be due to the fact that even at the lowest shear rate in this range, the shear forces acting on a particle are too large compared to the interparticle depletion attraction for stable vorticity-aligned logs to form.

We next explore if shear-induced patterning is seen at temperatures above pNIPAM's lower critical solution temperature (LCST) of about 32°C–33°C. Above this temperature, pNIPAM particles become more hydrophobic with an increased interparticle attraction. As the temperature of our sample increases from room temperature to 34°C, the interparticle attraction varies in a non-trivial way. As the temperature increases while remaining below the LCST, the pNIPAM particles decrease in size. This reduces the volume fraction of pNIPAM particles and reduces the strength of the depletion attraction. A quantitative picture of how the pNIPAM interparticle attraction varies as a function of temperature in the presence of a depletant is beyond the scope of this work (though the rich phenomena that similar pNIPAM-containing systems exhibit have been investigated previously by our lab [41] and by others [47]). However, we do see the effect of this change in interparticle attraction in Figure 1B. The storage and loss moduli, G' and G'', are measured as a function of temperature at a frequency of ω =10 rad/s with a strain amplitude of $\gamma = 3\%$. We observe that G' and G'' decrease with temperature and that while $G' > G''$ for lower temperatures, at around 31°C we observe more liquid-like behavior with $G' < G''$. We conjecture that this decrease in G' with increasing temperature and the transition

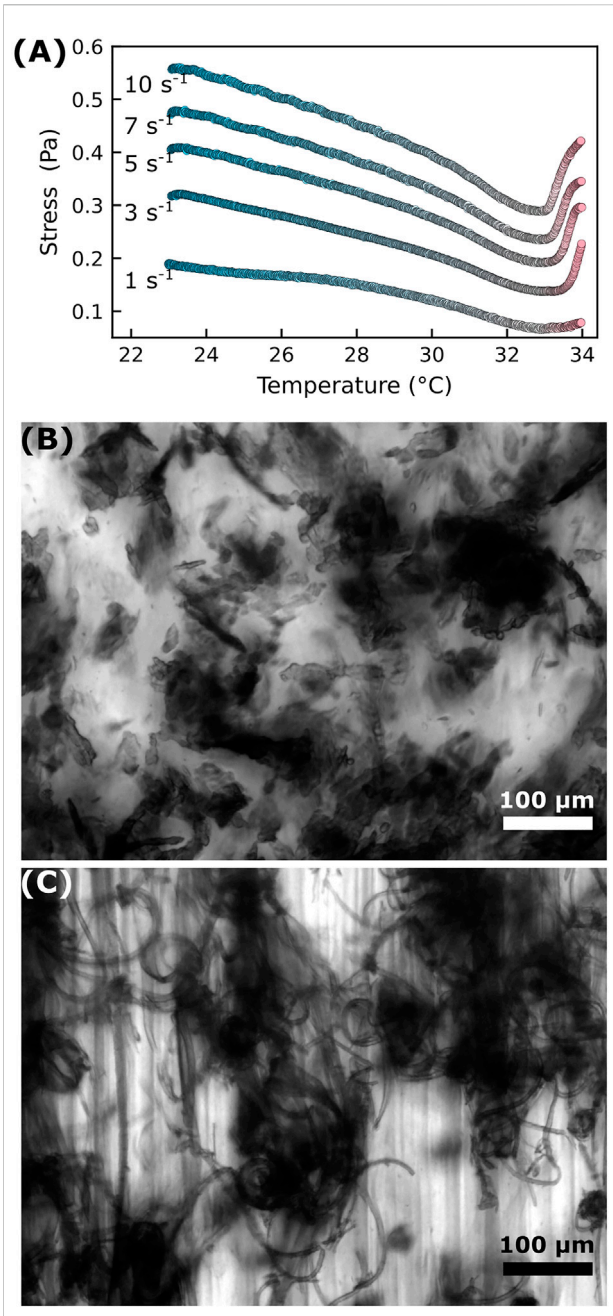

FIGURE 2
Shearing the sample as the temperature increases produces distinctly different cluster morphologies. **(A)** Samples are sheared at a constant rate of $\dot{\gamma}_{T\uparrow}$ while the temperature increases from 23°C to 34°C at a rate of 0.5°C/min. The stress is measured during this temperature ramp. For all values of the shear rate $\dot{\gamma}_{T\uparrow}$ used, we observe that the stress decreases as the temperature goes from room temperature to ~33°C. This is likely due to the decreasing volume fraction of the pNIPAM microgel particles as they decrease in size with increasing temperature. Above ~33°C, the stress increases with temperature as the increased hydrophobicity of the pNIPAM particles leads to stronger interparticle attraction. **(B)** Image of the sample immediately after this temperature ramp with a shear rate of $\dot{\gamma}_{T\uparrow} = 1\,s^{-1}$ taken with a 10× objective lens. **(C)** Image of the sample immediately after the temperature ramp with a shear rate of $\dot{\gamma}_{T\uparrow} = 7\,s^{-1}$. In comparison to **(B)**, the pNIPAM particles have aggregated into more fibrous and higher aspect ratio clusters.

from gel-like to liquid-like behavior is due to the decreasing volume fraction of pNIPAM particles and decreasing depletion attraction. Above 33°C, we observe a stiffer colloidal gel with G' returning to being larger than G''. The frequency dependent moduli for our colloid-polymer mixture at both 23°C and 34°C is shown in Supplementary Figure S1. While the pNIPAM particle volume fraction is larger at room temperature, the interparticle attraction is greater above the LCST which results in the elastic moduli being ~2× larger at 34°C than at 23°C.

At this higher temperature of 34°C, we do observe, with our rheo-optical setup (Figures 1C–F) the formation of vorticity-aligned flocs similar to what has been observed previously in other attractive suspensions or soft matter systems (see also Supplementary Videos S1–S3). The formation of such flocs coincides with an increase in the shear stress along with more variability in the stress as seen in Figure 1G. This increase in stress or viscosity associated with log-rolling floc formation is consistent with previous work on systems of colloidal rods [28], carbon black dispersions [24], and nanotube suspensions [21]. If, after the log-rolling flocs form, we leave the sample undisturbed at 34°C, then the logs seem to remain intact for at least several minutes but we have not investigated this thoroughly. However, if we bring the temperature back down to 23 C, then the pNIPAM particles will disperse away from the flocs.

Interestingly, we only observe the formation of the kind of vorticity-aligned flocs seen in Figures 1D,F in certain circumstances. If, after following the sample conditioning steps described in the Methods section (i.e., applying a shear of 1,000 s^{-1} for 120 s, −1,000 s^{-1} for 120 s, and allowing the sample to equilibrate at rest for 180 s), we increase the temperature to 34°C while the sample is at rest (i.e., no applied shear) and then, with the sample temperature held at 34°C, apply a steady shear of anywhere between 0.5 and 15 s^{-1} we do not observe the formation of flocs. That is, if $\dot{\gamma}_{T\uparrow} = 0$, then we observe no vorticity-aligned flocs for any value of $\dot{\gamma}_{hold}$ used. Instead, we observe isotropic aggregates of particles in the sheared sample which are smaller than the gap size and which do not appear to flocculate together or change in size or shape over time, at least as observed with our imaging setup. Further, we observe that the measured shear stress is steady with time and does not exhibit large fluctuations as we shear the sample at a constant rate. This is another indicator of little or no change in the sample's structure as it is sheared.

Instead of heating the sample to 34°C while the sample is quiescent, we also try applying a steady shear to the sample as we heat it from 23°C to 34°C at 0.5°C/min. That is, we set $\dot{\gamma}_{T\uparrow}$ to a value greater than zero. In Figure 2A, we show the stress as a function of temperature during this temperature ramp for a few different shear rates. For a given shear rate $\dot{\gamma}_{T\uparrow}$, stress initially decreases with temperature. This is likely due to the decreasing volume fraction of pNIPAM particles as the particles deswell and the concomitant reduction of the depletion attraction. The stress is a minimum at ~33°C, approximately pNIPAM's LCST. From

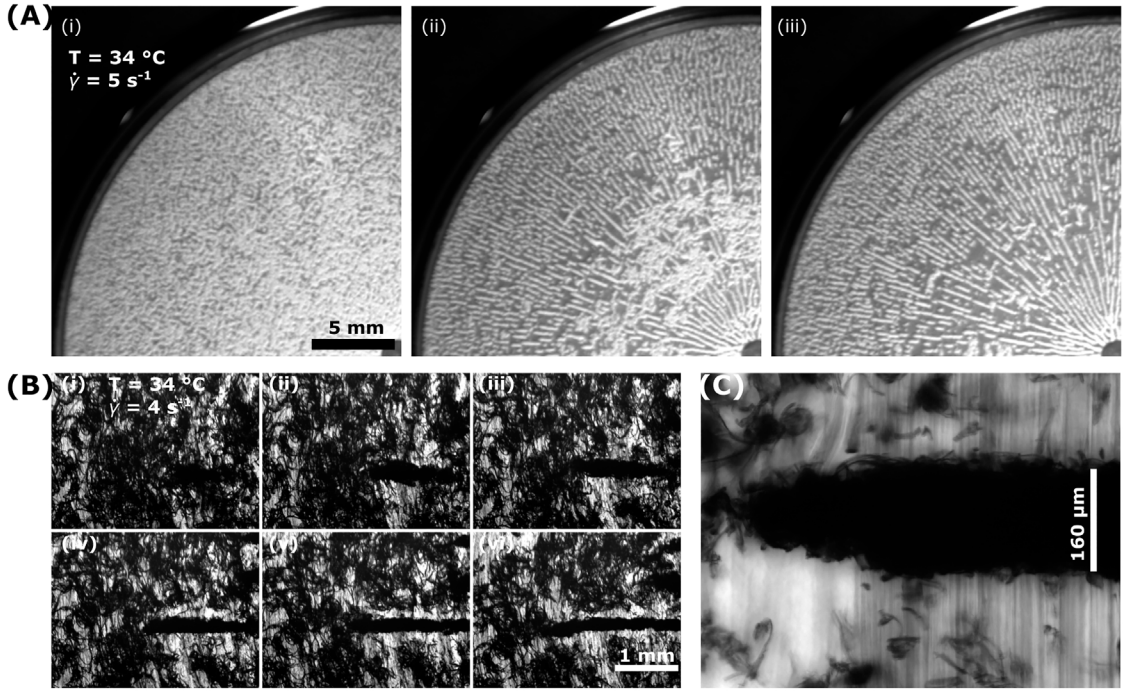

FIGURE 3
Shear-induced vorticity-aligned floc formation across scales. **(A)** Using a macro lens to capture a quarter of the parallel-plate geometry (diameter of 40 mm), we observe samples having undergone a temperature ramp to 34°C with a constant shear rate of $\dot{\gamma}_{T\uparrow} = 5\ s^{-1}$. Images are shown after the sample has reached 34°C and is being sheared at $\dot{\gamma}_{hold} = 5\ s^{-1}$. The time interval between each image in the set of three (i–iii) is 70 s. The first image (left) was taken seconds after the sample reached 34°C. While here we observe flocs throughout the geometry, we note that in other cases we observe flocs mainly near the center or near the edges of the geometry. **(B)** The initial formation of a vorticity-aligned floc is observed using a 2× objective while the sample is shared at $\dot{\gamma}_{hold} = 4\ s^{-1}$ after reading 34°C. The time interval between each image (i–vi) is 11.4 s. Counter-rotating of the bottom glass plate of the parallel-plate geometry was used to keep the floc in the field of view. Supplementary Video S1 captures this floc formation. **(C)** Image of a vorticity-aligned floc formed at 34°C using a shear rate of 4 s^{-1} taken with a 10× objective. The width of the floc is approximately equal to the parallel-plate gap height (here, $h = 157\ \mu m$).

33°C to 34°C, the stress increases, likely due to the stronger interparticle attraction above the LCST. The mesoscopic structures of our samples at 34°C are distinctly different depending on the value of this shear rate, $\dot{\gamma}_{T\uparrow}$. After the sample's temperature has reached 34°C, colloidal clusters are slightly elliptical in shape for lower shear rates (e.g., Figure 2B where $\dot{\gamma}_{T\uparrow} = 1\ s^{-1}$). But for higher $\dot{\gamma}_{T\uparrow}$, clusters take on a fibrous quality where the clusters are highly elongated (e.g., Figure 2C where $\dot{\gamma}_{T\uparrow} = 7\ s^{-1}$). See Supplementary Figure S2 for more such images.

We believe that the shear-rate-dependent shape of clusters can be understood considering the large body of work on how fluid droplets deform in shear flow. Though our colloid-polymer system exhibits gel-like behavior for most of the temperature range, our rheological (Figure 1B) and imaging (Supplementary Video S4) data shows liquid-like behavior at temperatures just below the LCST where colloid-dense and colloid-poor fluids likely coexist. Studies of flow-induced deformation of droplets and soft materials date back at least a century with the seminal work of G. I. Taylor [48, 49]. More recent experimental work on systems more resembling our own demonstrate that droplets sheared in confined geometries take on string-like elongated shapes with aspect ratios that increase with the shear rate [50] and that fluid-fluid phase separated colloid-polymer systems exhibit flow-elongated domains with aspect ratios dependent on the shear rate [51]. In our system, the low contrast between the colloid-dense regions and the continuous phase at temperatures below the LCST (given that the swollen pNIPAM particles are mostly water) make precise measurements of the shape of colloid-dense regions as a function of shear rate difficult. Nevertheless, we can use image autocorrelations to measure the approximate size of colloid-dense domains in the shear and vorticity directions as a function of shear rate at a constant temperature of 31°C. As seen in Supplementary Figure S3, the aspect ratio of these colloid-dense domains increases with increasing shear rate.

We believe that it is the morphology of the colloid-dense regions—a property dependent on the shear rate used as the sample is heated—that largely influences whether vorticity-aligned flocs form. Of course, as previous work has found,

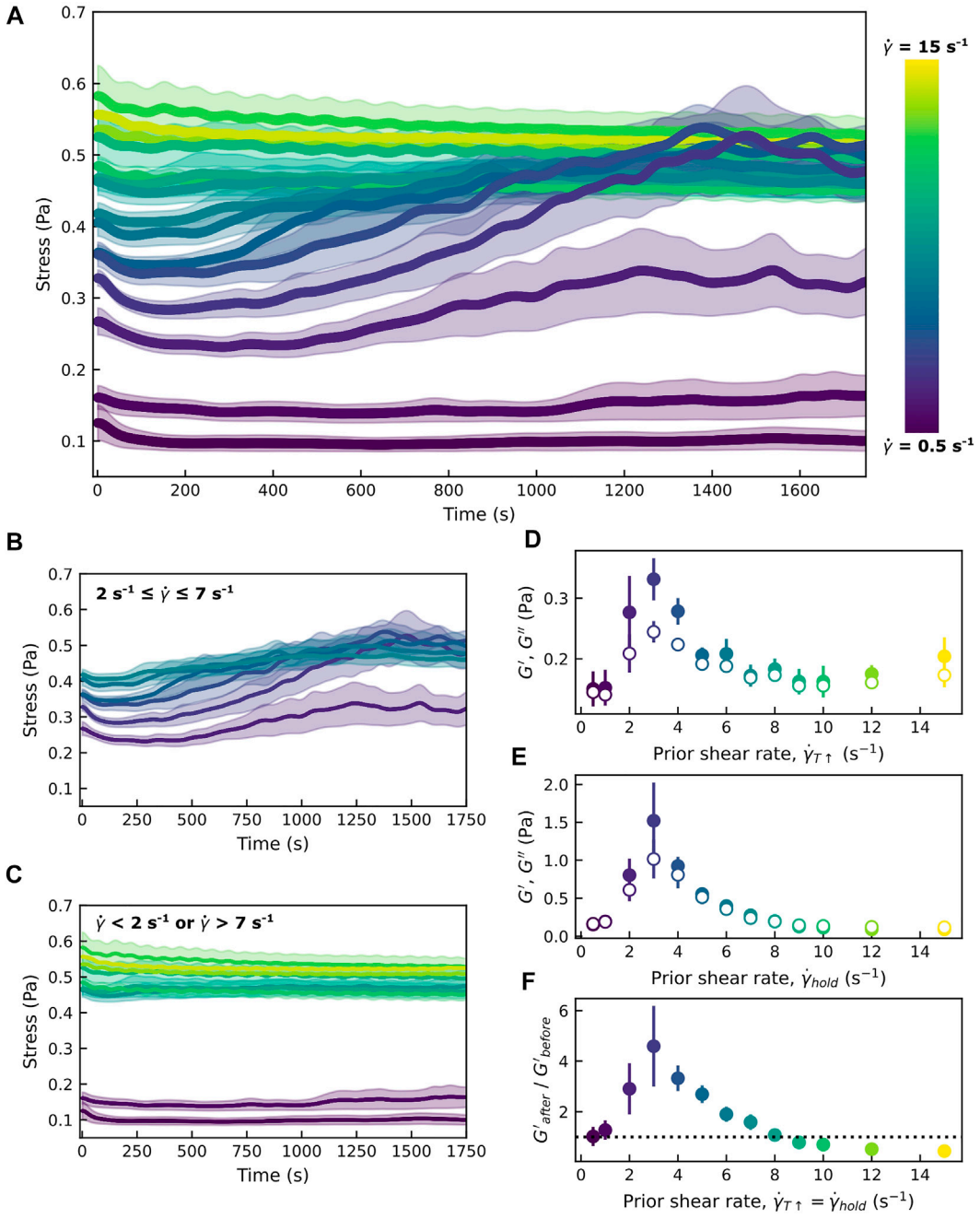

FIGURE 4
Shear-induced floc formation coincides with increases in the measured stress. **(A)** The colloid-polymer sample in a parallel-plate geometry is first heated to 34°C as described while subjected to shear at a rate $\dot{\gamma}_{T\uparrow}$. Following this temperature ramp, the sample is subjected to the same shear rate $\dot{\gamma}_{hold} = \dot{\gamma}_{T\uparrow}$ while being held at 34°C. We measure the stress as a function of time during this 30-min period of constant shear rate and constant temperature. Depending on the shear rate used, the stress remains relatively flat for the 30 min or shows an uptick with increased fluctuations. This increase in the stress coincides with floc formation. We observe this indication of floc formation for shear rates of 2–7 s^{-1}. The stress vs. time is shown for shear rates from 0.5 to 15 s^{-1} with the symbols indicating the mean over typically six runs. The shaded areas represent the mean ± standard error across the different runs. **(B)** Same as **(A)**, but only the data for shear rates of 2, 3, 4, 5, 6, and 7 s^{-1} are shown. These are the shear rates for which there is a noticeable increase in the stress with time and where vorticity-aligned logs form. **(C)** As with **(B)**, we show the same data in **(A)** but for only shear rates of 0.5, 1, 8, 9, 10, 11, 12, 13, 14, and 15 s^{-1}. **(D)** Oscillatory measurements are performed after the temperature ramp to 34°C. During this temperature ramp, the sample was sheared at $\dot{\gamma}_{T\uparrow}$. Plotted are the storage (G', solid symbols) and loss (G'', open symbols) moduli for a frequency of $\omega = 1$ rad/s and amplitude $\gamma_0 = 3\%$ as a function of the preceding shear rate $\dot{\gamma}_{T\uparrow}$. **(E)** Oscillatory measurements are performed after the sample is held at 34°C while subjected to a constant shear rate of $\dot{\gamma}_{hold}$ (set to the same value as the preceding $\dot{\gamma}_{T\uparrow}$ used during the temperature ramp) for 30 min. As in **(D)**, the storage and loss moduli are plotted as a function of $\dot{\gamma}_{hold}$. Outside of the range 2–7 s^{-1}, we observe more liquid-like responses ($G' \lesssim G''$). **(F)**
(*Continued*)

FIGURE 4 (Continued)
The ratio of the storage modulus measured before and after the 30-min hold at 34°C and constant shear rate $\dot{\gamma}_{hold}$ (equal to the preceding value for $\dot{\gamma}_{T\uparrow}$). That is, the ratio of G' in **(D)** and **(E)**. The dotted line corresponds to a ratio of 1. Only for shear rates between 2 and 7 s^{-1} do we observe that the storage modulus increases (ratio > 1) after this 30-min period. The error bars in **(D–F)**, as well as the shaded regions in **(A–C)**, represent the standard error across multiple runs of different samples (of identical composition) loaded onto the rheometer on different days.

other factors like gap height, particle volume fraction, and interparticle attraction also matter, but those factors are not systematically varied in our present work. We contend that a consideration of the mesoscale colloidal-cluster morphology explains why we see the formation of vorticity-aligned flocs for an intermediate range of shear rates.

For $2\,s^{-1} \lesssim \dot{\gamma}_{T\uparrow} = \dot{\gamma}_{hold} \lesssim 7\,s^{-1}$, we observe vorticity-aligned flocs forming within 30 min of steady shear after the sample has reached 34 °C. As seen in Figure 3, vorticity-aligned flocs are easily observed with our rheo-optical setup across a range of scales. Note that while in Figure 3A, vorticity-aligned flocs are seen throughout the sample geometry, in other instances, we observe flocs primarily towards the edges or near the center of the geometry, as one might expect for a parallel plate geometry where the shear rate varies with radial distance. The range of approximately 2 s^{-1}–7 s^{-1} is where we observe flocs throughout a large fraction of the geometry. Besides visual observation as seen in Figures 3A–C, floc formation can also be inferred from the measured shear stress as a function of time. As seen in Figures 4A–C, for some shear rates we observe that minutes or longer into the steady shear phase of our procedure there is a marked increase and fluctuations in the stress. We observe this for shear rates between 2 and 7 s^{-1}, whereas for shear rates less than 2 s^{-1} or greater than 7 s^{-1}, the stress varies little with time and shows no large fluctuations or increases. The stress is plotted versus time as logs form in Supplementary Figure S4 as well (see Supplementary Videos S2, S3 for movies of the floc formation seen in Supplementary Figure S4A).

Previous studies investigating the formation of vorticity-aligned flocs have noted an upper bound on the shear rate (a critical shear rate, $\dot{\gamma}_c$) above which such flocs do not form [25, 27, 28]. This critical shear rate depends on the degree of confinement ($\dot{\gamma}_c \sim h^{1.4}$ from [25, 27]). Our work likewise shows that if our colloidal system is sheared at too high of a rate, vorticity-aligned flocs are not observed. We have not yet explored how this depends on the gap height of our parallel plate geometry, but for the value $h \approx 150\,\mu m$ we find that $\dot{\gamma}_c \approx 8\,s^{-1}$.

However, our work also shows that there is a minimum shear rate below which vorticity-aligned flocs are not seen. We believe that this is due to how shear is deforming the colloid-dense mesoscale domains as the temperature increases and the interparticle interaction goes from a relatively weak depletion-induced attraction to a stronger hydrophobic attraction. At low shear rates, mesoscale colloidal clusters deform little due to the shear forces. At higher shear rates, colloidal clusters stretch out into high-aspect ratio structures. In comparison to more isotropic colloidal clusters, elongated clusters will form a larger number of connections with neighboring clusters. The fact that anisotropic particles can form a percolating network at a lower concentration than spherical particles has been shown in many studies of rod-shaped particles [28, 52]. In the experiments shown here, the concentration and aspect ratio of our pNIPAM colloidal particles are constants. But, the aspect ratios of the shear-deformed clusters do change. And just as rod-like particles will form space-spanning networks at a lower volume fraction than isotropic particles [52], elongated clusters will form more connections with neighboring clusters than isotropic clusters.

Moreover, the cluster morphology also affects the mechanical properties. After increasing the temperature from 23 to 34 °C during which we apply steady shear at a rate of $\dot{\gamma}_{T\uparrow}$, we perform oscillatory rheological measurements with the sample held at 34°C. The viscoelastic moduli from this data are shown in Figure 4D. We find the largest G' values are associated with prior shear rates $\dot{\gamma}_{T\uparrow}$ of between 2 and 4 s^{-1}. More work needs to be done to determine why the colloidal gel loses elasticity as $\dot{\gamma}_{T\uparrow}$ increases beyond 4 s^{-1}. Though very elongated clusters with a high aspect ratio may form a greater number of connections with surrounding clusters, perhaps the thinness of such clusters leads to a reduced elastic modulus in comparison to networks of thicker clusters with reduced aspect ratios. Or, perhaps at the higher shear rates, elongated clusters are quickly broken apart by shear forces. We also show G' and G'' measured immediately after the sample is sheared at $\dot{\gamma}_{hold}$ for 30 min at 34°C (before which the sample was sheared at $\dot{\gamma}_{T\uparrow} = \dot{\gamma}_{hold}$ during the temperature ramp to 34°C). As seen in Figures 4A,E, a solid-like mechanical response is observed for the range of shear rates where vorticity-aligned flocs form. Further, we show in Figure 4F the ratio of the elastic moduli after the 30 min of constant shearing and prior (that is, the ratio of the G' data in Figure 4E to that in Figure 4D). For shear rates between about 2 and 7 s^{-1}, this ratio is greater than one. Therefore, at these shear rates, the 30-min period of constant shearing increases the elastic moduli. For shear rates lower than 2 s^{-1} and higher than 7 s^{-1}, the period of constant shear reduced the elastic moduli. This again corroborates our optical imaging data (Figure 3) and stress vs. time data (Figures 4A–C) which shows that

shear-driven flocculation is occurring for an intermediate range of shear rates.

Conclusion

Our data suggests that an important factor influencing the propensity for shear-induced macroscopic patterning in our samples is the mesoscopic cluster morphology. Prior studies have shown how the degree of confinement (i.e., gap height), interparticle attraction, and volume fraction dictate whether vorticity-aligned log-rolling flocs will form. Our results show that for systems like ours the structure of the sample on the cluster scale also matters. A sample comprised of elongated, fiber-like colloidal clusters seems more likely to form shear-induced vorticity-aligned flocs than a sample containing isotropic colloidal clusters. This finding dovetails with recent work looking at the shear driven patterns of colloidal rod suspensions [28]. They found that vorticity-aligned flocs formed for rods at lower volume fractions than for spheres, due to the lower volume fraction of rods needed to form a percolating structure. From past work on colloidal rods [52], one can appreciate how shaping the colloidal clusters into elongated structures will more readily lead to a well-connected network if one considers the colloidal clusters as renormalized particles. In our work, we show how the colloidal clusters can be shaped using shear flow applied to the sample when the colloidal particle's attraction is weak enough to allow colloid-rich domains to stretch out in the direction of flow. However, for other systems, control over the cluster morphology could be achieved by using different external fields or the interparticle potential [53].

More generally, this work highlights the importance of the experimental history of a sample. How a colloidal gel's rheological properties depend on its shear history (i.e., rheological hysteresis) has been the subject of much research [54, 55]. For our thermoresponsive system, both the shear history and the temperature history are factors in the rheology and structure. This thermokinematic memory has been explored in other industrially relevant materials [56] and relates to recent work probing how temperature changes and the rate of temperature changes can (potentially in combination with shear) structure colloidal materials [47, 57–59].

Pattern formation due to flow in colloidal and complex fluids can be used to manufacture small-scale structures. It can also be a hinderance when material needs to flow through confined spaces, such as in 3D printing. Therefore, a complete understanding of shear driven structuration will help streamline current processing and potentially lead to new strategies for tuning soft materials.

Data availability statement

The raw data supporting the conclusion of this article will be made available by the authors, without undue reservation.

Author contributions

RM conceived and designed the study. RR and DT performed experiments. RM, RR, and DT analysed data. RM and RR wrote the manuscript. All authors helped revise and approve the submitted manuscript.

Funding

Support for this research came from a National Science Foundation Major Research Instrumentation award (CBET 1919429). Support also came from a Cottrell Scholars Award from the Research Corporation for Science Advancement to RM.

Conflict of interest

The authors declare that the research was conducted in the absence of any commercial or financial relationships that could be construed as a potential conflict of interest.

Publisher's note

Supplementary material

The Supplementary Material for this article can be found online at: https://www.frontiersin.org/articles/10.3389/fphy.2022.955006/full#supplementary-material

References

1. Fernandez-Nieves A, Puertas AM. *Fluids, colloids and soft materials: An introduction to soft matter physics*. John Wiley & Sons (2016).

2. Hensley A, Jacobs WM, Rogers WB. Self-assembly of photonic crystals by controlling the nucleation and growth of DNA-coated colloids. *Proc Natl Acad Sci U S A* (2022) 119(1):e2114050118. doi:10.1073/pnas.2114050118

3. Royall CP, Faers M, Fussell S, Hallett J. Real space analysis of colloidal gels: Triumphs, challenges and future directions. *J Phys : Condens Matter* (2021) 33: 453002. doi:10.1088/1361-648x/ac04cb

4. Rodriguez AMB, Binks BP. Capsules from Pickering emulsion templates. *Curr Opin Colloid Interf Sci* (2019) 44:107–29. doi:10.1016/j.cocis.2019.09.006

5. Brader JM. Nonlinear rheology of colloidal dispersions. *J Phys : Condens Matter* (2010) 22(36):363101. doi:10.1088/0953-8984/22/36/363101

6. Zhu C, Pascall AJ, Dudukovic N, Worsley MA, Kuntz JD, Duoss EB, et al. Colloidal materials for 3D printing. *Annu Rev Chem Biomol Eng* (2019) 10(1): 17–42. doi:10.1146/annurev-chembioeng-060718-030133

7. Vermant J, Solomon MJ. Flow-induced structure in colloidal suspensions. *J Phys : Condens Matter* (2005) 17(4):R187–216. doi:10.1088/0953-8984/17/4/r02

8. Joy M, Muangnapoh T, Snyder MA, Gilchrist JF. Flow-induced alignment of (100) fcc thin film colloidal crystals. *Soft Matter* (2015) 11(36):7092–100. doi:10.1039/c5sm01076d

9. Ackerson BJ, Pusey PN. Shear-induced order in suspensions of hard spheres. *Phys Rev Lett* (1988) 61(8):1033–6. doi:10.1103/physrevlett.61.1033

10. Cheng X, McCoy JH, Israelachvili JN, Cohen I. Imaging the microscopic structure of shear thinning and thickening colloidal suspensions. *Science* (2011) 333(6047):1276–9. doi:10.1126/science.1207032

11. Min Kim J, Eberle APR, Kate Gurnon A, Porcar L, Wagner NJ. The microstructure and rheology of a model, thixotropic nanoparticle gel under steady shear and large amplitude oscillatory shear (Laos). *J Rheology* (2014) 58(5):1301–28. doi:10.1122/1.4878378

12. Boromand A, Jamali S, Maia JM. Structural fingerprints of yielding mechanisms in attractive colloidal gels. *Soft Matter* (2017) 13(2):458–73. doi:10.1039/c6sm00750c

13. Colombo G, Kim S, Schweizer T, Schroyen B, Clasen C, Mewis J, et al. Superposition rheology and anisotropy in rheological properties of sheared colloidal gels. *J Rheology* (2017) 61(5):1035–48. doi:10.1122/1.4998176

14. Wang Y, Ewoldt RH. *New insights on carbon black suspension rheology – anisotropic thixotropy and anti-thixotropy* (2022). arXiv: 220205772 [cond-mat].

15. DeGroot JV, Macosko CW, Kume T, Hashimoto T. Flow-induced anisotropic SALS in silica-filled PDMS liquids. *J Colloid Interf Sci* (1994) 166(2):404–13. doi:10.1006/jcis.1994.1311

16. Pignon F, Magnin A, Piau J-M. Butterfly light scattering pattern and rheology of a sheared thixotropic clay gel. *Phys Rev Lett* (1997) 79(23):4689–92. doi:10.1103/physrevlett.79.4689

17. Cheng X, Xu X, Rice SA, Dinner AR, Cohen I. Assembly of vorticity-aligned hard-sphere colloidal strings in a simple shear flow. *Proc Natl Acad Sci U S A* (2012) 109(1):63–7. doi:10.1073/pnas.1118197108

18. Lin NYC, Cheng X, Cohen I. Biaxial shear of confined colloidal hard spheres: The structure and rheology of the vorticity-aligned string phase. *Soft Matter* (2014) 10(12):1969–76. doi:10.1039/c3sm52880d

19. Montesi A, Peña AA, Pasquali M. Vorticity alignment and negative normal stresses in sheared attractive emulsions. *Phys Rev Lett* (2004) 92(5):058303. doi:10.1103/physrevlett.92.058303

20. Mao C, Huang Y, Qiao Y, Zhang J, Kong M, Yang Q, et al. Vorticity-aligned droplet bands in sheared immiscible polymer blends induced by solid particles. *Langmuir* (2020) 36(16):4383–95. doi:10.1021/acs.langmuir.0c00511

21. Lin-Gibson S, Pathak JA, Grulke EA, Wang H, Hobbie EK. Elastic flow instability in nanotube suspensions. *Phys Rev Lett* (2004) 92(4):048302. doi:10.1103/physrevlett.92.048302

22. Ma AWK, Mackley MR, Rahatekar SS. Experimental observation on the flow-induced assembly of Carbon nanotube suspensions to form helical bands. *Rheol Acta* (2007) 46(7):979–87. doi:10.1007/s00397-007-0183-x

23. Osuji CO, Weitz DA. Highly anisotropic vorticity aligned structures in a shear thickening attractive colloidal system. *Soft Matter* (2008) 4(7):1388–92. doi:10.1039/b716324j

24. Negi AS, Osuji CO. New insights on fumed colloidal rheology—Shear thickening and vorticity-aligned structures in flocculating dispersions. *Rheol Acta* (2009) 48(8):871–81. doi:10.1007/s00397-008-0341-9

25. Grenard V, Taberlet N, Manneville S. Shear-induced structuration of confined carbon black gels: Steady-state features of vorticity-aligned flocs. *Soft Matter* (2011) 7(8):3920–8. doi:10.1039/c0sm01515f

26. Shakeel A, MacIver MR, van Kan PJM, Kirichek A, Chassagne C. A rheological and microstructural study of two-step yielding in mud samples from a port area. *Colloids Surf A: Physicochemical Eng Aspects* (2021) 624:126827. doi:10.1016/j.colsurfa.2021.126827

27. Varga Z, Grenard V, Pecorario S, Taberlet N, Dolique V, Manneville S, et al. Hydrodynamics control shear-induced pattern formation in attractive suspensions. *Proc Natl Acad Sci U S A* (2019) 116:12193–8. doi:10.1073/pnas.1901370116

28. Das M, Chambon L, Varga Z, Vamvakaki M, Swan JW, Petekidis G. Shear driven vorticity aligned flocs in a suspension of attractive rigid rods. *Soft Matter* (2021) 17(5):1232–45. doi:10.1039/d0sm01576h

29. Huang J, Xu J, Sheng Y, Zhu Y, Jiang W, Xu D, et al. Fabrication of polymer film with extraordinary conductive anisotropy by forming parallel conductive vorticity-aligned stripes and its formation mechanism. *Macromol Mater Eng* (2016) 301(6):743–9. doi:10.1002/mame.201600026

30. Mao C, Huang J, Zhu Y, Jiang W, Tang Q, Ma X. Tailored parallel graphene stripes in plastic film with conductive anisotropy by shear-induced self-assembly. *J Phys Chem Lett* (2013) 4(1):43–7. doi:10.1021/jz301811b

31. Romeo G, Fernandez-Nieves A, Wyss HM, Acierno D, Weitz DA. Temperature-controlled transitions between glass, liquid, and gel states in dense p-NIPA suspensions. *Adv Mater* (2010) 22(31):3441–5. doi:10.1002/adma.200904189

32. Yunker PJ, Chen K, Gratale MD, Lohr MA, Still T, Yodh AG. Physics in ordered and disordered colloidal matter composed of poly(N -isopropylacrylamide) microgel particles. *Rep Prog Phys* (2014) 77(5):056601. doi:10.1088/0034-4885/77/5/056601

33. Minami S, Watanabe T, Suzuki D, Urayama K. Rheological properties of suspensions of thermo-responsive poly(N -isopropylacrylamide) microgels undergoing volume phase transition. *Polym J* (2016) 48(11):1079–86. doi:10.1038/pj.2016.79

34. Appel J, Fölker B, Sprakel J. Mechanics at the glass-to-gel transition of thermoresponsive microgel suspensions. *Soft Matter* (2016) 12(9):2515–22. doi:10.1039/c5sm02940f

35. Karg M, Pich A, Hellweg T, Hoare T, Lyon LA, Crassous JJ, et al. Nanogels and microgels: From model colloids to applications, recent developments, and future trends. *Langmuir* (2019) 35(19):6231–55. doi:10.1021/acs.langmuir.8b04304

36. Chaudhary G, Ghosh A, Kang JG, Braun PV, Ewoldt RH, Schweizer KS. Linear and nonlinear viscoelasticity of concentrated thermoresponsive microgel suspensions. *J Colloid Interf Sci* (2021) 601:886–98. doi:10.1016/j.jcis.2021.05.111

37. Ramakrishnan S, Chen Y-L, Schweizer KS, Zukoski CF. Elasticity and clustering in concentrated depletion gels. *Phys Rev E* (2004) 70(4):040401. doi:10.1103/physreve.70.040401

38. Laurati M, Petekidis G, Koumakis N, Cardinaux F, Schofield AB, Brader JM, et al. Structure, dynamics, and rheology of colloid-polymer mixtures: From liquids to gels. *J Chem Phys* (2009) 130(13):134907. doi:10.1063/1.3103889

39. Zaccone A, Wu H, Del Gado E. Elasticity of arrested short-ranged attractive colloids: Homogeneous and heterogeneous glasses. *Phys Rev Lett* (2009) 103(20): 208301. doi:10.1103/physrevlett.103.208301

40. Whitaker KA, Varga Z, Hsiao LC, Solomon MJ, Swan JW, Furst EM. Colloidal gel elasticity arises from the packing of locally glassy clusters. *Nat Commun* (2019) 10(1):2237. doi:10.1038/s41467-019-10039-w

41. Dang S, Brady J, Rel R, Surineni S, O'Shaughnessy C, McGorty R. Core–shell droplets and microcapsules formed through liquid–liquid phase separation of a colloid–polymer mixture. *Soft Matter* (2021) 17:8300–7. doi:10.1039/d1sm01091c

42. Wang J, McGorty R. Measuring capillary wave dynamics using differential dynamic microscopy. *Soft Matter* (2019) 15(37):7412–9. doi:10.1039/c9sm01508f

43. Still T, Chen K, Alsayed AM, Aptowicz KB, Yodh AG. Synthesis of micrometer-size poly(N-isopropylacrylamide) microgel particles with

homogeneous crosslinker density and diameter control. *J Colloid Interf Sci* (2013) 405:96–102. doi:10.1016/j.jcis.2013.05.042

44. Borrega R, Cloitre M, Betremieux I, Ernst B, Leibler L. Concentration dependence of the low-shear viscosity of polyelectrolyte micro-networks: From hard spheres to soft microgels. *Europhys Lett* (1999) 47(6):729–35. doi:10.1209/epl/i1999-00451-1

45. Jamie EAG, Davies GJ, Howe MD, Dullens RPA, Aarts DGAL. Thermal capillary waves in colloid–polymer mixtures in water. *J Phys : Condens Matter* (2008) 20(49):494231. doi:10.1088/0953-8984/20/49/494231

46. Edelstein AD, Tsuchida MA, Amodaj N, Pinkard H, Vale RD, Stuurman N. Advanced methods of microscope control using μManager software. *J Biol Methods* (2014) 1(2):10. doi:10.14440/jbm.2014.36

47. Fussell SL, Royall CP, van Duijneveldt JS. *Controlling phase separation in microgel-polymeric micelle mixtures using variable quench rates* (2021). arXiv: 210404022 [cond-mat].

48. Taylor GI. The viscosity of a fluid containing small drops of another fluid. *Proc R Soc Lond Ser A, Containing Pap a Math Phys Character* (1932) 138(834):41–8.

49. Taylor GI. the formation of emulsions in definable fields of flow. *Proc R Soc Lond A: Math Phys Eng Sci* (1934) 146(858):501–23.

50. Pathak JA, Migler KB. Droplet–String deformation and stability during microconfined shear flow. *Langmuir* (2003) 19(21):8667–74. doi:10.1021/la0346907

51. Derks D, Aarts DGAL, Bonn D, Imhof A. Phase separating colloid polymer mixtures in shear flow. *J Phys : Condens Matter* (2008) 20(40):404208. doi:10.1088/0953-8984/20/40/404208

52. Solomon MJ, Spicer PT. Microstructural regimes of colloidal rod suspensions, gels, and glasses. *Soft Matter* (2010) 6(7):1391–400. doi:10.1039/b918281k

53. Soto-Bustamante F, Valadez-Pérez NE, Liu Y, Castañeda-Priego R, Laurati M. Clusters in colloidal dispersions with a short-range depletion attraction: Thermodynamic identification and morphology. *J Colloid Interf Sci* (2022) 618: 442–50. doi:10.1016/j.jcis.2022.03.061

54. Divoux T, Grenard V, Manneville S. Rheological hysteresis in soft glassy materials. *Phys Rev Lett* (2013) 110(1):018304. doi:10.1103/physrevlett.110.018304

55. Jamali S, Armstrong RC, McKinley GH. Multiscale nature of thixotropy and rheological hysteresis in attractive colloidal suspensions under shear. *Phys Rev Lett* (2019) 123(24):248003. doi:10.1103/physrevlett.123.248003

56. Geri M, Venkatesan R, Sambath K, McKinley GH. Thermokinematic memory and the thixotropic elasto-viscoplasticity of waxy crude oils. *J Rheology* (2017) 61(3): 427–54. doi:10.1122/1.4978259

57. Smith KM, Hsiao LC. Migration and morphology of colloidal gel clusters in cylindrical channel flow. *Langmuir* (2021) 37(34):10308–18. doi:10.1021/acs.langmuir.1c01287

58. Cardenas-Vasquez ED, Smith KM, Doolan TJ, Hsiao LC. Shear-induced microstructural variations in nanoemulsion-laden organohydrogel fibers. *ACS Appl Polym Mater* (2020) 2(2):594–603. doi:10.1021/acsapm.9b00979

59. Hsiao LC, Doyle PS. Celebrating Soft Matter's 10th Anniversary: Sequential phase transitions in thermoresponsive nanoemulsions. *Soft Matter* (2015) 11(43):8426–31. doi:10.1039/c5sm01581b

frontiers | Frontiers in Physics

TYPE Original Research
PUBLISHED 10 October 2022
DOI 10.3389/fphy.2022.1013805

OPEN ACCESS

EDITED BY
Linda S. Hirst,
University of California, Merced,
United States

REVIEWED BY
Jose Manuel Ruiz Franco,
Wageningen University and Research,
Netherlands
Davide Orsi,
University of Parma, Italy
Rae M. Robertson-Anderson,
University of San Diego, United States

*CORRESPONDENCE
Fabio Giavazzi,
fabio.giavazzi@unimi.it
Roberto Cerbino,
roberto.cerbino@univie.ac.at

†These authors have contributed equally to this work

‡PRESENT ADDRESS
Stefano Villa,
Max Planck Institute for Dynamics and Self-Organization, Göttingen, Germany;
Paolo Edera, ESPCI, Paris, France

SPECIALTY SECTION
This article was submitted to Soft Matter Physics,
a section of the journal
Frontiers in Physics

RECEIVED 07 August 2022
ACCEPTED 31 August 2022
PUBLISHED 10 October 2022

CITATION
Villa S, Edera P, Brizioli M, Trappe V, Giavazzi F and Cerbino R (2022), Quantitative rheo-microscopy of soft matter.
Front. Phys. 10:1013805.
doi: 10.3389/fphy.2022.1013805

Quantitative rheo-microscopy of soft matter

Stefano Villa[1†‡], Paolo Edera[1†‡], Matteo Brizioli[1], Veronique Trappe[2], Fabio Giavazzi[1*] and Roberto Cerbino[3*]

[1]Department of Medical Biotechnology and Translational Medicine, University of Milan, Milan, Italy, [2]Department of Physics, University of Fribourg, Fribourg, Switzerland, [3]Faculty of Physics, University of Vienna, Boltzmanngasse, Vienna, Austria

Direct observation of the microscopic material structure and dynamics during rheological shear tests is the goal of rheo-microscopy experiments. Microscopically, they shed light on the many mechanisms and processes that determine the mechanical properties at the macroscopic scale. Moreover, they permit for the determination of the actual deformation field, which is particularly relevant to assess shear banding or wall slip. While microscopic observation of the sample during mechanical probing is achieved by a variety of custom and commercial instruments, the possibility of performing quantitative rheology is not commonly available. Here, we describe a flexible rheo-microscopy setup that is built around a parallel-sliding-plate, stress-controlled shear cell, optimized to be mounted horizontally on a commercial microscope. Mechanically, soft materials with moduli ranging from few tens of Pa up to tens of kPa can be subjected to a variety of waveforms, ranging from standard step stress and oscillatory stress to more peculiar signals, such as triangular waves or any other signal of interest. Optically, the shear cell is designed to be compatible with different imaging methods (*e.g.* bright field or confocal microscopy). Most of the components of the shear cell are commercially available, and those that are not can be reproduced by a standard machine shop, easing the implementation of the rheo-microscopy setup in interested laboratories.

KEYWORDS

differential dynamic microscopy, rheology, microscopy, yield stress fluids, soft materials

1 Introduction

Although somehow pleonastic to point out, one of the main characteristics of soft matter is precisely its softness. Every time we open the refrigerator and sink a teaspoon into yogurt, when we spread chocolate cream on a slice of bread, or when we squeeze out the tube an appropriate amount of toothpaste on the toothbrush we realize that all these materials are profoundly different from a classic liquid (*e.g.*, water or apple juice) or solid (*e.g.*, ceramic or metal). Moreover, many soft materials are also *yield stress materials*, effectively behaving as solids for small perturbations yet flowing like liquids in the presence of sufficiently large applied forces.

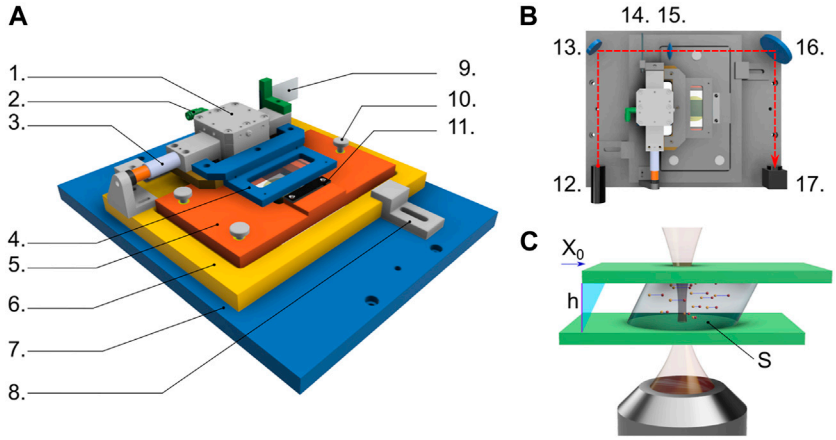

FIGURE 1
(A) Sketch of the key components of the shear cell: air bearing (1), inlet for compressed air (2), voice coil (3), holder for the upper glass slide (4), support of the lower glass slide (5), mounting base of the shear cell (6), microscope stage (7), clamping system fixing the cell mounting base to the microscope stage (8), ground glass (9), micrometric screws for controlling the gap distance *h* and the parallelism of the glass slides (10), pass-through hole enabling imaging with the underlying objective (11). The moving part of the shear cell, driven by the voice coil actuator, is composed by the moving parts of (1,3) plus parts (4,9). The entire block (5) lays on part (6) and its orientation can be finely tuned using the micrometric screws (10). **(B)** Top view of the shear cell also including the optical pathway and components used for the strain measurement via speckle field formation and detection: laser light source (12), mirror (13), ground glass solidly moving with the upper part of the shear cell (14), lens (15), mirror (16), and camera (17). **(C)** Sketch of the imaging geometry of the shear cell: the sample of cross-sectional area *S* is enclosed between the two glass slides placed at gap distance *h*; as the upper glass is moved by X_0 driven by the voice coil, the sample is sheared; the subsequent sample motion is monitored in time by imaging tracer particles with a long working distance objective, which can be positioned at different distance from the lower glass slide allowing to follow the sample dynamics at any selected plane *z* within the gap.

Such a rich rheological behavior arises from the underlying structural and dynamical complexity of the material constituents at one or more levels of organization. However, simultaneously characterizing the sample rheology, structure, and dynamics is not easily achieved experimentally. On one side, we have commercial rheometers, powerful and accurate instruments that grant access to the viscoelastic response of a material to a given strain/stress history in well-characterized geometries and in different shearing conditions; on the other side, we have commercial microscopes and scattering instruments that provide an accurate spatiotemporal map of the sample but are not conceived to be operated while the sample is mechanically perturbed.

This necessary trade-off has prompted several research groups to find a solution to combine the advantages of these approaches, ideally while maintaining a low level of instrumental complexity and a wide measurement range for rheological, structural, and dynamic parameters. Such combination has been implemented by relying on commercial rheometers [1–5], as well as on custom shear cells designed to work as rheometers [6–9][1]. The so-extracted information can be used for many purposes, such as correlating local material properties with the rheological response [14] or predicting materials failure from the analysis of failure precursors [15, 16].

In this work, building on seminal work by Aime et al. [8], we design, implement, and test a rheo-microscopy setup that is capable of performing a variety of rheological measurements while performing optical imaging of the sample via a commercial microscope. The core of the setup is a stress-controlled shear cell specifically designed for being used with different imaging configurations (*e.g.* bright field, confocal, ...) and for maximizing the optical access of microscope objectives in the close vicinity of the sample. To make our setup as reproducible as possible, most of the optical, electronic, and mechanical cell components are commercially available, and the entire setup is controlled with National Instruments Labview. In particular, we opted for a commercial electronic signal generator to produce a variety of arbitrary stress patterns, which beyond the most standard oscillatory and step-like profiles also allow for more complex inputs, such as for instance triangular profiles. Our setup also allows triggering the optical detection with the mechanical input, thereby enabling us to perform for instance echo-imaging during oscillatory tests. While the tests presented here are meant to highlight the capabilities of our setup and give an idea of how it could be used, the setup could be pushed further. For instance, remaining in the framework of simple shear oscillation experiments, one could go beyond echo-imaging

1 Commercial solutions such as the RheOptiCAD described in Ref. [10] can be used to investigate the microscopic dynamics under controlled shear strain conditions, as done for instance in Ref. [11]. However, the main limitation is that they do not provide a quantification of the stress, which makes them a "deformation tool" [10, 12, 13] rather than a rheometer. In addition, with this kind of cell one can usually apply only continuous shear or oscillatory shear deformations.

and study the intra-cycle dynamics to obtain information also on non-affine particle displacements; more complex shear profiles could also be used, such as chirped stress profiles or superpositions of simple signals.

Our rheo-microscopy setup is relatively simple to implement and quite robust to use for the multi-scale characterization of the link between the rearrangements occurring in soft materials under controlled stress and the evolution of their rheological properties.

2 Materials and methods

In a nutshell, the shear cell (Figure 1A) consists of a temporally controlled electrical current that feeds a magnetic actuator; the magnetic actuator exerts thus a controlled force on the upper part of the shear cell, which results in a rigid horizontal translation of the upper glass slide with respect to the lower one, which remains fixed. Similar to [8], the motion of the upper glass slide is accurately measured by optical cross-correlation of a speckle pattern that translates solidly with the upper glass slide (Figure 1B), so that one can impose a controlled stress profile and measure with nanometer precision the instantaneous strain. The optomechanical design is such that, when the cell is mounted on a commercial inverted microscope, all the sample planes comprised between the two glass slides can be visualized by proper positioning of the microscope objective (Figure 1C). In the following subsections, we describe in detail the different components and the typical data analysis procedures.

2.1 Shear cell description

The cell is built on the design described in Ref. [8]. It allows imposing a controlled stress, by means of a voice coil actuator, and accurately measuring the shear strain, by using optical speckle correlation analysis. While we keep these key elements unchanged, our implementation focuses on optimizing some aspects of the original design for use with a commercial inverted optical microscope, in our case the *Nikon Eclipse Ti*.

Beyond the obvious requirement of physically coupling the cell to the microscope while mounting it horizontally, which is fulfilled via a suitably designed microscope stage (7 in Figure 1A), another key requirement is maximizing the clear aperture on the bottom side to ensure the possibility of forming images within the samples at an arbitrary position within the entire sample thickness h. The mounting base (6 in Figure 1A) and the support of the bottom glass slide (5 in Figure 1A) are thus designed so to grant access to the tip of both long and short working distance microscope objectives, whose vertical position remains limited only by the presence of the bottom glass slide confining the sample. Another important design criterion concerns the shape of the glass slides confining the sample: on one side, one would want to use a large area of contact with the sample, which increases the effect of the applied force in the case of soft materials with small elastic modulus; on the other side, a large glass slide limits the free path of the moving stage, which in turn limits the maximum achievable strain. Our design, still making use of standard microscope slides for both the top and the bottom plates, allows us to flexibly change the shape of the bottom glass slide by suitable cutting. Here we use two options: a 60 mm × 24 mm slide mounted with the longer side orthogonal to the shear direction, which results in a maximum sample area of 4.5 cm^2 and a maximum moving stage free path of 25 mm; a second geometry, conceived to maximize the sample area in order to access to lower stresses, is obtained with the bottom slide measuring 65 mm × 26 mm, and mounted parallel to the top one (maximum sample area 12 cm^2, moving stage free path 1 mm). More information is provided in the Supplementary Information.

The top glass slide is mounted on a rigid frame (4 in Figure 1A), which translates rigidly and solidly with the body of the voice coil actuator (3 in Figure 1A). The rigid frame (4) has no other degrees of freedom and its distance from support (5) is varied by turning three micrometric screws that move the support (5); the three screws thus control the gap distance h and the parallelism between the two glass slides. The value of h is easily measured with the graduated vertical translator of the microscope, quantifying the distance between the two planes at which the upper side of the bottom glass and the lower face of the top glass can be sharply imaged. The parallelism between the two plates is checked by inspection of the fringe pattern arising when a red laser (638 nm diode laser, *0638L-13A, Integrated Optics*) impinges on the empty cell. The doubly reflected light from the two glass slides generates an interference pattern whose fringes spacing is maximized when the two slides are parallel. In order to maximize the number of visible fringes, we use for the alignment a low magnification objective (*Nikon Plan UW 2x/0.06*, working distance 7.5 mm). With this procedure, the parallelism is granted with an accuracy of about $3 \cdot 10^{-4}$ rad (see Supplementary Information).

2.2 Stress application

Following [8], we feed an arbitrary current to a magnetic actuator (*Moticont* linear voice coil motor *lvcm-013-032-02*), which transforms the input current into a force by making use of a copper coil. This force is eventually exerted on the sample through the upper glass surface that is mounted on a stage sliding with reduced friction on an horizontal compressed-air rail (*PI* glide RB Linear Air Bearing Module *A-101.050*). As a distinctive element of our implementation, we use a commercially available source measure unit (SMU, *NI PXIe-4138*), mounted together with a *NI PXIe-8840* controller in a *NI PXIe-1071* chassis. The controller can operate under both *MS*

Windows or proprietary *National Instruments* real time operating system. Real time operation is preferable to improve execution performances at high frequency; however, in this work we have been operating the device under *MS Windows 10*, due to the lack of support of our USB3 camera in the real time operating system. On the other hand, the adoption of a popular operating system like *MS Windows 10* makes our setup easy to replicate, and very versatile.

We used *NI Labview* to program the SMU to supply currents up to 1 A with a noise-limited resolution of 1 μA, and with a microsecond time precision. Beyond standard continue (Section 4.4) and oscillatory (Sections 4.1 and 4.2) current (stress) profiles, a multitude of differently-shaped temporal stress profiles can be obtained, including triangular (Section 4.3) profiles, and modulated or chirped signals; the possibility to set more complex stress profiles could be also used for superposition rheology experiments [17]. Of note, we also found it useful to have the possibility to add an offset current to finely balance possible residual gravity effects due to the non-perfect leveling of the microscopy stage. Finally, since an SMU combines features of a power supply and digital multimeter device, we can impose a current profile $I(t)$ and simultaneously read the voltage $V(t)$ across the voice coil, which provides an estimate of the electric impedance of the magnet that we can use to monitor the magnet behavior checking for instance whether we approach its tolerance limit.

Calibration of the voice coil force-intensity ratio f_c was performed by using a precision balance measuring the force exerted by the coil for a fixed value of current in the range $10^{-4} \leq I \leq 1$ A (currents larger than 1 A were not used to avoid coil damage). In agreement with the results in Ref. [8] we found that f_c is essentially independent on the current intensity, but depends on the relative position d between the magnet and the coil. In our experiments, we choose to work around $d = 12$ mm ($d = 0$ mm corresponds to the magnet completely inside the coil), where for excursions up to 5 mm, we obtained $f_c = (0.909 \pm 0.002)$ NA^{-1} (see Supplementary Information). In these conditions, for a typical gap of 300 µm, we obtain strains exceeding 800%. Also, considering typical sample areas of the order of $0.1 - 10$ cm^2, the explored current range corresponds to an applied stress range of $0.1—10^5$ Pa, even though below 1 Pa (*i.e.* for currents smaller than 1 mA), we systematically observe a slight asymmetry between the amplitude of the stress obtained for negative and positive values of currents with the same amplitude (see Supplementary Information).

After calibration, the shear cell can impose controlled stress profiles to perform rheological tests (see Section 2.3 for the needed measurement of the strain) and for pre-conditioning of the sample before the tests. In the code we developed for the shear cell control and data acquisition, we implemented two rejuvenation pre-conditioning stress profiles: an oscillatory profile with constant frequency, and with large and constant stress maintained for an arbitrary time duration; and an oscillatory profile at constant frequency with stress decreasing from a large value to the value that the operator wants to use for the subsequent measurement. All the data in this work were obtained by using the high-stress oscillation rejuvenation protocol, imposing a rejuvenating strain of about 200%.

2.3 Speckle correlation based strain measurement

We implement a simple and compact optical correlation strain sensor (see Figure 1B) [8] to quantify the sample shear strain: a collimated laser beam (658 nm diode laser, *DH658-60-3, Picotronic*) impinges perpendicularly onto a ground glass (100 mm × 100 mm Square N-BK7 Ground Glass Diffusers, *Thorlabs*, homemade custom cut) that is rigidly mounted on the moving stage; a plano-convex lens with focal length 29.9 mm is positioned 33 mm after the ground glass and 330 mm before the speckle acquisition camera (*Ximea MQ042MG-CM* USB3.0 camera, sensor pixel size 5.5 µm, sensor size 2048 × 2048) in order to form a 10x magnified image of the ground glass, resulting in an effective pixel size of about half a micrometer. The image of the laser-illuminated ground glass appears covered in speckles whose size on the detector is ≈ 9 µm (roughly corresponding to 2 pixels).

With this configuration, we acquire a sequence of images of a region of interest (ROI) of 2048 × 16 pixels, with the long side oriented along the direction of motion of the moving stage. From the spatial cross-correlation between consecutive frames the displacement of the speckle pattern, and thus of the moving stage, between the frames is recovered as the correlation peak position with a subpixel resolution of 0.02 pixels. With reference to the specific *NI Labview* implementation, a producer loop records the images and stores them in a buffer, and a consumer loop analyzes the correlations and determines the instantaneous velocity. For the aforementioned ROI, the consumer loop speed is the same as the producer one for acquisition frequencies up to 90 Hz. For larger acquisition frequencies, images accumulate in the buffer, and the speckle analysis must be performed offline. The dimension of the buffer allows us to easily keep a 1 KHz speckle pattern acquisition for a duration of some seconds and ensures that we can perform tests at tens of Hertz for hundreds of shear cycles. If needed, the limit for real-time analysis could be pushed at higher frequencies by using a camera supported by the real-time operating system described in Section 2.2.

2.4 Microscopy acquisition

All the experiments described in this manuscript are performed on fairly transparent samples. In this case tracer

particles need to be added to monitor the local displacement field and to outline the occurrence of plastic rearrangements.

Imaging of the tracers is performed with a commercial optical microscope (*Nikon Eclipse Ti*), set for Koehler illumination. To minimize the contribution of particles that are not in the microscope object plane, the depth-of-focus is made as small as $L_f \simeq 20\,\mu$m by keeping the condenser (NA = 0.52) diaphragm completely open. Images are acquired by a second *Ximea MQ042MG-CM* USB3.0 camera at the imposed acquisition frequency and stored in a circular buffer: while simultaneously performing rheology experiments, full frame (2048 × 2048 pixels) image acquisition at 10 Hz (25 Hz with 2 × 2 binning) can be performed without filling the RAM for at least 1 hour; full frame acquisitions at larger frequencies are possible but only for a few seconds. Imaging data presented in the present paper are acquired with a 20×, 0.45 NA long-working-distance objective, resulting in a field-of-view size of 563 × 563 μm^2.

2.5 Triggered image acquisitions

For rheology experiments with a periodic stress profile (*e.g.* for stress oscillation experiments), we implemented the possibility of microscopy images acquisitions in echo mode [11]: we acquire for each period a fixed integer number n of images and repeat a similar acquisition over a very large number of periods (typically 100 – 1000); the resulting video is then divided into its n stroboscopic components, each of them capturing the sample temporal evolution for ideally the same applied stress after exactly one period and multiples of it (echoes). As already pointed out in Ref. [11], the presence of tiny (less than 1 ms) mismatches between the stress and the sampling frequency may be negligible at the single period time scale but becomes important if the delay accumulates over a long measurement (order of 300 iterations), as it implies apparent drifts in the echo analysis.

To minimize such temporal mismatches, we use hardware triggering of the voice coil, the speckle camera, and the sample imaging camera. To this aim, we use the National Instrument SMU to send an output trigger at the end of every current signal period iteration. An operational amplifier in a non-inverting configuration increases the amplitude and duration (with a low-pass filter) of the trigger signal in order to make it detectable by the two cameras. Once the trigger signal is received, every camera acquires a fixed number of frames per period (typically 10 for the imaging camera and 50-80 for the speckle camera). The camera then awaits the following trigger signal before starting the subsequent acquisition sequence. In this way, any mismatch between the imposed and the effective acquisition frequencies does not accumulate a time delay between applied stress and acquired images, thus avoiding apparent drift in image acquisition. Moreover, the synchronization of the applied stress with the image acquisition reduces the uncertainty of the phase delay between the applied stress and the consequent measured strain. Without synchronization, the strain detection begins with the first acquired frame after the application of the stress, which would not give control of the starting phase. With triggering, the delay is given by the trigger precision $\delta_t \simeq 1$ μs, which corresponds to an error on the phase delay that is bounded from above by $\delta_\phi = 2\pi f_\sigma \delta_t$, where f_σ is the imposed stress frequency. In typical experiments with $f_\sigma < 100$ Hz, one has $\delta_\phi < 10^{-3}$ rad (to be compared with $\delta_\phi \simeq 10^{-1}$ rad without trigger), an error that can be safely neglected, being smaller than the precision limit imposed by the finite number of acquired points per period.

2.6 Preparation and loading of the samples

To fill the shear cell with the sample, the upper glass slide support is easily unmounted, and both glass slides are carefully cleaned before sample loading. With the exception of the Sylgard sample (see below), all samples are prepared *ex situ* and subsequently placed in the shear cell by using a spatula or a pipette. The upper slide support is then put back in its place by carefully checking that the sample drop remains within the perimeter of the upper and lower glass. To assess the imposed stress $\sigma = F/S$ from the applied force F, we measure the sample cross-sectional area S by imaging the sample once loaded using a smartphone. For this purpose, we position the smartphone on a holder placed at a distance that minimizes field distortions and parallax errors. Spatial calibration of the effective image pixel size is obtained by using as a reference length the known distance between the cell edges while the contour of the drop is obtained trough a manual polygonal segmentation using the Matlab *drawnpolygon* function. For samples subjected to evaporation, such as Carbopol, several pictures of the sample area are taken during the measurement in order to retrieve the area as a function of time. Tests with Carbopol samples over four consecutive hours revealed that tracking the temporal changes of S is of fundamental importance to obtain a correct rheological characterization of the sample, as changes in S dominate over the moduli changes due to the water evaporation-induced concentration change of the sample, which turned out to be negligible. Contact angles different from $\pi/2$ between the sample and the glass slides can introduce errors in the evaluation of the effective area S due to the presence of a meniscus (especially for liquid samples like glycerol and silicon oil). A more precise evaluation of the area can be in principle obtained for non-evaporating samples by adding an accurately known volume of sample in the shear cell, but sample viscosity makes this operation practically quite difficult in most cases. Another possibility, beyond the aim of the present paper, is an in-depth study on possible treatments of the glass slides to reach for a given sample a contact angle of $\pi/2$ in order to reduce the meniscus and thus the error in the evaluation of S. Tracers have been dispersed only in the Carbopol

samples since Sylgard and the purely viscous liquids have been only used to verify the capability of the shear cell in properly measuring the macroscopic rheology of well-characterized samples.

2.6.1 Viscous liquids

In order to test the behaviour of the cell with simple viscous fluids, we used glycerol (*Sigma Glycerol* for molecular biology, ≥99.0%) and silicon oil (*BlueStar Silicon Bluesil 47V30000*, nominal viscosity 30 Pa·s). Frequency sweeps at $T = 23.5 \pm 0.5^{\circ}$C (the same at which the shear cell measurement reported in Section 4.1 were performed) performed with an *Anton Paar Physica MCR300* rheometer in a cone and plate geometry provided a viscosity $\eta = 29.2 \pm 0.3$ Pa·s for the silicon oil. Glycerol at 99% is expected to have a nominal viscosity of 1.19 Pa·s at room temperature (20 °C) [18]. However, the high hygroscopicity of glycerol at concentrations close to 100% causes the real viscosity of the sample during the measurement to be noticeably lower [19].

2.6.2 Sylgard

Sylgard samples are prepared by adding the curing agent (*Sylgard 184 curing agent, Dow Corning*) to the base (*Sylgard 184 Base, Dow Corning*) in the proportion 1:50. The components are mixed directly on the bottom slide of the shear cell, by keeping the drop shape as circular as possible. The upper slide is then closed and the sample is left to dry at room temperature for at least 48 h. Because of the strong adhesion of the Sylgard on glass, we used untreated microscope slides as cell glass slides.

2.6.3 Carbopol

For preparing the Carbopol samples we followed the procedure described in [11]: samples are prepared at the desired concentration by dispersing *Carbopol 971P NF* (*Lubrizol*) powder in MilliQ water while stirring for several days and controlling the pH through the addition of NaOH 10 M. After preparation, tracers (Polystyrene particles of 2 μm diameter, *Microparticles GmbH*) are dispersed at a volume fraction of 0.05%. The size of the tracers was chosen to be slightly larger than the mesh size of the sample, as discussed in Ref. [11]. Dispersion is reached by mixing with a spatula and by spinning for a few seconds on a centrifuge to get rid of gas bubbles. In order to reduce sample-glass slip, both the glass slides are frosted with sandpaper, by carefully leaving unfrosted a small circular area of diameter 5 mm to allow optical imaging.

3 Data analysis

3.1 Extracting the macroscopic rheological properties of the sample

Measuring the speckle displacement on the camera provides a measure of the displacement $X_0(t)$ of the ground glass and consequently the displacement of the upper glass slide of the cell (see Figure 1A). The speckle displacement (in pixel) between two consecutive frames is calculated with a cross-correlation analysis that gives a resolution of 0.02 pixels (see also Section 2.3). Displacements between non-consecutive images are obtained as sums of displacements between consecutive ones. The effective pixel size is measured by displacing the moving stage along its whole range while acquiring the speckle field. The corresponding displacement (in pixels) obtained from the speckle correlation analysis is then compared with the effective distance travelled by the moving stage measured with a caliper. From this procedure, we obtain an effective pixel size $d_{pixel} = 0.49 \pm 0.01$ μm. Considering the aforementioned subpixel resolution and speckle ROI dimensions (Section 2.3), our device is therefore able to detect displacements ranging from 10 nm to 500 μm. For a typical gap of 300 μm and a typical speckle image acquisition frequency of 80 Hz, one has a minimum measurable strain of $3 \cdot 10^{-5}$ and a maximum measurable strain rate of 133 s^{-1}. In practice, the minimum detectable strain is larger due to mechanical noise sources, such as vibrations and air flows in the vicinity of the cell.

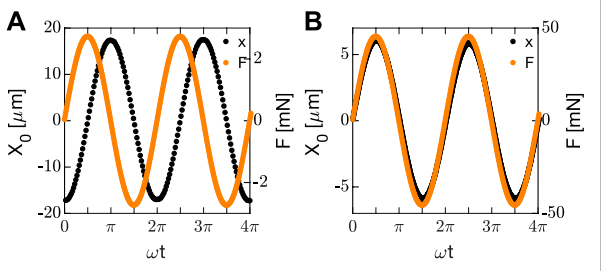

FIGURE 2
Applied force (orange) and resulting displacement (black) obtained measuring silicon oil at $\omega = 2.46$ rad/s **(A)** and Sylgard at $\omega = 0.1$ rad/s **(B)**.

From $F(t)$ and $X_0(t)$, the stress and strain time evolution are directly accessible as $\gamma(t) = X_0(t)/h$ and $\sigma(t) = F(t)/S$, respectively. In the linear range, we expect that the response to an applied oscillatory stress $\sigma(t) = F(t)/S = \sigma_0 \sin \omega t$ with frequency ω and amplitude $\sigma_0 = F_0/S$ is an oscillatory strain $\gamma(t) = X_0(t)/h = A_0 \sin(\omega t - \phi)$ with the same frequency and a phase delay ϕ. In this case, the sample complex modulus G^* is obtained as the ratio between stress and strain

$$G^* = \frac{\sigma}{\gamma} = \frac{\sigma_0}{\gamma_0} e^{i\phi}. \tag{1}$$

Elastic and loss moduli can be recovered as the real and imaginary part of G^* respectively

$$\begin{cases} G' = \dfrac{\sigma_0}{\gamma_0} \cos\phi \\ G'' = \dfrac{\sigma_0}{\gamma_0} \sin\phi \end{cases} \tag{2}$$

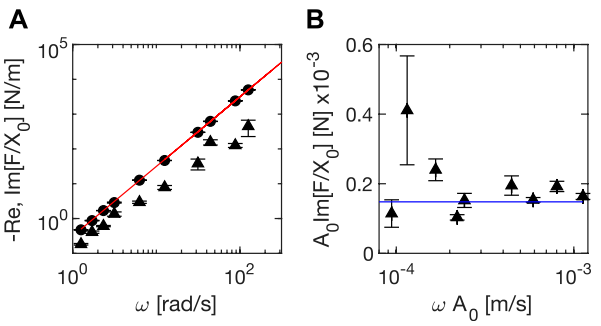

FIGURE 3
(A) – Re $[F/X_0]$ (circles) and Im $[F/X_0]$ (triangles) as a function of ω from a frequency sweep experiment performed with the empty cell. Continuous red line is a quadratic fit of – Re $[F/X_0]$, which provides the estimate $m = 0.314 \pm 0.006$ Kg for the mass of the moving stage. **(B)** A_0Im $[F/X_0]$, recovered from the same data of **(A)**, as a function of the maximum velocity ωA_0.

In principle, once ϕ, $\gamma_0 = A_0/h$ and σ_0 are known, the elastic and loss moduli can be directly recovered. In practice, we find that air movements around the sliding stage can introduce random drifts, whose effects are negligible for stiff samples but can become important when $G = |G^*| \leq 100$ Pa. Such drifts can be corrected for through a suitable fit with the expression

$$X_0(t) = A\sin(\omega t - \varphi) + f_{pol}(t) \tag{3}$$

where $f_{pol}(t)$ is a polynomial function accounting for the drift contribution (see Supplementary Information). By fitting the function in Eq. 3 to the measured displacement $X_0(t)$, we obtain an estimate of the drift term $f_{pol}(t)$. A simple sinusoidal function $A_0\sin(\omega_0 t - \phi)$ is then fitted to the corrected data $X_0'(t) = X_0(t) - f_{pol}(t)$. The best fitting parameters A_0, ω_0, and ϕ, correspond to the displacement amplitude, the oscillation frequency, and the relative phase between the oscillatory forcing signal and the response displacement, respectively. For ease of notation, we will indicate in the following the upper glass displacement corrected by drift with X_0.

Typical results of the applied force $F(\omega t)$ and the resulting displacement obtained for our perfectly viscous and elastic reference systems, silicon oil and Sylgard, are shown in Figure 2. As expected, the viscous sample displays a phase shift of $\pi/2$ while the elastic one is in phase with the forcing signal.

3.1.1 Inertia and friction

In a stress-controlled rheology experiment, a prescribed temporal profile of shear stress values is applied to the sample and the resulting deformation is measured as a relative strain. The motion of the moving stage of our shear cell is, however, not only determined by the applied stress and the material mechanical properties, but also by inertial and dissipative contributions of the shear cell components. These contributions are particularly relevant in oscillatory measurements and can be quantified with calibration measurements performed with the empty cell. For these, we can write

$$m\ddot{X}_0 = F - \xi\dot{X}_0 + F_{fr} \tag{4}$$

where m is the mass of the moving stage, responsible for the inertial contribution to the dynamics, ξ is the viscous drag inherent to the shear cell, and F_{fr} is a sliding friction contribution. The latter is ideally equal to zero in a perfect frictionless device. In real devices, however, it is a constant force always opposing the direction of motion, which needs to be accounted for.

Using a magnet to apply an oscillating force $F = F_0 e^{i\omega t}$ at frequency ω, we expect in first approximation a sinusoidal displacement with the same frequency, as $X_0 = A_0 e^{i(\omega t - \phi)}$. The sliding friction contribution is therefore expected to be a square wave $F_{fr} = -F_{fr,0}\text{sign}(\dot{X}_0)$, where $F_{fr,0}$ is the modulus of the sliding friction. For the sake of analytical simplicity, we expand F_{fr} in Fourier series arresting to the first order, thus approximating the sliding friction contribution to a sinusoidal oscillation $F_{fr} = -iF_{fr,0}e^{i(\omega t - \phi)}$ in phase opposition to the velocity $\dot{X}_0 = i\omega A_0 e^{i(\omega t - \phi)}$. By making explicit the time dependencies and dividing by $e^{i(\omega t - \phi)}$, Eq. 4 becomes:

$$F_0 e^{i\phi} = -m\omega^2 A_0 + i\left(\xi\omega A_0 + F_{fr,0}\right) \tag{5}$$

that can be rewritten as:

$$\begin{cases} F_0\cos\phi = -m\omega^2 A_0 \\ F_0\sin\phi = \xi\omega A_0 + F_{fr,0} \end{cases} \tag{6}$$

We show in Figure 3A the results obtained from a frequency sweep performed with the empty cell for $\text{Re}[F/X_0] = (F_0/A_0)\cos\phi$ (circles) and $\text{Im}[F/X_0] = (F_0/A_0)\sin\phi$ (triangles). Within the investigated frequency range, the phase-shifted component $(F_0/A_0)\sin\phi$ is always smaller in absolute value than the in-phase component $(F_0/A_0)\cos\phi$; this shows that the inertial contribution always dominates over the viscous one. As expected, the in-phase response is compatible with a quadratic dependence on ω; the corresponding best-fitting curve is shown as a red continuous line. From the fit, a value of $m = 0.314 \pm 0.006$ Kg is obtained.

By contrast, the phase-shifted contribution is not increasing linearly with frequency, as one would expect for viscous friction only; this suggests that sliding friction has to be taken into account. In order to assess the relative importance of the two different dissipative contributions, we report $F_0\sin\phi$ as a function of ωA_0 in Figure 3B. Clearly, $F_0\sin\phi$ is almost frequency independent, which is expected for sliding friction contributions. Thus, viscous dissipation appears to be negligible compared to dissipation by sliding friction. We can therefore determine the value of the sliding friction contribution as $F_{fr,0} = \langle F_0\sin\phi\rangle_{\omega A_0} = 0.15 \pm 0.03$ mN.

By taking these results into account, we can rewrite Eq. 2 to include inertia and dissipation effects, which gives:

$$\begin{cases} G' = \dfrac{\sigma_0}{\gamma_0}\cos\phi + I\omega^2 \\ G'' = \dfrac{\sigma_0}{\gamma_0}\sin\phi - \dfrac{F_{fr,0}}{\gamma_0 S} \end{cases} \tag{7}$$

where $I = m\frac{h}{S}$. In this work, we use these equations to extract the viscoelastic moduli from stress oscillation experiments, which requires that inertia and sliding friction are systematically characterized with the empty cell before performing a measurement.

The procedure just described operates a correction of G'' for the sliding friction contribution, which is approximated with a sinusoidal instead of a square wave. We opted for such a simplified treatment because it enables us to operate a correction directly on the fit parameters using Eq. 7 instead of Eq. 2. An alternative route would consist in directly subtracting the square wave friction contribution from X_0 before the fit. This procedure would introduce an additional fitting step of the strain to recover ϕ and properly subtract the friction contribution, before fitting again the strain data. Our simplified correction turns out to be more effective, as it lowers by half a decade (from $5 \cdot 10^{-3}$ N to 10^{-3} N) the minimum applied force that can be considered to result in reliable measurements (see next section). We thus decided not to launch a more rigorous treatment, which would result in additional distortions of the strain profile for applied forces lower than 10^{-3} N, where static friction contributions would also be needed to be taken into account.

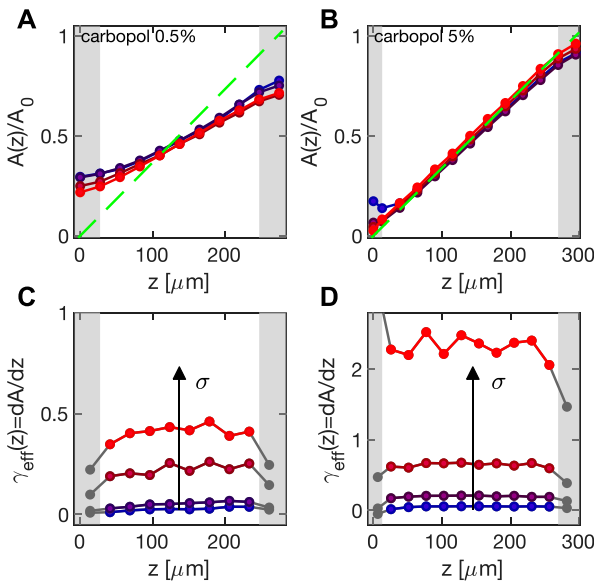

FIGURE 4
(A,B) Deformation profile $A(z)$ normalized by the macroscopic deformation amplitude A_0 as determined from the speckle correlation analysis. Data obtained for Carbopol 0.5% **(A)** and 5% **(B)** at $\omega = 2\pi$ rad/s for stress amplitudes ranging from $\sigma = 1.5$ Pa (blue) to $\sigma = 13$ Pa (red) for Carbopol 0.5%, and from $\sigma = 11$ Pa (blue) to $\sigma = 190$ Pa (red) for Carbopol 5%. Green dashed line denotes the ideal strain profile presumed in any macroscopic rheology experiment. Gray patches mark gap regions in which the amplitude estimation is biased by finite depth-of-focus. **(C,D)** Corresponding effective local strain $\gamma_{eff}(z)$, evaluated using relation 8 for Carbopol 0.5% **(C)** and 5% **(D)**. Gray marks correspond to the z for which the estimation of the local strain is not reliable.

3.2 Analysis of the microscopy images: mapping the effect of shear at the local scale

The local counterpart of the macroscopic response of the material is investigated through the analysis of the tracer dynamics imaged with the camera. By shifting the object plane we can map the microscopic dynamics across the entire gap (z-scan), and extract information about the affine and non-affine components of the particle displacement. This information can be used to obtain a characterization of the mesoscopic shear profile across the gap (*i.e.* in the gradient direction) as well as of the microscopic particle rearrangements in the shear and vorticity directions. Microscopy images can be analyzed with a variety of approaches [20], including particle tracking (PT) [21, 22], particle imaging velocimetry (PIV) [23, 24], and differential dynamic microscopy (DDM) [25, 26] methods.

3.2.1 Mapping the effective strain across the sample gap

A key feature of our rheo-microscopy approach is that we can measure the effective strain across the gap by tracking the tracers at different positions in z. This feature is particularly useful to inspect for slip and shear banding [27]. To have a certain slip of the sample at the cell boundaries is often the case, and generally leads to an overestimation of the strain measured macroscopically with both shear cells and rheometers. Similarly, the non-linear behavior of many soft materials involves shear banding, which also introduces important deviations from the ideal strain profile.

To recover the effective strain within the sample during oscillatory experiments, we first measure the apparent gap $\tilde{h}$ as the difference between the two positions along the microscope optical axis for which we obtain two sharp images of the top and bottom glass slides with the sample loaded on the cell. As the refractive index of the sample is always larger than 1, such measurement returns an apparent gap lower than the real gap h measured with the empty cell, an effect known as focal shift. Once the apparent gap is determined, we perform a z-scan with a given step length, typically of 25 μm, moving downwards from the upper glass. In a typical experiment, we impose an oscillatory stress at a given amplitude σ_0 and frequency ω on

the top plate; the stress is thereby transmitted to all planes (even in case of wall slip or shear banding). For each position $\tilde{z}_i \in [0, \tilde{h}]$ of the apparent gap we then recover the effective strain by applying the procedure introduced for a strain-controlled cell in [11]. In short, we acquire a fast time-lapse of a duration at least of three oscillation periods (see Supplementary Video SM1), and we evaluate the displacement profile $\mathbf{X}(\tilde{z}_i, t)$ by cross-correlating consecutive images of the acquired stack. By fitting $\mathbf{X}(\tilde{z}_i, t)$ to a sinusoidal function of time, we estimate the displacement amplitude $A(\tilde{z}_i)$, which we map onto the real gap by using the simple relation $z_i = \tilde{z}_i h/\tilde{h}$. We then evaluate the local effective z-dependent strain as

$$\gamma(z) = \partial A(z)/\partial z. \tag{8}$$

Representative displa-cement profiles $A(z)$ obtained in oscillation experiments ($\omega = 2\pi$ rad/s) with Carbopol 0.5% and 5% are shown in respectively Figures 4A,B, where $A(z)$ is normalized by the strain amplitude A_0 estimated from the speckle correlation analysis. Different datasets refer to different values of the applied stresses: $\sigma \in [1.5 - 17]$ Pa for the 0.5% sample, and $\sigma \in [11 - 190]$ Pa for the 5% sample. For both samples, the deformation profiles indicate the absence of shear banding even at the yielding transition, which occurs at $\sigma \sim 15$ Pa (0.5%) and $\sigma \sim 130$ Pa (5%). Compared to the data obtained for Carbopol 5%, $A(z)/A_0$ obtained for Carbopol 0.5% clearly deviates from the expected strain profile (green dashed line in Figures 4A,B), denoting a notable, weakly stress-dependent slip. Close to the cell boundaries (gray regions in Figure 4), our results are affected by the depth-of-focus L_f of the microscope (see Section 2.4), which defines the thickness of the axial region contributing to a microscope image centered around the ideal object plane. When such plane lies in the region defined by $z \in [L_f/2, h - L_f/2]$, the contributions to the amplitude displacements from the planes above and below the ideal object plane substantially average out for symmetry. However, such cancellation does not occur close to the top and bottom slides (gray regions in Figure 4), and cross-correlation analysis in the top (bottom) region leads systematically to a lower (higher) estimation of the actual amplitude. Within this frame, both the axial resolution and the size of the excluded volume can be improved using a higher numerical aperture objective, providing a smaller L_f. Even though a further way to enhance the z resolution would be to use confocal microscopy, we did not find this issue to be a limiting factor in our experiments, as we restricted our attention only to the region $z \in [L_f/2, h - L_f/2]$ (white regions in Figure 4). This approach remains compatible with our cell and can be taken in case one is interested in systems presenting heterogeneity of the deformation field on the scales of a few microns [12, 28].

3.2.2 Echo-dynamics in oscillation experiments

To study irreversible plastic rearrangements within the sample, we use the echo scheme described in Section 2.5). In this configuration, an oscillatory stress with amplitude σ_0 and frequency ω is imposed and a long image sequence of a fixed integer number n of images for each period is acquired. For each acquisition we therefore obtain n different echo sequences that correspond to different phases of the oscillatory stress. To estimate the shear-induced echo-dynamics, we consider each value of the phase separately. For each of them, we first calculate a background image $I_0(\mathbf{x})$ as the median image over the entire image sequence, which we subtract from all the images. The so-obtained sequence is then rigidly registered by using the Image-J plugin *Stack-Reg*, and choosing as a reference image the one that lies in the middle of the acquisition. At the end of the registration, we save the transformation matrix of each image in the sequence, which we subsequently use for pre-processing the images in MATLAB, where the rest of the analysis is performed by exploiting echo-particle tracking and echo-differential dynamic microscopy (Echo-DDM) as briefly presented below and described in more detail in [11].

3.2.2.1 Echo-particle tracking

The registered images are convoluted with a Wiener filter (standard deviation 2 μm) and subsequently analyzed with a particle-tracking code developed in Ref. [22] and available online[2] to obtain single particle trajectories $[x^{(i)}(t), y^{(i)}(t)]$ (typically $\sim$ 500). During shearing, we find that the displacement is not always perfectly uniform within the field-of-view: on top of a constant average translation a more complex displacement field is also observed. These non-rigid contributions result from local meso- and macroscopic rearrangements probably due to local differences in the adhesion of the sample on the glass slides and effects of finite size and inhomogeneities of the sample. These non-rigid contributions, (which would be undetectable in a standard rheological measurements) although much smaller than the rigid translation due to shearing, become relevant in echo mode, as they lead to a ballistic-like contribution to the particle dynamics. In order to reduce their effect, we adopted a mutual-particle tracking approach [29].

Considering two particles $i = 1, 2$ subjected to local drifts $\mathbf{u}$ (1) and $\mathbf{u}$ (2), respectively, we can write the particle positions at time t along the vorticity (x) and shear (y) direction as:

$$x^{(i)}(t) = x_0^{(i)}(t) + u_x^{(i)}(t),$$
$$y^{(i)}(t) = y_0^{(i)}(t) + u_y^{(i)}(t),$$

where $(x_0^{(i)}, y_0^{(i)})$ is the true particle dynamics. If the particles are close enough so that are subjected to the same velocity field $\mathbf{u}^{(i)}$

2 https://github.com/dsseara/microrheology.

and hydrodynamic correlations are negligible, the mean square displacement (MSD) evaluated over the relative position of the particles $[\Delta x^{(i,j)}, \Delta y^{(i,j)}] = [x^{(i)}(t) - x^{(j)}(t), y^{(i)}(t) - y^{(j)}(t)]$, along the vorticity and shear directions yields to:

$$\begin{aligned} MSD_v(\Delta t) &= \frac{1}{2}\langle|\Delta x^{(i,j)}(t+\Delta t) - \Delta x^{(i,j)}(t)|^2\rangle \\ &= \langle|x_0^{(i)}(t+\Delta t) - x_0^{(i)}(t)|^2\rangle \\ MSD_s(\Delta t) &= \frac{1}{2}\langle|\Delta y^{(i,j)}(t+\Delta t) - \Delta y^{(i,j)}(t)|^2\rangle \\ &= \langle|y_0^{(i)}(t+\Delta t) - y_0^{(i)}(t)|^2\rangle \end{aligned} \quad (9)$$

where the average is performed over all initial times t, all the pair of particles (i, j) within a distance d (typically ~ 20 μm) such that $\langle u_{x,y}^{(i)}(t+\Delta t) u_{x,y}^{(j)}(t)\rangle = u_{x,y}^2 \delta(\Delta t)$ or equivalently $u_{x,y}^{(i)} \simeq u_{x,y}^{(j)}$, and over all the echo phases.

Similarly, we can compute the particle mutual-displacement probability distribution functions (PDF), along the vorticity and shear direction, respectively:

$$P_v(\Delta x, \Delta t) = \langle\delta\left[\Delta x - \left(\Delta x^{(i,j)}(t+\Delta t) - \Delta x^{(i,j)}(t)\right)\right]\rangle, \quad (10)$$

$$P_s(\Delta y, \Delta t) = \langle\delta\left[\Delta y - \left(\Delta y^{(i,j)}(t+\Delta t) - \Delta y^{(i,j)}(t)\right)\right]\rangle. \quad (11)$$

3.2.2.2 Echo-DDM

As introduced and described in [11], echo-DDM consists of a differential dynamic microscopy (DDM) analysis of each registered echo image sequence [25, 26]. In brief, we compute the 2D spatial Fourier transform $\hat{I}(\mathbf{q}, t)$ of the image intensity $I(\mathbf{x}, t)$, which was previously multiplied by a windowing function [30]; we then evaluate the *image structure function* $D(\mathbf{q}, \Delta t) = \langle|\hat{I}(\mathbf{q}, t+\Delta t) - \hat{I}(\mathbf{q}, t)|^2\rangle$, where the average is computed over all the initial times t. The image structure function is strictly related to the *intermediate scattering function* $f(\mathbf{q}, \Delta t)$ (ISF), through the relation:

$$D(\mathbf{q}, \Delta t) = a(\mathbf{q})[1 - \Re\{f(\mathbf{q}, \Delta t)\}] + b(\mathbf{q}), \quad (12)$$

where a($\mathbf{q}$) encodes the sample scattering properties and the microscope transfer function for the scattering amplitude, b($\mathbf{q}$) accounts for the camera noise and $\Re\{f\}$ indicates the real part (see *e.g.* Refs. [26, 31] for additional details).

In order to compute the ISF, we estimate $a(\mathbf{q})$ as and $b(\mathbf{q})$ as follows. $b(\mathbf{q})$ could be in principle estimated as the limit for $\Delta t \to 0$ of $D(\mathbf{q}, \Delta t)$, as $f(\mathbf{q}, \Delta t \to 0) = 1$. However, since Δt is finite, we evaluate $b(\mathbf{q})$ as the intercept of a quadratic fit over small time-interval at the origin to $D(\mathbf{q}, \Delta t)$ (first five points). Analogously, $a(\mathbf{q})$ could in principle be estimated by taking the limit for $\Delta t \to \infty$ of $D(\mathbf{q}, \Delta)$, since $f(\mathbf{q}, \Delta t \to \infty) = 0$. Nevertheless, the finite acquisition time does not allow to capture the full-relaxation process for all the wave vectors $\mathbf{q}$. For this reason, we decide to evaluate $a(\mathbf{q})$ from the power spectra of the background corrected images [32]:

$$a(\mathbf{q}) = \langle|\hat{I}(\mathbf{q}, t) - \hat{I}_0(\mathbf{q})|^2\rangle - b(\mathbf{q}), \quad (13)$$

where $\hat{I}_0(\mathbf{q})$ is the Fourier transform of the background image $I_0(\mathbf{x})$. Knowing $a(\mathbf{q})$ and $b(\mathbf{q})$, we can invert Eq. 12 to obtain $f(\mathbf{q}, \Delta t)$. In order to isolate the dynamics along the shear and vorticity direction, we then perform an azimuthal average on the $\mathbf{q}$-plane restricted to narrow angular aperture $\Delta\theta$ perpendicularly oriented along the principal axes. The dynamics is then extracted by fitting the ISFs assuming a specific functional model for the statistics of the displacements. Eventually, as we do not observe any phase-dependent effects, we average the dynamical parameters of the best fitting curves over the all different phases.

It is worth noticing that while echo-particle tracking clearly requires seeding the sample with tracer particles, which must be large enough to be individually resolved, and dispersed at a suitably low volume fraction in order to avoid particle overlaps within the images, echo-DDM analysis is subjected to much less stringent constraints. In particular, as shown for example in Ref. [33], where DDM is used to perform passive microrheology, also particles well below the diffraction limit can be exploited. Moreover, if the optical contrast provided by the intrinsic optical inhomogeneities within the sample is large enough, the addition of tracers could be not even necessary.

3.2.3 Creep and recovery

Creep and recovery experiments allow distinguishing between recoverable and unrecoverable strain. To better understand the microscopic processes and mechanisms underlying this difference, it is useful to combine this test with the study of the microscopic dynamics. To this aim, we acquire an image sequence and use the Image-J plugin *Stack-Reg* to obtain the transformation matrices of the rigid translation that describe each image of the sequence. In parallel, we convolve each image with a Wiener kernel (of standard deviation 2 μm) and extract the positions of the particles by using the same Matlab code developed for echo-particle tracking. We then use the transformation matrices to remove the rigid translation contribution from each particle position. Finally, we link all the particle positions to obtain the non-affine particles' trajectories in time. To properly isolate the non-affine contribution to the particle displacements, we consider only the vorticity component of the motion. Unfortunately, mismatches between camera orientation and shear direction can be present. Therefore, as a first step, we compute the angles on the (x, y)-plane between two consecutive time steps so that the creep curve can be projected along one single direction. We then use these angles to project the trajectories of the particles along the true shear and vorticity direction, respectively. The non-affine dynamics is then extracted by computing the mutual-MSD and the PDF along the vorticity direction (Eq. 9 and 10).

10.3389/fphy.2022.1013805

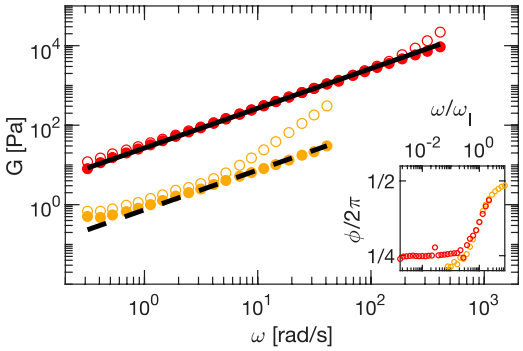

FIGURE 5
Amplitude G of the complex modulus G^* as obtained from frequency sweep measurement on glycerol (orange circles) and silicon oil (red circles). Empty (full) circles are obtained without (with) correction for inertia and friction. In the inset, we report the measured phase as a function of ω/ω_I without the correction. The lines are linear fits representing the expected (Newtonian) behavior.

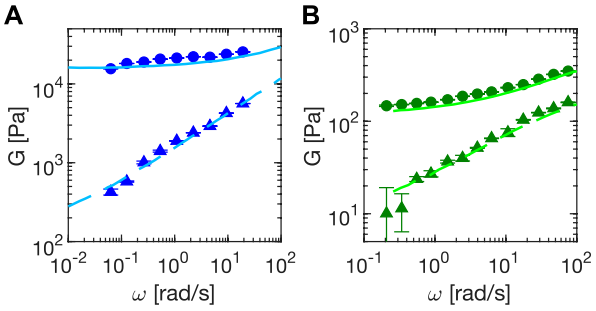

FIGURE 6
Storage (circles) and loss (triangles) moduli relative to **(A)** Sylgard (elastic sample) and **(B)** Carbopol 5% (yield stress sample) as a function of the oscillation frequency ω in oscillatory shear tests. Lines correspond to storage (continuous) and loss (dashed) moduli obtained with a commercial rheometer. Frequency sweeps are made at constant strain (1.5 ± 0.2% and 1.42 ± 0.09% for Sylgard and Carbopol, respectively). All data are corrected for inertia and sliding friction as described in the main text.

4 Experimental results on standard and yield-stress materials

In order to assess the capabilities of our setup, we performed a series of different experiments with standard elastic and viscous samples, as well as with Carbopol-based yield-stress fluids. We first focus on small amplitude oscillatory shear (SAOS) frequency sweeps in order to evaluate the performance of our cell in recovering the frequency-dependent storage and loss moduli in the linear regime. We then report the results of large amplitude oscillatory shear (LAOS) amplitude sweeps to assess the potential of rheo-microscopy experiments and to link local rearrangements to non-linear rheology. Moreover, to illustrate the versatility of our setup, we perform rheology experiments with triangular stress profiles. Finally, preliminary results of creep and recovery rheo-microscopy experiments are presented. For all these experiments the focus is on highlighting the main features of our setup; a study of the physical implications of the phenomena that are showcased here goes beyond the scope of the present work and will be performed in future studies.

4.1 SAOS frequency sweeps

In order to check the performance of our shear cell in terms of mechanical characterization, we first performed SAOS frequency sweeps with purely viscous materials: glycerol and silicon oil. The oscillation frequency varied from 0.3 rad/s to a sample-dependent upper frequency, this upper bound (50 rad/s for glycerol, 400 rad/s for silicon oil) marking the point at which inertial effects become dominant over material's response.

For both samples, we report in Figure 5 the absolute value of the modulus $G = |G^*|$ obtained from the data analysis described in Section 3.1. Empty circles indicate the modulus obtained with Eq. 2, before correcting for inertia and friction, whereas full circles are obtained after correcting for these effects by using Eq. 7. It appears evident how the samples behave like ideal viscous fluids ($G' = 0$ and $G'' = \eta\omega = G$), only once the corrections have been applied. Without the correction, the contribution of inertia becomes relevant for $\omega > \omega_I$, with $\omega_I = \eta/I$. For $\omega \ll \omega_I$ both moduli grow linearly with ω, whereas for $\omega \gg \omega_I$ the expected quadratic scaling due to the term $I\omega^2$ in Eq. 7 is observed. The transition from the viscous to the inertial regime at $\omega = \omega_I$ can be also appreciated by looking at the inset, where the phase delay of the strain is reported as a function of ω/ω_I: as the frequency increases the phase transits from a plateau value at $\pi/2$, the expected phase difference for a viscous sample, to the phase opposition characterizing inertial regime. Deviations from the expected linear behavior remain for glycerol at low frequencies, also after correction, these are residual effects of the sliding friction that in this regime is comparable with the material response.

We extract the viscosity of both samples by fitting a linear function of the experimental data after correction, which provides for glycerol (dashed line) and silicon oil (continuous line) viscosities equal to $\eta = 0.86 \pm 0.05$ Pa·s and $\eta = 26.6 \pm 0.3$ Pa·s, respectively. While the value for glycerol is in the range of expected values, also considering hydration [18, 19], the value for silicon oil is ~ 10% smaller than the one measured with a rheometer (Section 2.6), which we attribute to a comparable error in our estimate of the sample area due to meniscus formation after being loaded in the cell.

10.3389/fphy.2022.1013805

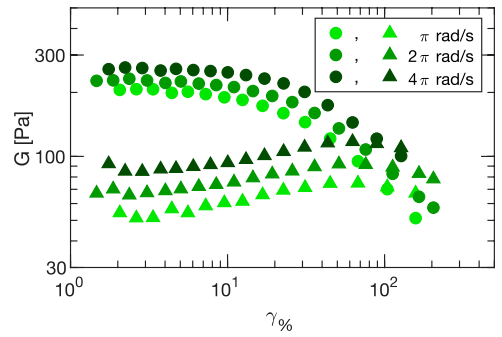

FIGURE 7
Storage (circles) and loss (triangles) moduli obtained from amplitude sweeps from the linear to the LAOS regime performed on Carbopol 5%. Different colors correspond to different angular frequencies ω equal to π rad/s (light green), 2π rad/s (green) and 4π rad/s (dark green). Error bars are smaller than the data points. All data are corrected for inertia and sliding friction as described in the main text.

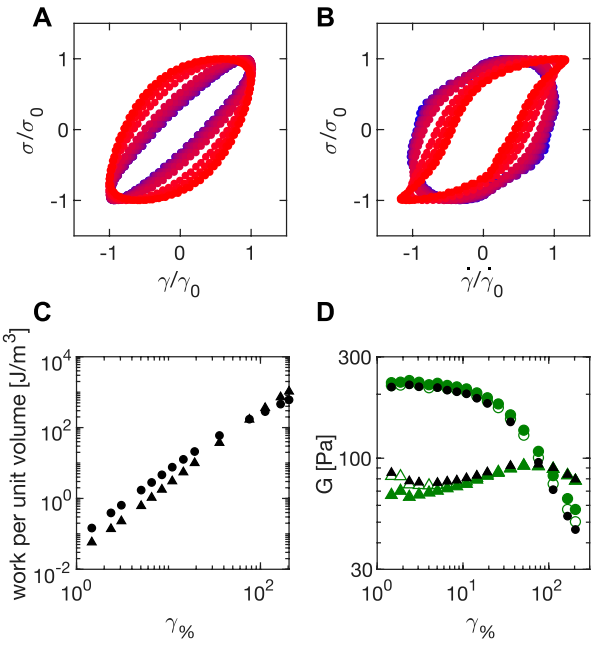

FIGURE 8
Amplitude sweeps for Carbopol 5% during LAOS at $\omega = 2\pi$ rad/s **(A)** Lissajous plot of the normalized stress $\sigma(t)$ versus the normalized strain $\gamma(t)$. Color scale progressively goes from low stresses (blue points, $\sigma_0 = 3.5$ Pa) to large stresses (red points, $\sigma_0 = 190$ Pa). **(B)** Lissajous plot of the normalized stress $\sigma(t)$ versus the normalized strain rate $\dot{\gamma}(t)$. Color scale is the same as in **(A)**. **(C)** Dissipated energy per unit volume W_D (triangle) and elastic energy per unit volume W_E (circles) as obtained from the Lissajous plots in **(A)** and **(B)**, respectively. **(D)** Storage (black circles) and loss (black triangles) moduli as obtained from the closed integral of the Lissajous plots. In green, we report the results obtained with a sinusoidal fit of $\gamma(t)$: full green symbols represent data corrected with inertia and sliding friction corrections and were already shown in Figure 7; both black and empty green symbols represent uncorrected data obtained from Lissajous integrals and from the fit, respectively.

We report in Figure 6 results of frequency sweeps experiments with Sylgard (Figure 6A) and Carbopol 5% (Figure 6B). The experimental error bars, evaluated as the standard deviation of the mean over three different consecutive realizations, are typically smaller than the symbols, with the only exception of the loss modulus of Carbopol, due to an increasing uncertainty on the value of the phase. Lower precision in the phase determination mainly results from the increased duration of the experiments, which also increases the likelihood of an external perturbation of the system. Such an effect is less pronounced for Sylgard, whose large modulus makes it less sensitive to spurious perturbations and drifts. Overall, the storage and loss moduli for both samples can be measured over more than two decades in frequency, and are in agreement with rheology data obtained in Ref. [34] (Sylgard) and with our measurements with the rheometer (Carbopol 5%), as described in Section 2.6.

4.2 LAOS amplitude sweep

One of the most interesting applications of our setup lies in its capability to apply large amplitude oscillatory shears to a soft viscoelastic material, and simultaneously observe and characterize the rearrangements of suspended tracers within the sample.

The results of amplitude sweeps performed at different frequencies ($\omega = \pi$, 2π and 4π rad/s) with Carbopol 5% are plotted in Figure 7, and show the expected behavior for a yield stress fluids: for small strain amplitudes (linear regime) the behavior is substantially elastic (*i.e.* the loss modulus is much smaller than the storage one) and the moduli are almost amplitude independent. Increasing the amplitude, we observe a progressive drop of G', a peak in G'', and the crossover between G' and G''. The crossover depends on the sampling frequency but is typically found for strain amplitudes between 80% and 100%. The fact that in our setup we observe an increase of G'' at the lowest probed strains is caused by the increasing contribution of sliding friction for decreasing values of the applied stress. In the SAOS regime, sliding friction effects are a consequence of our simplified treatment of friction, which sets a lower limit $G'' \sim \sigma_{fr,0}/\gamma_0$ to frequency and amplitude sweeps. It is to be noted, however, that for a prescribed value of the sliding friction, such a limit can be pushed to lower values by increasing the sample area.

It is important to stress that the values for G' and G'' that we have obtained in LAOS tests originate from fitting the measured strain profile with a sinusoidal function. This procedure is the same used in commercial rheometers. From the temporal evolution of stress and strain within a period, we obtain

Lissajous plots of stress as a function of the strain (Figure 8A) and of the strain rate (Figure 8B). To this aim, we first correct both the stage position and velocity for the drift contributions, which is done by subtracting from the raw data, the polynomial drift function $f_{pol}(t)$, and its analytical time derivative $\dot{f}_{pol}(t)$, respectively (see also Section 3.1). From the drift corrected position and velocity, the strain $\gamma(t)$ and the strain rate $\dot{\gamma}(t)$ are retrieved dividing by the gap. The average strain $\hat{\gamma}(t) = \sum_{n=0}^{N-1} \gamma(t + nT)$, with $t \in [0, T)$, is computed by averaging the strain over all the N measured periods. The average strain rate $\hat{\dot{\gamma}}(t)$ is evaluated analogously.

To recover the temporal evolution of the stress, we divide the applied force by the measured area $\sigma(t) = F(t)/S$. Given the extreme precision of the SMU in supplying the signal, there is an extremely low discrepancy (average relative deviation $\Delta F/F < 4 \cdot 10^{-16}$) between consecutive measured periods of $F(t)$. We can therefore choose the first period of σ and, by assuming that it is virtually identical to the average over all the periods, identify the average stress $\hat{\sigma}$ with it. Since the sampling frequency is different for force and displacement measurements, to recover Lissajous plots a direct association must be made between $\hat{\sigma}$ on one side and $\hat{\gamma}$ and $\hat{\dot{\gamma}}$ on the other side. We perform this association by considering the discrete measurement times t of the strain and interpolating $\hat{\sigma}$ at these times.

Combining all these steps, we obtain the Lissajous plots in Figures 8A,B, where we report for Carbopol 5% the values of $\hat{\sigma}$, $\hat{\gamma}$ and $\hat{\dot{\gamma}}$ normalized with σ_0, γ_0, and $\omega\gamma_0$. These plots reproduce the typical response for a yield stress fluid [35], with the stress-strain plot (8A) increasingly deviating from linearity and the stress-strain rate plot (8B) increasingly deviating from the initial elliptical shape, as the applied stress increases.

Beyond giving a very powerful visual representation of the rheological changes occurring within a material as the amplitude increases, the Lissajous plots in Figures 8A,B can be also used to extract quantitative information. In particular, the area under stress as a function of strain during a cycle quantifies the value of dissipated energy per unit volume [36]:

$$W_D = \oint \hat{\sigma}(\hat{\gamma}) d\hat{\gamma}. \tag{14}$$

Similarly, the elastic energy per unit volume is given by the area under stress as a function of strain during a cycle:

$$W_E = \frac{1}{\omega} \oint \hat{\sigma}(\hat{\dot{\gamma}}) d\hat{\dot{\gamma}} \tag{15}$$

These two quantities, calculated for Carbopol 5% at $\omega = 2\pi$ rad/s are shown in Figure 8C, where it appears immediately that a strain value can be identified beyond which the dissipated energy W_D overcomes the stored energy W_E. By definition, this value coincides with the crossover point between the moduli G' and G'' (see Figure 7), which we can also estimate from the Lissajous analysis as

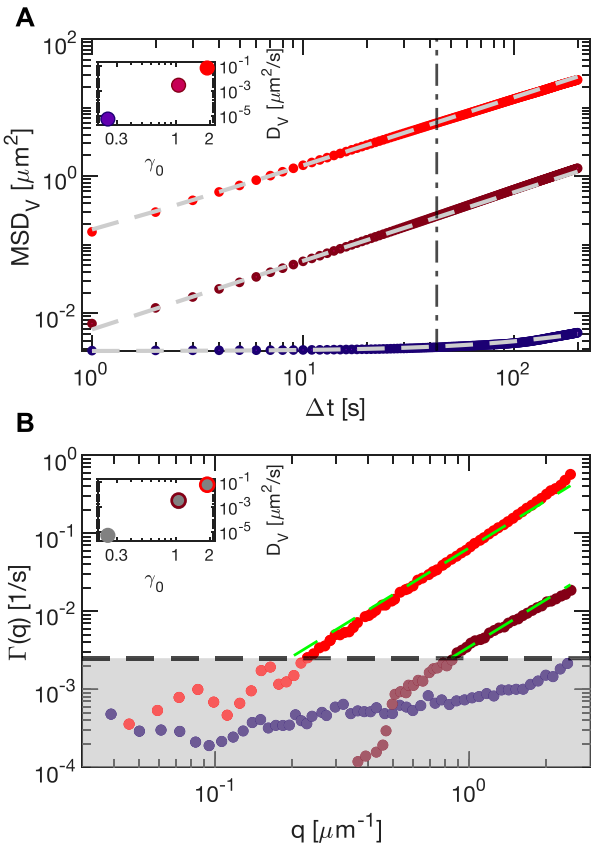

FIGURE 9
Microscopic, shear-induced dynamics of tracers embedded in Carbopol 5% shared at $\omega = 2\pi$ rad/s with strain amplitudes 24.5% (blue), 105% (purple) and 188% (red). **(A)** mean square displacement obtained from echo particle tracking analysis in the vorticity direction. Gray dashed lines are best fit with fitting function $MSD_v = \sigma_{MSD} + 2D_v\Delta t$. In the inset, we plot the diffusivity obtained from the fit as a function of the measured strain. **(B)** Relaxation rate from echo-DDM analysis of the same experiments. Green dashed lines are best fitting curves with the function $\Gamma = D_v q^2$. Gray shaded area identifies the region where fits are not reliable. In the inset, the diffusivity obtained from the fit (colored points) is compared with the one obtained from the PT analysis (gray points).

$$G'_{liss} = \frac{W_E}{\pi\gamma_0^2} \tag{16}$$

$$G''_{liss} = \frac{W_D}{\pi\gamma_0^2}. \tag{17}$$

The results obtained for the storage and loss moduli by using the Lissajous plots are reported in Figure 8D, where they are shown to agree with the results from the sinusoidal fit before operating the correction for inertia and friction, which is not implemented in the Lissajous plots. This agreement validates our different analyses.

In order to explore the microscopic counterpart of the yielding transition, we analyzed the shear-induced

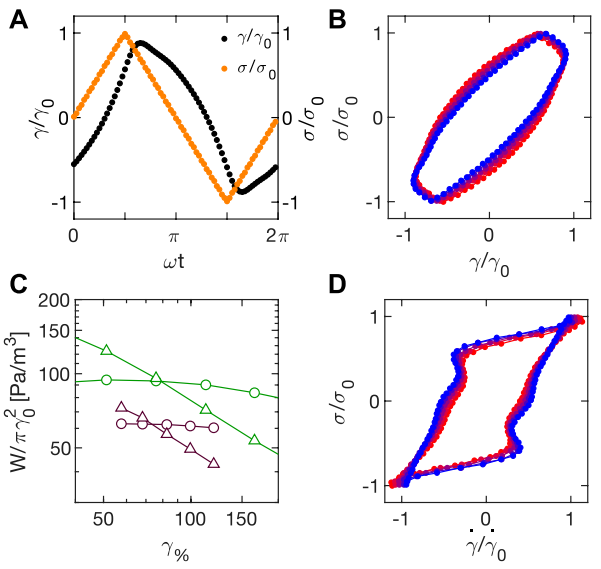

FIGURE 10
(A) Normalized stress σ/σ_0 (orange) and strain γ/γ_0 (black) during a triangular wave amplitude sweep at $\omega_1 = 2\pi$ rad/s. **(B)** Lissajous plot of the normalized stress σ/σ_0 as a function of the normalized strain γ/γ_0 relative to a triangular wave amplitude sweep at $\omega_1 = 2\pi$ rad/s. Colormap goes from blue to red as applied stress increases from 55 to 89 Pa. **(C)** Elastic (triangles) and dissipated (circles) energy normalized to $\pi\gamma_0^2$ as a function of the strain amplitude obtained for an amplitude sweep with a sinusoidal (green) and a triangular (purple) waveform. **(D)** Lissajous plot of the normalized stress σ/σ_0 as a function of the normalized strain rate $\dot{\gamma}/\dot{\gamma}_0$ relative to the same experiment of **(B)**.

stroboscopic dynamics of embedded tracers for different strain amplitudes (Supplementary Movies SM2 and SM3). We first perform particle tracking analysis of the echo dynamics induced in the vorticity direction by shearing the sample Carbopol 5% at $\omega = 2\pi$ rad/s (amplitude sweep). In Figure 9A, we report the mean squared displacement (MSD) calculated (using 400 consecutive frames, and with 10 recorded points per period) for strain amplitudes 24.5% (blue), 105% (purple) and 188% (red). All the reported MSDs exhibit a linear behavior suggesting a diffusive-like behavior of the tracers that was previously observed in Ref. [11] with a similar Carbopol sample. The tracer mobility increases with the strain amplitude, but for small amplitudes exhibits an offset due to the tracking localization error. For this reason, we fitted the MSDs with a diffusive model accounting for the offset (dashed lines in the plot): $MSD_v = \sigma_{MSD} + 2D_v\Delta t$. The resulting D_v (inset of Figure 9) strongly depends on the strain amplitude, and spans over 4 orders of magnitude when the strain is increased by a factor of 10. Echo-DDM analysis of the same images (Figure 9B) provides q-dependent relaxation rates $\Gamma(q)$ that are extracted by fitting the experimental ISFs to the model $f(q, \Delta t) = \exp(-\Gamma(q)\Delta t)$. The gray shadow corresponds to the region for which the estimation of the relaxation rates $\Gamma(q)$ is not reliable since the relaxation times of $f(\mathbf{q}, \Delta t)$ for some wave vectors qs are longer than the acquisition time. By fitting the reliable points for the relaxation rate with a quadratic model $\Gamma(q) = D_v q^2$, which is typical for Brownian diffusion, we find a very good agreement between the diffusivity obtained by particle tracking and DDM, as shown in the inset. The agreement between PT and DDM is encouraging, as the former can be applied to investigate heterogeneous samples, whereas the latter is suited for small particles or for very dense non-index-matched complex fluids without recurring to tracers.

4.3 Triangular wave

During LAOS experiments one induces in the sample some microscopic, irreversible rearrangements that are larger for increasing strain amplitudes. While a sinusoidal perturbation of the sample is a simple, natural way to explore the frequency dependence of the sample mechanical properties, both strain and strain rates change during the period, thus making difficult the determination of the rearrangements dependence on these two parameters. A triangular wave, conversely, is characterized by a constant stress rate (unless a sign) while stress linearly changes in time. As a complementary oscillatory characterization, we therefore implemented the possibility to generate a triangular-wave stress with period $2\pi/\omega_1$ and amplitude σ_0 as

$$\sigma(t) = \frac{2\sigma_0}{\pi}\arcsin\sin(\omega_1 t) \tag{18}$$

Although periodic, this function is not characterized by the single frequency ω_1 but by an infinite series of frequencies $\omega_n = n\omega_1$ with $n = 1, 3, \ldots, \infty$ according to its Fourier series

$$\sigma(t) = \frac{8\sigma_0}{\pi^2}\sum_{n=1,3,\ldots,\infty}\frac{(-1)^{(n-1)/2}}{n^2}\sin\omega_n t. \tag{19}$$

Experimental normalized[3] stress and strain profiles obtained during a triangular wave amplitude sweep with Carbopol 5% at $\omega_1 = 2\pi$ rad/s close to yielding ($\gamma_0 = 68\%$), are reported in Figure 10A. While the applied stress is a neat triangular wave, the corresponding strain is shark-fin shaped. Indeed, the strain response to a triangular stress is expected to be triangular only in the linear regime.

Information on the viscoelastic response for different stresses can be recovered from the analysis of the Lissajous plots, as described in Section 4.2. Triangular stresses as a function of strain and strain rate for different amplitudes are reported in Figures

3 Here, γ_0 is the strain amplitude evaluated from a fit of the measured strain with a triangular wave. Although the triangular wave fit is not optimal to reproduce the strain time evolution, it is suitable for a normalization whose sole purpose is to make data visualization more effective.

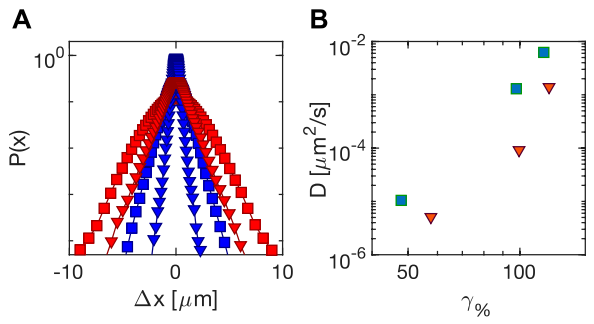

FIGURE 11
Echo particle tracking analysis of the dynamics of tracers in Carbopol 5% **(A)** Probability distribution for a time delay Δt = 43 s of the tracer displacements: squares (triangles) are obtained with sinusoidal (triangular) stress, whose amplitude is 98.6 ± 0.8% (blue) and 118 ± 2% (red). **(B)** Diffusion coefficients of the tracers as a function of strain amplitude for sinusoidal (squares) and triangular (triangles) stress profiles.

10B,D, respectively. Of note, the stress-strain Lissajous evolves from a fairly defined rectangle to a more non-linear shape as stress increases (from blue to red). Also in this case, we can retrieve the elastic W_E and dissipated W_D energy from the circular integral of the data reported in Figures 10B,D, respectively. The results of this analysis for strains around the crossover are shown in Figure 10C (purple), after normalization with $\pi\gamma_0^2$. In contrast with the similar quantities obtained during a sinusoidal amplitude sweep (see Figure 8D and Figure 10C, green), here it is not correct to interpret $W/(\pi\gamma_0^2)$ as modulus, as they are defined as the response to a sinusoidal perturbation. However, the results obtained with the triangular wave exhibit a similar trend of the ones obtained with a sinusoidal perturbation, but the former are systematically smaller, as expected from the inequality

$$|\sigma_0 \sin(\omega_1 t)| \leq \left|\frac{2\sigma_0}{\pi} \arcsin \sin(\omega_1 t)\right|. \quad (20)$$

Turning now to the local dynamics, we decided to compare in the same range of strains the results of echo PT analysis for both a triangular and a sinusoidal perturbation of Carbopol 5% across the yielding transition. We plot in Figure 11A the probability distribution of the displacements at time delay Δt = 43 s for the triangular (triangles) and the sinusoidal (squares) stress application. For both types of perturbation, distributions exhibits marked exponential tails. This combination of non-Gaussian statistics of the displacement and linear (Fickian) scaling of the MSD with time has been found to be a recurring feature of particles moving in heterogeneous environments [37, 38]. Remarkably, for the same measured strain amplitude (same color on the plot) distributions are sensibly larger for sinusoidal stress application. This picture is confirmed when the diffusion coefficients are extracted from PT analysis as a function of the strain amplitude (Figure 2B): shear-induced diffusion is less pronounced in the presence of triangular stresses compared to sinusoidal ones, suggesting that, at the same applied strain amplitude, shear-induced diffusion seems to correlate with the energy injected macroscopically per unit volume. The observed difference between the microscopic dynamics caused by triangular and sinusoidal stress profiles is particularly relevant from a methodological point of view, as it shows how being able to impose a variety of controlled stress profiles on the sample can be pivotal in connecting the microscopic dynamics with the macroscopic rheology of the sample. Future work will focus on other stress profiles, such as for instance chirped ones.

4.4 Creep and recovery

Creep and recovery tests have been performed with Sylgard and Carbopol, as prototypical elastic and viscoelastic materials, while simultanously studying the dynamics of embedded tracers. By switching on the magnet at $t = 0$ we create a sudden increase of the stress from zero to a value σ_0 (step-stress or creep). If a constant stress is applied to an elastic sample, the strain is expected to increase until reaching - after a transient - an equilibrium strain γ_0, from which the storage modulus can be recovered. As the applied stress return to zero (recovery phase), recovered strain can be measured as well, from which information on the dissipation can be derived [39].

In Figure 12A, we report the compliance $J = \gamma/\sigma_0$ measured during a creep and recovery experiment on a Sylgard sample with shear modulus $4.5 \cdot 10^4$ Pa. The applied stresses span in a range of two decades from 53 to 8,300 Pa (inset of Figure 12A). The lower stress limit is set by the displacement detection: given the gap h = 332 μm, a strain of 0.1% corresponds in this measurement to a displacement of about 0.4 μm. This limit could be therefore in principle reduced by a factor 3 if the gap is increased to 1 mm. The upper limit, corresponding to a strain of 18%, comes from the high current intensity (1.3 A) necessary to reach the imposed stress of 8,300 Pa (area $1.4 \cdot 10^{-4}$ m^2). These high currents are indeed close to the magnet loading limits. The purely elastic nature of Sylgard is confirmed both by the superposition of the compliances for all the values of applied stress, and by the complete recovery that is observed for long times. In the inset, the plateau strain obtained from an exponential fit of the creep part of $\gamma(t)$ is reported as a function of the applied stress. The superposed yellow dashed line is a linear fit from which the shear modulus $G = 4.5 \cdot 10^4$ Pa is recovered. Green points are the strain obtained from oscillatory experiments at three different σ_0 obtained with the same sample.

In Figure 12C, we show the compliances obtained from a series of creep and recovery experiments performed with Carbopol 5% for different imposed stresses. Carbopol flows

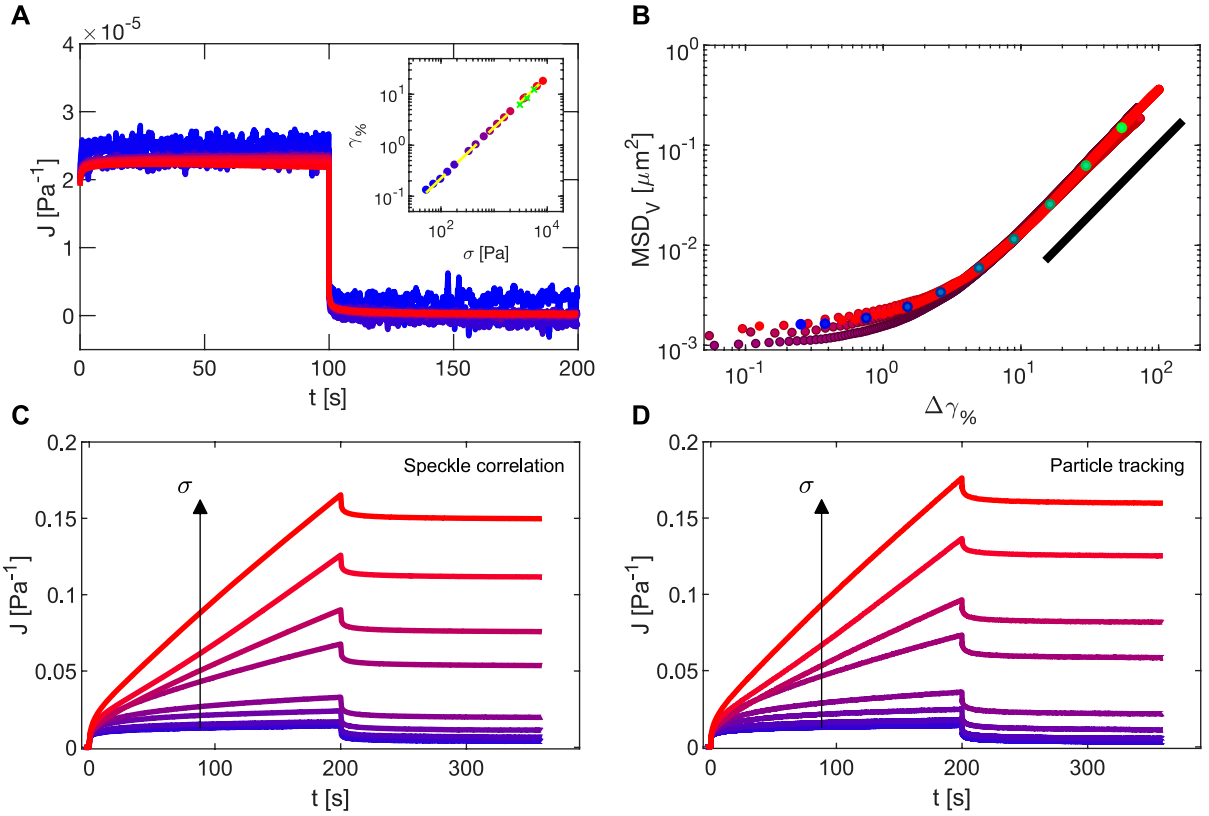

FIGURE 12
(A) Compliance measured in a series of creep and recovery experiments on a Sylgard sample with shear modulus $4.5 \cdot 10^4$ Pa. Color scale ranges from the lower (blue) to the highest (red) applied stress, accordingly to the values reported on the abscissa of the inset, where the fitted strain creep plateau values are reported. In the inset, dashed white line is a linear fit of the plateau strains. Green points are the results obtained in oscillatory regime on the same sample. **(B)** MSD in the vorticity direction as a function of the strain, recovered from the four largest applied stresses of the dataset of C, on which it is possible to identify a constant strain rate on the time interval [40, 150] s. The black line is a guide to the eye, representing a power law with exponent 1.4 **(C)** Macroscopic compliance measured from speckle correlation in a series of creep and recovery experiments with Carbopol 5%. Color scale ranges on the applied stresses ranging from σ = 4.7 Pa (blue) to σ = 51.8 Pa (red). **(D)** Local compliance measured from PT for the same experiment.

for stress values around yielding, as for an imposed constant stress the strain does not approach a plateau value but linearly increases with time until stress holds. Lack of superposition of compliances for different stresses, even below yielding stress, and the lack of complete recovery testify the exit from the linear regime characterising lower stresses. Tracking the tracer particles as described in Section 3.2.3, we obtain the corresponding local compliance (Figure 12D), in excellent agreement with the global one in Figure 12C.

In the last analysis, we quantified the non-affine dynamics present when the system is flowing at a constant shear rate during creep tests. In Figure 12B we show the MSD in the vorticity direction corresponding to the four measurements with stresses close to yielding (28.2, 33.0, 37.7, and 51.8 Pa) as a function of the incremental strain $\Delta\gamma = \Delta t\dot{\gamma}$. The nice collapse of the curves suggests that non-affine dynamics depends only on strain and not on strain rate. This can be explained by the fact that, as in a typical yield stress material, the stress response for the probed strain rate values is constant. Conversely from what has been found in [40] for a jammed emulsion, the estimated MSD show superdiffusive scaling $\sim \gamma^{1.4}$, which suggests that non-affine dynamics is directionally-persistent. However, a detailed discussion of this behaviour is beyond the scope of this study.

5 Conclusion

Here we describe a new rheo-microscopy setup that combines a stress-controlled rheometer with particle tracking and differential dynamic microscopy analysis of the motility of tracer particles. We tested the advantages and limitations of our

setup with a variety of samples and tests, which were made possible by its versatility and flexibility. All the mechanical parts of the shear cell can easily be reproduced in any machine shop once having the technical drawings. All the remaining constitutive parts are commercially available, which makes the setup easily reproducible in any laboratory equipped with compressed air circuit. To further lower the barrier to implementation, we described in detail all the tests performed on the cell, the working principle of the acquisition protocol, and the data analysis algorithms.

A key feature of our setup is that it allows imaging of the entire sample height by means of long working distance objectives and optimized clear apertures. In such a way, by taking movies at different planes the cell allows extracting z-resolved information, which in turn provides a direct quantification of sample slip at the shear cell walls and makes it an excellent tool to investigate shear bending phenomena, thus allowing both a mesoscopic and a microscopic characterization of the deformation field. We believe that this capability will be of great help to settle important and long-standing issues, such as for instance the connection between shear banding and the microscopic structure and dynamics occurring within the banded material [27, 41, 42].

The wide range of accessible shearing frequencies, strain, and stresses allows for the exploration of both SAOS and LAOS regimes, with different types of periodic stress profiles, while simultaneously performing echo-imaging to separate non-affine displacements from affine ones and investigate shear-induced dynamics. Here we found evidence that, as the stress, and consequently the strain, increases during an amplitude sweep on a viscoelastic sample, shear-induced diffusion becomes faster (Section 4.2). By comparing different functional shapes of the applied periodic stress, we evidenced how such rearrangements are not only proportional to the amplitude of the strain the sample undergoes but depends on the energy absorbed and dissipated by the material during the whole shearing period (Section 4.3). Finally, we provide a different characterization by quantifying the local dynamics in non-periodic creep experiments, pointing out that non-affine dynamics is independent from the strain rate (Section 4.4).

Superposition rheology experiments could also be easily implemented, as well as comparative studies on the effect on sample properties of different pre-shearing procedures. The main limitation of the current design is the failure to operate when the applied stress is too small, a limit that can be easily overcome by increasing the sample area. Future perspectives foresee the possibility of also making strain-controlled experiments (with a feedback loop as in a commercial rheometer) and testing the cell with different imaging techniques, *e.g.* confocal microscopy.

Data availability statement

The raw data supporting the conclusion of this article will be made available by the authors, without undue reservation.

Author contributions

PE, VT, FG, and RC conceived the project and designed the experimental apparatus. SV assembled and tested the apparatus; SV and MB performed experiments; SV and MB analyzed the data. VT, FG, and RC coordinated the experimental activity. SV, MB, and RC wrote the first draft of the manuscript. All authors contributed to manuscript revision and read and approved the submitted version.

Funding

This work has been supported by: the Associazione Italiana per la Ricerca sul Cancro (AIRC) to FG and SV (MFAG#22083), the Swiss National Science Foundation (grant 172514) to VT.

Acknowledgments

The authors thank Stefano Aime and Giuliano Zanchetta for extensive and stimulating discussions. We thank IMCD Italia SpA for the kind gift of the Carbopol sample.

Conflict of interest

The authors declare that the research was conducted in the absence of any commercial or financial relationships that could be construed as a potential conflict of interest.

Publisher's note

Supplementary material

The Supplementary Material for this article can be found online at: https://www.frontiersin.org/articles/10.3389/fphy.2022.1013805/full#supplementary-material.

References

1. Besseling R, Isa L, Weeks ER, Poon WC. Quantitative imaging of colloidal flows. *Adv Colloid Interf Sci* (2009) 146:1–17. doi:10.1016/j.cis.2008.09.008

2. Dutta S, Mbi A, Arevalo RC, Blair DL. Development of a confocal rheometer for soft and biological materials. *Rev scientific Instr* (2013) 84:063702. doi:10.1063/1.4810015

3. Sentjabrskaja T, Chaudhuri P, Hermes M, Poon W, Horbach J, Egelhaaf S, et al. Creep and flow of glasses: Strain response linked to the spatial distribution of dynamical heterogeneities. *Sci Rep* (2015) 5:11884–11. doi:10.1038/srep11884

4. Koumakis N, Moghimi E, Besseling R, Poon WC, Brady JF, Petekidis G. Tuning colloidal gels by shear. *Soft Matter* (2015) 11:4640–8. doi:10.1039/c5sm00411j

5. Pommella A, Philippe AM, Phou T, Ramos L, Cipelletti L. Coupling space-resolved dynamic light scattering and rheometry to investigate heterogeneous flow and nonaffine dynamics in glassy and jammed soft matter. *Phys Rev Appl* (2019) 11:034073. doi:10.1103/physrevapplied.11.034073

6. Chan HK, Mohraz A. A simple shear cell for the direct visualization of step-stress deformation in soft materials. *Rheol Acta* (2013) 52:383–94. doi:10.1007/s00397-013-0679-5

7. Lin NY, McCoy JH, Cheng X, Leahy B, Israelachvili JN, Cohen I. A multi-axis confocal rheoscope for studying shear flow of structured fluids. *Rev Scientific Instr* (2014) 85:033905. doi:10.1063/1.4868688

8. Aime S, Ramos L, Fromental JM, Prevot G, Jelinek R, Cipelletti L. A stress-controlled shear cell for small-angle light scattering and microscopy. *Rev Scientific Instr* (2016) 87:123907. doi:10.1063/1.4972253

9. Singh A, Tateno M, Simon G, Vanel L, Leocmach M. Immersed cantilever apparatus for mechanics and microscopy. *Meas Sci Technol* (2021) 32:125603. doi:10.1088/1361-6501/ac1c1d

10. Boitte JB, Vizcaïno C, Benyahia L, Herry JM, Michon C, Hayert M. A novel rheo-optical device for studying complex fluids in a double shear plate geometry. *Rev Scientific Instr* (2013) 84:013709. doi:10.1063/1.4774395

11. Edera P, Brizioli M, Zanchetta G, Petekidis G, Giavazzi F, Cerbino R. Deformation profiles and microscopic dynamics of complex fluids during oscillatory shear experiments. *Soft Matter* (2021) 17:8553–66. doi:10.1039/d1sm01068a

12. Shin S, Dorfman KD, Cheng X. Effect of edge disturbance on shear banding in polymeric solutions. *J Rheology* (2018) 62:1339–45. doi:10.1122/1.5042108

13. Tu MQ, Lee M, Robertson-Anderson RM, Schroeder CM. Direct observation of ring polymer dynamics in the flow-gradient plane of shear flow. *Macromolecules* (2020) 53:9406–19. doi:10.1021/acs.macromol.0c01362

14. Song J, Zhang Q, de Quesada F, Rizvi MH, Tracy JB, Ilavsky J, et al. Microscopic dynamics underlying the stress relaxation of arrested soft materials. *Proc Natl Acad Sci U S A* (2022) 119:e2201566119. doi:10.1073/pnas.2201566119

15. Pommella A, Cipelletti L, Ramos L. Role of normal stress in the creep dynamics and failure of a biopolymer gel. *Phys Rev Lett* (2020) 125:268006. doi:10.1103/physrevlett.125.268006

16. Cipelletti L, Martens K, Ramos L. Microscopic precursors of failure in soft matter. *Soft matter* (2020) 16:82–93. doi:10.1039/c9sm01730e

17. Dhont JK, Wagner NJ. Superposition rheology. *Phys Rev E* (2001) 63:021406. doi:10.1103/physreve.63.021406

18. Volk A, Kähler CJ. Density model for aqueous glycerol solutions. *Exp Fluids* (2018) 59:75–4. doi:10.1007/s00348-018-2527-y

19. Grover D, Nicol J. The vapour pressure of glycerin solutions at twenty degrees. *J Soc Chem Industry* (1940) 59:175–7.

20. Cerbino R. Quantitative optical microscopy of colloids: The legacy of jean perrin. *Curr Opin Colloid Interf Sci* (2018) 34:47–58. doi:10.1016/j.cocis.2018.03.003

21. Crocker JC, Grier DG. Methods of digital video microscopy for colloidal studies. *J Colloid Interf Sci* (1996) 179:298–310. doi:10.1006/jcis.1996.0217

22. Pelletier V, Gal N, Fournier P, Kilfoil ML. Microrheology of microtubule solutions and actin-microtubule composite networks. *Phys Rev Lett* (2009) 102:188303. doi:10.1103/PhysRevLett.102.188303

23. Adrian RJ. Scattering particle characteristics and their effect on pulsed laser measurements of fluid flow: Speckle velocimetry vs particle image velocimetry. *Appl Opt* (1984) 23:1690–1. doi:10.1364/ao.23.001690

24. Raffel M, Willert C, Wereley S, Kompenhans J. *Particle image velocimetry. experimental fluid mechanics*, 10. Berlin: Springer (2007). p. 978.

25. Cerbino R, Trappe V. Differential dynamic microscopy: Probing wave vector dependent dynamics with a microscope. *Phys Rev Lett* (2008) 100:188102. doi:10.1103/physrevlett.100.188102

26. Giavazzi F, Brogioli D, Trappe V, Bellini T, Cerbino R. Scattering information obtained by optical microscopy: Differential dynamic microscopy and beyond. *Phys Rev E* (2009) 80:031403. doi:10.1103/physreve.80.031403

27. Divoux T, Fardin MA, Manneville S, Lerouge S. Shear banding of complex fluids. *Annu Rev Fluid Mech* (2016) 48:81–103. doi:10.1146/annurev-fluid-122414-034416

28. Boukany PE, Wang SQ, Ravindranath S, Lee LJ. Shear banding in entangled polymers in the micron scale gap: A confocal-rheoscopic study. *Soft Matter* (2015) 11:8058–68. doi:10.1039/c5sm01429h

29. Pönisch W, Zaburdaev V. Relative distance between tracers as a measure of diffusivity within moving aggregates. *Eur Phys J B* (2018) 91:27–7. doi:10.1140/epjb/e2017-80347-5

30. Giavazzi F, Edera P, Lu PJ, Cerbino R. Image windowing mitigates edge effects in differential dynamic microscopy. *Eur Phys J E* (2017) 40:97–9. doi:10.1140/epje/i2017-11587-3

31. Giavazzi F, Cerbino R. Digital Fourier microscopy for soft matter dynamics. *J Opt* (2014) 16:083001. doi:10.1088/2040-8978/16/8/083001

32. Cerbino R, Piotti D, Buscaglia M, Giavazzi F. Dark field differential dynamic microscopy enables accurate characterization of the roto-translational dynamics of bacteria and colloidal clusters. *J Phys : Condens Matter* (2017) 30:025901. doi:10.1088/1361-648x/aa9bc5

33. Edera P, Bergamini D, Trappe V, Giavazzi F, Cerbino R. Differential dynamic microscopy microrheology of soft materials: A tracking-free determination of the frequency-dependent loss and storage moduli. *Phys Rev Mater* (2017) 1:073804. doi:10.1103/physrevmaterials.1.073804

34. Prabowo F, Wing-Keung AL, Shen HH. Effect of curing temperature and cross-linker to pre-polymer ratio on the viscoelastic properties of a pdms elastomer. *Adv Mat Res* (2015) 1112:410–3. doi:10.4028/www.scientific.net/amr.1112.410

35. Laurati M, Egelhaaf S, Petekidis G. Plastic rearrangements in colloidal gels investigated by Laos and ls-echo. *J Rheology* (2014) 58:1395–417. doi:10.1122/1.4872059

36. Donley GJ, Singh PK, Shetty A, Rogers SA. Elucidating the G″ overshoot in soft materials with a yield transition via a time-resolved experimental strain decomposition. *Proc Natl Acad Sci U S A* (2020) 117:21945–52. doi:10.1073/pnas.2003869117

37. Wang B, Kuo J, Bae SC, Granick S. When brownian diffusion is not Gaussian. *Nat Mater* (2012) 11:481–5. doi:10.1038/nmat3308

38. Brizioli M, Sentjabrskaja T, Egelhaaf SU, Laurati M, Cerbino R, Giavazzi F. Reciprocal space study of brownian yet non-Gaussian diffusion of small tracers in a hard-sphere glass. *Front Phys* (2022) 10:408. doi:10.3389/fphy.2022.893777

39. Calzolari D, Bischofberger I, Nazzani F, Trappe V. Interplay of coarsening, aging, and stress hardening impacting the creep behavior of a colloidal gel. *J Rheology* (2017) 61:817–31. doi:10.1122/1.4986465

40. Vasisht VV, Dutta SK, Del Gado E, Blair DL. Rate dependence of elementary rearrangements and spatiotemporal correlations in the 3d flow of soft solids. *Phys Rev Lett* (2018) 120:018001. doi:10.1103/physrevlett.120.018001

41. Ozawa M, Berthier L, Biroli G, Rosso A, Tarjus G. Random critical point separates brittle and ductile yielding transitions in amorphous materials. *Proc Natl Acad Sci U S A* (2018) 115:6656–61. doi:10.1073/pnas.1806156115

42. Fielding SM. Shear banding in soft glassy materials. *Rep Prog Phys* (2014) 77:102601. doi:10.1088/0034-4885/77/10/102601

frontiers | Frontiers in Physics

TYPE Original Research
PUBLISHED 18 November 2022
DOI 10.3389/fphy.2022.991540

OPEN ACCESS

EDITED BY
Luca Cipelletti,
Université de Montpellier, France

REVIEWED BY
Gabriel A. Caballero-Robledo,
Unidad Monterrey, Mexico
Stefano Aime,
École Supérieure de Physique et de Chimie Industrielles de la Ville de Paris, France

*CORRESPONDENCE
Jeffrey S. Urbach,
urbachj@georgetown.edu

SPECIALTY SECTION
This article was submitted to Soft Matter Physics, a section of the journal Frontiers in Physics

RECEIVED 11 July 2022
ACCEPTED 07 November 2022
PUBLISHED 18 November 2022

CITATION
Miller JM, Blair DL and Urbach JS (2022), Order and density fluctuations near the boundary in sheared dense suspensions. *Front. Phys.* 10:991540. doi: 10.3389/fphy.2022.991540

Order and density fluctuations near the boundary in sheared dense suspensions

Joia M. Miller, Daniel L. Blair and Jeffrey S. Urbach*

Department of Physics and Institute for Soft Matter Synthesis and Metrology, Georgetown University, Washington, DC, United States

We introduce a novel approach to reveal ordering fluctuations in sheared dense suspensions, using line scanning in a combined rheometer and laser scanning confocal microscope. We validate the technique with a moderately dense suspension, observing modest shear-induced ordering and a nearly linear flow profile. At high concentration (ϕ = 0.55) and applied stress just below shear thickening, we report ordering fluctuations with high temporal resolution, and directly measure a decrease in order with distance from the suspension's bottom boundary as well as a direct correlation between order and particle concentration. Higher applied stress produces shear thickening with large fluctuations in boundary stress which we find are accompanied by dramatic fluctuations in suspension flow speeds. The peak flow rates are independent of distance from the suspension boundary, indicating that they likely arise from transient jamming that creates solid-like aggregates of particles moving together, but only briefly because the high speed fluctuations are interspersed with regions flowing much more slowly, suggesting that shear thickening suspensions possess complex internal structural dynamics, even in relatively simple geometries.

KEYWORDS

shear flow, rheology, colloids, shear thickening, order-disorder, phase transition

1 Introduction

Flowing dense suspensions of colloidal particles appear in a wide range of important industrial processes, and the presence of flow can dramatically modify the suspension microstructure, which in turn impacts flow properties (reviewed in [1–3]). In particular, the presence of simple shear modifies the well-understood phase behavior of dense suspensions of nearly monodisperse colloidal particles in equilibrium. Modest shear promotes layering which enhances crystallization, while higher shear rates often disrupt crystalline order [1, 3–8]. In addition, the bulk response of the suspension can be very sensitive to the material close to the confining boundaries [9–12]. Planar boundaries promote the formation of layers of particles parallel to the boundaries [9, 13], enabling more efficient shearing as layers slide past each other with reduced close particle interactions, and a resulting reduction in the local viscosity [14–16]. The layering also enhances ordering within the layer, and in many circumstances the sliding layers show a

high degree of hexagonal ordering, similar to what is seen in two dimensional colloidal crystals [12, 17]. In many dense suspensions, the shear thinning arising from increased layering is followed by dramatic shear thickening when the applied stress exceeds a critical value, with the increase in viscosity attributable to a transition from primarily hydrodynamic particle interactions at low stress to frictional interactions at high stress (reviewed in [18]). The onset of frictional interactions will likely disrupt layering [19], a scenario confirmed by recent computer simulations [20]. A variety of evidence suggests that strong shear thickening is accompanied by complex spatiotemporal dynamics, including fluctuations in flow speed, local stress, and particle concentration [21–35]. These results highlight the need for methods that can probe the dynamics of dense colloidal suspension with high spatial and temporal resolution. Here we introduce a new approach to assessing dynamic ordering using a combined rheometer and laser scanning confocal microscope [35], where the laser scanning is limited to one spatial direction. In this case the scan is perpendicular to the flow direction, and the suspension flow is primarily responsible for the temporal evolution of the recorded intensity. We validate the technique using a moderately dense suspension (volume fraction $\phi = 0.52$), where only modest shear-induced ordering is observed. At higher concentration ($\phi = 0.55$) and applied stress just below the onset of shear thickening, we measure ordering fluctuations with high temporal resolution, and directly measure the decrease in ordering with distance from the bottom boundary of the suspension. We also observe a direct correlation between ordering and particle concentration, with local regions of high order corresponding to high particle concentrations, consistent with recent observations from computer simulations [20]. Higher applied stress produces shear thickening, and we find that the large fluctuations in boundary stress that underlie thickening are accompanied by dramatic fluctuations in suspension flow rates. The peak flow rates are independent of distance from the suspension boundary, indicating that they arise from transient jamming that creates solid like aggregates of particles moving together. Such aggregates must be short-lived because the high speed fluctuations are interspersed with regions flowing much more slowly, suggesting that shear thickening suspensions possess very complex internal structural dynamics, even in relatively simple geometries.

2 Approach

For particulate suspensions, particle velocities are often extracted from image sequences by particle tracking or correlation analysis (PIV) [36]. Particle tracking typically requires that the time between images is small compared to the time for a particle to move an interparticle separation (so that each particle can be unambiguously identified in successive images). Thus for a frame rate f and an interparticle spacing δ, the flow speed must satisfy $v_{max}^{imaging} \ll f\delta$. The typical small δ in dense suspensions requires either a vanishingly small v_{max} or extremely high frame rate f for successful tracking. PIV can, in principle, handle larger displacements between images, but only if the particle configuration maintains a consistent distinctive pattern so that there is a clear unique peak in the spatial cross-correlation between images, which is typically not the case for the dense suspensions studied here.

We use an alternative approach here, inspired by fluid dynamics and machine vision applications where the motion of material past point or line detectors is used to infer speeds and structure [37, 38]. We take advantage of the rapid scan rate of a laser scanning confocal microscope, where the point of focus is rapidly scanned back and forth in one direction, which we will call the x axis, with the normal rastering perpendicular to the scan line in the focal plane disabled (Figure 1A). We illustrate the principle with a simple example: A fluorescent particle transiting the line will produce a local intensity extremum, from which its x position can be determined. The time it takes the particle to transit the line can be measured by the length of the ridge produced when a position-time intensity surface is generated (Figure 1B). If the center of the particle is in the plane of focus and neglecting the effects of the finite optical resolution, the magnitude of the component of the particle velocity perpendicular to the line can be determined as $v = D/T$, where D is the particle diameter and T the transit time. The requirement that the transit time is long compared to the time between scans means that the flow speed must be $v_{max}^{line} \ll sD$, where s is the scan rate and D the particle diameter. Because the scan rate for laser scanning confocal microscopy is two to three orders of magnitude larger than the frame rate (the time to generate a 2D image is approximately the scan duration times the number of lines in an image), and the interparticle spacing in dense suspensions is comparable to the particle diameter, $\delta \sim D$, $v_{max}^{line} \gg v_{max}^{imaging}$. Figure 1C shows a representative position-time intensity surface generate by our system (Leica SP5, scan rate 8,000 Hz), where the passage of individual 1 μm diameter particles with transit times ~ 5 ms indicating speeds of ~ 200 $\mu m/s$ can be clearly identified despite the high particle density $\phi \approx 0.55$. In practice individual particles cannot be robustly identified at from the data, and the position of the particles relative to the plane of focus is variable, so we instead extract speeds from characteristic lengths extracted from correlation analyses, as described below and detailed in Methods. The technique works equally well for non-fluorescent particles in a fluorescent suspending fluid, which is the approach we use in what follows.

The situation sketched above describes motion advection purely in the direction of the shear flow, but the linescan measurement will also be affected by other components of the flow velocity. Because of the geometry, the speed in the flow direction will normally be of order $\dot{\gamma}z$, where $\dot{\gamma}$ is the shear rate

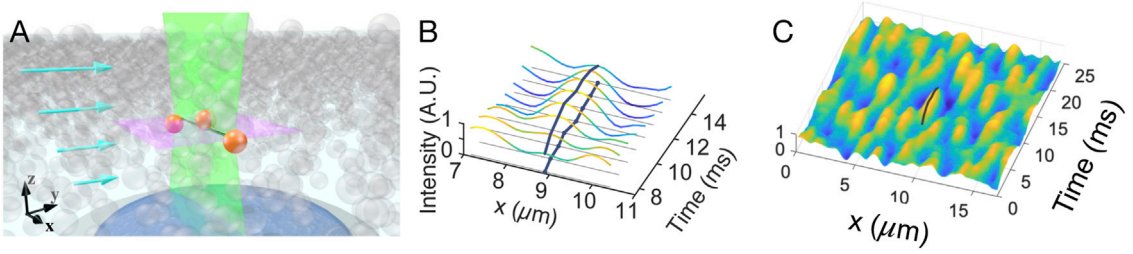

FIGURE 1
(A) Schematic of linescan imaging of a sheared dense suspension. The illumination laser rapidly scans back and forth, focused along the green line. Particles transiting the line are illuminated (orange). The imaging region for the usual 2D laser scan is indicated by the dashed line, and the arrows represent the average velocity field of the sheared suspension. The depth of focus (effective width of the image plane in z) depends on the optical setup, and is ~ 1 μm here) **(B)** Graphical representation of the linescan data, where the continuous colored lines represent a small portion of each individual scan, separated by a short interval. A fluorescent particle transiting the scan region produces a local intensity maximum (marked with a black line). **(C)** Rendering of linescan data showing the passage of many particles. The transit time can be determined by the length of the ridge (black line) (Note that in what follows the solvent is fluorescent but the particles are not, so the transit of particles produces local intensity minima).

and z is the distance in the gradient direction from the bottom surface to the focus of the scan line (Figure 1A). In the cases considered here, the transverse velocity components are expected to be much smaller, but it is important to keep this consideration in mind when interpreting the linescan data.

A related approach has been used to measure flow profiles in capillary and microfluidic systems (reviewed in [39, 40]) where fluorescence correlation spectroscopy (FCS) is employed to extract speeds using fluorescent single molecules or nanoparticles [41]. The exact shape of the intensity autocorrelation function depends on the relative importance of diffusion and advection, but when diffusion is negligible compared to advection (as is the case in the situations considered here), the intensity autocorrelation function is a Gaussian with a width determined by the flow speed and the size of the illumination volume [42]. By varying the scan orientation relative to the flow direction, the full (average) three dimensional velocity vector can be determined [43, 44]. In those applications, however, the volume fraction of the fluorescent species is always low, so they are reasonably assumed to be distributed randomly. In the results presented below, spatial ordering dramatically affects the spatiotemporal intensity fluctuations, complicating the determination of the flow speed but revealing novel behavior in dense colloidal shear flow.

Validation: To verify the accuracy of the linescan approach under these conditions, we performed tests on a moderately dense suspension, volume fraction $\phi = 0.52$, where the viscosity is only weakly non-Newtonian, under constant shear rate conditions. Figure 2 shows three representative kymographs, each generated from 512 scans (65 ms total time), showing the range of speeds from the slowest ($\dot{\gamma} = 10\ s^{-1}$; $z = 3\ \mu m$) to the fastest ($\dot{\gamma} = 30\ s^{-1}$; $z = 20\ \mu m$). The wide range of transit times is evident, as is the appearance of regions of hexagonal ordering, which will be considered in the next section. Rather than identifying individual particles, we can quantify the length and time scales of the intensity variations using correlation analyses, with faster flow producing more rapid fluctuations along the time axis. In particular, as detailed in Methods, we calculate the speed of the flow by the rate of decay of the autocorrelation in the time direction (vertical in Figure 2). This produces a very precise measurement of the fluctuation timescale, but conversion to speed requires knowing the length scale associated with the decay in the density autocorrelation. At the volume fractions considered here ($\phi \sim 0.5$) that is of order the particle diameter, but the exact value is sensitive to the local structure of the suspension. Thus, as discussed in the Methods section, there is some uncertainty in the absolute value of the measured speeds, and likely some correlation between the local order and the calculated speed. In future work we plan to more fully characterize these effects with further experimental tests and comparisons with computer simulations.

We acquired a series of 900 kymographs at heights above the bottom boundary of $z = 3, 6, 10, 20\mu$m, for constant applied shear rates of$\dot{\gamma} = 10, 20, 30 s^{-1}$. The resulting flow profiles are presented in Figure 3A, with error bars given by the standard deviation of each series. Figure 3B shows the same data, with the speed scaled by the speed of the top plate, $v_p = \dot{\gamma} d$, where $d \approx 150\ \mu m$ is the width of the rheometer gap at the imaging position (For the cone-plate geometry used here, the gap is a continuous function of radius, but changes relatively little over the $\approx 65\ \mu m$ scan range.) The data collapse, with no free parameters, to a unique, nearly linear profile that demonstrates the wide range of speeds over which the technique provides precise speed measurements. The deviation from an affine profile close to the wall likely arises from a combination of wall slip, layering, and ordering (because the ordering is strongest close to the wall and, as indicated above, spatial order will have an effect on the calculated speed). Finally, we note that these measurements are taken at relatively high flow rates, so Brownian Motion or particle sedimentation are not

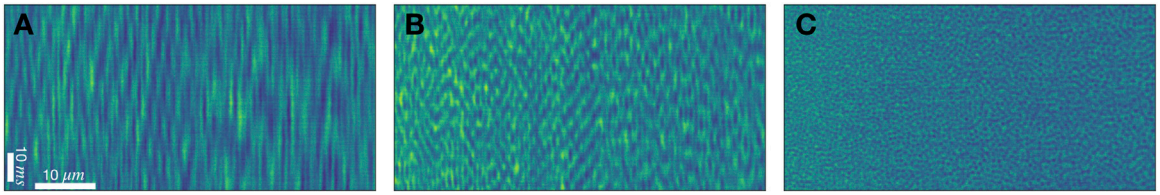

FIGURE 2
Representative space-time kymographs generated from linescans (horizontal) stacked vertically taken in a sheared dense suspension of silica particles of diameter 1 μm, ϕ = 0.52, at different shear rates. The spheres are not fluorescent, and a fluorescent dye is added to the solvent. **(A)** $\dot{\gamma} = 10\ s^{-1}$, $z = 3\ \mu m$, **(B)** $\dot{\gamma} = 20\ s^{-1}$, $z = 6\ \mu m$, **(C)** $\dot{\gamma} = 30\ s^{-1}$, $z = 20\ \mu m$. Each image consists of 512 scans, for an elapsed time of 65 ms.

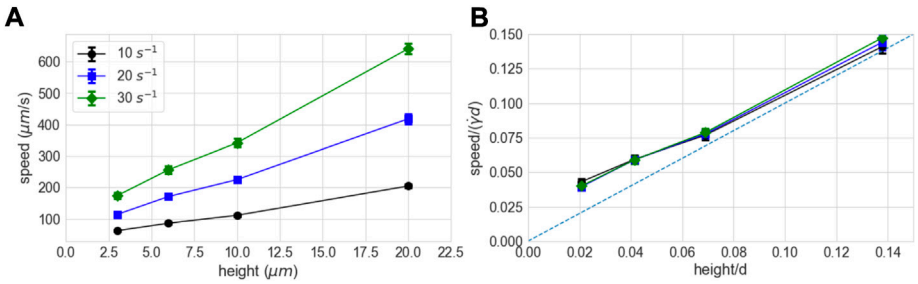

FIGURE 3
(A) Flow profiles for constant shear rate generated from linescan data at different heights (ϕ = 0.52), at different constant shear rates. **(B)** Particle speeds scaled by the speed of the top plate of the rheometer, $\dot{\gamma}d$, as a function of height above the bottom surface, scaled by the rheometer gap. Error bars are standard deviations (N = 900). Dashed line corresponds to purely affine flow with no wall slip.

significant on the timescale of the decay of the intensity autocorrelation function (see Discussion).

3 Results

Here we report the results of a dense suspension of 1 μm silica spheres at a volume fraction $\phi \approx 0.55$. The flow curve from bulk rheology for this sample is shown in Figure 4, and exhibits behavior similar to previous reports of shear thickening in similar systems [18], and in particular matches that of our previous results measuring local boundary stress fluctuations of the same system [35]. The viscosity shows substantial shear thinning (viscosity decreasing as applied shear stress is increased) until a critical stress of $\sigma_c \approx 20$ Pa, at which point strong shear thickening is observed. The transition occurs at a shear rate of $\dot{\gamma}_c \approx 10\ s^{-1}$, which corresponds to a Peclet number $Pe = \dot{\gamma}r^2/D_o \approx 500$, where $D_o = k_BT/6\pi\eta r$ is the diffusion coefficient for an isolated sphere of radius r in a solvent of viscosity η [1–3] (approximately 80 $mPa \cdot s$ for the 80:20 glycerol: water mixture used here. Note that the high concentrations used here substantially modify particle diffusion). Figure 4B shows shear rate vs time for constant applied stresses of 20, 50, and 100 Pa, corresponding to the conditions for the kymographs reported below. The increasing shear rate fluctuations with increasing stress is characteristic of a suspension showing strong shear thickening [18].

3.1 Order and density fluctuations before the onset of shear thickening

As summarized in Section 1, the shear thinning observed for applied stress $\sigma < \sigma_c$ is generally attributed to shear induced ordering, where organization of the monodisperse spheres into layers, and hexagonal ordering with the layers, reduces the viscosity by reducing collisions as the layers slide past one another. Figure 5 shows representative kymographs at σ = 20 Pa, at three different heights. At $z = 3\ \mu m$ above the bottom surface, the kymograph (top) reveals a very regular hexagonal lattice, elongated along the time axis because the particle speed is relatively small. Defects in the hexagonal order tend to be extended in the flow (time) directions, e.g. at the top right of the panel. The left side of the kymograph shows a region of relatively low order, which is uncommon at this height, as quantified below. At $z = 10\ \mu m$ (middle), regions of hexagonal

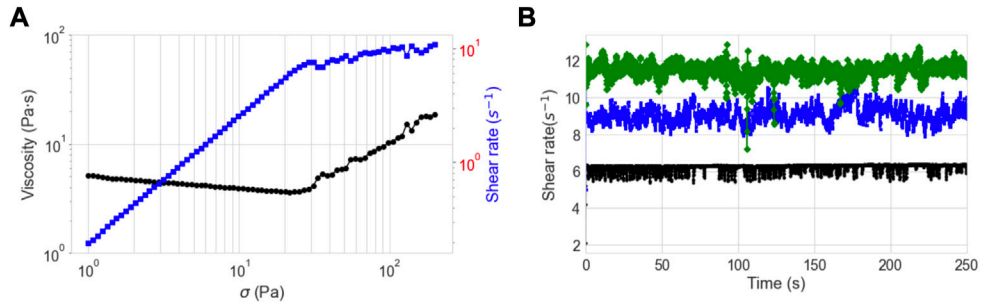

FIGURE 4
(A) Viscosity (○) and shear rate (■) as a function of applied shear stress for the suspension used in this study, composed of silica particles of diameter 1.0 μm, $\phi \approx 0.55$. **(B)** Representative plots of shear rate vs time for a constant applied stress of 20 (bottom), 50 (middle) and 100 (top) Pa. Specifically, the time series shown correspond to the kymographs reported at $z = 3\ \mu m$.

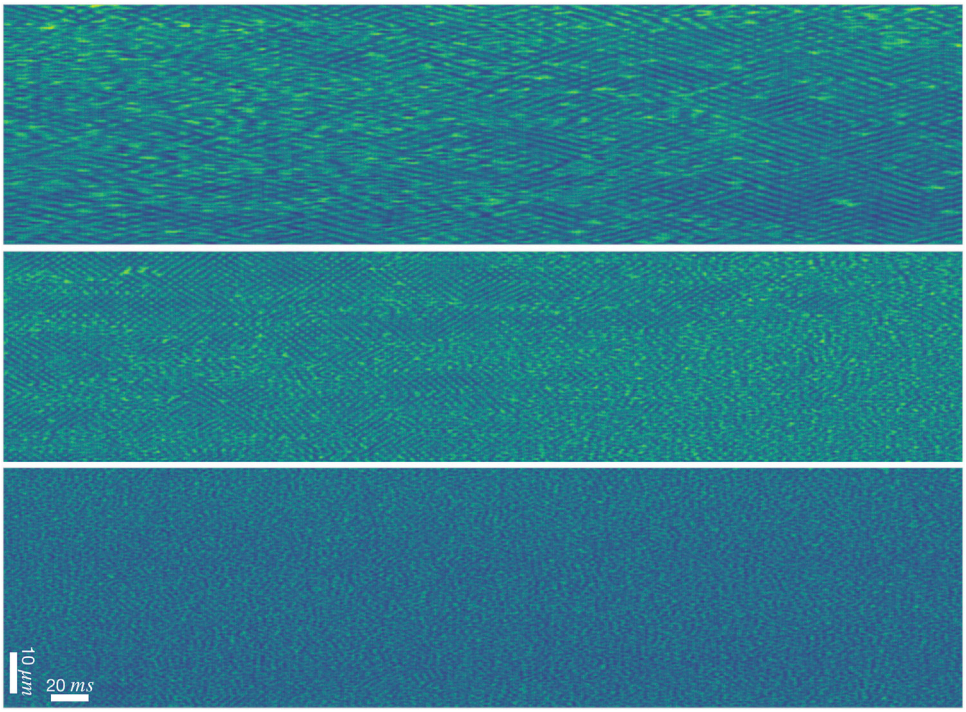

FIGURE 5
Representative space-time kymographs generated from linescans (vertical) stacked horizontally at 20 Pa constant applied stress at heights of 3 μm (top), 10 μm (middle), and 20 μm above the bottom surface. Each image consists of 4,096 scans, for an elapsed time of 520 ms (Note that the orientation is different than Figure 2, with time on the horizontal axis).

order show up as small islands in a sea of disorder, with a tendency to be longer in the time direction than in the spatial (vorticity) direction. Particle extent and separations in the time direction are proportional to the flow speed, so comparing dimensions requires rescaling by the flow speed (Supplementary Figure S1), or, more simply, counting the number of particle diameters in the different directions. The interpretation of the kymographs as direct images of 2D particle arrangements presumes that the rate of particle rearrangement is relatively slow compared to the rate at which structures traverse the scan region. The persistence of the hexagonal order suggests that this is a reasonable approximation.

In addition to revealing the existence and shape of small islands of order, the kymographs show that the ordered regions

are darker than regions of disorder. This can be seen clearly in the islands present at $z = 10\mu m$, where the overall intensity is lower in the islands than around them (Figure 5, middle), but is also evident at $z = 3\ \mu m$ (top), where the small regions of disorder are brighter than their surroundings. Because the fluorescent dye is in the solvent, brighter regions correspond to a *lower* concentration of colloidal particles. Below we quantify the correlation between order and low intensity, and show that is substantial at all heights at 20 Pa applied stress. This observation is consistent with simulations of dense suspensions of monodisperse particles, where a correlation between local ordering and high particle concentration was observed [20].

Quantifying the degree of hexagonal order in the kymographs is complicated by several factors. The images generated by individual particles depend on the height of the particle relative to imaging position. As discussed above, the particles tend to order in layers, and the patterns will be different when the center of the particle layer is at the linescan height compared to when the space between the layers aligns with the scan. A further complication arises from the fact that the 1 μm diameter of the particles is only a little larger than the resolution of the optical microscope, so particle images are not well separated. Finally, the distortion of the image in the flow direction depends on the speed of the flow, which fluctuates in time. Despite these complications we have found that we can extract a robust quantitative measure of the flow speed and order in each kymograph by calculating the two-dimensional intensity autocorrelation function, $g(\vec{r})$, for the entire kymograph, rescaling distances in the time direction by the flow speed, and then calculating the degree of hexagonal order present at $|\vec{r}| = r_o$, where r_o is the first peak in the angle averaged correlation function $g(r)$. This measure, described in more detail in Section 5, produces a complex scalar that is analogous to the quantity C_6 used in [2]. We use that name here, but note that because of the complications described above, even a fully ordered kymograph will produce a C_6 with a magnitude that is considerably less than unity (in what follows, C_6 refers to the magnitude of the complex order parameter).

Figure 6 shows a portion of the timeseries of speed, C_6, and average intensity generated from kymographs at $z = 10\ \mu m$. The first eight points in the time series correspond to the image shown in Figure 5 (middle). The decrease in order in the image (moving right to left) shows as a decrease in C_6 from ≈ 0.5 to < 0.3. Over the same region, the intensity increases modestly but significantly, as evident both in the image and the graph. The full timeseries shows that there is a reasonably consistent anticorrelation between C_6 and intensity, consistent with the qualitative impression from small scale variations in individual images, but that there are also significant fluctuations that appear uncorrelated. The correlations can be quantified by the Pearson correlation coefficient, and we find C(C_6,intensity) = {−0.19, −0.37, −0.34, −0.58} at heights $z = \{3, 6, 10, 20\}\mu m$. The effects are particularly significant at the intermediate heights, where the fluctuations in C_6 are largest. This negative correlation with intensity indicates that the ordered regions have a higher particle concentration, presumably as a consequence of more efficient packing.

A modest positive correlation can be observed between order and speed, which is consistent with an ordering-induced increase in local velocity close to the wall, but is complicated by the fact that the correlation analysis used to determine the flow speed likely has a weak dependence on order (see Methods). Finally, we note that the orientation of the hexagonal order is such that intensity peaks and valleys always align in the flow direction, corresponding to a phase angle for the complex order parameter ≈ 0 (data not shown). By contrast, the order seen at $\phi = 0.52$, while considerably weaker (Figure 2), has a phase angle $\approx \pi/6$ (Supplementary Figure S3).

The change in flow speed and order with distance from the bottom surface can be seen most clearly from histograms, as shown in Figure 7. The speeds increase with height, as expected, with a significant increase in the spread of speeds that is roughly proportional to the speed increase. Specifically, the ratio of the standard deviation to the mean speed is {0.14, 0.19, 0.21, 0.17} for heights $z = \{3, 6, 10, 20\}\mu m$, respectively. The slightly higher fractional spread at 6 and 10 μm likely arises from the coupling between order and speed mentioned above. The change in order with height is much more dramatic, showing uniformly high order 3 μm above the bottom surface, occasional disordered regions at $6\mu m$, roughly equal order and disorder at $10\mu m$, and mostly disordered at 20 μm. This behavior is summarized in Figure 8, which shows the average and standard deviations for speed and order as a function of height. Figure 8 also includes the data from 50 Pa applied stress, which shows very similar trends. The increase in curvature of the flow profile close to the boundary indicates a lower local viscosity. Boundary-induced ordering and an associated viscosity decrease in dense suspensions has been seen previously, but the high speed imaging approach used here enables us to quantify spatio-temporal fluctuations in previously inaccessible regimes.

3.2 Fluctuations associated with shear thickening

At higher applied stresses, the suspension shows substantial shear thickening and the nature of the fluctuations change dramatically. We have previously shown that shear thickening is associated with large fluctuations in stresses at the boundary of the sheared suspension [31–35], and specifically for the particles used here shear thickening is associated with a proliferation of the regions of high stress that propagate in the flow direction with approximately half the speed of the top plate ($v_p = \dot{\gamma} d$) [35]. Here local stress measurements at the bottom boundary are limited to a small region ($62 \times 62\ \mu m^2$) but still show clustered spikes of high stress that propagate in the flow

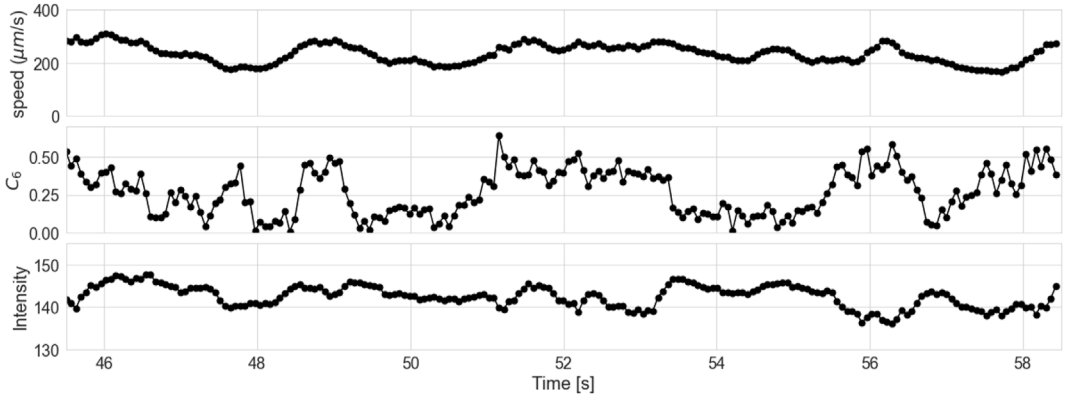

FIGURE 6
Section of time series of speed, hexagonal order, and intensity generated from kymographs at applied stress 20 Pa and height 10 μm. The first eight data points correspond to the image shown in Figure 5 (middle).

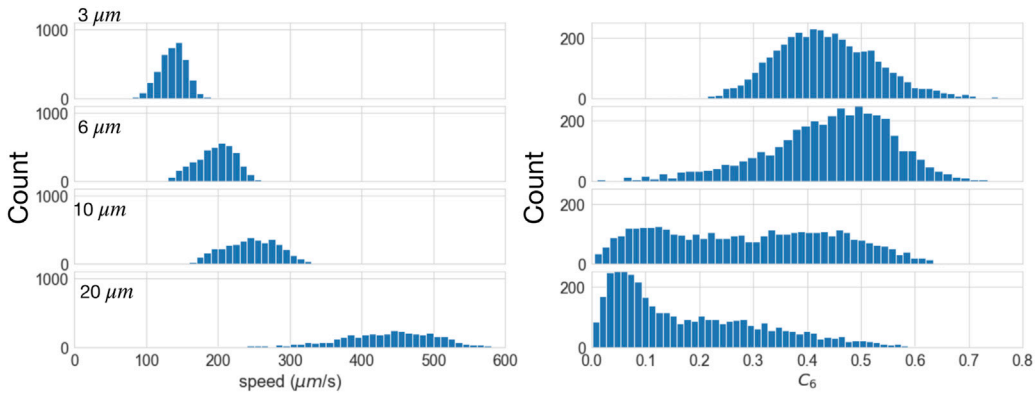

FIGURE 7
Histograms of speed and order generated from kymographs at applied stress 20 Pa (Each height: 3,900 kymographs, 65 ms each).

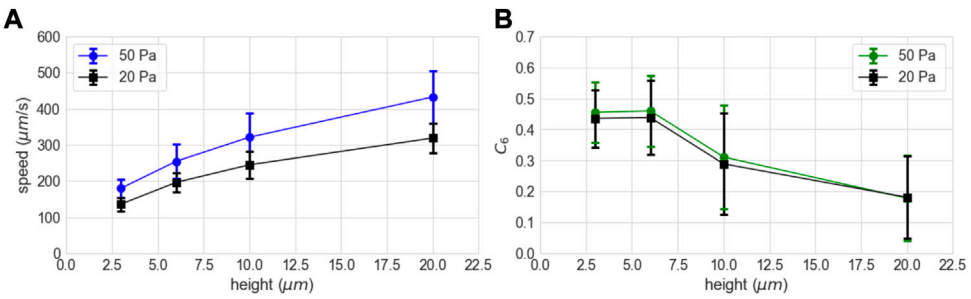

FIGURE 8
Profiles of average velocity **(A)** and order **(B)** for 20 and 50 Pa applied stress. Error bars are standard deviations (N = 3,900).

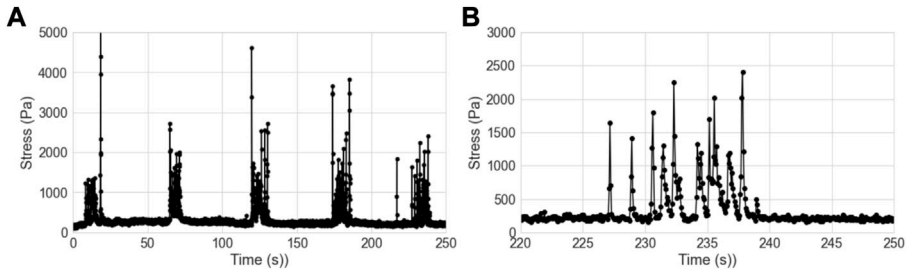

FIGURE 9
(A) Boundary stress (component in the flow direction) for 100 Pa applied stress. **(B)** Expanded view of one cluster of events from data shown in **(A)**.

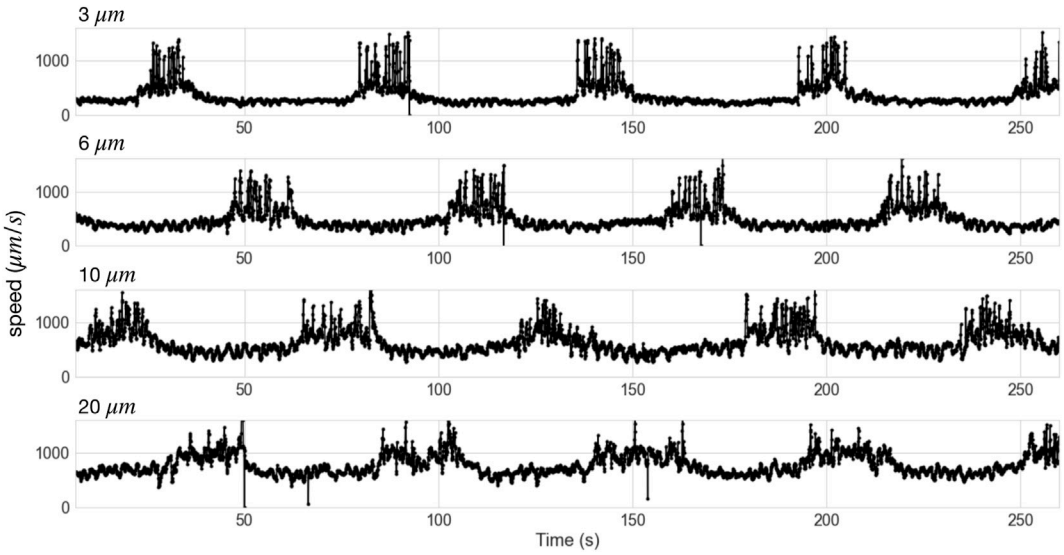

FIGURE 10
Full timeseries of speeds for 100 Pa applied stress at heights of 3, 6, 10, and 20 μm.

direction, plotted in Figure 9A. The intermittent spikes are similar in magnitude and duration to those previously observed, but the clustering was not reported previously. The connection with those and other results is discussed below, but for what follows the important observation is that the boundary stress shows regularly spaced clusters of intermittent high stress spikes. Figure 9B shows an expanded view or one cluster of events, clearly showing the presence of large discrete spikes in the boundary stress with durations $\approx 100 - 500$ ms (consistent with all time series reported, the data points are separated by 65 ms).

Figure 10 shows the velocity time series for four different heights at 100 Pa applied stress. The clustering of intermittent events is consistent in every data set (Each time series is a different measurement run, and is different from the run that produced the boundary stress shown in Figure 9.) Thus we can be confident that the intermittent spikes in speed represent the flow fluctuations that are associated with the intermittent high boundary stress spikes. Interestingly, the spacing between the clusters, $\sim 65\ s$, is roughly 1/2 of the rotation period for the rheometer tool, suggesting that the clusters reflect stable features propagating in the flow direction with speed $v_p/2$.

Figure 11 shows the time series for a cluster of spikes at each observed height, with the time axis shifted so that in each set the spikes start at the same time. The kymograph at the top of the figure, showing a single speed spike at $z = 3\mu m$, indicates that before the spike, the particles exhibit a high degree of hexagonal ordering, consistent with the behavior observed at this height at lower applied stress. The transition to high speed flow is

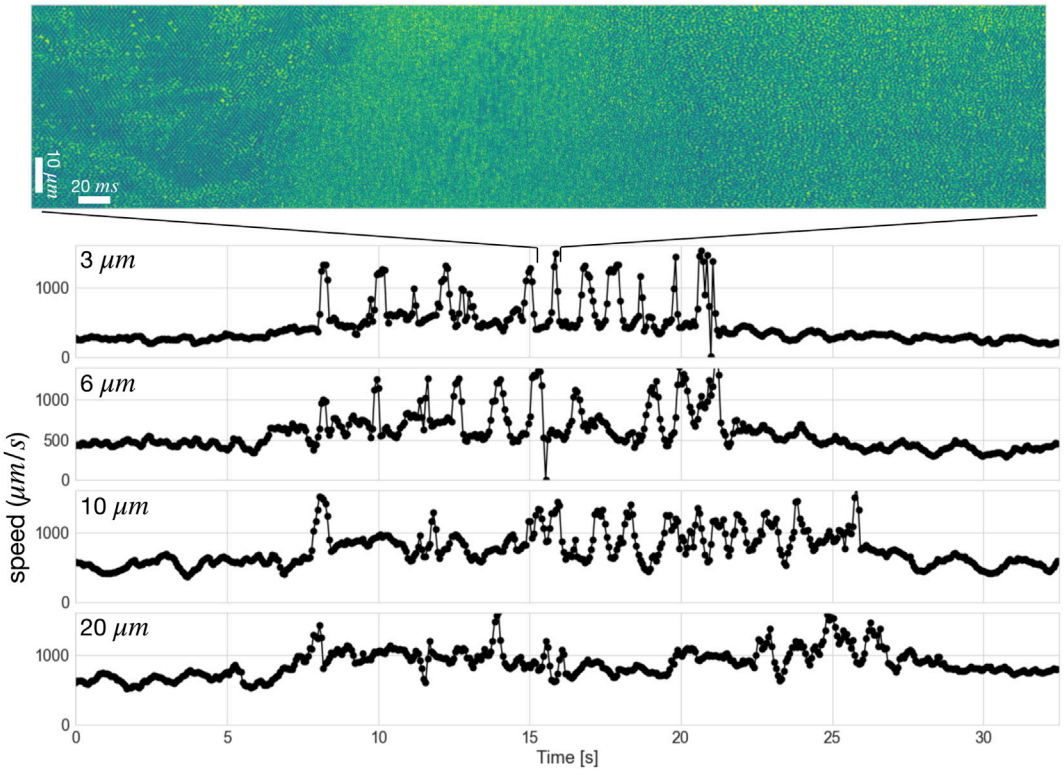

FIGURE 11
Timeseries of speed for 100 Pa applied stress at heights of 3, 6, 10, and 20 μm during one burst of high speed events. The image shows a kymograph from a single event. The initial times are shifted so the bursts start at approximately the same time.

evidenced by a remarkably sharp boundary that extends primarily along the vorticity direction, but with some meandering in the flow direction, consistent with the fluctuations in boundary stress reported previously [35]. A complete absence of ordering and a significant increase in average intensity marks the period of high speed flow, suggesting a region of reduced particle concentration, although there are correlations between speed and intensity introduced by the instrumentation, and further calibration will be required to separate measurement effects from concentration when the speed variation is large. The transition back to lower speed flow is also quite rapid, but the hexagonal ordering takes longer to recover. These features are consistent across the high speed events, as shown by the time series of speed, c_6, and intensity at 3 μm (Supplementary Figure S2).

Also evident in Figure 10 is that the speed differential between the spikes and the background is smaller at larger z, indicating that the events represent a more dramatic speed-up close to the bottom boundary. Finally, the clusters appear to be more spread out at larger z. Since the periodicity is independent of z, the propagation speed of the clusters should be independent of z, so the spreading of the clusters with height suggests that the spatial extent of the region of high stress increases with depth.

We can use the clustering of high speed events in the velocity time series to quantify the region of "normal" flow, away from the events (the specific segmentation is shown in Supplementary Figure S3). Figure 12A shows the flow profile obtained during those time periods, and the overall shape closely matches that seen at lower stresses (Figure 8). The agreement is made more evident by scaling the measured speeds by the average shear rate as reported by the rheometer (Figure 12B), where all three profiles overlap, with no free parameters. Something very different happens during the high speed events. We find empirically that selecting the highest 60 speeds from the 3,900 measurement points provides a reasonable measure of the peak speeds during the high speed events (Supplementary Figure S4), and we find that the average of those top speeds is nearly height independent (Figure 12). Scaling the peak speeds by average the speed of the top plate shows that the height-independent speed is on the order of v_p, consistent with a solid jammed aggregate moving with the speed of the top plate, perhaps with some slip (Note however, as discussed below, that the high speed events are quite likely associated with substantial non-affine flows, and thus it is possible that flows in the gradient direction contribute to the decay of the correlation and thus to the calculated speed.) Imaging of the bottom layer of

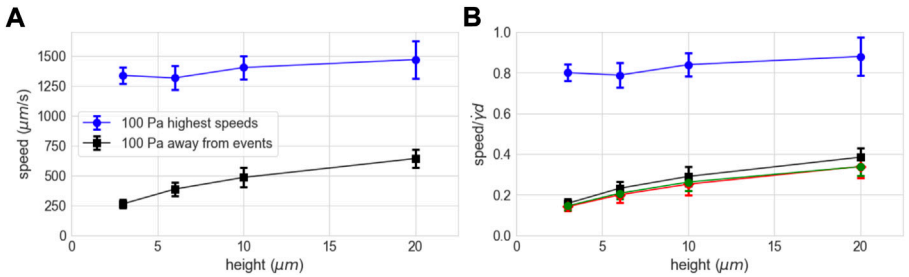

FIGURE 12
(A) Average speed at different heights from portions of the time series away from the high speed events, and average speed for the highest speeds in each time series (N = 60). **(B)** Data in **(A)** scaled by the speed of the top plate, with the scaled profiles from 20 to 50 Pa for comparison (Figure 8A).

particles confirms that the high speed fluctuations are associated with large slip of that layer. Those apparent aggregates are intertwined with regions of the suspension where the particles are flowing much slower (Figure 11), which is inconsistent with a single solid aggregate. These results provide the first direct measurements of the structure of the velocity field inside of high stress fluctuations in shear thickening suspensions.

4 Discussion

4.1 Order and concentration fluctuations before the onset of shear thickening

The dynamics revealed by high speed linescan imaging presented above are consistent with previous observations of boundary induced ordering in sheared dense monodisperse suspensions, but provide a more detailed picture of the spatiotemporal dynamics and demonstrate the presence of a strong connection between ordering and concentration fluctuations. Planar boundaries enhance layering in colloidal suspensions, and the layering can reduces viscous dissipation, producing shear banding [12, 16, 20]. Hexagonal ordering of monodisperse particles within layers of sheared suspension has also been seen in a variety of circumstances, starting with the seminal work of Ackerson and coworkers [4, 45]. Particularly relevant to this work, an imaging study by Wu et al. observed fluctuation in hexagonal ordering during the process of shear-induced melting in a confined suspension arising from the nucleation of localized domains that temporarily lost and regained their ordered structure [6]. Similar behavior has been reproduced in computer simulations [12, 17]. Recent simulation results reported that defects in crystalline order are associated with local decrease in particle concentration [20]. It is perhaps not surprising that the interplay between shear flow, crystal nucleation, and shear-induced crystal breakup produces a complex phase diagram with complex dynamics [3]. Here we show that for a monodisperse suspension at high packing fraction and high Peclet number ($Pe \sim 50$Figure 60), the transition from mostly ordered to mostly disordered occurs ~ 10 particle diameters from the boundary (Figure 8), and is associated with rapid temporal fluctuations in order, speed, and concentration (Figure 6). The concentration fluctuations are particularly significant, because the local increase in particle concentration seen in ordered domains requires an compensating decrease in solvent concentration, which implies the existence of local fluid migration. These results indicate that an accurate quantitative model for ordering fluctuations in sheared monodisperse suspensions at high Peclet number must include the flow and pore pressure fields responsible for relative flow between the particulate and fluid phases [30, 34, 46, 47].

4.2 Fluctuations associated with high local stresses during shear thickening

The high speed imaging approach employed here has revealed that localized high boundary stresses are accompanied by large rapid speed increases near the boundary, as well as a loss of order (Figure 11). Recent simulation results showed that the transition from hydrodynamic to frictional interparticle interactions that is believed to underlie strong shear thickening [18] is associated with a disruption of layering and ordering [20]. It seems likely that we are observing a similar transition, from relatively low stress, lubricated particle interactions producing layered, ordered low viscosity flow, to high stress, frictional particle interactions producing high viscosity disordered flow in the regions that produce high boundary stress. This transition appears to be remarkably sharp, with a boundary that is only a few particles wide (Figure 11, top). Also remarkable is the observation that the particle speeds during these events are independent of depth (Figure 12). This suggests that the particles are moving together,

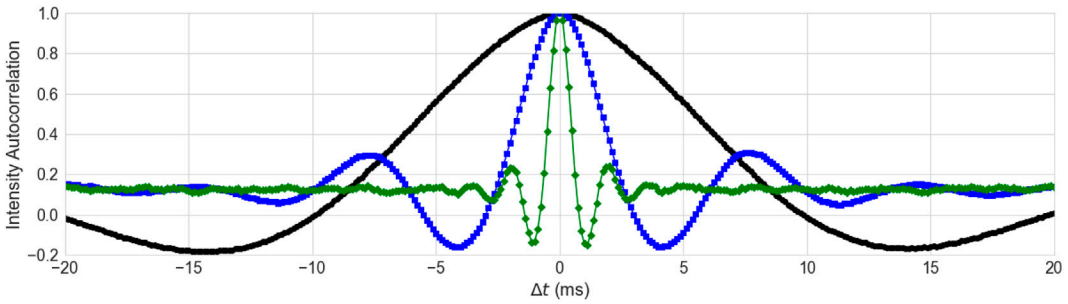

FIGURE 13
Normalized intensity autocorrelation function $g(\Delta t)$ as defined in Methods for the three kymographs shown in Figure 2, $\dot{\gamma} = 10\ s^{-1}$, $z = 3\ \mu m$ (○), $\dot{\gamma} = 20\ s^{-1}$, $z = 6\ \mu m$ (■), and $\dot{\gamma} = 30\ s^{-1}$, $z = 20\ \mu m$ (◆). The width of the central peak and the position of the first minimum are proportional to the flow speed, for fixed positional configurations, but both measures are have a some sensitivity to the presence of positional order.

as a jammed aggregate, similar to the model proposed to explain propagating high normal stresses observed in cornstarch suspensions [29]. It is important to note, however, that the linescan measurements performed here do not distinguish between flow components perpendicular to the scan direction (i.e. in the flow or gradient directions). As discussed above, under usual flow conditions the component of the velocity in the flow direction, of order $\dot{\gamma}z$, will be large compared to any non-affine flows, but the transient jamming observed during shear thickening is clearly unusual, so more complicated large-scale non-affine flows are likely. Further measurements, for example addinge measurements with linescans oriented in the flow direction, are needed to get a clearer picture of the flow profile during the high stress events.

More generally, measurements of nearly affine flow away from the localized high stresses, both in this system and in cornstarch [34], combined with the rapid fluctuation in velocity measured during the clusters of events (Figure 11), suggests a complicated flow field. Furthermore, although instrumental effect preclude a direct measurement of particle concentration during the high speed events, the longstanding connection between frictional interactions and dilatancy [18], evidenced by our observation of fluid migration associated with high stress fluctuations in cornstarch suspensions [34], suggests that relative flow between the particulate and fluid phases likely plays an important role in the observed speed fluctuations.

These observations contribute to a growing body of evidence indicating that the shear thickening transitions typically involved complex spatiotemporal dynamics with structures propagating in the flow direction, including dilatant fronts [23, 25], local deformations of the air-sample interface at the edge of the rheometer tool [26, 30], local normal stresses in sheared cornstarch [29], concentration fluctuations appearing as periodic waves moving in the direction of flow [28], and high shear stress at the suspension boundary [31, 32, 34, 35]. The specifics of the dynamics vary considerably, presumably indicating a sensitivity to the details of the suspension and the measurement geometry. This sensitivity is perhaps not surprising, given that shear thickening involves instabilities that can produce discontinuities in material parameters. The location of those discontinuities in a uniform extended system represent a broken symmetry, and thus in any physical realization will be very sensitive to the parameter variations (e.g. of shear rate, rheometer gap, distance from suspension boundary) that are present in all experimental systems.

Here we have presented an initial application of a powerful new approach that reveals spatiotemporal dynamics of sheared dense suspensions with high spatial and temporal resolution. With further testing and validation the approach has the potential to provide accurate and precise measurements of local speed, structure, and particle concentration, and should provide a new avenue to answer open questions about dense suspensions under flow.

5 Methods

All experimental suspensions were composed of 0.9 μm silica beads (Bang's Lab) in an index-matched (80/20 v/v) glycerol/water mixture. For imaging purposes, fluorescein sodium salt was added to the suspension so that the unlabeled spheres could be imaged as dark spots in a fluorescent background. Rheological measurements were performed on a stress-controlled rheometer (Anton Paar MCR 301) mounted on an inverted confocal (Leica SP5) microscope [35] using a cone-plate geometry with a diameter 25 mm. The linescan data was acquired with a ×60 objective at a radius of 2/3 of the plate diameter, where the rheometer gap is $d \approx 145\ \mu m$.

Linescan analysis: A typical data set is composed of a one to two million scans, with the scan direction aligned along the vorticity axis (perpendicular to the flow and the gradient). For visualization, we typically divide the set into a series of 2D arrays,

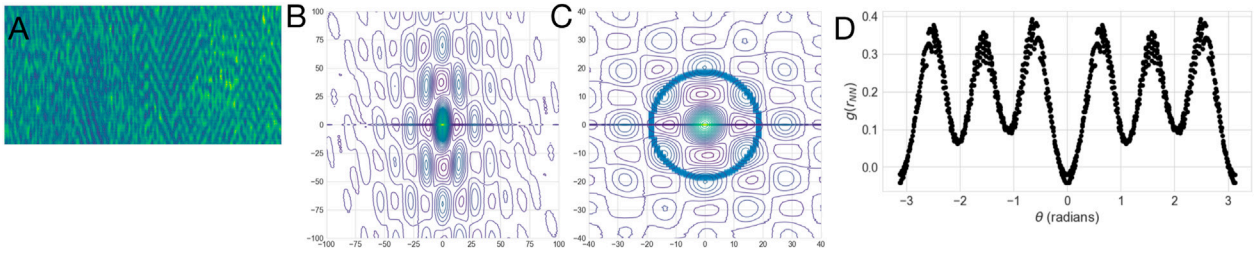

FIGURE 14
(A) Example kymograph showing moderate hexagonal ordering. **(B)** Two-dimensional autocorrelation of **(A)**, with the central region used to determine the peak widths highlighted. **(C)** 2D autocorrelation with vertical distances rescaled so that the central peak is circularly symmetric. The ring represents points whose distance from the origin is equal to the expected average inter-particle spacing. **(D)** Intensity as a function of angle for the ring of points identified in **(C)**, resulting in a C_6 with magnitude 0.36 and angle 0.03 radians.

with one dimension (horizontal) given by the number of pixels per scan (here 1,024), and the other dimension (vertical) given by the chosen number of scans per image, in this case 512 scans. Figure 14A shows an example image generated from 1 μm diameter non-fluorescent spheres in a fluorescent bFigure 5ackground, 10 μm above the bottom of the sheared suspension, similar to those shown in Figure 5. Individual particles show up as dark ovals. In principle, the vertical axis of each oval could be used to measure the speed of each particle. In practice, in many places identifying individual particles is challenging, and we have found correlation analyses more reliable (This arises in part because we have no control of the position of particles relative to the plane of focus, and the image will include contributions from particles that are $\approx$ 1 μm above or below the focal plane). Note also that the orientation of the ovals provides a measure for the component of the flow in the vorticity direction. Here that component is always small, and is not included in our analysis. An alternative approach, not employed here, would be to orient the scan line along the flow direction. This would enable very precise measurements of flow speed, as particles move along the line, but would not reveal spatial structure in the flow-vorticity plane.

One approach to extract a characteristic transit time from the linescan intensity data, $I(x, t)$, is to calculate the autocorrelation in the time direction, $g(\Delta t) = <\delta I(x, t)\delta I(x, t + \Delta t)>_{x,t}/<\delta I(x,t)^2>_{x,t}$, where $\delta I(x, t) = I(x, t) - <I(x, t)>_{x,t}$. The range of x and t to include in the averages can be varied depending on the spatial and temporal resolution required by the effective particle size. Slower shear rates require averaging over larger time windows so as to capture at least one full particle transit. For the conditions in this study we found that 512 scans provides enough data for robust correlation analysis while still allowing adequate temporal resolution. Figure 13 shows $g(\Delta t)$ for the three images displayed in Figure 2.

The location of the first minimum in the autocorrelation, $t_{\min}$ can be precisely identified algorithmically, and provides a measure that is proportional to the speed of the flow. We expect that $v_{flow} = l_{flow}/2t_{\min}$, where l_{flow} is approximately equal to the spacing between particles in the flow direction. More precisely, l_{flow} should be equal to the first minimum in the average instatntaneous density autocorrelation calculated along the flow axis. Unfortunately that quantity is unknown. Assuming it does not change with time, $v_{flow} \propto 1/t_{\min}$. Similarly, the minimum of the autocorrelation in the space direction provides a direct measure of the spacing in the x (vorticity) direction, specifically $l_{vorticity} = 2x_{\min}$. We find that this measure does not depend directly on the flow speed, but is quite sensitive to local hexagonal ordering. In part because of this sensitivity, and in part because we are interested in quantitative measures of hexagonal order, we have instead employed a slightly more complex analysis approach based on the 2D autorcorrelation function, but we have found that the speed variations are essentially indistinguishable from those calculated with the 1D correlation analysis.

Using a 2D correlation analysis, we can quantify the hexagonal order that is evident in Figure 14A. It is important to remember that the image is not a snapshot of the two-dimensional particle arrangement, as the top of the image is generated at an earlier time than the bottom. However, if the structure of the suspension evolves slowly compared to the time to generate an image, it will in fact be an accurate representation of the spatial arrangement of the particles, with the vertical separations expanded (or compressed) by a factor $\alpha = (s \cdot d)/v_{flow}$, where s is the scan rate, d is the actual spatial separation, and v is the speed of the flow. Figure 14B shows a contour plot of the two-dimensional spatial autocorrelation, $G(\vec{r})$, of the image shown in A. The sixfold symmetry is evident, as is the expansion in the vertical direction. Note that $G(\vec{r})$ is large along the horizontal axis ($y = 0$). This is likely a consequence of fluctuations in the laser intensity on a sub-millisecond timescale. These fluctuations can be filtered out, but for our purposes it is sufficient to simply exclude the horizontal axis from our analysis of $G(\vec{r})$. Fitting the central peak of $G(\vec{r})$ (highlighted region in Figure 14B) to a 2D Gaussian provides an accurate measure of the width in the flow direction, Δy (number of scan lines) which in inversely proportional to the speed, $v_{flow} = \delta \cdot s/\Delta y$. Determining the scale factor δ, the width of the central peak in $G(\vec{r})$ in physical units, is a significant source of

uncertainty in the measurement. The particle diameter is known precisely, but δ also depends on the particle separation, and is also somewhat sensitive to the degree of order. We have estimated δ from looking at $G(x)$ (the correlation along the scan direction) in flows with no detectable order, where we find that the peak width is 0.2 times the distance to the first peak in $G(x)$. Assuming the first peak in G(x) is at a location $d_{peak} = d_{particle}/\phi^{-1/3} \approx 1.2^{*}d_{particle}$, we find $\delta \approx 1.2^{*}d_{particle}/5$. This conversion enables us to provide speed measurements in physical units, but further tests will be required to validate the accuracy of the results. For the measurements described here, the ~ 10% uncertainty in the exact value of the proportionality constant does not impact the conclusions, but systematic effects of ordering on Δy may impact some results, e.g. the apparent correlation between order and speed in the measurements at 20 Pa.

Using the measured width Δy, we can rescale the flow direction to produce a symmetric $G(\vec{r})$. Figure 14C shows a contour plot of the rescaled $G(\vec{r})$, and thus represents our measure of the average spatial structure of the imaged region. In the results presented below, we are primarily interested in measuring the degree of hexagonal order in the suspension. We can quantify this by measuring the intensity as a function of angle at a distance r_{NN} from the origin, where r_{NN} is the position of the first maximum in $G(r)$, approximately the average nearest neighbor separation. The points included in the calculation of are highlighted in Figure 14, and the resulting data $G(r_{NN}, \theta)$ is shown in Figure 14D. A complex scaler C_6 representing the hexagonal order can be calculated according to

$$C_6 = \frac{\int_0^{2\pi} G(r_{NN}, \theta)\exp^{-i6\theta}\, d\theta}{\int_0^{2\pi} G(r_{NN}, \theta) d\theta}. \quad (1)$$

Boundary stress microscopy. BSM measurements (Figure 9 were performed as described in [32, 35], but employing elastic films of relatively high modulus ($G \sim 1\ MPa$) to minimize possible effects of boundary compliance. Briefly, elastic films thickness 50 ± 3 μm were deposited by spin coating PDMS (Sylgard 184; Dow Corning) and a curing agent on 40 mm diameter glass cover slides (Fisher Sci) that were cleaned thoroughly by plasma cleaning and rinsing with ethanol and deionized water [35]. After deposition of PDMS, the slides were cured at 85 °C for 2 h. After curing, the PDMS was functionalized with 3-aminopropyl triethoxysilane (Fisher Sci) using vapor deposition for 40 min. Carboxylate-modified fluorescent spherical beads of radius 0.5 μm with excitation/emission at 520/560 nm were attached to the PDMS surface. Before attaching the beads to functionalized PDMS, the beads were suspended in a solution containing PBS solution (Thermo-Fisher). The concentration of beads used was 0.006% solids. The surface stresses at the interface were calculated using an extended traction force technique and codes given in Ref. [48]. Taking the component of the surface stress in the flow (velocity) direction, we obtain the scalar field $\sigma_{BSM}(\vec{r}, t)$, representing the spatiotemporally varying surface stress. The data shown in Figure 9 are a spatial average of each field, $< \sigma_{BSM}(\vec{r}, t) >_t$.

Data availability statement

The original contributions presented in the study are included in the article/Supplementary Material, further inquiries can be directed to the corresponding author.

Author contributions

JM, DB, and JU designed research; JM performed research; JM, DB, and JU analyzed data; and JM, DB, and JU wrote the paper.

Funding

This work was supported by the National Science Foundation (NSF) under Grant No. DMR-1809890. JU is supported, in part, by the Georgetown Interdisciplinary Chair in Science Fund.

Acknowledgments

The authors thank Peter Olmsted and Emanuela Del Gado for helpful discussions.

Conflict of interest

The authors declare that the research was conducted in the absence of any commercial or financial relationships that could be construed as a potential conflict of interest.

Publisher's note

Supplementary material

The Supplementary Material for this article can be found online at: https://www.frontiersin.org/articles/10.3389/fphy.2022.991540/full#supplementary-material

References

1. Vermant J, Solomon MJ. Flow-induced structure in colloidal suspensions. *J Phys : Condens Matter* (2005) 17:R187–216. doi:10.1088/0953-8984/17/4/r02

2. Morris JF. A review of microstructure in concentrated suspensions and its implications for rheology and bulk flow. *Rheol Acta* (2009) 48:909–23. doi:10.1007/s00397-009-0352-1

3. Lettinga MP. Fluids, colloids and soft materials: An introduction to. *Soft Matter Phys* (2016) 2016:81–110. doi:10.1002/9781119220510.ch6

4. Chen LB, Zukoski CF, Ackerson BJ, Hanley HJM, Straty GC, Barker J, et al. Structural changes and orientaional order in a sheared colloidal suspension. *Phys Rev Lett* (1992) 69:688–91. doi:10.1103/physrevlett.69.688

5. Holmqvist P, Lettinga MP, Buitenhuis J, Dhont JKG. Crystallization kinetics of colloidal spheres under stationary shear flow. *Langmuir* (2005) 21:10976–82. doi:10.1021/la051490h

6. Wu YL, Derks D, Blaaderen A, Imhof A. Melting and crystallization of colloidal hard-sphere suspensions under shear. *Proc Natl Acad Sci U S A* (2009) 106:10564–9. doi:10.1073/pnas.0812519106

7. Derks D, Wu YL, Blaaderen AV, Imhof A. Dynamics of colloidal crystals in shear flow. *Soft Matter* (2009) 5:1060–5. doi:10.1039/b816026k

8. Richard D, Speck T. The role of shear in crystallization kinetics: From suppression to enhancement. *Sci Rep* (2015) 5:14610. doi:10.1038/srep14610

9. Shereda LT, Larson RG, Solomon MJ. Boundary-driven colloidal crystallization in simple shear flow. *Phys Rev Lett* (2010) 105:228302. doi:10.1103/physrevlett.105.228302

10. Cheng X, Xu X, Rice SA, Dinner AR, Cohen I. Assembly of vorticity-aligned hard-sphere colloidal strings in a simple shear flow. *Proc Natl Acad Sci U S A* (2012) 109:63–7. doi:10.1073/pnas.1118197108

11. Xu X, Rice SA, Dinner AR. Influence of interlayer exchanges on vorticity-aligned colloidal string assembly in a simple shear flow. *J Phys Chem Lett* (2013) 4:3310–5. doi:10.1021/jz401722j

12. Mackay FE, Pastor K, Karttunen M, Denniston C. Modeling the behavior of confined colloidal particles under shear flow. *Soft Matter* (2014) 10:8724–30. doi:10.1039/c4sm01812e

13. Villada-Balbuena A, Jung G, Zuccolotto-Bernez AB, Franosch T, Egelhaaf SU. Layering and packing in confined colloidal suspensions. *Soft Matter* (2022) 18:4699–714. doi:10.1039/d2sm00412g

14. Kulkarni SD, Morris JF. Ordering transition and structural evolution under shear in Brownian suspensions. *J Rheology* (2009) 53:417–39. doi:10.1122/1.3073754

15. Pieper S, Schmid HJ. Layer-formation of non-colloidal suspensions in a parallel plate rheometer under steady shear. *J Non-Newtonian Fluid Mech* (2016) 234:1–7. doi:10.1016/j.jnnfm.2016.04.004

16. Küçüksönmez E, Servantie J. Shear thinning and thickening in dispersions of spherical nanoparticles. *Phys Rev E* (2020) 102:012604. doi:10.1103/physreve.102.012604

17. Myung JS, Song S, Ahn KH. Dynamics of model-stabilized colloidal suspensions in confined Couette flow. *J Non-Newtonian Fluid Mech* (2013) 199:29–36. doi:10.1016/j.jnnfm.2013.06.004

18. Morris JF. Shear thickening of concentrated suspensions: Recent developments and relation to other phenomena. *Annu Rev Fluid Mech* (2020) 52:121–44. doi:10.1146/annurev-fluid-010816-060128

19. Lee J, Jiang Z, Wang J, Sandy AR, Narayanan S, Lin XM. Unraveling the role of order-to-disorder transition in shear thickening suspensions. *Phys Rev Lett* (2018) 120:028002. Not sure what this means. doi:10.1103/PhysRevLett.120.028002

20. Goyal A, Gado ED, Jones SZ, Martys NS. Ordered domains in sheared dense suspensions: The link to viscosity and the disruptive effect of friction. *J Rheology* (2022) 66:1055–65. doi:10.1122/8.0000453

21. Boersma WH, Baets PJM, Laven J, Stein HN. Time-dependent behavior and wall slip in concentrated shear thickening dispersions. *J Rheology* (1991) 35:1093–120. doi:10.1122/1.550167

22. Lootens D, Damme H, Hébraud P. Giant stress fluctuations at the jamming transition. *Phys Rev Lett* (2003) 90:178301. doi:10.1103/PhysRevLett.90.178301

23. Nakanishi H, Si N, Mitarai N. Fluid dynamics of dilatant fluids. *Phys Rev E* (2012) 85:011401. doi:10.1103/PhysRevE.85.011401

24. Guy BM, Hermes M, Poon WCK. Towards a unified description of the rheology of hard-particle suspensions. *Phys Rev Lett* (2015) 115:088304. doi:10.1103/physrevlett.115.088304

25. Nagahiro SI, Nakanishi H. Negative pressure in shear thickening band of a dilatant fluid. *Phys Rev E* (2016) 94:062614. doi:10.1103/PhysRevE.94.062614

26. Hermes M, Guy BM, Poon WCK, Poy G, Cates ME, Wyart M. Unsteady flow and particle migration in dense, non-Brownian suspensions. *J Rheology* (2016) 60:905–16. doi:10.1122/1.4953814

27. Saint-Michel B, Gibaud T, Manneville S. Uncovering instabilities in the spatiotemporal dynamics of a shear-thickening cornstarch suspension. *Phys Rev X* (2018) 8:031006. doi:10.1103/PhysRevX.8.031006

28. Ovarlez G, Le AVN, Smit WJ, Fall A, Mari R, Chatté G, et al. Density waves in shear-thickening suspensions. *Sci Adv* (2020) 6:eaay5589. doi:10.1126/sciadv.aay5589

29. Gauthier A, Pruvost M, Gamache O, Colin A. A new pressure sensor array for normal stress measurement in complex fluids. *J Rheology* (2021) 65:583–94. doi:10.1122/8.0000249

30. Maharjan R, O'Reilly E, Postiglione T, Klimenko N, Brown E. Relation between dilation and stress fluctuations in discontinuous shear thickening suspensions. *Phys Rev E* (2021) 103:012603. doi:10.1103/physreve.103.012603

31. Rathee V, Blair DL, Urbach JS. Dynamics and memory of boundary stresses in discontinuous shear thickening suspensions during oscillatory shear. *Soft Matter* (2020) 17:1337–45. doi:10.1039/d0sm01917h

32. Rathee V, Blair DL, Urbach JS. Localized transient jamming in discontinuous shear thickening. *J Rheology* (2020) 64:299–308. doi:10.1122/1.5145111

33. Rathee V, Arora S, Blair DL, Urbach JS, Sood AK, Ganapathy R. Role of particle orientational order during shear thickening in suspensions of colloidal rods. *Phys Rev E* (2020) 101:040601. doi:10.1103/physreve.101.040601

34. Rathee V, Miller J, Blair DL, Urbach JS. Localized stress fluctuations drive shear thickening in dense suspensions. *Proc Natl Acad Sci U S A* (2022) 114:8740–5. doi:10.1073/pnas.1703871114

35. Dutta SK, Mbi A, Arevalo RC, Blair DL. Development of a confocal rheometer for soft and biological materials. *Rev Sci Instrum* (2013) 84:063702. doi:10.1063/1.4810015

36. Besseling R, Isa L, Weeks ER, Poon WC. Quantitative imaging of colloidal flows. *Adv Colloid Interf Sci* (2009) 146:1–17. doi:10.1016/j.cis.2008.09.008

37. Taylor GI. The spectrum of turbulence. *Proc R Soc Lond A* (1938) 164:476–90. doi:10.1098/rspa.1938.0032

38. He G, Jin G, Yang Y. Space-time correlations and dynamic coupling in turbulent flows. *Annu Rev Fluid Mech* (2017) 49:51–70. doi:10.1146/annurev-fluid-010816-060309

39. Koynov K, Butt HJ. Fluorescence correlation spectroscopy in colloid and interface science. *Curr Opin Colloid Interf Sci* (2012) 17:377–87. doi:10.1016/j.cocis.2012.09.003

40. Dong C, Ren J. Coupling of fluorescence correlation spectroscopy with capillary and microchannel analytical systems and its applications. *ELECTROPHORESIS* (2014) 35:2267–78. doi:10.1002/elps.201300648

41. Kunst BH, Schots A, Visser AJWG. Detection of flowing fluorescent particles in a microcapillary using fluorescence correlation spectroscopy. *Anal Chem* (2002) 74:5350–7. doi:10.1021/ac0256742

42. Gösch M, Blom H, Holm J, Heino T, Rigler R. Hydrodynamic flow profiling in microchannel structures by single molecule fluorescence correlation spectroscopy. *Anal Chem* (2000) 72:3260–5. doi:10.1021/ac991448p

43. Pan X, Yu H, Shi X, Korzh V, Wohland T. Characterization of flow direction in microchannels and zebrafish blood vessels by scanning fluorescence correlation spectroscopy. *J Biomed Opt* (2007) 12:014034. doi:10.1117/1.2435173

44. Pan X, Shi X, Korzh V, Yu H, Wohland T. Line scan fluorescence correlation spectroscopy for three-dimensional microfluidic flow velocity measurements. *J Biomed Opt* (2009) 14:024049. doi:10.1117/1.3094947

45. Ackerson BJ. Shear induced order and shear processing of model hard sphere suspensions. *J Rheology* (1990) 34:553–90. doi:10.1122/1.550096

46. Meer D. Impact on granular beds. *Annu Rev Fluid Mech* (2016) 49:463–84. doi:10.1146/annurev-fluid-010816-060213

47. O'Neill RE, Royer JR, Poon WCK. Liquid migration in shear thickening suspensions flowing through constrictions. *Phys Rev Lett* (2019) 123:128002. doi:10.1103/physrevlett.123.128002

48. Style RW, Boltyanskiy R, German GK, Hyland C, MacMinn CW, Mertz AF, et al. Traction force microscopy in physics and biology. *Soft Matter* (2014) 10:4047. doi:10.1039/c4sm00264d

frontiers | Frontiers in Physics

TYPE Original Research
PUBLISHED 18 November 2022
DOI 10.3389/fphy.2022.1055441

OPEN ACCESS

EDITED BY
Roberto Cerbino,
University of Vienna, Austria

REVIEWED BY
Fabio Giavazzi,
University of Milan, Italy
Paolo Malgaretti,
Helmholtz Institute Erlangen-Nürnberg, Germany

*CORRESPONDENCE
Janet Y. Sheung,
jsheung@scrippscollege.edu

SPECIALTY SECTION
This article was submitted to Soft Matter Physics,
a section of the journal
Frontiers in Physics

RECEIVED 27 September 2022
ACCEPTED 31 October 2022
PUBLISHED 18 November 2022

CITATION
Sheung JY, Garamella J, Kahl SK, Lee BY, McGorty RJ and Robertson-Anderson RM (2022), Motor-driven advection competes with crowding to drive spatiotemporally heterogeneous transport in cytoskeleton composites.
Front. Phys. 10:1055441.
doi: 10.3389/fphy.2022.1055441

Motor-driven advection competes with crowding to drive spatiotemporally heterogeneous transport in cytoskeleton composites

Janet Y. Sheung[1,2]*, Jonathan Garamella[3], Stella K. Kahl[1], Brian Y. Lee[2], Ryan J. McGorty[3] and Rae M. Robertson-Anderson[3]

[1]W. M. Keck Science Department, Scripps College, Claremont, CA, United States, [2]W. M. Keck Science Department, Pitzer College, Claremont, CA, United States, [3]Physics and Biophysics Department, University of San Diego, San Diego, CA, United States

The cytoskeleton—a composite network of biopolymers, molecular motors, and associated binding proteins—is a paradigmatic example of active matter. Particle transport through the cytoskeleton can range from anomalous and heterogeneous subdiffusion to superdiffusion and advection. Yet, recapitulating and understanding these properties—ubiquitous to the cytoskeleton and other out-of-equilibrium soft matter systems—remains challenging. Here, we combine light sheet microscopy with differential dynamic microscopy and single-particle tracking to elucidate anomalous and advective transport in actomyosin-microtubule composites. We show that particles exhibit multi-mode transport that transitions from pronounced subdiffusion to superdiffusion at tunable crossover timescales. Surprisingly, while higher actomyosin content increases the range of timescales over which transport is superdiffusive, it also markedly increases the degree of subdiffusion at short timescales and generally slows transport. Corresponding displacement distributions display unique combinations of non-Gaussianity, asymmetry, and non-zero modes, indicative of directed advection coupled with caged diffusion and hopping. At larger spatiotemporal scales, particles in active composites exhibit superdiffusive dynamics with scaling exponents that are robust to changing actomyosin fractions, in contrast to normal, yet faster, diffusion in networks without actomyosin. Our specific results shed important new light on the interplay between non-equilibrium processes, crowding and heterogeneity in active cytoskeletal systems. More generally, our approach is broadly applicable to active matter systems to elucidate transport and dynamics across scales.

KEYWORDS

fluorescence microscopy, myosin, single-particle tracking, differential dynamic microscopy, cytoskeleton, actin, microtubule

1 Introduction

The cytoplasm is a crowded, heterogeneous, out-of-equilibrium material through which macromolecules and vesicles traverse to perform critical cellular processes such as mitosis, endocytosis, migration, and regeneration [1–4]. Macromolecules and particles diffusing through the cytoplasm and other similar materials have been shown to exhibit widely varying and poorly understood anomalous transport properties that deviate significantly from normal Brownian diffusion. In particular, the mean-squared displacement, *MSD*, often does not scale linearly with lag time Δt, but is instead better described by $MSD \sim \Delta t^{\alpha}$ where $\alpha < 1$ or $\alpha > 1$ for subdiffusion or superdiffusion, respectively. The distributions of displacements (i.e., van Hove distributions) also often deviate from Gaussianity and can display exponential tails at large displacements [5–8]. The cytoskeleton–an active composite of filamentous proteins including actin, microtubules, and intermediate filaments, along with their associated motor proteins–plays a key role in these observed anomalous transport properties [9–11]. Such anomalous transport phenomena are not just observed in cytoskeleton, but are ubiquitous in numerous other active and crowded soft matter systems, making their characterization and understanding of broad interest.

In steady-state, the thermal transport of particles through *in vitro* cytoskeletal systems exhibit varying degrees of subdiffusion and non-Gaussianity depending on the types and concentrations of filaments and crosslinking proteins [5, 6, 12, 13]. For example, single-particle tracking (SPT) of particles in composites of entangled actin filaments and microtubules, has revealed increasing degrees of subdiffusion (α decreasing from ~0.95 to ~0.58) as the molar ratio of semiflexible actin filaments to rigid microtubules increased [6]. The corresponding SPT van Hove distributions were reported to be non-Gaussian, displaying larger than expected probabilities for very small and large displacements, indicative of particles being caged in the filament mesh and hopping between cages.

Differential dynamic microscopy (DDM), which uses Fourier-space analysis to measure the timescales over which particle density fluctuations decay, has also been used to measure transport and quantify anomalous characteristics over larger spatiotemporal scales compared to SPT [5, 14, 15].

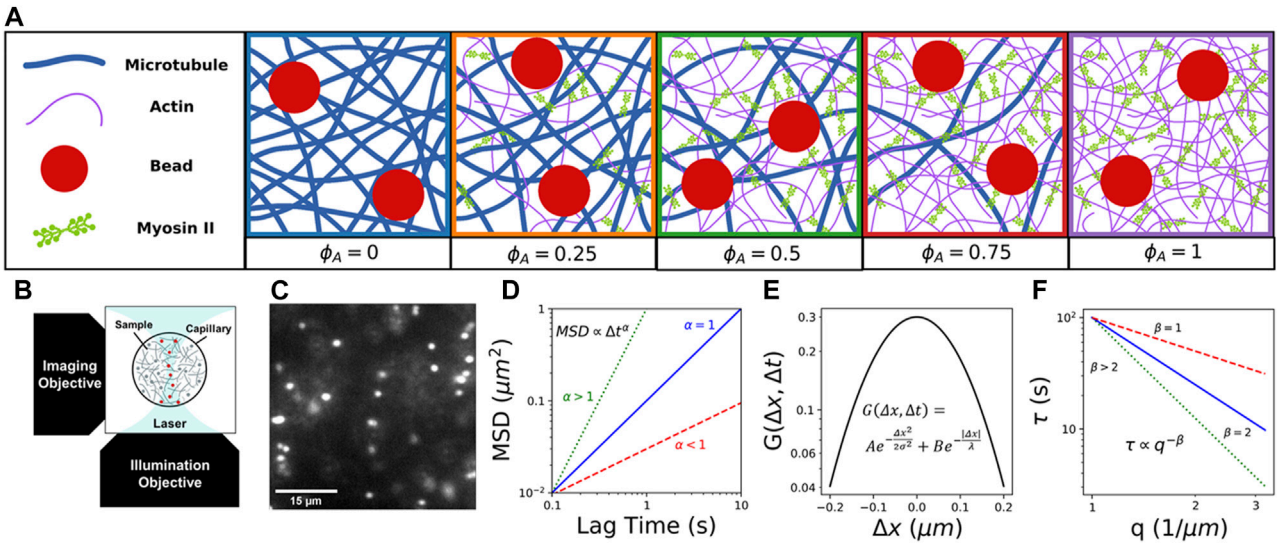

FIGURE 1
Combining light sheet microscopy with real-space single-particle tracking (SPT) and reciprocal-space differential dynamic microscopy (DDM) to characterize particle transport in active cytoskeletal composites. **(A)** We create composites of co-entangled microtubules (blue) and actin filaments (purple) driven out-of-equilibrium by myosin II minifilaments (green). We track the motion of embedded 1 μm beads (red) in composites with varying molar fractions of actomyosin, which we denote by the fraction of actin comprising the combined molar concentration of actin and tubulin (5.8 μM): ϕ_A = 0. 0.25, 0.5, 0.75, 1. In all cases, the molar ratio of myosin to actin is fixed at 0.08. **(B)** Schematic of the light-sheet microscope we use for data collection, which provides the necessary optical sectioning to capture dynamics in dense three-dimensional samples. **(C)** Example frame from time-series of 1 μm beads embedded in a cytoskeleton composite, used to characterize particle transport in active crowded systems. **(D)** Cartoon of expected mean-squared displacements (*MSD*) of embedded particles *versus* lag time Δt, which we compute *via* single-particle tracking (SPT) and fit to a power law $MSD \tilde{\Delta} t^{\alpha}$ to determine the extent to which particles exhibit normal Brownian diffusion ($\alpha = 1$, blue), subdiffusion ($\alpha < 1$, red), or superdiffusion ($\alpha > 1$, green). **(E)** Cartoon van Hove distribution *G* of *x*- and *y*-direction particle displacements $\Delta d = \Delta x \cup \Delta y$ for a given lag time Δt computed from SPT trajectories. The distribution shown is described by a sum of a Gaussian and exponential function $G(\Delta d, \Delta t) = Ae^{-\Delta d^2/2\sigma^2} + Be^{-|\Delta d|/\lambda}$, as is often seen in crowded and confined systems and those that display heterogeneous transport. **(F)** Cartoon of expected characteristic decorrelation times $\tau(q)$ as a function of wave number *q*, which we compute by fitting the image structure function computed from DDM analysis. We determine the scaling exponent β from the power-law $\tau(q) \sim q^{-\beta}$ to determine if transport is diffusive ($\beta = 2$, blue), subdiffusive ($\beta > 2$, green), or ballistic ($\beta = 1$, red).

DDM analysis of a time-series of images provides a characteristic decay time τ as a function of the wave vector q which typically follows power-law scaling $\tau(q) \sim q^{-\beta}$ [15, 16], with β relating to the anomalous scaling exponent α *via* $\beta = 2/\alpha$. Specifically, $\beta = 2$, > 2, < 2 and 1 correspond to diffusive, subdiffusive, superdiffusive, and ballistic motion (Figure 1F). DDM analysis of actin-microtubule composites corroborated the SPT results described above, with subdiffusive β values tracking with α values [5, 6]. However, we note that while the relation $\beta = 2/\alpha$ can be used to directly compare dynamics measured *via* SPT and DDM, α derived from this relation may not match that determined from SPT, in particular for systems that display multiple dynamic regimes at different spatiotemporal scales.

Similar SPT and DDM experiments demonstrated that crosslinking of actin and/or microtubules introduced bi-phasic transport with the subdiffusive scaling exponents dropping from $\alpha \approx 0.5$–0.7 to $\alpha \approx 0.25$–0.4 (depending on crosslinker type) after $\Delta t \approx 3$ s, due to strong caging and reduced thermal fluctuations of filaments. At the same time, van Hove distributions were well fit to a sum of a Gaussian and exponential, and the non-Gaussianity parameter increased, indicating enhanced heterogeneity [5, 6, 8, 12, 17].

Numerous studies have also investigated transport in non-equilibrium cytoskeleton networks, in which activity is introduced *via* motor proteins, such as actin-associated myosin II and microtubule-associated kinesin [2, 10, 18–21]. These studies have shown evidence of vesicle movement strongly tracking with actin movement, microtubule-dependent flow, and the simultaneous presence of subdiffusive and ballistic transport dynamics. While the majority of these active matter studies have been on systems of either actin or microtubules, recent studies have used DDM and optical tweezers microrheology to characterize the dynamics of actin-microtubule composites pushed out-of-equilibrium by myosin II minifilaments straining actin filaments [14, 22, 23]. These studies showed that active actin-microtubule composites exhibited ballistic-like ($\alpha \approx 2$) contractile motion, rather than randomly-oriented diffusion or subdiffusion, with speeds that increased with increasing fraction of actin in the composites, due to increased composite flexibility [14, 23]. Myosin-driven contractile motion and restructuring was also reported to increase viscoelastic moduli and relaxation timescales and induce clustering and increased heterogeneity of the initially uniform mesh [22].

However, particle transport through active actin-microtubule composites–likely dictated by the complex combination of active processes, crowding, and interactions between mechanically distinct filaments—has remained largely unexplored. The majority of studies that have examined the combined effect of activity and crowding have been *in vivo* [1, 24–29], where a large number of conflating variables that are difficult to tune make teasing out the effect of each contribution and mechanism highly non-trivial.

Here, we take advantage of the tunability of *in vitro* reconstituted cytoskeleton composites to systematically investigate the coupled effects of non-equilibrium activity, crowding, and heterogeneity on particle transport. We combine fluorescence light sheet microscopy (fLSM) with single-particle tracking (SPT) and differential dynamic microscopy (DDM) to examine the anomalous transport of micron-sized particles within active composites of myosin II minifilaments, actin filaments, and microtubules with varying molar fractions of actin and tubulin (Figure 1A). We leverage the optical sectioning and low excitation power of fLSM (Figure 1B) to capture particle trajectories with a temporal resolution of 0.1s for durations up to 400 s (Figure 1C). Using both SPT and DDM provides transport characterization over a broad spatiotemporal range that spans ~10^{-1} -10^{2} s and ~10^{-1} - 10 μm. From measured SPT trajectories, we compute ensemble-averaged *MSD*s and associated anomalous scaling exponents α (Figure 1D), as well as corresponding distributions of particle displacements, i.e., van Hove distributions (Figure 1E), for varying lag times Δt. To expand the spatiotemporal range of our measurements and provide an independent measure of transport characteristics, we use DDM to analyze particle density fluctuations in Fourier space, and evaluate the power-law dependence of decorrelation times τ on wave vector q, i.e., $\tau(q) \sim q^{-\beta}$ (Figure 1F).

2 Materials and methods

2.1 Protein preparation

We reconstitute rabbit skeletal actin (Cytoskeleton, Inc. AKL99) to 2 mg/ml in 5 mM Tris–HCl (pH 8.0), 0.2 mM $CaCl_2$, 0.2 mM ATP, 5% (w/v) sucrose, and 1% (w/v) dextran; porcine brain tubulin (Cytoskeleton T240) to 5 mg/ml in 80 mM PIPES (pH 6.9), 2 mM $MgCl_2$, 0.5 mM EGTA, and 1 mM GTP; and rabbit skeletal myosin II (Cytoskeleton MY02) to 10 mg/ml in 25 mM PIPES (pH 7.0), 1.25 M KCl, 2.5% sucrose, 0.5% dextran, and 1 mM DTT. We flash freeze all proteins in single-use aliquots and store at -80°C. We reconstitute the UV-sensitive myosin II inhibitor, (-)-blebbistatin (Sigma B0560) in anhydrous DMSO and store at -20°C for up to 6 months. Immediately prior to experiments, we remove enzymatically dead myosin II from aliquots using centrifugation clarification, as previously described [14, 22].

2.2 Composite network assembly

We prepare actin-microtubule composites by mixing actin monomers, tubulin dimers and a trace amount of 1 μm diameter carboxylated microspheres (Polysciences) in PEM-100 (100 mM PIPES, 2 mM $MgCl_2$, and 2 mM EGTA), 0.1% Tween-20, 1 mM ATP, and 1 mM GTP, and incubating at 37°C for 30 min to allow

for polymerization of actin filaments and microtubules. We coat microspheres (beads) with AlexaFluor594 BSA (Invitrogen) to visualize the particles and prevent nonspecific interactions with the composite [30, 31]. We fix the combined molar concentration of actin and tubulin to $c = c_A + c_T = 5.8\,\mu M$ and the ratio of myosin to actin to R=0.08, and vary the molar fraction of actin in the composite ($c_A/c = \phi_A$) from $\phi_A = 0$ to 1 in 0.25 increments (Figure 1A). To stabilize actin filaments and microtubules, we add an equimolar ratio of phalloidin to actin and a saturating concentration of Taxol (5 μM) [32, 33]. We add an oxygen scavenging system (45 μg/ml glucose, 0.005% β-mercaptoethanol, 43 μg/ml glucose oxidase, 7 μg/ml catalase) to inhibit photobleaching, and add 50 μM blebbistatin to control actomyosin activity.

2.3 Sample preparation and imaging

We pipet prepared composites into capillary tubing with an inner diameter of x=800 μm and length of y=10 mm, then seal with epoxy. Microspheres are imaged using a custom-built fLSM with a 10× 0.25 NA Nikon Plan N excitation objective, a 20× 1.0 NA Olympus XLUMPlanFLN detection objective, and an Andor Zyla 4.2 CMOS camera [5]. A 561 nm laser is formed into a sheet to image the microspheres, while a collimated 405 nm laser is used to deactivate the blebbistatin, thereby activating actomyosin activity. Each acquisition location is at least 1 mm away from the previous one to ensure that there is no myosin activity when the image acquisition begins. For SPT, we collect ≥15 time-series consisting of ≥2000 frames, each with a 1000×300 pixel (194×58 μm^2) field of view (FOV), at 10 frames per second (fps). For DDM, we collect ≥3 time-series of ≥4000 frames, each with a 768×266 pixel (149×52 μm^2) FOV, at 10 fps. The x and y axes of each FOV are aligned with the cross-section and length of the capillary sample chamber, respectively.

2.4 Single-particle tracking

We use the Python package Trackpy [34] to track particle trajectories and measure the x- and y- displacements $(\Delta x, \Delta y)$ of the beads as a function of lag times Δt = 0.1 s–50 s. From the particle displacements, we use a custom-written Python script to calculate the time-averaged mean-squared displacement of the ensemble, $MSD(\Delta t) = \frac{1}{2}\left([\Delta x(\Delta t)]^2 + [\Delta y(\Delta t)]^2\right)$, from which we compute anomalous scaling exponents, α, *via* $MSD \sim \Delta t^{\alpha}$ for each Δt range in which we observe a single power-law. We compute MSDs for lag times $\Delta t \leq 180$ s, but limit our power-law fitting to $\Delta t \leq 40$ s for $\phi_A = 0$ and $\Delta t \leq 100$ s for $\phi_A = 0.75$ and 1, as noise from low statistics dominates the data at larger lag times for these composites.

Additionally, we compute van Hove probability distributions of particle displacements, $G(\Delta d, \Delta t)$ (Figure 1E), where $\Delta d = \Delta x \cup \Delta y$, for 10 different lag times that span Δt = 0.1 s to 15 s. Following previous works [5–7], we fit each distribution for a given lag time to a sum of a Gaussian and exponential function: $G(\Delta d) = Ae^{-\Delta d^2/2\sigma^2} + Be^{-|\Delta d|/\lambda}$, where A is the amplitude of the Gaussian term, σ^2 is the variance, B is the amplitude of the exponential term, and λ is the exponential decay constant.

2.5 Differential dynamic microscopy

We obtain the image structure function $D(q, \Delta t)$, where q is the magnitude of the wave vector, following our previously described methods [12, 35]. We fit each image structure function, or DDM matrix, to the following function:

$$D(q,\Delta t) = A(q)\left[1 - \exp\left[-\left(\Delta t/\tau(q)\right)^{\gamma(q)}\right]\right] + B(q)$$

where $\tau(q)$ is the density fluctuation decay time, γ is the stretching exponent, A is the amplitude, and B is the background [5, 6]. In practice, we fit each $D(q,\Delta t)$ out to Δt = 100 s, beyond which noise due to low statistics dominates the signal. From the fits, we determine the q-dependent decay time $\tau(q)$, which is a measure of the timescale over which particle density fluctuations decorrelate over a given lengthscale $l = 2\pi/q$. By fitting $\tau(q)$ to a power-law (i.e., $\tau(q) \sim q^{-\beta}$) we determine the dominant mode of transport, with β = 2, >2, and <2, indicating normal Brownian diffusion, subdiffusion and superdiffusion, respectively. We fit $\tau(q)$ for $q = 1 - 4\,\mu m^{-1}$, with the (i) upper and (ii) lower bounds set by the (i) optical resolution of our setup and (ii) finite image size and Δt range over which we fit $D(q,\Delta t)$, respectively. These effects lead to (i) unphysical upticks in $\tau(q)$ curves for $q > 4\,\mu m^{-1}$ and (ii) q-independent plateaus for $q < 1\ \mu m^{-1}$ (Supplementary Figure S1).

We also examine the stretching exponent $\gamma(q)$ that we extract from fitting $D(q,\Delta t)$ as another transport metric, with $\gamma(q) < 1$ indicative of confined and heterogeneous dynamics [5, 36–38] and $\gamma(q) > 1$ indicative of active ballistic-like motion [14, 39–41]. Finally, we evaluate the q-dependence of $\gamma(q)$ to ensure that the expected insensitivity to q, necessary for unequivocal determination and interpretation of the scaling exponent β, holds for all cases (Supplementary Figure S2).

3 Results and discussion

To elucidate the combined effects of non-equilibrium activity and steric hindrance on particle transport in crowded active matter, we leverage the tunability of reconstituted cytoskeleton composites [42] and the power of coupling real-space (SPT) and

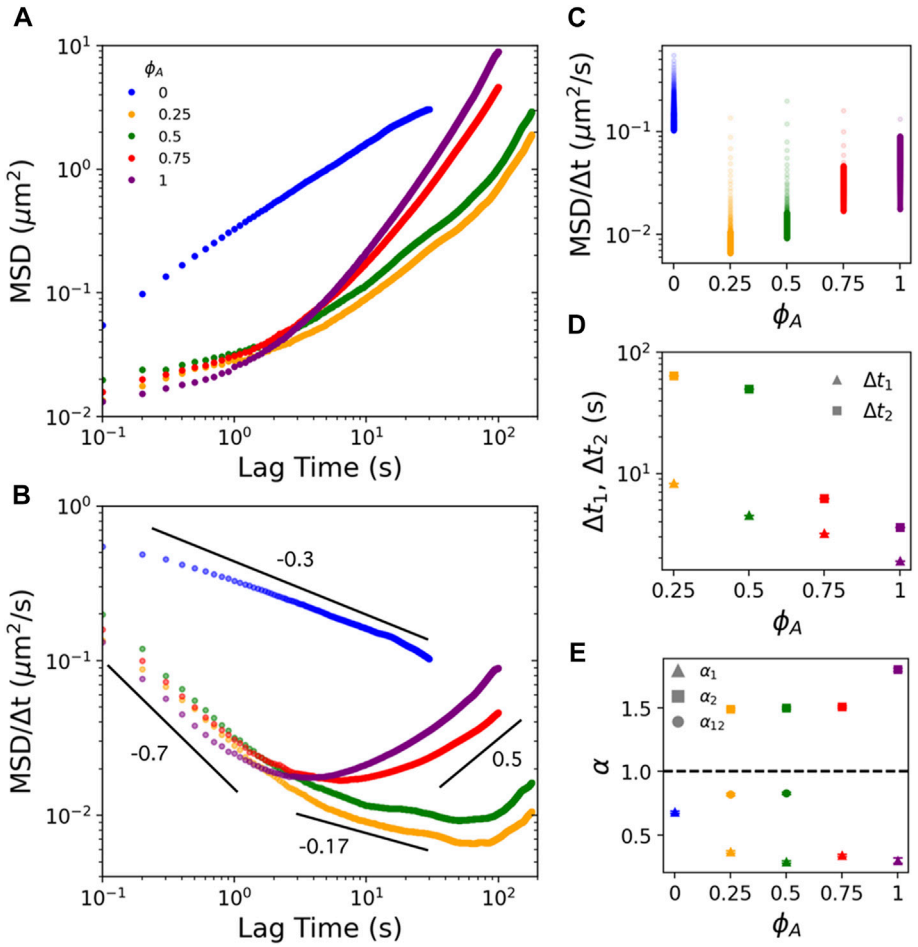

FIGURE 2
Actomyosin activity in actin-microtubule composites endows multi-phasic particle transport marked by pronounced subdiffusion at short lag times and superdiffusion at long lag times. **(A)** Mean-squared displacements (*MSD*) plotted *versus* lag time Δt for myosin-driven actin-microtubule composites with molar actin fractions of $\phi_A = 0$ (blue), 0.25 (gold), 0.50 (green), 0.75 (red), and 1 (purple). Fits of the data to $MSD \sim \Delta t^{\alpha}$ over different Δt ranges (shown in (B)) determine the anomalous scaling exponents α_i that describe the dynamics (see Figure 1). **(B)** Mean-squared displacements scaled by lag time ($MSD/\Delta t$) plotted *versus* lag time Δt delineate regions of subdiffusion (negative slopes) and superdiffusion (positive slopes). Color coding is according to the legend in **(A)**. Black lines indicate fits to $MSD \sim \Delta t^{\alpha}$ over the short ($\Delta t < \Delta t_1$), long ($\Delta t > \Delta t_2$) and intermediate ($\Delta t_1 < \Delta t < \Delta t_2$) time regimes where each curve is well-fit by a single power law. **(C)** Data shown in B plotted *versus* actin fraction ϕ_A, with all $MSD/\Delta t$ values for each ϕ_A plotted along the same vertical, with the gradient indicating increasing Δt from light to dark. The magnitude of each data point is proportional to a transport rate, with higher values indicating faster motion. **(D)** Lag time at which each composite transitions out of initial subdiffusive transport (Δt_1) and transitions into superdiffusivity (Δt_2). **(E)** Anomalous scaling exponents α_i derived from fits shown in **(B)** for $\Delta t < \Delta t_1$ ($i = 1$), $\Delta t > \Delta t_2$ ($i = 2$), and $(\Delta t_1 < \Delta t < \Delta t_2)$ ($i = 1, 2$). Dashed line at $\alpha = 1$ represents scaling indicative of normal Brownian diffusion. Values above and below the line indicate superdiffusion and subdiffusion, respectively. Note that only $\phi_A = 0.25$ and 0.5 composites exhibit an intermediate $\alpha_{1,2}$ regime. For both **(C)** and **(D)** error bars indicate standard error of the mean. Color-coding in all subfigures matches the legend in **(A)**.

reciprocal space (DDM) transport analysis, to robustly characterize particle transport as a function of active substrate content. Specifically, we tune the composition of actomyosin-microtubule composites to display a wide range of transport characteristics by varying the molar fraction of actomyosin, which we denote by the molar actin fraction ϕ_A, keeping the myosin molarity fixed at 8% of ϕ_A (Figure 1A, Methods).

In Figure 2A, we plot the ensemble-averaged *MSD* as a function of lag time Δt for particles diffusing in composites of varying ϕ_A. While $\phi_A = 0$ (no actomyosin) exhibits subdiffusive transport across the entire Δt range, with $\alpha \simeq 0.67$, all $\phi_A > 0$ composites display multi-phasic transport which is subdiffusive ($\alpha_1 < 1$) at short Δt and superdiffusive ($\alpha_2 > 1$) at long Δt. To more clearly show the transition from subdiffusion to superdiffusion, we plot $MSD/\Delta t$ *versus* Δt (Figure 2B), which is a horizontal line for normal Brownian diffusion with the Δt-independent magnitude proportional to the diffusion coefficient. Positive and negative slopes correspond to superdiffusion and subdiffusion, respectively, with $MSD/\Delta t \sim \Delta t^1$ indicating ballistic motion. Corresponding $MSD/\Delta t$

magnitudes are proportional to Δt-dependent transport coefficients. While all $\phi_A > 0$ composites exhibit similar general trends with Δt, the lag time at which the dynamics transition from subdiffusive to superdiffusive, along with the degree to which α_1 and α_2 deviate from 1, depend non-trivially on ϕ_A. Moreover, as clearly seen in Figure 2C, while α values for active composites ($\phi_A > 0$) transition to superdiffusive at longer lag times, the magnitudes of the transport coefficients remain nearly an order of magnitude smaller than that of the inactive network ($\phi_A = 0$) at any given Δt.

To evaluate the ϕ_A-dependence of the multi-phasic behavior, we first compute the lag times at which composites transition out of initial subdiffusive scaling, denoted as Δt_1, and transition into superdiffusive scaling, denoted as Δt_2. We note that the *MSD*s for $\phi_A = 0.75$ and 1 both exhibit a continuous transition from initial subdiffusion (quantified by α_1) to a final superdiffusive regime (quantified by α_2), seen as a smooth concave-up curve between the two power-law regimes. Conversely, *MSD*s for $\phi_A = 0.25$ and 0.5 exhibit an extended power-law regime in this transition with weakly subdiffusive scaling exponent α_{12}. To quantify Δt_1, we compute the largest lag time for which linear regression of $\log MSD$ *versus* $\log \Delta t$ over the range $\Delta t \in [0.1\,\text{s}, \Delta t_1]$ yields $R^2 > 0.99$. We define Δt_2 as the lag time at which $MSD/\Delta t$ exhibits a local minimum (i.e. where α crosses over from <1 to >1) (Figure 2C). We find that both timescales decrease with increasing ϕ_A as does the separation between the timescales ($\Delta t_2 - \Delta t_1$), suggesting that the rate of particle motion mediated by directed motor-driven network dynamics increases with increasing ϕ_A. In other words, the time it takes for the active dynamics to be 'felt' by the particles, driving them out of their confined subdiffusive motion, decreases with increasing ϕ_A.

To understand this phenomenon, we consider that active ballistic transport would only be detectable at timescales in which the network motion can move a bead more than the minimum resolvable displacement: $\Delta t_a \approx (100\,\text{nm})/(\textit{network speed})$. Using reported speed values of $v \approx 2.2 - 85$ nm/s for similar myosin-driven composites [23], we compute $\Delta t_a \approx (100\,\text{nm})/v \approx 1 - 50\text{s}$, aligning with our Δt_1 and Δt_2 values, and thus corroborating that the deviation from subdiffusion and transition to superdiffusion is due to myosin-driven ballistic motion. Moreover, the previously reported speeds generally decreased with decreasing ϕ_A, such that Δt_a should increase as ϕ_A decreases, just as we see in Figure 2B.

To determine the extent to which motor-driven transport and confinement contribute to the particle dynamics, we next evaluate the anomalous scaling exponents in the short, intermediate, and long Δt regimes by performing power-law fits to the *MSD*s in each regime (Figures 2B,E). Surprisingly, the scaling exponents in the $\Delta t < \Delta t_1$ regime for all active composites ($\phi_A > 0$) are markedly smaller (more subdiffusive) than the inactive composite ($\phi_A = 0$), with ϕ_A-dependent values of $\alpha_1 \simeq 0.29 - 0.37$ compared to $\alpha_1 \simeq 0.68$ for the $\phi_A = 0$ network. To understand the decrease in α_1 with increasing ϕ_A for the active composites, as well as the unexpected ~2-fold reduction in α_1 for active composites, we turn to previous studies [5, 6], that reported that, in the absence of any crosslinking, steady-state actin-microtubule composites exhibit subdiffusion with scaling exponents that decrease from $\alpha \approx 0.82$ to $\alpha \approx 0.56$ as ϕ_A increases from 0 to 1. This monotonic ~30% decrease with increasing ϕ_A, similar to the ~25% decrease we observe with increasing ϕ_A, was suggested to arise from increased composite mobility that entrains the bead motion as rigid microtubules are replaced with semiflexible actin filaments [6, 12]. This mobility is paired with a decreasing mesh size as ϕ_A increases, which, in turn, increases composite viscoelasticity and particle confinement, both of which contribute to decreasing α [6].

To understand the lower α_1 values we measure, compared to those previously reported for steady-state composites, we look to previous studies on $\phi_A = 0.5$ actin-microtubule composites with varying types of static crosslinking. In these studies, subdiffusion is much more extreme ($\alpha \approx 0.33$) when actin filaments are crosslinked to each other compared to no crosslinking ($\alpha \approx 0.64$) [5]. Taken together, our results suggest that the ~2-fold reduction in α_1 between $\phi_A = 0$ and $\phi_A > 0$ composites likely arises from myosin motors acting as static crosslinkers on timescales shorter than the timescale over which they can actively translate the composite. As described above, myosin acting as a static crosslinker for $\Delta t < \Delta t_1$ is consistent with previously reported speeds for myosin-driven composites [5, 6], as well as reported actomyosin turnover rates [24]. The weak decrease in α_1 with increasing ϕ_A likely arises from the decreasing mesh size and increasing mobility of the network as ϕ_A increases [43], as described above.

Examining the long-time regime, $\Delta t > \Delta t_2$, our results show that the scaling exponent α_2 is largely insensitive to ϕ_A for all composites (i.e., $0 < \phi_A < 1$) with an average value of $\alpha_2 \simeq 1.5$, only modestly lower than $\alpha_2 \simeq 1.8$ measured for $\phi_A = 1$. However, the lag time at which superdiffusive α_2 scaling emerges is an order of magnitude larger for $\phi_A = 0.25$ and 0.5 composites compared to $\phi_A > 0.5$. Moreover, $\phi_A = 0.25$ and 0.5 composites display nearly identical intermediate subdiffusive scaling regimes, absent for $\phi_A > 0.5$, with an average scaling exponent of $\alpha_{12} \simeq 0.83 \pm 0.2$. Taken together, these results suggest that the timescale over which motor-driven dynamics dominates particle transport scales with the fraction of active substrate [23], while the superdiffusive signature of the active transport is controlled by the motor:substrate ratio (which we hold fixed across composites).

To shed further light on the mechanisms underlying the anomalous transport shown in Figure 2, we compute van Hove distributions $G(\Delta d, \Delta t)$, where $\Delta d = \Delta x \cup \Delta y$, for two decades of lag times ($\Delta t = 0.1 - 15\,s$) (Figure 3A). From the distributions, we first compute anomalous scaling exponents α, to corroborate our *MSD* analysis, by recalling that the full width at half maximum, *FWHM*, for a Gaussian distribution scales with

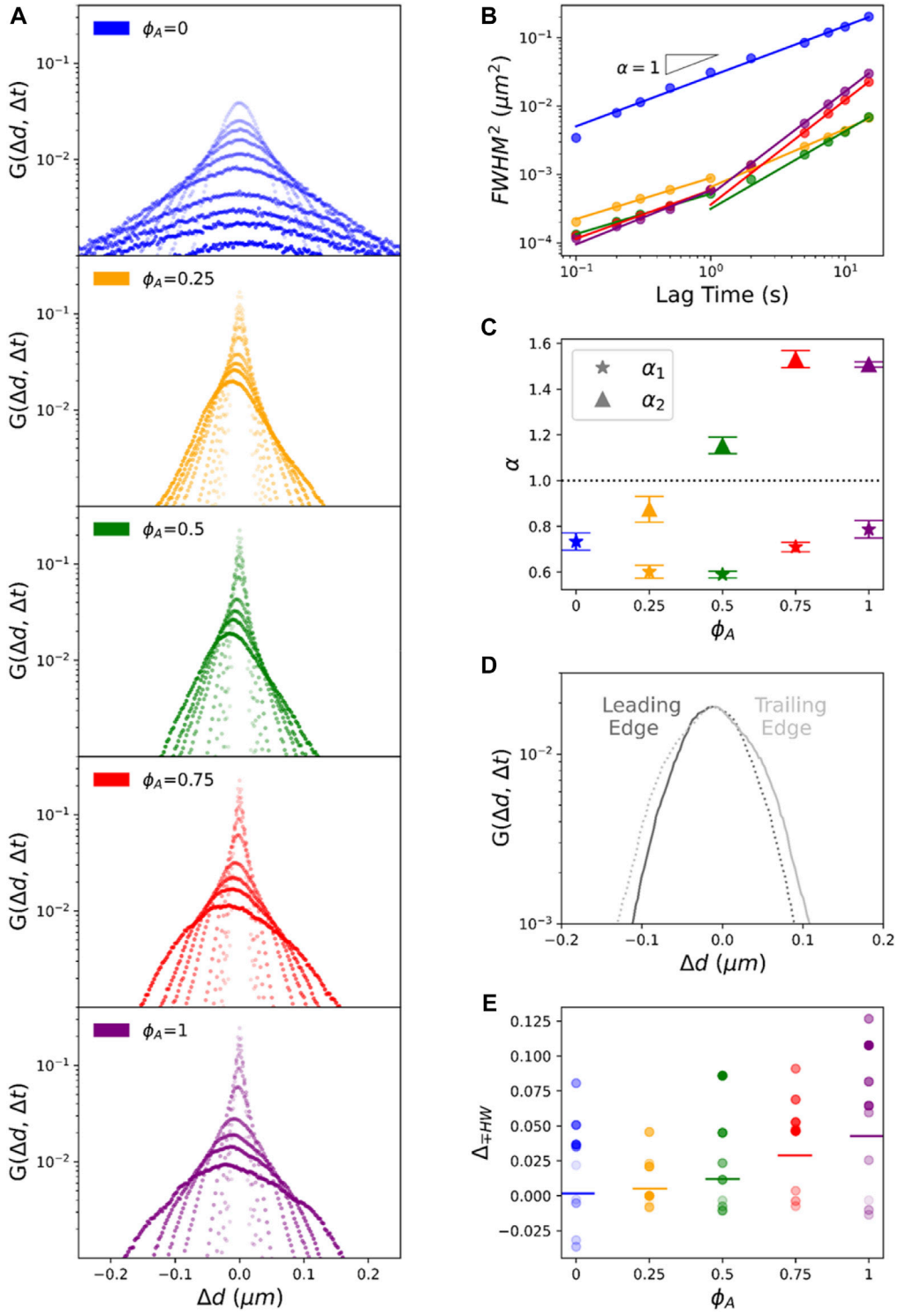

FIGURE 3
Asymmetric non-Gaussian van Hove distributions reveal a combination of heterogeneous subdiffusion and advective transport of particles in active composites. **(A)** van Hove distributions $G(\Delta d, \Delta t)$ of particle displacements $\Delta d = \Delta x \cup \Delta y$, measured *via* SPT, for lag times Δt = 0.1, 0.2, 0.3, 0.5, 1, 2, 3, 5, 10, 15 *s* denoted by the color gradient going from light to dark for increasing Δt. Each panel corresponds to a different composite demarked by their ϕ_A value with color-coding as in Figure 2. **(B)** The square of the full width at half-maximum $(FWHM)^2$ *versus* lag time Δt for each composite shown in **(A)**. Solid lines are fits to $(FWHM)^2 \sim \Delta t^{\alpha_i}$. For $\phi_A > 0$ composites we fit short ($\Delta t \leq 1$ s) and long ($\Delta t \geq 1$ s) lag time regimes separately. **(C)** The scaling exponents α as functions of ϕ_A determined from the fits shown in B, where α_1 (stars) and α_2 (triangles) correspond
(*Continued*)

FIGURE 3 (Continued)
to scalings for the short and long Δt regimes, respectively. The dashed horizontal line denotes scaling for normal Brownian diffusion. **(D)** A sample $G(\Delta d, \Delta t)$ distribution ($\phi_A = 0.75$ at $\Delta t = 10\ s$) showing the asymmetry about the mode value Δd_{peak}. We divide each distribution into a leading edge (dark grey, displacements of the same sign as Δd_{peak} and greater in magnitude) and the trailing edge (light grey, the remaining part of the distribution). To clearly demonstrate the asymmetry, we mirror each edge about Δd_{peak} using dashed lines. **(E)** The fractional difference of the half-width at half maximum *HWHM* of the trailing (-) edge from the leading (+) edge, ($\Delta_{\mp HW} = HWHM_- - HWHM_+)/\ HWHM_+$), for each ϕ_A and Δt. Color coding and gradient indicate ϕ_A and Δt, respectively, as in **(A)**. Horizontal bars through each distribution denote the mean.

the standard deviation σ as $FWHM = 2\sqrt{2\,ln\,2}\,\sigma$. Because $\sigma^2 \sim \Delta d^2$ by definition, and $MSD(\Delta t) \sim (\Delta d(\Delta t))^2 \sim \Delta t^{\alpha_i}$, we determine α_i by computing the $FWHM$ for each distribution and fitting the Δt-dependent values to the power-law $FWHM(\Delta t) \sim (\Delta t)^{\alpha_i/2}$ (Figure 3B) [7, 44]. As shown in Figures 3B,C, $FWHM(\Delta t)$ for $\phi_A = 0$ fits well to a single power-law, with $\alpha \simeq 0.7$, nearly indistinguishable from that computed from the MSD, across the entire Δt range. Conversely, informed by the multi-phasic MSD scaling we observe for active composites (Figure 2C), we fit $FWHM(\Delta t)$ for each active composite to separate power-law functions over short ($0.15\ s < \Delta t < 1\ s$) and long ($1\ s < \Delta t < 15\ s$) lag times, relative to the average Δt_1 we determine from MSD fits. Further, similar to the ϕ_A-dependence of α_1 and α_2 values determined from MSDs, the scaling exponents determined from $FWHM$, increase with increasing ϕ_A, with α_1 (for $\Delta t < 1\ s$) increasing from ~0.62 to ~0.85, similar to values reported for steady-state actin-microtubule composites [6], and α_2 (for $\Delta t > 1\ s$) spanning from subdiffusive to superdiffusive. Higher α_1 values compared to those determined from MSDs are likely due to the lower Δt resolution in $FWHM$ fitting and the single Δt value used to divide the two regimes. Likewise, the lower α_2 values for $\phi_A = 0.25$ and 0.5 compared to those measured from MSDs are a result of treating all $\Delta t > \Delta t_1$ data as obeying a single power-law rather than separate α_{12} and α_2 scaling.

While our analysis described above assumes Gaussian distributions, Figure 3A shows that nearly all distributions have distinct non-Gaussian features similar to those reported for steady-state actin-microtubule composites [5, 7]. In particular, $G(\Delta d, \Delta t)$ distributions for the inactive network ($\phi_A = 0$) exhibit pronounced exponential tails at large displacements. This non-Gaussianity, seen in other crowded and confined soft matter systems [7], is a signature of heterogeneous transport and can also indicate caging and hopping between cages.

The distributions for active composites are even more complex, with asymmetries and peaks at $\Delta d \neq 0$ (Figure 3A), not readily predictable from our MSD analysis. The first interesting feature we investigate is the non-zero mode value Δd_{peak} that increases in magnitude with increasing Δt, indicating directed ballistic-like motion, thereby corroborating our superdiffusive scaling exponents. Perhaps less intuitive is the robust asymmetry between the 'leading (+) edge' and 'trailing (-) edge' of each distribution, which we define by splitting each distribution about its peak, Δd_{peak}. Specifically, the leading edge is the part of the distribution that has displacements of the same sign as Δx_{peak} and greater in magnitude, while the remaining part is the trailing edge (Figure 3D). We observe that for most distributions the leading edge appears more Gaussian-like while the trailing edge exhibits pronounced large-displacement 'tails'. To broadly quantify this asymmetry, we evaluate the half-width at half-maximum ($HWHM$) for the leading (+) and trailing (-) edges of each distribution and compute the percentage increase in $HWHM$ for the trailing *versus* leading edge: $\Delta_{\mp HW} = (HWHM_- - HWHM_+)/\ HWHM_+$ (Figure 3E). We find that $\Delta_{\mp HW}$ is positive for all active composites and increases with increasing ϕ_A, demonstrating that the asymmetry is a direct result of active composite dynamics which contribute more to the transport as the actomyosin content increases.

We also note that the asymmetry shown in Figure 3A is always in the negative direction (to the left). To determine the directionality of this asymmetry we evaluate the distributions of Δx and Δy values separately (Supplementary Figure S3), which show that the asymmetry for $G(\Delta y, \Delta t)$ is more pronounced and negative compared to the smaller positive anisotropy seen in $G(\Delta x, \Delta t)$. This bias is likely due to the geometry of the sample chamber that has a y-direction length that is >10× the x-direction width of the chamber.

To determine if this directionality is a reproducible microscale bias or is an ensemble result of averaging over trials with positive and negative anisotropies, we evaluate the van Hove distributions for each trial of the $\phi_A = 1$ case (that exhibits the most pronounced asymmetry) (Supplementary Figure S4). We observe that nearly all $G(\Delta x, \Delta t)$ and $G(\Delta y, \Delta t)$ distributions skew to $+x$ and $-y$, respectively, with $G(\Delta y, \Delta t)$ asymmetries being more pronounced, such that $G(\Delta d, \Delta t)$ skews in the negative direction. This systematic effect corroborates our understanding that the directional bias is due to the sample chamber geometry that provides more freedom in the y-direction for the composite to restructure and flow.

To more quantitatively characterize the rich transport phenomena revealed in Figure 3, we first fit each $G(\Delta d, \Delta t)$ to a sum of a Gaussian and an exponential (see Methods), as done for steady-state cytoskeleton composites [5–7]. Figure 4A compares the distributions and their fits for all composite formulations at $\Delta t = 0.3\ s$ (top panel) and $10\ s$ (bottom panel),

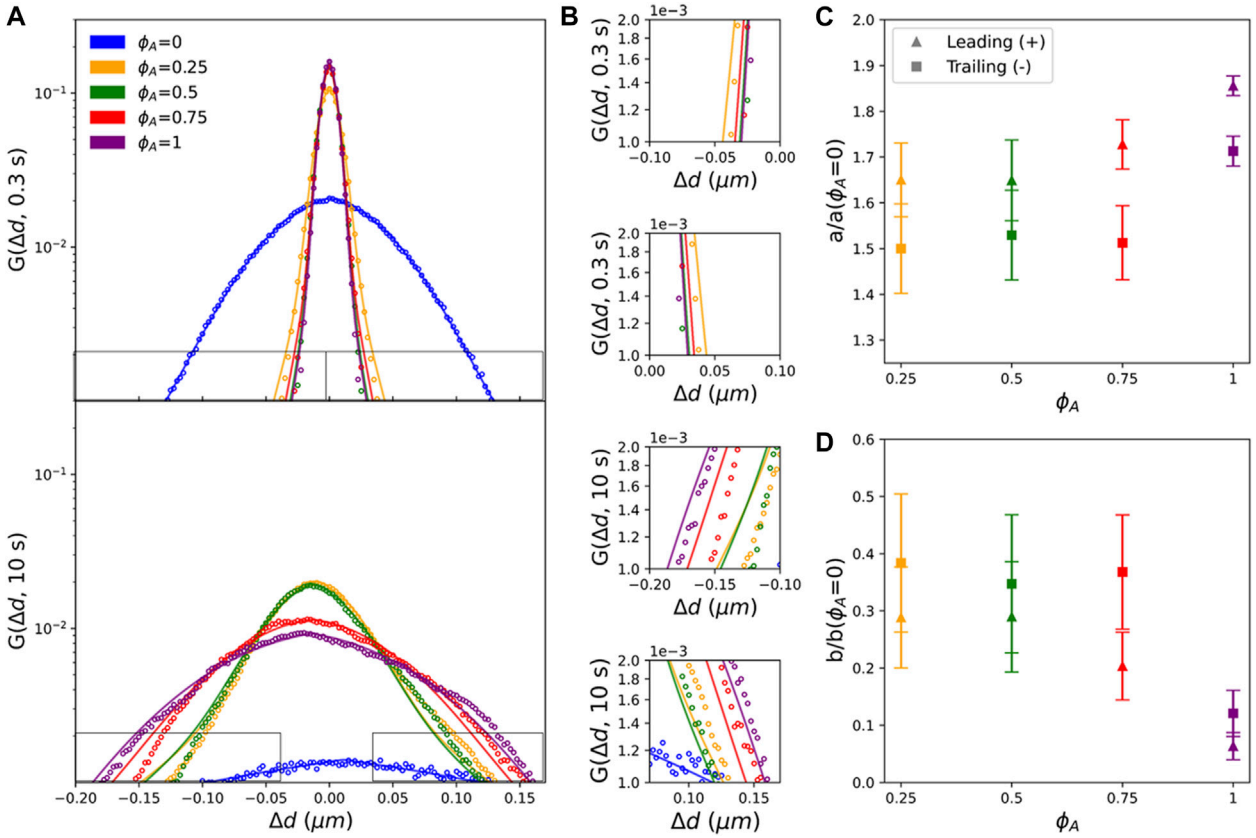

FIGURE 4
Actomyosin activity reduces heterogeneous non-Gaussian diffusivity and endows Gaussian-like advective transport. **(A)** Comparing van Hove distributions of composites with different ϕ_A (see legend) at lag times of $\Delta t = 0.3\,s$ (top) and $\Delta t = 10\,s$ (bottom). Color-coded solid lines are fits of each distribution to the sum of a Gaussian and an exponential: $G(\Delta d) = Ae^{-\frac{\Delta d^2}{2\sigma^2}} + Be^{-\frac{|\Delta d|}{\lambda}}$. Black rectangles indicate regions of the distributions that are shown zoomed-in in **(B)**. **(C)** Fractional amplitude of the Gaussian term in each fit, $a = A/(A + B)$, normalized by the corresponding value for $\phi_A = 0$. Fits are performed separately for the leading (+, triangles) and trailing (-, squares) edges of each distribution. Data shown are the averages and standard deviations across all lag times for each ϕ_A. **(D)** Fractional amplitude of the exponential term in each fit, $b = A/(A + B)$, normalized by the corresponding value for $\phi_A = 0$. Fits are performed separately for the leading (+, triangles) and trailing (-, squares) edges of each distribution. Data shown are the averages and standard deviations across all lag times for each ϕ_A.

and Figure 4B displays zoom-ins of the corresponding leading and trailing edges. As shown, while this sum describes the inactive network distributions reasonably well, it overestimates leading edge displacements and underestimates trailing edge displacements of the active networks (Figure 4B). This asymmetry suggests that the leading edges are more Gaussian-like and the trailing edges are more exponential-like. To account for this asymmetry, we fit each half of each distribution separately to a one-sided sum of a Gaussian and exponential and evaluate the relative contributions from the Gaussian and exponential terms. As detailed in the Methods, we denote the amplitude of the Gaussian term and exponential term as A and B, respectively, such that their relative contributions are $a = A/(A + B)$ and $b = B/(A + B)$.

As shown in Figures 4C,D, in which a and b are normalized by the corresponding $\phi_A = 0$ value and plotted for each ϕ_A, active composites are more Gaussian-like ($a/a(\phi_A = 0) > 1$) and less exponential ($b/b(\phi_A = 0) < 1$) than the inactive system for both leading and trailing edges. This result suggests that the active processes that induce contraction and flow of the composites likewise reduce transport heterogeneity and intermittent hopping, possibly by promoting mixing and advection. Consistent with this interpretation is the observation that the Gaussian contribution a increases with increasing ϕ_A and is consistently larger for the leading edge, which consists of displacements oriented with the direction of the myosin-driven composite motion (Figure 4C).

Conversely, the increased contribution from the exponential term for the trailing edge, implies that displacements comprising these exponential tails are dominated by heterogeneous transport modes such as hopping between heterogeneously distributed cages [6, 7]. To better understand this effect, we recall that

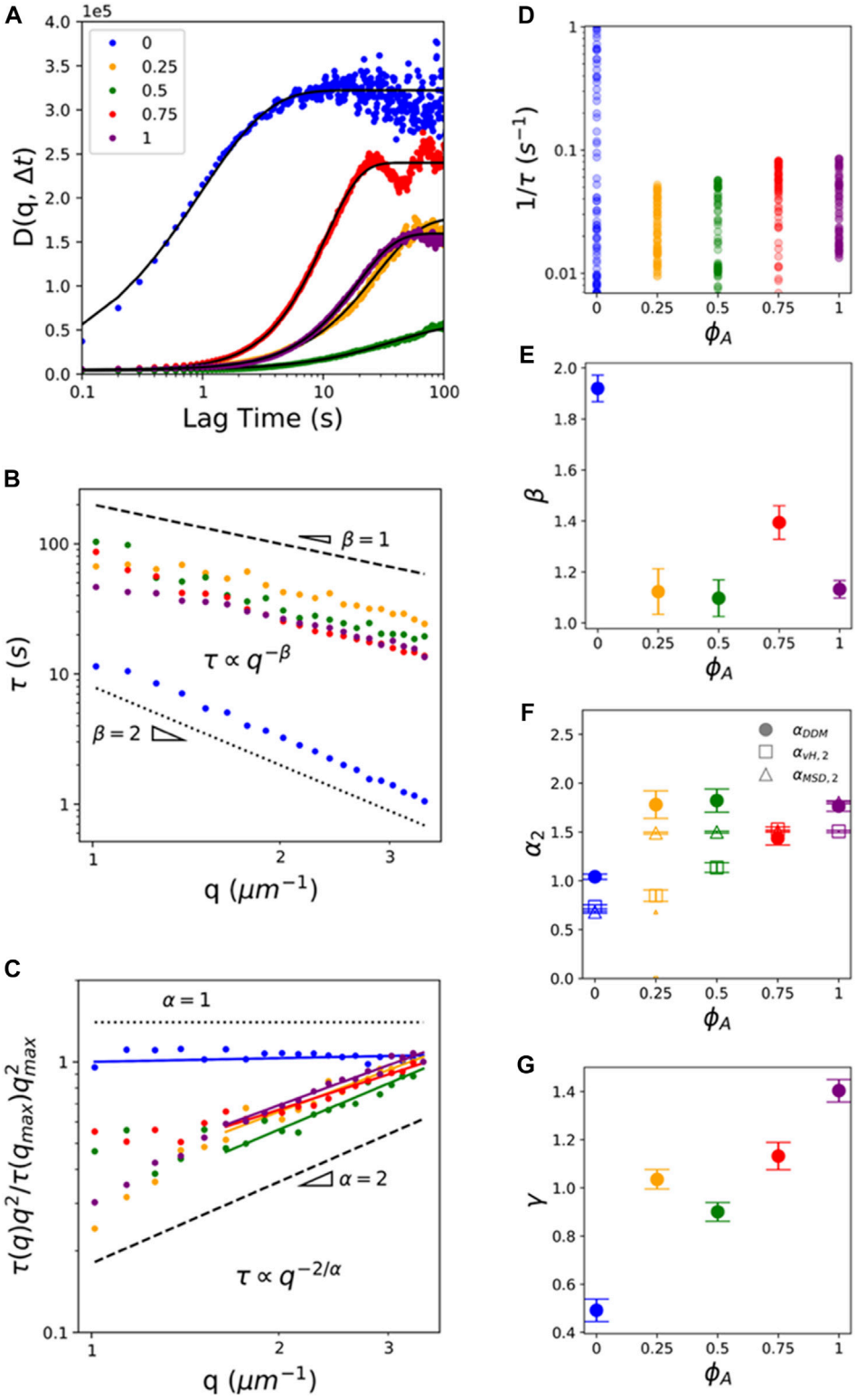

FIGURE 5
DDM analysis reveals ballistic-like transport of particles entrained in active composites at mesoscopic spatiotemporal scales. **(A)** Sample image structure functions $D(q, \Delta t)$ for composites with actin fractions ϕ_A indicated in the legend. All curves shown are evaluated at $q = 3.92\,\mu m^{-1}$, and solid black lines are fits to the data to determine corresponding q-dependent decay times $\tau(q)$ and stretching exponents γ, as described in Methods. **(B)** Decay times $\tau(q)$ for each composite shown in **(A)**. Dashed and dotted black lines show scaling $\tau(q) \sim q^{-\beta}$ for ballistic ($\beta = 1$) and diffusive ($\beta = 2$)
(*Continued*)

FIGURE 5 (Continued)
transport. **(C)** $\tau(q) \times q^2$, normalized by $\tau(q_{max}) \times (q_{max})^2$, for the data shown in **(B)**. Horizontal dotted line and unity-sloped dashed line correspond to scaling indicative of normal diffusion ($\alpha = 2/\beta = 1$) and ballistic motion ($\alpha = 2/\beta = 2$). Color-coded solid lines correspond to power-law fits, with the corresponding exponents β and α shown in **(E)** and **(F)**. For $\phi_A > 0$ composites, the fitting range is truncated to $q > 1.5\,\mu m^{-1}$ where a single power-law is observed. **(D)** Scatter plot of $1/\tau(q)$, a measure of the transport rate, for all measured q values for each ϕ_A. Color coding and gradient indicate ϕ_A and q, respectively, with light to dark shades of each color indicating increasing q values. **(E)** DDM scaling exponents β determined from fits shown in **(C)**. **(F)** Anomalous scaling exponents α_2 determined from $\tau(q)$ fits (filled circles, $\alpha_{DDM} = 2/\beta$), as well as the large-Δt regime fits of the *MSD*s (open triangles, $\alpha_{MSD,2}$) and van Hove distributions (open triangles, $\alpha_{vH,2}$) measured *via* SPT (see Figures 2, 3). Error bars indicate 95% confidence intervals of fits. **(G)** Stretching exponent $\gamma(q)$, averaged over all q values, for each composite ϕ_A, with error bars indicating standard error.

particle displacements comprising the trailing edge are lagging behind the bulk translational motion of the composite. As the composite moves and restructures, a fraction of the particles remain caged in the moving composite and thus move along with it, corresponding to displacements comprising the leading edge, whereas a fraction of the particles are squeezed out or hop out of composite cages and into new 'trailing' cages. It is also likely that as the composite contracts and forms more heterogeneous structures and larger open voids that characteristic 'hopping' displacements, as well as displacements withing cages, may increase and become more heterogeneous, thereby enhancing exponential tails.

To expand the range of length and time scales over which we probe the non-equilibrium transport, and provide an independent measure of the dynamics, we complement our real-space SPT analysis with Fourier-space DDM analysis, as described in the Methods and previously [5, 6, 14]. Briefly, we compute the radially-averaged image structure function $D(q, \Delta t)$ of the Fourier transform of image differences as a function of wave vector q and lag time Δt. From fits of $D(q, \Delta t)$ to a function with a stretched exponential term (see Methods, Figure 5A), we determine the q-dependent characteristic decay time $\tau(q)$ and stretching exponent $\gamma(q)$ for each composite (Figure 5), which characterize the dynamics. $\tau(q)$ typically exhibits power-law scaling $\tau(q) \sim q^{-\beta}$ where β is related to the anomalous scaling exponent α *via* $\beta = 2/\alpha$, such that $\beta > 2$, $\beta = 2$, $\beta < 2$ and $\beta = 1$ correspond to, respectively, subdiffusive, normal diffusive, superdiffusive, and ballistic motion. Stretching exponents $\gamma(q)$ are typically independent of q (see Supplementary Figure S2), with q-averaged values of $\gamma = 1$ for normal Brownian motion, $\gamma < 1$ for crowded and confined systems [15, 40] and $\gamma > 1$ for active transport [15, 45].

As shown in Figure 5B, $\tau(q)$ curves for all active composites follow scaling indicative of superdiffusive or ballistic transport while the $\phi_A = 0$ system more closely follows diffusive scaling. Further, $\tau(q)$ for $\phi_A = 0$ is an order of magnitude lower than for all active composites, indicating that particle transport is faster for the inactive composite, in line with our results shown in Figure 2C, despite the displacements exhibiting diffusive rather than ballistic-like motion. This effect can be more clearly seen in Figure 5D, which displays the q-dependent distribution of $\tau(q)^{-1}$ values, a measure of dynamic decorrelation rates, for each ϕ_A. As shown, τ^{-1} values for $\phi_A = 0$ are an order of magnitude larger than those for $\phi_A > 0$ composites. Figure 5D also shows that decorrelation rates in active composites increase modestly with increasing ϕ_A suggesting that transport is dictated primarily by active restructuring and flow, rather than crowding and confinement, which increases as actomyosin content increases. The lack of subdiffusive scaling or crossovers from sub-to super-diffusive dynamics for active composites (as our SPT analysis shows) can be understood as arising from the larger length and time scales DDM probes. Namely, DDM spans lengthscales of $l = 2\pi/q \simeq 1.6 - 6.28\,\mu m$ and timescales of $\tau \simeq 20 - 100\,s$ (Figure 5A) compared to the $\sim 0.1 - 1.5\,\mu m$ and $\sim 0.1 - 100\,s$ length and timescales accessible to SPT. As we describe in Methods, the lower bound on measurable lengthscales (upper bound on q) for DDM is set by the optical resolution limit of our setup, which is circumvented in SPT by using sub-pixel localization algorithms. At the same time, SPT is bounded at larger spatiotemporal scales by the duration of individual bead trajectories. The different scales that DDM and SPT are able to accurately probe is exactly the reason we use them both to fully characterize the dynamics of our system.

To better visualize differences in $\tau(q)$ scaling between composites we plot $\tau(q) \times q^2$ normalized by $\tau(q_{max}) \times (q_{max})$ (Figure 5C). Diffusive transport manifests as a horizontal line, as we see for $\phi_A = 0$, while ballistic-like motion follows a power-law scaling of 1, which roughly describes the $\phi_A > 0$ curves. To quantify the DDM scaling exponent β that describes the dynamics, we fit each $\tau(q)$ curve to a power-law (i.e., $\tau(q) \sim q^{-\beta}$) (Figures 5C,E). For the active composites, we restrict our fitting range to $q > 1.5\,\mu m^{-1}$, in which a single power-law is observed. For smaller q values (larger length and time scales), we note that $\phi_A = 0.25$ and 1 composites exhibit roughly ballistic motion whereas $\phi_A = 0.5$ and 0.75 exhibit roughly diffusive dynamics (Figure 5C) [15, 16]. However, we restrict further quantification and interpretation of this small-q regime as it comprises relatively few data points and low statistics. Over the range that we fit our data, we find that $\beta \simeq 2.02$ for the inactive composite, indicative of diffusive dynamics, whereas active composites exhibit near-ballistic values of $\beta \simeq 1.03 - 1.26$, which are largely independent of ϕ_A, similar to our α_2 values measured *via* SPT (Figure 2E). To directly compare β values to the anomalous scaling exponents α that we determine from SPT

(Figure 2E, Figure 3E), we plot $\alpha_{DDM} = 2/\beta$ (Figures 5C,F) with the α_2 values we determined from the *MSD*s and van Hove distributions in the large Δt regime ($> \Delta t_2$), which we denote as $\alpha_{MSD,2}$ and $\alpha_{vH,2}$. Scaling exponents determined from all three methods are broadly similar, with active composites displaying larger α values than the $\phi_A = 0$ system. We attribute small differences between α_{DDM}, $\alpha_{vH,2}$, and $\alpha_{MSD,2}$, which are most apparent for $\phi_A = 0.25$ and 0.5, to the different timescales probed by each method. Namely, all systems tend to subdiffusion at short lag times and free diffusion or ballistic motion at large lag times. As such, we expect $\alpha_{vH,2}$ which spans the shortest lag times ($\Delta t = 1 - 15$ s) to be the lowest while α_{DDM} which spans the largest timescales to be the largest, which is indeed what we measure. Likewise, we expect $\phi_A = 0$ to exhibit subdiffusion over short timescales (measured *via* SPT) and tend towards free diffusion at larger timescales (measured *via* DDM), as shown in Figure 5F.

Finally, to shed light on the competing contributions from motor-driven dynamics *versus* confinement and crowding to transport at larger spatiotemporal scales, we evaluate the dependence of the stretching exponent γ on ϕ_A. Figure 5G shows that transport in the inactive network is described by $\gamma \simeq 0.79 \pm 0.02$, over the q range we examine (Supplementary Figure S2), indicating that confinement dominates over active dynamics (i.e., $\gamma < 1$), whereas all $\phi_A > 0$ composites exhibit $\gamma > 1$, indicative of transport governed largely by active dynamics. Moreover, γ generally increases as the actomyosin fraction increases, corroborating the dominant role that active composite dynamics plays in the rich transport phenomena we reveal [15].

We note that while other active systems display a return to Gaussian dynamics at long timescales (e.g., 46), we find no evidence of this return due to the relatively slow active network dynamics compared to other active systems. However, our inactive system ($\phi_A = 0$) exhibits Gaussian dynamics at the larger timescales probed by DDM, indicating that the long-time ballistic dynamics we measure in the active composites ($\phi_A > 0$) are indeed due to motor activity and not from drift, flow or other experimental artifacts or bias.

4 Conclusion

Here, we couple real-space SPT and Fourier-space DDM to characterize particle transport across three decades in time ($\sim 10^{-1}$–10^{2} s) and two decades in space ($\sim 10^{-1}$—10 μm) in biomimetic composites that exhibit both pronounced crowding and confinement as well as active motor-driven restructuring and flow. Using our robust approach, we discover and dissect novel transport properties that arise from the complex interplay between increasing activity and confinement as the actomyosin fraction increases. Myosin motors induce ballistic-like contraction, restructuring and flow of the composites, leading entrained particles to exhibit similar superdiffusive, advective and Gaussian-like transport. Conversely, steric entanglements, connectivity and slow thermal relaxation of cytoskeletal filaments mediate heterogeneous, subdiffusive transport of confined particles.

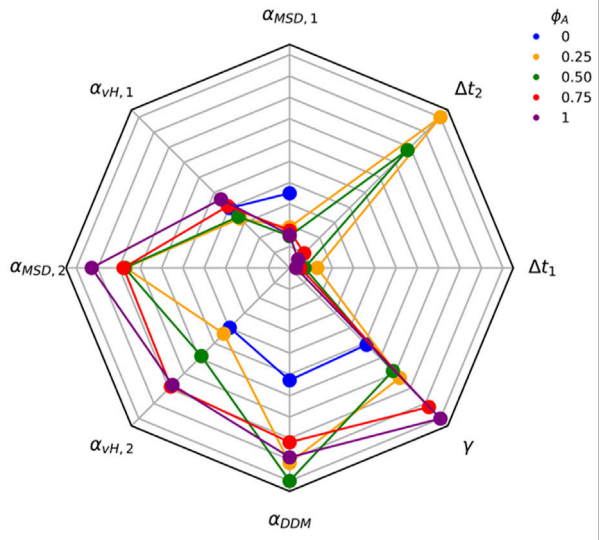

ϕ_A	0	0.25	0.5	0.75	1
$\alpha_{MSD,1}$	0.68 ± 0.01	0.37 ± 0.01	0.29 ± 0.01	0.34 ± 0.01	0.30 ± 0.02
$\alpha_{vH,1}$	0.73 ± 0.02	0.60 ± 0.02	0.59 ± 0.01	0.71 ± 0.03	0.79 ± 0.05
$\alpha_{MSD,2}$	0.68 ± 0.01	1.49 ± 0.01	1.50 ± 0.01	1.51 ± 0.01	1.80 ± 0.01
$\alpha_{vH,2}$	0.73 ± 0.02	0.85 ± 0.06	1.14 ± 0.05	1.53 ± 0.02	1.51 ± 0.01
α_{DDM}	0.98 ± 0.02	1.78 ± 0.11	1.94 ± 0.14	1.59 ± 0.06	1.72 ± 0.08
γ	0.79 ± 0.02	1.13 ± 0.02	1.06 ± 0.01	1.43 ± 0.01	1.54 ± 0.01
Δt_1	-	8.3	4.5	3.2	1.9
Δt_2	-	64	50	6.2	3.6

FIGURE 6
A robust suite of metrics reveals complex scale-dependent transport resulting from competition between motor-driven active dynamics, crowding and network connectivity. The 8-variable spider plot shows how the key metrics we use to characterize transport depend on ϕ_A (color-code shown in legend). A greater distance from the center signifies a larger magnitude. α values determined from DDM (α_{DDM}), SPT *MSDs* ($\alpha_{MSD,1}$, $\alpha_{MSD,2}$, $\alpha_{vH,1}$, $\alpha_{vH,2}$ and SPT van Hove distributions ($\alpha_{vH,1}$, $\alpha_{vH,2}$) are scaled identically for direct comparison, as are the two timescales determined from *MSD* s ($\Delta t_1, \Delta t_2$). The stretching exponent γ is scaled independently. The table provides the values with error for each metric plotted.

Figure 6 summarizes and compares the key metrics we present in Figures 2–5 that characterize these complex transport properties. Importantly, as highlighted in Figure 6, while there is clear difference between the inactive and active networks for nearly all of the transport metrics we present, we emphasize that there are very few clear monotonic dependences on ϕ_A for the active composites. This complexity is a direct result of the competition between motor-driven active dynamics, crowding and connectivity—all of which increase with increasing actomyosin content. These intriguing transport characteristics have direct implications in key cellular processes in which actomyosin and microtubules synergistically interact, such as cell migration, wound healing,

cytokinesis, polarization and mechano-sensing [23]. Moreover, our robust measurement and analysis toolbox and tunable active matter platform, along with the complex transport phenomena we present, are broadly applicable to a wide range of active matter and biomimetic systems of current intense investigation.

Data availability statement

The datasets generated and analyzed for this manuscript are available from the corresponding author on reasonable request.

Author contributions

JS analyzed and interpreted the data and wrote the paper; JG collected and helped analyze the data; SK and BL helped analyze data and prepare figures; RM conceived and guided the project, developed analysis code, helped analyze and interpret the data, and helped write the paper; RR-A conceived and guided the project, interpreted the data, and wrote the paper.

Funding

This work was supported by National Institutes of Health R15 Awards (R15GM123420, 2R15GM123420-02) to RMR-A and RJM, William M. Keck Foundation Research Grant to RMR-A, and NSF RUI Award (DMR-2203791) to JYS.

Acknowledgments

We thank AX, NB, and JK for help with data analysis and visualization. We thank GL for help with composite design. We thank DA for insightful discussions.

Conflict of interest

The authors declare that the research was conducted in the absence of any commercial or financial relationships that could be construed as a potential conflict of interest.

Publisher's note

All claims expressed in this article are solely those of the authors and do not necessarily represent those of their affiliated organizations, or those of the publisher, the editors and the reviewers. Any product that may be evaluated in this article, or claim that may be made by its manufacturer, is not guaranteed or endorsed by the publisher.

Supplementary material

The Supplementary Material for this article can be found online at: https://www.frontiersin.org/articles/10.3389/fphy.2022.1055441/full#supplementary-material

References

1. Mogre SS, Brown AI, Koslover EF. Getting around the cell: Physical transport in the intracellular world. *Phys Biol* (2020) 17:061003. doi:10.1088/1478-3975/aba5e5

2. Brangwynne CP, Koenderink GH, MacKintosh FC, Weitz DA. Intracellular transport by active diffusion. *Trends Cel Biol* (2009) 19:423–7. doi:10.1016/j.tcb.2009.04.004

3. Burute M, Kapitein LC. Cellular logistics: Unraveling the interplay between microtubule organization and intracellular transport. *Annu Rev Cel Dev Biol* (2019) 35:29–54. doi:10.1146/annurev-cellbio-100818-125149

4. Gardel ML, Schneider IC, Aratyn-Schaus Y, Waterman CM. Mechanical Integration of actin and Adhesion dynamics in cell migration. *Annu Rev Cel Dev Biol* (2010) 26:315–33. doi:10.1146/annurev.cellbio.011209.122036

5. Anderson SJ, Garamella J, Adalbert S, McGorty RJ, Robertson-Anderson RM. Subtle changes in crosslinking drive diverse anomalous transport characteristics in actin–microtubule networks. *Soft Matter* (2021) 17:4375–85. doi:10.1039/d1sm00093d

6. Anderson SJ, Matsuda C, Garamella J, Peddireddy KR, Robertson-Anderson RM, McGorty R. Filament Rigidity Vies with mesh size in determining anomalous diffusion in cytoskeleton. *Biomacromolecules* (2019) 20:4380–8. doi:10.1021/acs.biomac.9b01057

7. Wang B, Kuo J, Bae SC, Granick S. When Brownian diffusion is not Gaussian. *Nat Mater* (2012) 11:481–5. doi:10.1038/nmat3308

8. Sokolov IM. Models of anomalous diffusion in crowded environments. *Soft Matter* (2012) 8:9043. doi:10.1039/c2sm25701g

9. Burla F, Mulla Y, Vos BE, Aufderhorst-Roberts A, Koenderink GH. From mechanical resilience to active material properties in biopolymer networks. *Nat Rev Phys* (2019) 1:249–63. doi:10.1038/s42254-019-0036-4

10. Koenderink GH, Dogic Z, Nakamura F, Bendix PM, MacKintosh FC, Hartwig JH, et al. An active biopolymer network controlled by molecular motors. *Proc Natl Acad Sci U S A* (2009) 106:15192–7. doi:10.1073/pnas.0903974106

11. Alberts B. *Molecular Biology of the Cell*. New York: Garland Science (2017).

12. Regan K, Wulstein D, Rasmussen H, McGorty R, Robertson-Anderson RM. Bridging the spatiotemporal scales of macromolecular transport in crowded biomimetic systems. *Soft Matter* (2019) 15:1200–9. doi:10.1039/c8sm02023j

13. Wulstein DM, Regan KE, Garamella J, McGorty RJ, Robertson-Anderson RM. Topology-dependent anomalous dynamics of ring and linear DNA are sensitive to cytoskeleton crosslinking. *Sci Adv* (2019) 5:eaay5912. doi:10.1126/sciadv.aay5912

14. Lee G, Leech G, Rust MJ, Das M, McGorty RJ, Ross JL, et al. Myosin-driven actin-microtubule networks exhibit self-organized contractile dynamics. *Sci Adv* (2021) 7:eabe4334. doi:10.1126/sciadv.abe4334

15. Cerbino R, Cicuta P. Perspective: Differential dynamic microscopy extracts multi-scale activity in complex fluids and biological systems. *J Chem Phys* (2017) 147:110901. doi:10.1063/1.5001027

16. Cerbino R, Trappe V. Differential Dynamic Microscopy: Probing wave vector dependent dynamics with a microscope. *Phys Rev Lett* (2008) 100:188102. doi:10.1103/physrevlett.100.188102

17. Burov S, Jeon J-H, Metzler R, Barkai E. Single particle tracking in systems showing anomalous diffusion: The role of weak ergodicity breaking. *Phys Chem Chem Phys* (2011) 13:1800–12. doi:10.1039/c0cp01879a

18. Scholz M, Weirich KL, Gardel ML, Dinner AR. Tuning molecular motor transport through cytoskeletal filament network organization. *Soft Matter* (2020) 16:2135–40. doi:10.1039/c9sm01904a

19. Needleman D, Dogic Z. Active matter at the interface between materials science and cell biology. *Nat Rev Mater* (2017) 2:17048–14. doi:10.1038/natrevmats.2017.48

20. Foster PJ, Fürthauer S, Shelley MJ, Needleman DJ. Active contraction of microtubule networks. *eLife* (2015) 4:e10837. doi:10.7554/elife.10837

21. Vale RD. The molecular motor toolbox for intracellular transport. *Cell* (2003) 112:467–80. doi:10.1016/s0092-8674(03)00111-9

22. Sheung JY, Achiriloaie DH, Currie C, Peddireddy K, Xie A, Simon-Parker J, et al. Motor-driven restructuring of cytoskeleton composites leads to tunable time-varying Elasticity. *ACS Macro Lett* (2021) 10:1151–8. doi:10.1021/acsmacrolett.1c00500

23. Lee G, Leech G, Lwin P, Michel J, Currie C, Rust MJ, et al. Active cytoskeletal composites display emergent tunable contractility and restructuring. *Soft Matter* (2021) 17:10765–76. doi:10.1039/d1sm01083b

24. Drechsler M, Giavazzi F, Cerbino R, Palacios IM. Active diffusion and advection in Drosophila oocytes result from the interplay of actin and microtubules. *Nat Commun* (2017) 8:1520. doi:10.1038/s41467-017-01414-6

25. Rezaul K, Gupta D, Semenova I, Ikeda K, Kraikivski P, Yu J, et al. Engineered Tug-of-War between kinesin and Dynein controls direction of microtubule Based transport *in vivo*. *Traffic* (2016) 17:475–86. doi:10.1111/tra.12385

26. Brangwynne CP, Koenderink GH, MacKintosh FC, Weitz DA. Cytoplasmic diffusion: Molecular motors mix it up. *J Cel Biol* (2008) 183:583–7. doi:10.1083/jcb.200806149

27. Ganguly S, Williams LS, Palacios IM, Goldstein RE. Cytoplasmic streaming in Drosophila oocytes varies with kinesin activity and correlates with the microtubule cytoskeleton architecture. *Proc Natl Acad Sci U S A* (2012) 109:15109–14. doi:10.1073/pnas.1203575109

28. Goldstein RE, van de Meent J-W. A physical perspective on cytoplasmic streaming. *Interf Focus* (2015) 5:20150030. doi:10.1098/rsfs.2015.0030

29. Kural C, Serpinskaya AS, Chou YH, Goldman RD, Gelfand VI, Selvin PR. Tracking melanosomes inside a cell to study molecular motors and their interaction. *Proc Natl Acad Sci U S A* (2007) 104:5378–82. doi:10.1073/pnas.0700145104

30. Valentine MT, Perlman Z, Gardel M, Shin J, Matsudaira P, Mitchison T, et al. Colloid Surface Chemistry critically Affects multiple particle tracking measurements of biomaterials. *Biophys J* (2004) 86:4004–14. doi:10.1529/biophysj.103.037812

31. Weigand WJ, Messmore A, Tu J, Morales-Sanz A, Blair DL, Deheyn DD, et al. Active microrheology determines scale-dependent material properties of Chaetopterus mucus. *PLOS ONE* (2017) 12:e0176732. doi:10.1371/journal.pone.0176732

32. Jordan MA, Wilson L. Microtubules as a target for anticancer drugs. *Nat Rev Cancer* (2004) 4:253–65. doi:10.1038/nrc1317

33. Jordan MA, Toso RJ, Thrower D, Wilson L. Mechanism of mitotic block and inhibition of cell proliferation by taxol at low concentrations. *Proc Natl Acad Sci U S A* (1993) 90:9552–6. doi:10.1073/pnas.90.20.9552

34. Allan DB, Caswell T, Keim NC, van der Wel CM, Verweij RW. *soft-matter/trackpy: Trackpy v0.5.0* (2021). doi:10.5281/zenodo.4682814

35. Wulstein DM, Regan KE, Robertson-Anderson RM, McGorty R. Light-sheet microscopy with digital Fourier analysis measures transport properties over large field-of-view. *Opt Express* (2016) 24:20881–94. doi:10.1364/oe.24.020881

36. Jacob JDC, He K, Retterer ST, Krishnamoorti R, Conrad JC. Diffusive dynamics of nanoparticles in ultra-confined media. *Soft Matter* (2015) 11:7515–24. doi:10.1039/c5sm01437a

37. He K, Babaye Khorasani F, Retterer ST, Thomas DK, Conrad JC, Krishnamoorti R. Diffusive dynamics of nanoparticles in Arrays of Nanoposts. *ACS Nano* (2013) 7:5122–30. doi:10.1021/nn4007303

38. Burla F, Sentjabrskaja T, Pletikapic G, van Beugena J, Koenderink GH. Particle diffusion in extracellular hydrogels. *Soft Matter* (2020) 16:1366–76. doi:10.1039/c9sm01837a

39. Cipelletti L, Manley S, Ball RC, Weitz DA. Universal aging features in the restructuring of fractal colloidal gels. *Phys Rev Lett* (2000) 84:2275–8. doi:10.1103/physrevlett.84.2275

40. Giavazzi F, Trappe V, Cerbino R. Multiple dynamic regimes in a coarsening foam. *J Phys : Condens Matter* (2021) 33:024002. doi:10.1088/1361-648x/abb684

41. Alvarado J, Cipelletti L, Koenderink GH. Uncovering the dynamic precursors to motor-driven contraction of active gels. *Soft Matter* (2019) 15:8552–65. doi:10.1039/c9sm01172b

42. Ricketts N, Gurmessa B, Robertson-Anderson M, Microscale R. Mechanics of Plug-and-Play *in vitro* cytoskeleton networks. In: Antonio Bastidas Pacheco G, Ali Kamboh A, editors. *Parasitology and microbiology research*. IntechOpen (2020). doi:10.5772/intechopen.84401

43. Ricketts SN, Francis ML, Farhadi L, Rust MJ, Das M, Ross JL, et al. Varying crosslinking motifs drive the mesoscale mechanics of actin-microtubule composites. *Sci Rep* (2019) 9:12831. doi:10.1038/s41598-019-49236-4

44. Gal N, Lechtman-Goldstein D, Weihs D. Particle tracking in living cells: A review of the mean square displacement method and beyond. *Rheol Acta* (2013) 52:425–43. doi:10.1007/s00397-013-0694-6

45. Cho JH, Cerbino R, Bischofberger I. Emergence of Multiscale dynamics in colloidal gels. *Phys Rev Lett* (2020) 124:088005. doi:10.1103/physrevlett.124.088005

46. Morin A, Lopes Cardozo D, Chikkadi V, Bartolo D. Diffusion, subdiffusion, and localization of active colloids in random post lattices. *Phys Rev E* (2017) 96:042611. doi:10.1103/physreve.96.042611

frontiers | Frontiers in Physics

TYPE Original Research
PUBLISHED 29 November 2022
DOI 10.3389/fphy.2022.1055393

OPEN ACCESS

EDITED BY
Ryan McGorty,
University of San Diego, United States

REVIEWED BY
Francisco Alarcón,
University of Guanajuato, Mexico
Nicoletta Gnan,
National Research Council (CNR), Italy

*CORRESPONDENCE
Alberto Fernández-Nieves,
a.fernandeznieves@ub.edu

SPECIALTY SECTION
This article was submitted to Soft Matter Physics,
a section of the journal
Frontiers in Physics

RECEIVED 27 September 2022
ACCEPTED 14 November 2022
PUBLISHED 29 November 2022

CITATION
Chang Y-W, Cruz-Acuña R, Tennenbaum M, Fragkopoulos AA, García AJ and Fernández-Nieves A (2022), Quantifying epithelial cell proliferation on curved surfaces. *Front. Phys.* 10:1055393. doi: 10.3389/fphy.2022.1055393

Quantifying epithelial cell proliferation on curved surfaces

Ya-Wen Chang[1,2], Ricardo Cruz-Acuña[3,4], Michael Tennenbaum[1], Alexandros A. Fragkopoulos[1], Andrés J. García[4,5] and Alberto Fernández-Nieves[1,6,7,8]*

[1]School of Physics, Georgia Institute of Technology, Atlanta, GA, United States, [2]Department of Chemical Engineering, Texas Tech University, Lubbock, TX, United States, [3]Wallace H. Coulter Department of Biomedical Engineering, Georgia Institute of Technology, Atlanta, GA, United States, [4]Parker H. Petit Institute for Bioengineering and Bioscience, Georgia Institute of Technology, Atlanta, GA, United States, [5]George W. Woodruff School of Mechanical Engineering, Georgia Institute of Technology, Atlanta, GA, United States, [6]Department of Condensed Matter Physics, University of Barcelona, Barcelona, Spain, [7]ICREA-Institucio Catalana de Recerca i Estudis Avancats, Barcelona, Spain, [8]Institute for Complex Systems (UBICS), University of Barcelona, Barcelona, Spain

Out-of-plane curvature is an important, but poorly explored geometric parameter that influences cell behavior. We address the impact of curvature on epithelial proliferation through monitoring how MDCK cells proliferate on planar and curved toroidal hydrogel substrates with a broad range of Gaussian curvatures. We illustrate in detail the imaging processing methodology to characterize curved surfaces and quantify proliferation of cells. We find that MDCK cells grow readily on both curved and flat surfaces and can cover the entire surface of the toroidal structure as long as the initial seeding is uniform. Our analysis shows that proliferation does not depend on Gaussian curvature within the range probed in our experiment, but rather on cell density. Despite epithelial proliferation is insensitive to the curvature range presented in this study, the toroidal-construct fabrication technique and image processing methodology may find utility for probing cell processes like collective migration, as it involves long-range force transmission.

KEYWORDS

curved (hyper-) surfaces, toroid, polymer gels, MDCK cells, cell proliferation, confocal microscopy

1 Introduction

The physical environment of tissue plays a significant role in controlling the dynamic properties of cells, and through mechanical transduction, work synchronously with the chemical cues and biomolecular signaling processes to direct cell proliferation, migration, differentiation, and apoptosis [1–4]. Relevant physical parameters include stiffness, confinement, topology, and geometry. While many of these have been investigated extensively, substrate curvature has recently been highlighted as one of the least explored and perhaps most overlooked properties, despite its omnipresence in the *in vivo* environment [5, 6].

Subcellular topology on the order of nano- and micrometers, like those in fibril collagen matrixes or electrospun fibers, are well known to influence single cell alignment,

cytoskeleton organization, and the direction in which cells grow [7, 8], a phenomena referred to as contact guidance [9]. The influence of larger geometric features that are on the order of a cell or more on cell behavior, however, are relatively unknown. Recently, several groups have shown evidence that macroscale curvature can direct cytoskeleton organization and cell alignment for different cell types, albeit to different extent depending on the cell type and confluency. Bade et al. showed that isolated human vascular smooth muscle cells and mouse embryonic fibroblasts on cylinders align weakly with the cylinder axis when the cylinder radius is larger than the cell size, while cells within confluent monolayers align strongly [10]. The study by Yu et al. showed that the density effect on epithelial cell alignment within confluent monolayers is enhanced on convex surfaces compared to concave surfaces [11]. An elevated cell polarization-marker expression was also found when comparing epithelial growth on curved versus flat surfaces. Curvature also drives distinct migration behavior [12–15] and can induce cell sheet delamination *via* large-scale force sensing and transmission [16, 17]. Madin-Darby Canine Kidney (MDCK) epithelial cells have been shown to sense curvature through nuclear shape changes [18], grow to have different cell heights [19], and elongate [20–23] and even migrate [24] differently depending on substrate curvature. Noteworthily, curvature effects on proliferation, the cellular process associated with cell fate and metastatic state in epithelial tissue, has yet to be explored and will be the focus of this study. Previous studies of cells on patterned planar substrates have suggested that in-plane curvature and tension at the cell interface is an important factor regulating proliferation [25]. However, these geometric confinements do not reflect the out-of-plane curvature seen in native tissue architectures; many epithelial structures in biology have, in fact, out-of-plane curvature, including instentinal villi, tubes and ascini [26, 27].

Fabrication of precisely curved and smooth surfaces at the micrometer-to-millimeter scale is challenging. Methods to create curved substrates such as hemispheres, circular channels, and cylinders include micromachining, photolithography, chemical etching, electrospinning, and replica molding of microfabricated or precision-printed 3D structures [6, 28, 29]. Substrate materials range from glass, quartz, synthetic polymers, polydimethylsiloxane elastomers to hydrogels, with the choice of substrate material often depending on the availability of fabrication techniques. Simple geometries based on spheres and cylinders have been the most used. Curvature at any point along surfaces can be characterized by its Gaussian and mean curvatures, which are the product and the mean of the two principal curvatures at that point, respectively. Tortuous organs and vessels can have a range of positive to negative Gaussian curvatures that are not reflected in spheres or in cylindrical geometries. Spheres or spherical caps have constant positive Gaussian curvature and constant mean curvature, and cylinders have zero Gaussian curvature and constant mean curvature. In this work, we use a supported 3D printing technique [30–32] to generate toroidal hydrogels that have varying signs of Gaussian curvature along their surface.

Other challenges for accessing curvature effects on cell behavior stem from the three-dimensional nature of the resultant constructs, which makes imaging and morphological assessment more difficult than in planar surfaces. Various tools and open-source software or add-ons have been developed for 3D/4D data visualization and morphological analysis of developing tissues [33–35]. Here, we built on our previous work to quantify biofilms and active systems on toroidal surfaces [36, 37], incorporating 3D cell segmentation tools [38], to extract quantitative data on the effect of curvature on epithelial proliferation.

In particular, we investigate the effect of Gaussian curvature on epithelial proliferation by growing model MDCK epithelial cells on toroidal-shaped hydrogels with curvatures on the order of ten cell lengths (sub-millimeters). To quantify how curvature affects proliferation, we develop methods to locate cells on surfaces and evaluate the curvature where each cell attaches. We also introduce a robust 3D segmentation scheme and an intensity comparison method for accurate identification of proliferating cells. We find that proliferation, measured by tracking the percentage of proliferating cells within the population, is independent of Gaussian curvature within the range probed in our experiments. Additionally, we find that proliferation is strongly affected by cell density on both toroidal and planar substrates, suggesting the relevance of acquiring time-dependent data when looking at active, dynamic systems like cells. Our work opens the door to additional studies with surfaces with higher curvatures and different cell types that could model a variety of complex real-life systems.

2 Materials and methods

2.1 Cell culture, substrate preparation, and imaging

2.1.1 Cell culture

Madin-Darby canine kidney cells strain II (MDCK II) were obtained from Sigma-Aldrich and were maintained in Eagle's minimal essential media (EMEM; ATCC) supplemented with fetal bovine serum (Life Technologies) at 10% (vol/vol), penicillin (100 IU/ml), and streptomycin (100 μg/ml) under standard tissue culture conditions (humidified 5% CO_2 and 37°C). MDCKs were passaged at 70~80% confluence from the culture surface and reseeded to the required cell density on hydrogel surfaces.

2.1.2 Fabrication of planar and toroidal substrates

To prepare planar polyacrylamide (PA) hydrogels, solutions containing acrylamide, bis-acrylamide,

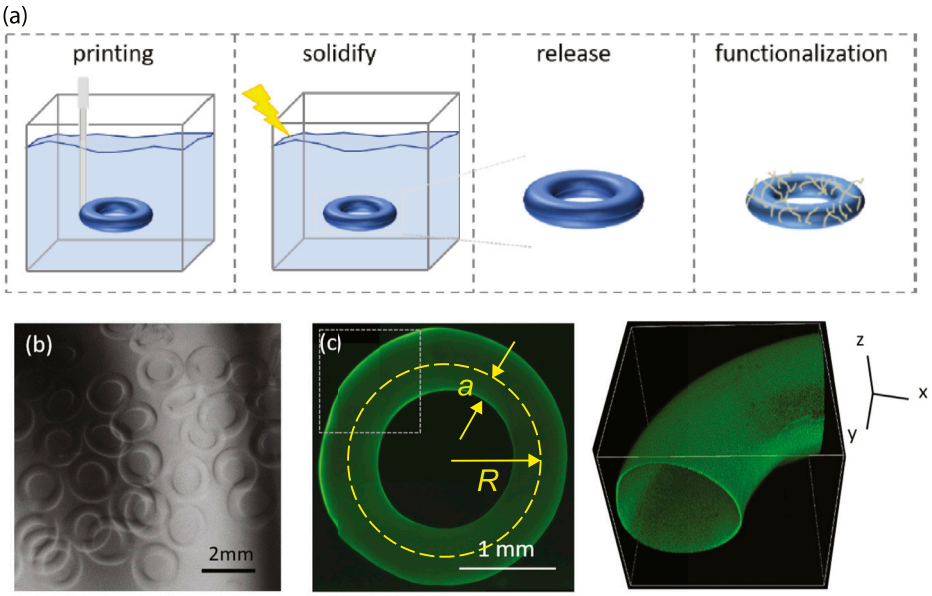

FIGURE 1
(A) Schematic of a hydrogel tori made by printing into a silicone support bath that is subsequently surface-activated *via* protein grafting. **(B)** Image of PA toroidal hydrogels in water after being released from the support bath. The dark regions are shadows of objects placed in the light path to enhance contrast of the hydrogel edge viewed with bright field imaging. **(C)** Confocal images of collagen-coated PA toroidal hydrogels viewed in 2D (left) *via* maximum intensity projection onto the xy-plane and in 3D (right) for the section of the hydrogel highlighted with a square box in the 2D image. Geometric parameters of a torus: ring radius *R* and tube radius *a*.

tetramethylethylenediamine (TEMED), and potassium persulfate were cast into 9 mm-diameter disks using silicone molds (Sigma Press-To-Seal silicone isolator, 2 mm thick) and allowed to polymerize for 15 min at room temperature. The hydrogel disks were then rinsed with and stored in deionized water. To prepare toroidal PA hydrogels, we replace the catalyst TEMED and the persulfate initiator with 0.2% of photoinitiator Irgacure 2959 and added 1% Pluronic F127 to reduce interfacial tension and be able to make small toroidal droplets. Similar to the preparation of toroidal poly-N-isopropylacriamide hydrogels [31], toroidal droplets of the precursor solution were made by injecting the solution *via* a 34-gauge needle into a rotating bath of silicone-oil-based yield stress material consisting of 84% Dow Corning 9041 silicone elastomer blend and 16% 10cst silicone oil, after which the sample was polymerized with a UV-curing spot lamp (BlueWave 75 with 5 mm-lightguide) at an intensity of 370 mW/cm^2 for 10 s. The photopolymerized toroidal PA hydrogels were removed from the yield-stress material and cleaned repeatedly with 0.01% Tween 20 and water for 5 times or until no silicone oil residue remained (Figure 1A). The PA toroidal hydrogels were stored in deionized water at 45°C until use (Figure 1B).

Before cells were seeded onto the hydrogels, the substrates were UV-sterilized and functionalized with collagen I. We adapted the PA hydrogel functionalization scheme of Yamatoto et al [39]. The basis of the procedure consisted in hydrolysing the PA hydrogels with 0.1 M NaOH for 1.5 h at 45°C. The carbonyl groups generated in this way were then activated at room temperature and pH 7 using 1-ethyl-3-[3-dimethylaminopropyl]carbodiimide hydrochloride (EDC) and N-hydroxysulfosuccinimide (NHS) at 36 mM and 72 mM, respectively, after which the unreacted EDC and NHS were removed through repeated rinsing with phosphate buffer. The activated hydrogels were then submerged in a collagen-I solution containing fluorescein-labeled collagen and unlabeled collagen at 1:6 ratio and a total collagen concentration of 0.2 mg/ml for ~12 h at 4°C. Excess collagen was rinsed off with phosphate buffer and the gels were stored in phosphate buffer containing 0.01% sodium azide at 4°C until use (Figure 1C). The fluorescein-labeled collagen was synthesized and purified according to the following procedure [40]: 5 ml of rat tail collagen-I was dialyzed against 0.05 M borate buffer containing 0.04 M NaCl at pH 9.5. The solution was then reacted with fluorescein isothiocyanate overnight at 4°C. The excess fluorescein reagent was removed by dialysis, first against borate buffer and then against 0.2% acetic acid solution. The protein concentration of the fluorescein-labeled collagen solution was determined from the absorption intensity at 280 nm using a Nanodrop Spectrophotometer.

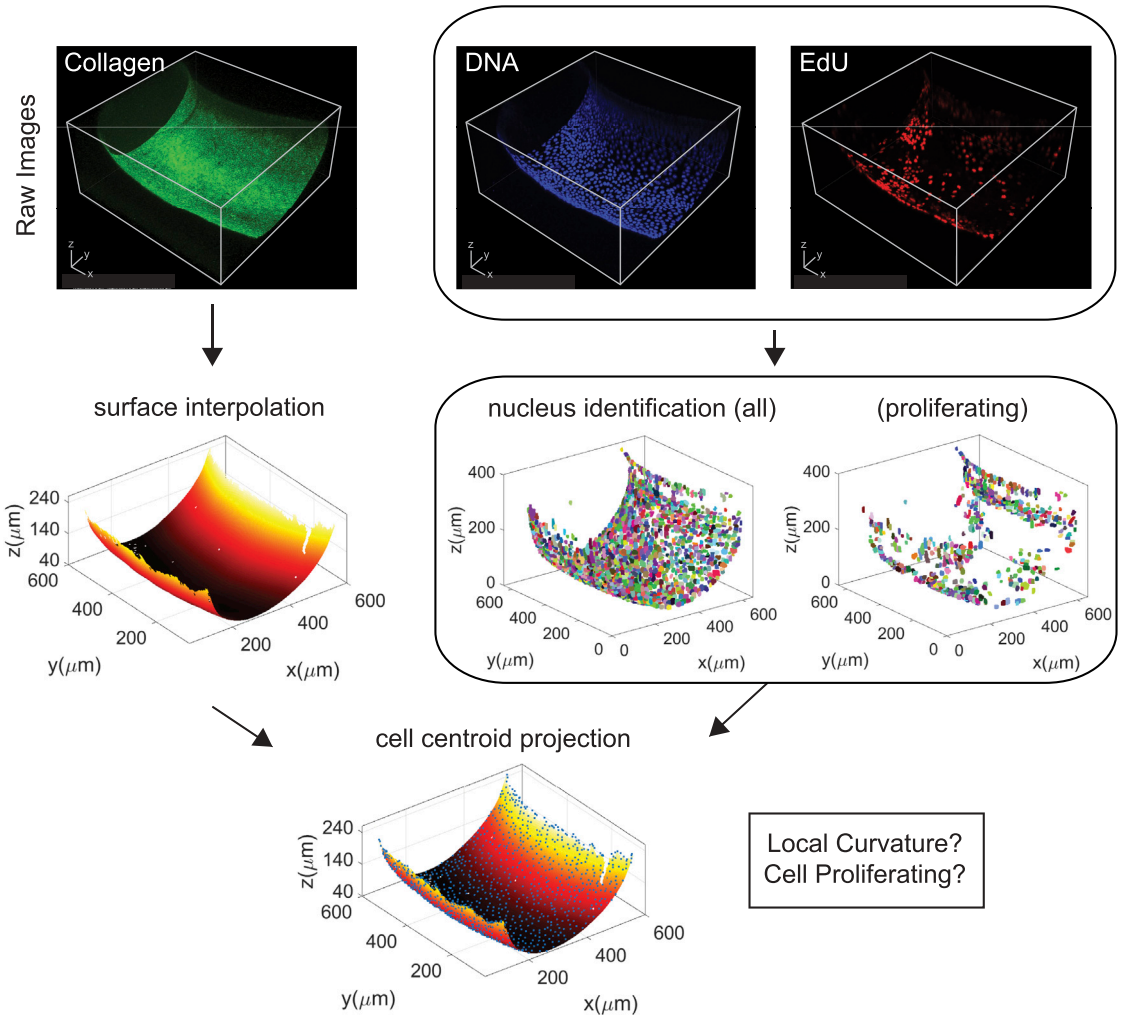

FIGURE 2
Workflow of confocal data processing of MDCK II cells on a toroidal hydrogel section.

2.1.3 Cell treatment and staining

For planar substrate experiments, we place each hydrogel disk in 48 well plates and seeded the cells statically at 300 cells/mm^2. The seeding density was controlled by adding a known number of cells, as estimated using a hemocytometer, to each well. For toroidal substrate experiments, individual toroidal hydrogels were placed into 2-ml tubes containing either 10^4 or 4×10^4 cells/mL and incubated for 2 h with periodic mixing by gently inverting the tube three times every 15 min. The cell-coated toroidal gels were then gently rinsed with fresh medium to remove non-adherent cells and transferred into ultra-low attachment plates. Cells were allowed to spread and grow on the substrate at least overnight before they were assayed. Proliferation was assayed using the Click-iT EdU Imaging Kit (Life Technologies) to identify those that are actively proliferating or synthesizing DNA in the population. The procedure consisted in exposing the cells to EdU-containing growth media for 30 min, and then fixing and staining for EdU incorporation according to the manufacturer's instructions. This was combined with immunostaining: Cells were fixed in 4% formaldehyde, blocked and permeabilized with universal blocking buffer (1% bovine serum albumin, 1% goat serum, 0.1% fish skin gelatin, 0.5% Triton X-100, and 0.05% sodium azide in PBS), and incubated with primary antibody anti-E-cadherin DECMA-1 (Sigma), followed by the secondary antibody goat anti-rat IgG Alexa Fluor 633 (Life Technologies) and nuclei DNA stain (Hoechst 33342). All assayed cells were triple-labeled for E-cadherin, nuclei, and EdU-containing nuclei.

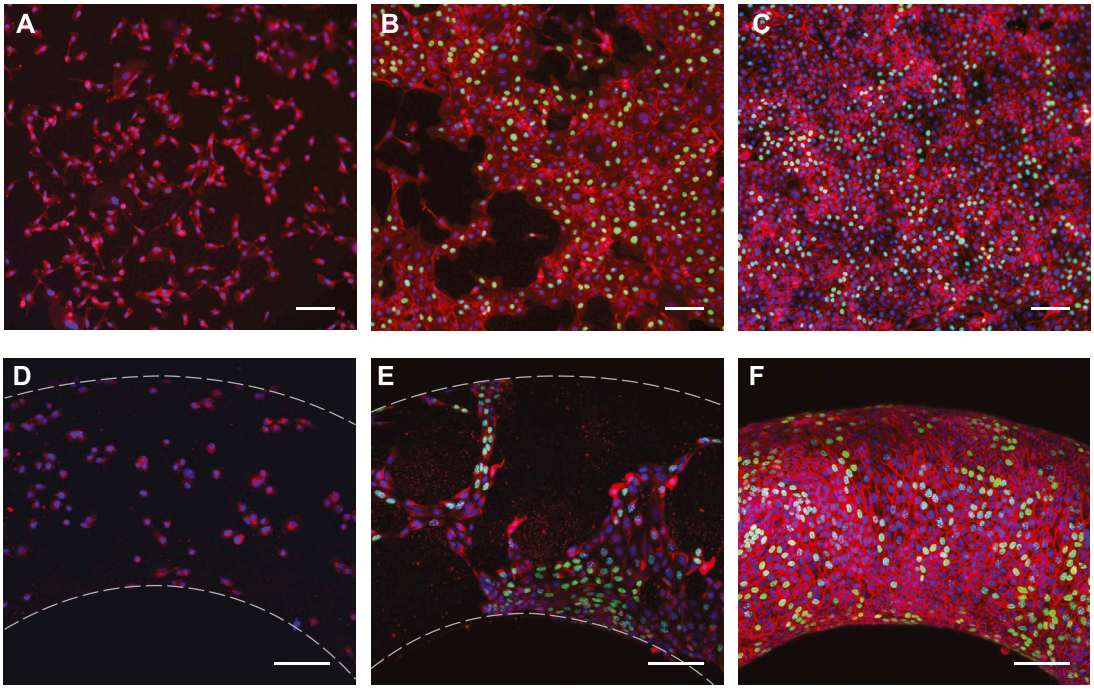

FIGURE 3
Fluorescence microscopy images of MDCK II cells cultured on planar (top row) and toroidal (bottom row) PA hydrogels after **(A,D)** 2 h **(B,E)** 26 h, and **(C,F)** 52 h. Images in the bottom row are maximum intensity projections of confocal stacks. Samples were stained for nuclei (DNA) and E-cadherin, which are false-colored in blue and red, respectively. Newly synthesized DNA was labeled by EdU for the 26 and 52 h samples, shown in green. Scale bars: 100 μm.

2.1.4 Imaging

All stained samples were placed in chambered coverglass for imaging. Planar samples were imaged with a 10× objective on a Nikon Ni-U upright microscope equipped with a Ds-Ri2 CMOS camera. 3D images of toroidal samples were taken on a Nikon A1R confocal microscope using a 20× objective with a resolution of 1.24 μm in the xy-plane and 2 μm along the z-axis. Images were acquired using Nikon NIS-Elements software on both systems. Up to four fluorescent channels were used.

2.2 Image data analysis

All images were processed using custom-written MATLAB codes. Three widefield fluorescent image datasets and five 3D confocal image datasets are used in the analysis. Each dataset consists of a minimum of 24 image stacks from three replicated experiments. Each image stack was analyzed separately and the results were aggregated post-processing.

2.2.1 Multi-channel confocal data processing

Multi-channel confocal images of MDCK II cells on collagen-functionalized toroidal hydrogels were separated into individual z-stacks and processed according to the workflow shown in Figure 2: We start by reconstructing the substrate or adherent surface from the FITC-collagen channel. This is accomplished by image binarization and locating the lowest voxel that contains labeled collagen at each xy-position, followed by surface smoothing. We used Otsu's method to determine the threshold value for binarization, which finds the optimum threshold value that minimizes the total error of fitting two Gaussian distributions, one corresponding to the background and the other to the foreground [41]. We also remove connected objects that have a diameter of 1.2 μm or lower, a cutoff size that efficiently eliminates noise in the data while keeping the large connected volumes that constitute the gel surface. The smoothing algorithm for the interface is based on minimizing the residual sum-of-squares between the input and output interface combined with a penalty function proportional to the resultant curvature [42] (see supplementary information). This method requires an input smoothing parameter s that tunes the strength of the penalty function. The value of the square root of s is an estimate of the size of features in pixels that are smoothed out. Hence, the parameter is chosen to be only a few pixels, large enough to remove the local experimental noise, but small enough to

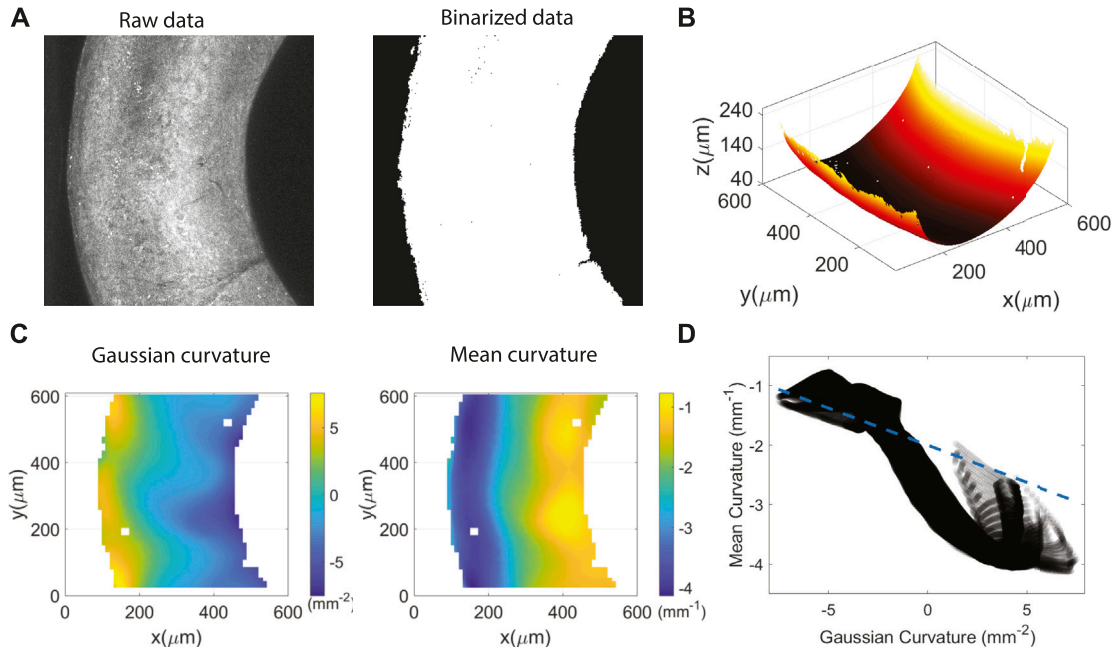

FIGURE 4
Image processing with collagen channel. The dimensions of the toroidal gels are $a \approx 0.2$ mm and $R \approx 0.7$ mm (aspect ratio $\zeta = R/a = 3.5$) as measured by fitting circles to bright field images of multiple tori. **(A)** Maximum intensity projection of the raw data and the binarized data after thresholding. **(B)** 3D view of the interpolated and smoothed surface from locating the lowest point of each xy-postion through the entire image stack. **(C)** Gaussian and mean curvatures of the surface. **(D)** Gaussian versus mean curvature of every point on the surface. The dashed line represents the theoretical relationship between H and K for a torus with a tube radius of 250 μm and a ring radius of 800 μm.

retain the overall curvature of the system. The reconstructed surface is then triangulated (Supplementary Figure S1), and the Gaussian and mean curvatures are measured using local displacement vectors and changes in the surface normal [36].

Separately, we identify each individual cell nucleus from the nuclei channel. First, the image was binarized using the triangle algorithm for thresholding, where the threshold value is determined by constructing a line between the maximum and minimum non-zero values in the histogram and finding the value with the maximum distance from the constructed line to the histogram distribution [43]. This thresholding strategy was chosen due to the absence of an apparent foreground and background in the intensity histograms and is best represented with a single distribution instead of two (see comparison of histogram distribution for collagen versus nuclei channel in Supplementary Figure S2). Then, a 3D cell segmentation routine that uses the watershed algorithm in the CellSegm toolbox [38] was implemented. Connected volumes smaller than a cutoff size were filtered while those larger than a critical size were passed through the watersheld splitting algorithm (Supplementary Figures S3, S4). An additional filtering step consists in measuring the distance of cell centroids to the reconstructed substrate and removing any cell that is over 20 μm away from the surface, as the height of an adhered epithelial monolayer is within 10 μm from the substrate [44]; doing this removes noise and any volume that is not an adherent cell. We then combined the processed data from the FITC-collagen channel and the nuclei channel, namely the reconstructed substrate and the segmented cell volumes, and projected the centroid of each cell onto the surface by finding the closest point on the collagen surface to each cell (Supplementary Figure S5), which enables the identification of each cell with their corresponding adherent substrate location as well as its curvature. Finally, as the EdU stain co-localize with nuclei DNA stain, we referenced the nuclei channel to determine cell volumes within which intensities in the proliferation channel will be integrated and compared to determine which cells were actively proliferating during the assay (Supplementary Figure S6).

2.2.2 Wide-field fluorescence data processing

For cells on planar substrates, only two channels were used for data processing, namely the nuclei and proliferation channel. A 2D version of the cell segmentation routine used in confocal data processing is employed to find the individual cell nuclei.

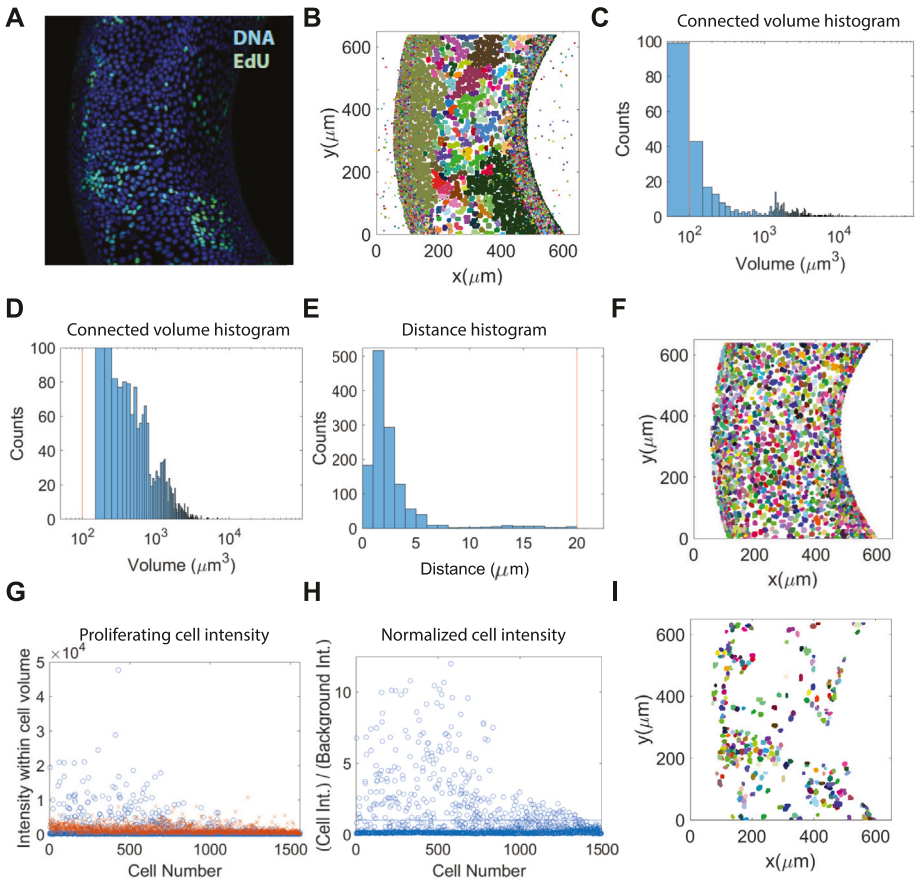

FIGURE 5
Proliferation and nuclei data segmentation results. **(A)** Merged maximum intensity projection from the whole nuclei staining (DNA) and proliferation channel (EdU). **(B)** xy-projected view of processed nuclei data showing connected volume elements. **(C,D)** Cell volume histogram before **(C)** and after **(D)** segmentation. **(E)** Histogram of cell centroid-to-surface distance. The vertical line at 20 μm is the cut-off distance. **(F)** xy-projected view of processed nuclei data after segmentation. **(G)** Sum of voxel intensities in every cell volume of all cells as detected in the proliferation (EdU) channel. The crosses represent the corresponding background intensity, as defined in the text. **(H)** Normalized cell intensity over background intensity for all cell volumes. The horizontal line marks the intensity cutoff for proliferating cells. **(I)** xy-projected view of proliferating cells using the I_{cell}/I_b = 1 cutoff criteria.

3 Results and discussion

3.1 Epithelial proliferation on planar and curved hydrogel surfaces

To examine the role of substrate curvature on cell population growth, we culture MDCK II cells on top of bio-adhesive polymer hydrogels that are toroidal-shaped. The surface of the hydrogel is functionalized with a mixture of unlabeled and FITC-labeled collagen. As a control, we also seed cells on top of planar hydrogels with identical composition and surface treatment. This ensures that all hydrogels, despite shape, have identical mechanical properties and present the same protein density for cell attachment. The elastic modulus of the hydrogels is $\mathcal{O}(10)$ kPa, which is two orders of magnitude stiffer than that of epithelial tissues. The mesh size of such stiff gels is much smaller than the cell size, hence cells cannot penetrate into the bulk hydrogel and remain on the surface. In static cultures with planar substrates, cells sediment on top of the hydrogel and establish spread morphology within 2 hours (Figure 3A). Cells continue proliferating at 26 h and 52 h, and mature into robust epithelial structures, as characterized by the formation of large cohesive cell clusters and mature cell-cell junctions enriched with E-cadherin (Figures 3B,C). For curved substrates, cells are dynamically seeded at concentrations and duration determined experimentally, where consistent cell attachment and robust seeding density control is demonstrated. Note that the agitation method has also been optimized to prevent large location-dependent shear differences, and consequently preferential adhesion during dynamic culture (Supplementary Figure S7). After the initial attachment (Figure 3D), toroidal gel supported cells are maintained in static culture, similarly to those on planar substrates. We do not observe any curvature-directed

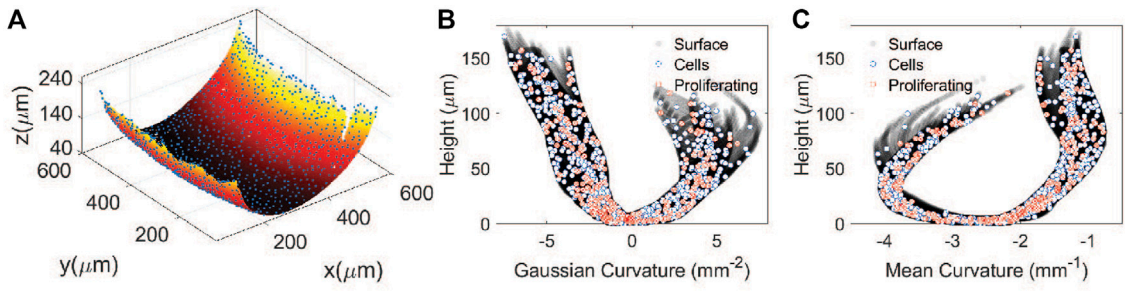

FIGURE 6
Identification of cells with substrate curvature. **(A)** Projection of cell centroids onto the recontructed hydrogel surface. **(B)** Gaussian curvature versus height for each cell. **(C)** Mean curvature versus height for each cell. The filled circles are points on the surface. The open circles represent all the cells and the crosses are proliferating cells.

migration, i.e., there is no depletion of cell clusters from any specific regions on the toroidal gel, as the cell-free domains appear everywhere. Overtime, the cohesive patches merge and cover the entire hydrogel surface with an epithelial monolayer (Figures 3E,F and Supplementary Figure S8).

3.2 Quantifying the role of curvature on cell proliferation

To quantify any spatial variation in proliferation, three-dimensional data containing substrate surface, nuclei of all and proliferating (false-labeled green in Figures 3B,C,E,F) MDCK cells on toroidal gels was collected and analyzed. Multiple image stacks were taken of a single toroid to cover as much of the toroidal surface as possible and three independent toroid were imaged at each condition. Note that only the lower half of the toroid was imaged as the loss in intensity becomes significant as light passes through two layers of dense tissue. Each image stack was then processed as follows:

3.2.1 Surface extraction and curvature calculation

To the confocal images from the collagen channel, we apply an intensity threshold using Otsu's method as described in the methods section for each slice (each z-position) of the image. The threshold is scaled by the mean intensity of each slice, thus ensuring that light attenuation as we move deeper into the sample is accounted for. We then locate the surface by finding the lowest point with labeled collagen, and apply a smoothing parameter that is a few microns to eliminate voxel-level noise and artificial roughness from data extraction (Figures 4A,B). To measure the Gaussian curvature K and the mean curvature H, we follow the methods by Ellis et al. [36], fitting the triangulated surface to the Weingarten curvature matrix, and calculate K and H at each (x,y) point on the surface (Figures 4C,D). The range of Gaussian and mean curvatures sampled in the toroidal section is in the range $(-6, 6)$ mm^{-2} and $(-4, -1)$ mm^{-1}, respectively. Note $H < 0$, as we choose the normal of a curve in an elliptic region of the surface to have negative normal curvature. As expected, the value of K becomes negative towards the inside of the torus, where $|H|$ also becomes smaller. The Gaussian and mean curvature of a torus, a surface obtained by revolving a circle of radius a, about a central axis, vary along the surface and are solely functions of the tube radius a, the ring radius R, and the polar angle in the circular cross section. The structures here, however, are not that of a torus but a toroid. This is better observed by representing each surface point with Gaussian and mean curvature, where we capture the deviation of the surface from that of a torus. The H versus K curve of our hydrogel section (Figure 4D) is only loosely linearly related and does not fit well with the known relationship between the two curvatures: $H = -(\frac{a}{2} + \frac{1}{2a}K)$. This is not surprising as the toroidal drop templates themselves are not perfect tori due to the manufacturing method, which relied on expanding a circular jet in a yield stress material that typically results in the creation of toroidal drops with non-circular cross-sections.

3.2.2 3D cell segmentation and validation of proliferation

For stained nuclei (DNA), we implement the triangle algorithm for thresholding (Supplementary Figure S2). To identify solid objects, i.e., cell nuclei, in our images, we find connected (voxel) elements that are above a certain size to be potential cell nuclei volumes (Figures 5A,B). We then apply the 3D watersheld algorithm to segment cell volumes that do not have distinct boundaries between neighboring cells. Cell volume histogram before and after segmentation show that connected volumes of multiple cells are successfully split into smaller individual volumes, corresponding to single cell nuclei (Figures 5C,D). The last filtering step is based on cell centroid-to-surface distance, where any segmented volume whose centroid distance from the surface is larger than one

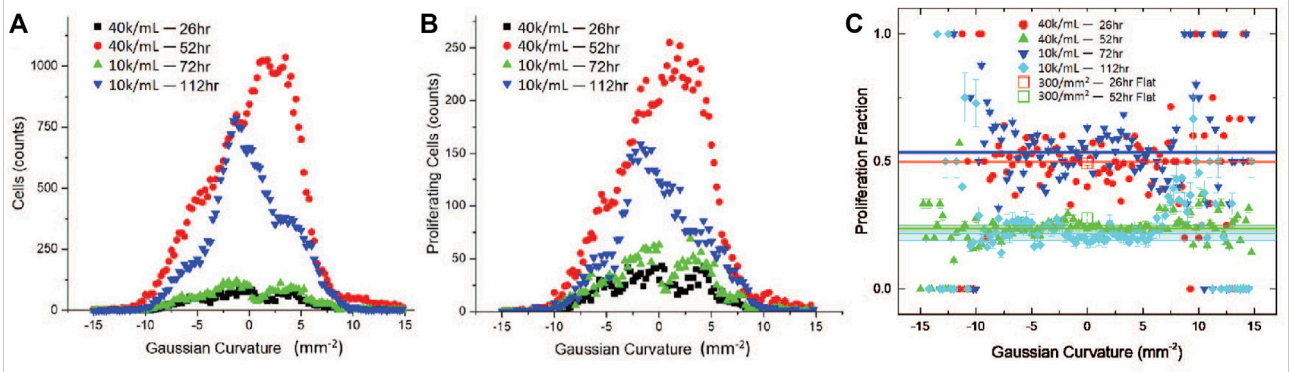

FIGURE 7
Proliferation as a function of curvature. **(A)** Number of cells as a function of Gaussian curvature on toroidal gels. **(B)** Number of proliferating cells as a function of Gaussian curvature on toroidal gels. **(C)** Proliferation fraction as a function of Gaussian curvature on toroidal and planar gel surfaces. Solid symbols are toroidal gel data and open symbols are planar gel data. The horizontal lines are averages over all Gaussian curvature ranges for toroidal data, with standard errors estimated from the background ± 10%.

typical cell size is removed (Figures 5E,F). This removes any remaining noise or cell volumes that are not attached to the gel surface.

To distinguish proliferating from non-proliferating cells, we compare the average intensity within the cell volume to that of the background in the EdU channel. Since most of the voxels in the EdU image stack contains no cells, the background intensity I_b is defined as the average intensity of all voxels $\bar{I}$, plus five standard deviations σ: $I_b = \bar{I} + 5\sigma$. We then add up the voxel intensity within each cell volume, as shown in Figure 5G. To compare with the background intensity, we normalize the cell intensity by the number of voxels in the cell volume, noted as I_{cell}. This is equivalent to taking the mean intensity within the cell volume. The cell is then considered proliferating if its intensity is such that $I_{cell}/I_b > 1$, as shown in Figure 5H. The population whose intensity falls below this threshold is removed, leaving the cell volumes of only the proliferating cells (Figure 5I).

3.2.3 Locating cells on the hydrogel surface

Combining the interpolated surface and segmented nuclei data allow us to re-parametrize each cell in terms of the local curvature of the substrate. The centroid of each cell, obtained from the 3D cell segmentation procedure is projected onto the collagen surface, as shown in Figure 6A. This is done by finding the point on the surface with the shortest distance to the cell centroid. Since curvatures K and H are calculated at each point on the surface (Figures 4C,D), we can map the xyz-coordinate of each projected cell centroid onto the curvature plane. Note that all points on the surface have a unique (x,y) coordinate because we only image the bottom half of the toroid. With this, each proliferating and non-proliferating cell can be identified by its local Gaussian and mean curvatures on the substrate, as shown by the discrete points in Figures 6B,C.

3.2.4 Proliferation versus substrate curvature

To determine whether there are correlations between proliferation and local substrate curvature, we aggregate processed data from multiple image stacks and from at least three replicas with identical conditions, namely seeding density and incubation time, and bin the results by Gaussian curvature. Figures 7A,B show the number of all cells N_{all} and proliferating cells N_p in 0.25 mm^2 Gaussian curvature bins for four different conditions: starting cell concentrations of 4×10^4 cell/mL, incubated for 26 and 52 h, and of 10^4 cell/mL, incubated for 72 and 112 h. The fraction of cycling cells during the 30-min proliferation assay is determined by dividing the number of proliferation cells by all cells N_p/N_{all} in each bin. We find that the proliferation fraction is independent of Gaussian curvatures in the (−10,10) mm^{-2} range of our studies, which include cultures on both toroidal and flat surfaces (Figure 7C). Proliferation fractions outside of this range ($K < -10$ and $K > 10$ mm^{-2}) appear larger, but the data is noisy and not so reliable due to the smaller number of cells counted. Instead, the proliferation fraction depends more strongly on the incubation time and the seeding density of the MDCK II cells. Increasing incubation time for cells on flat substrates and toroidal substrates all show reduction in the proliferation fraction N_p/N_{all}: Proliferation fraction decreased from ~50% to ~25% when the incubation time increased from 26 h to 52 h for cells grown on flat substrates with a seeding area density of ~300/mm^2 and on toroidal gel substrates when seeded at 40K/ml. Similar values were also observed for cells grown on toroidal gels seeded at 10K/ml, but at longer incubation times, namely 72 h and 112 h. This can be explained by considering the time required to reach similar cell densities or cell area for a lower seeding concentration. The decrease in proliferation fraction with increasing incubation time or cell packing density (Table 1),

TABLE 1 Average cell density and proliferation fraction.

Sample	Average density (Cells/mm^2)	N_p/N_{all}
Torus 40k/ml – 26 h	600 ± 300	0.50 ± 0.10
Torus 40k/ml – 52 h	5100 ± 500	0.24 ± 0.10
Torus 10k/ml – 72 h	1300 ± 600	0.53 ± 0.07
Torus 10k/ml – 112 h	5200 ± 600	0.22 ± 0.22
Flat – 26 h	190 ± 70	0.49 ± 0.06
Flat – 52 h	600 ± 200	0.30 ± 0.08

on the other hand, is consistent with collective behavior and contact inhibition of proliferation of epithelial cells, where a progressive decrease in proliferation is observed until mitotic arrest is achieved [45, 46].

4 Conclusion

We have introduced a 3D printing-based fabrication technique to generate "living" toroidal constructs and detailed a method of analysis for quantifying proliferation of epithelial cells on toroidal surfaces. We have shown that reconstructing 3D surfaces and mapping cell positions onto curved substrates can help determine whether curvature plays a role in epithelial proliferation. We found that, within the curvature range of our experiments, carried out on toroidal surfaces of dimensions $a \approx 0.2$ mm and $R \approx 0.7$ mm, proliferation is independent of Gaussian curvature. We also found that proliferation is influenced by the overall cell density regardless of the substrate geometry or seeding density. The results here suggest that curvature at this length scale has no overriding effect on the rate of proliferation for epithelial cells. However, additional work on substrates with higher curvatures, preferably up to one or a couple inverse cell sizes, is desirable to further address whether curvature can be used to affect cell proliferation. In fact, there is recent work reporting that the rate for MDCK cells to achieve confluency changes for curvatures on the order of the inverse cell size [47].

Data availability statement

The raw data supporting the conclusions of this article will be made available by the authors upon reasonable request.

Author contributions

All authors listed have made a substantial, direct, and intellectual contribution to the work and approved it for publication.

Acknowledgments

We thank support from MCIN/AEI/10.13039/501100011033/FEDER, UE (Grant No. PID2021-122369NB-100).

Conflict of interest

The authors declare that the research was conducted in the absence of any commercial or financial relationships that could be construed as a potential conflict of interest.

Publisher's note

All claims expressed in this article are solely those of the authors and do not necessarily represent those of their affiliated organizations, or those of the publisher, the editors and the reviewers. Any product that may be evaluated in this article, or claim that may be made by its manufacturer, is not guaranteed or endorsed by the publisher.

Supplementary material

The Supplementary Material for this article can be found online at: https://www.frontiersin.org/articles/10.3389/fphy.2022.1055393/full#supplementary-material

References

1. Watt FM, Huck WTS. Role of the extracellular matrix in regulating stem cell fate. *Nat Rev Mol Cel Biol* (2013) 14:467–73. doi:10.1038/nrm3620

2. Lo CM, Wang HB, Dembo M, Wang YL. Cell movement is guided by the rigidity of the substrate. *Biophysical J* (2000) 79:144–52. doi:10.1016/s0006-3495(00)76279-5

3. Engler AJ, Sen S, Sweeney HL, Discher DE. Matrix elasticity directs stem cell lineage specification. *Cell* (2006) 126:677–89. doi:10.1016/j.cell.2006.06.044

4. Haga H, Irahara C, Kobayashi R, Nakagaki T, Kawabata K. Collective movement of epithelial cells on a collagen gel substrate. *Biophysical J* (2005) 88:2250–6. doi:10.1529/biophysj.104.047654

5. Baptista D, Teixeira L, van Blitterswijk C, Giselbrecht S, Truckenmüller R. Overlooked? Underestimated? Effects of substrate curvature on cell behavior. *Trends Biotechnol* (2019) 37:838–54. doi:10.1016/j.tibtech.2019.01.006

6. Callens SJP, Uyttendaele RJC, Fratila-Apachitei LE, Zadpoor AA. Substrate curvature as a cue to guide spatiotemporal cell and tissue organization. *Biomaterials* (2020) 232:119739. doi:10.1016/j.biomaterials.2019.119739

7. Lanfer B, Hermann A, Kirsch M, Freudenberg U, Reuner U, Werner C, et al. Directed growth of adult human white matter stem cell–derived neurons on aligned fibrillar collagen. *Tissue Eng A* (2010) 16:1103–13. doi:10.1089/ten.tea.2009.0282

8. Rovensky Y, Samoilov V. Morphogenetic response of cultured normal and transformed fibroblasts, and epitheliocytes, to a cylindrical substratum surface. Possible role for the actin filament bundle pattern. *J Cel Sci* (1994) 107:1255–63. doi:10.1242/jcs.107.5.1255

9. Flemming RG, Murphy CJ, Abrams GA, Goodman SL, Nealey PF. Effects of synthetic micro- and nano-structured surfaces on cell behavior. *Biomaterials* (1999) 20:573–88. doi:10.1016/s0142-9612(98)00209-9

10. Bade ND, Kamien RD, Assoian RK, Stebe KJ. Curvature and Rho activation differentially control the alignment of cells and stress fibers. *Sci Adv* (2017) 3: e1700150. doi:10.1126/sciadv.1700150

11. Yu SM, Oh JM, Lee J, Lee-Kwon W, Jung W, Amblard F, et al. Substrate curvature affects the shape, orientation, and polarization of renal epithelial cells. *Acta Biomater* (2018) 77:311–21. doi:10.1016/j.actbio.2018.07.019

12. Pieuchot L, Marteau J, Guignandon A, Dos Santos T, Brigaud I, Chauvy PF, et al. Curvotaxis directs cell migration through cell-scale curvature landscapes. *Nat Commun* (2018) 9:3995. doi:10.1038/s41467-018-06494-6

13. Yevick HG, Duclos G, Bonnet I, Silberzan P. Architecture and migration of an epithelium on a cylindrical wire. *Proc Natl Acad Sci U S A* (2015) 112:5944–9. doi:10.1073/pnas.1418857112

14. Bade ND, Xu T, Kamien RD, Assoian RK, Stebe KJ. Gaussian curvature directs stress fiber orientation and cell migration. *Biophysical J* (2018) 114:1467–76. doi:10.1016/j.bpj.2018.01.039

15. Xi W, Sonam S, Beng Saw T, Ladoux B, Teck Lim C. Emergent patterns of collective cell migration under tubular confinement. *Nat Commun* (2017) 8:1517. doi:10.1038/s41467-017-01390-x

16. Broaders KE, Cerchiari AE, Gartner ZJ. Coupling between apical tension and basal adhesion allow epithelia to collectively sense and respond to substrate topography over long distances. *Integr Biol* (2015) 7:1611–21. doi:10.1039/C5IB00240K

17. Yamashita T, Kollmannsberger P, Mawatari K, Kitamori T, Vogel V. Cell sheet mechanics: How geometrical constraints induce the detachment of cell sheets from concave surfaces. *Acta Biomater* (2016) 45:85–97. doi:10.1016/j.actbio.2016.08.044

18. Assoian RK, Bade ND, Cameron CV, Stebe K. Cellular sensing of micron-scale curvature: A frontier in understanding the microenvironment. *Open Biol* (2019) 9: 190155. doi:10.1098/rsob.190155

19. Luciano M, Xue SL, De Vos WH, Redondo-Morata L, Surin M, Lafont F, et al. Cell monolayers sense curvature by exploiting active mechanics and nuclear mechanoadaptation. *Nat Phys* (2021) 17:1382–90. doi:10.1038/s41567-021-01374-1

20. Harmand N, Huang A, Henon S. 3D shape of epithelial cells on curved substrates. *Phys Rev X* (2021) 11:031028. doi:10.1103/physrevx.11.031028

21. Yu SM, Li B, Amblard F, Granick S, Cho YK. Adaptive architecture and mechanoresponse of epithelial cells on a torus. *Biomaterials* (2021) 265:120420. doi:10.1016/j.biomaterials.2020.120420

22. Rougerie P, Pieuchot L, Silva dos Santos R, Marteau J, Bigerelle M, Chauvy P, et al. Topographical curvature is sufficient to control epithelium elongation. *Sci Rep* (2020) 10:14784. doi:10.1038/s41598-020-70907-0

23. Yip AK, Huang P, Chiam KH. Cell-cell adhesion and cortical actin bending govern cell elongation on negatively curved substrates. *Biophysical J* (2018) 114: 1707–17. doi:10.1016/j.bpj.2018.02.027

24. Werner M, Petersen A, Kurniawan NA, Bouten CVC. Cell-perceived substrate curvature dynamically coordinates the direction, speed, and persistence of stromal cell migration. *Adv Biosyst* (2019) 3:1900080. doi:10.1002/adbi.201900080

25. Nelson CM, Jean RP, Tan JL, Liu WF, Sniadecki NJ, Spector AA, et al. Emergent patterns of growth controlled by multicellular form and mechanics. *Proc Natl Acad Sci U S A* (2005) 102:11594–9. doi:10.1073/pnas.0502575102

26. Maechler FA, Allier C, Roux A, Tomba C. Curvature dependent constraints drive remodeling of epithelia. *J Cel Sci* (2019) 132:jcs222372. doi:10.1242/jcs.222372

27. Schock F, Perrimon N. Molecular mechanisms of epithelial morphogenesis. *Annu Rev Cel Dev Biol* (2002) 18:463–93. doi:10.1146/annurev.cellbio.18.022602.131838

28. Liu T, Chien CC, Parkinson L, Thierry B. Advanced micromachining of concave microwells for long term on-chip culture of multicellular tumor spheroids. *ACS Appl Mater Inter* (2014) 6:8090–7. doi:10.1021/am500367h

29. Bidan CM, Kommareddy KP, Rumpler M, Kollmannsberger P, Fratzl P, Dunlop JWC. Geometry as a factor for tissue growth: Towards shape optimization of tissue engineering scaffolds. *Adv Healthc Mater* (2013) 2:186–94. doi:10.1002/adhm.201200159

30. Pairam E, Le H, Fernández-Nieves A. Stability of toroidal droplets inside yield stress materials. *Phys Rev E* (2014) 90:021002. doi:10.1103/PhysRevE.90.021002

31. Chang YW, Dimitriyev MS, Souslov A, Nikolov SV, Marquez SM, Alexeev A, et al. Extreme thermodynamics with polymer gel tori: Harnessing thermodynamic instabilities to induce large-scale deformations. *Phys Rev E* (2018) 98:020501. doi:10.1103/PhysRevE.98.020501

32. Bhattacharjee T, Zehnder SM, Rowe KG, Jain S, Nixon RM, Sawyer WG, et al. Writing in the granular gel medium. *Sci Adv* (2015) 1:e1500655. doi:10.1126/sciadv.1500655

33. Barbier de Reuille P, Routier-Kierzkowska AL, Kierzkowski D, Bassel GW, Schüpbach T, Tauriello G, et al. MorphoGraphX: A platform for quantifying morphogenesis in 4D. *eLife* (2015) 4:e05864. doi:10.7554/eLife.05864

34. Heller D, Hoppe A, Restrepo S, Gatti L, Tournier AL, Tapon N, et al. EpiTools: An open-source image analysis toolkit for quantifying epithelial growth dynamics. *Dev Cel* (2016) 36:103–16. doi:10.1016/j.devcel.2015.12.012

35. Royer LA, Weigert M, Günther U, Maghelli N, Jug F, Sbalzarini IF, et al. ClearVolume: Open-source live 3D visualization for light-sheet microscopy. *Nat Methods* (2015) 12:480–1. doi:10.1038/nmeth.3372

36. Ellis PW, Pearce DJG, Chang YW, Goldsztein G, Giomi L, Fernandez-Nieves A. Curvature-induced defect unbinding and dynamics in active nematic toroids. *Nat Phys* (2017) 14:85–90. doi:10.1038/nphys4276

37. Chang YW, Fragkopoulos AA, Marquez SM, Kim HD, Angelini TE, Fernandez-Nieves A. Biofilm formation in geometries with different surface curvature and oxygen availability. *New J Phys* (2015) 17:033017. doi:10.1088/1367-2630/17/3/033017

38. Hodneland E, Kögel T, Frei DM, Gerdes HH, Lundervold A. CellSegm - a MATLAB toolbox for high-throughput 3D cell segmentation. *Source Code Biol Med* (2013) 8:16. doi:10.1186/1751-0473-8-16

39. Yamamoto M, Yanase K, Tabata Y. Generation of type I collagen gradient in polyacrylamide hydrogels by a simple diffusion-controlled hydrolysis of amide groups. *Materials* (2010) 3:2393–404. doi:10.3390/ma3042393

40. Baici A, Cohen G, Fehr K, Böni A. A handy assay for collagenase using reconstituted fluorescein-labeled collagen fibrils. *Anal Biochem* (1980) 108:230–2. doi:10.1016/0003-2697(80)90574-6

41. Otsu N. A threshold selection method from gray-level histograms. *IEEE Trans Syst Man Cybern* (1979) 9:62–6. doi:10.1109/tsmc.1979.4310076

42. Garcia D. Robust smoothing of gridded data in one and higher dimensions with missing values. *Comput Stat Data Anal* (2010) 54:1167–78. doi:10.1016/j.csda.2009.09.020

43. Zack GW, Rogers WE, Latt SA. Automatic measurement of sister chromatid exchange frequency. *J Histochem Cytochem* (1977) 25:741–53. doi:10.1177/25.7.70454

44. Zehnder S, Suaris M, Bellaire M, Angelini T. Cell volume fluctuations in MDCK monolayers. *Biophysical J* (2015) 108:247–50. doi:10.1016/j.bpj.2014.11.1856

45. Puliafito A, Hufnagel L, Neveu P, Streichan S, Sigal A, Fygenson DK, et al. Collective and single cell behavior in epithelial contact inhibition. *Proc Natl Acad Sci U S A* (2012) 109:739–44. doi:10.1073/pnas.1007809109

46. Venugopal B, Mogha P, Dhawan J, Majumder A. Cell density overrides the effect of substrate stiffness on human mesenchymal stem cells' morphology and proliferation. *Biomater Sci* (2018) 6:1109–19. doi:10.1039/C7BM00853H

47. van Gaal RC, Miltenburg RPRS, Kuriniawan NA, Bouten CVC, Dankers PYW. Renal epithelial cell responses to supramolecular thermoplastic elastomeric concave and convex structures. *Adv Mater Inter* (2021) 8:20001490. doi:10.1002/admi.202001490

frontiers | Frontiers in Physics

TYPE Original Research
PUBLISHED 09 January 2023
DOI 10.3389/fphy.2022.1007861

OPEN ACCESS

EDITED BY
Alberto Fernandez-Nieves,
Catalan Institution for Research and Advanced Studies (ICREA), Spain

REVIEWED BY
Gerhard Jung,
UMR5221 Laboratoire Charles Coulomb (L2C), France
Hai-Bin Yu,
Huazhong University of Science and Technology, China

*CORRESPONDENCE
Norihiro Oyama,
Norihiro.Oyama.vb@mosk.tytlabs.co.jp
Takeshi Kawasaki,
kawasaki@r.phys.nagoya-u.ac.jp

SPECIALTY SECTION
This article was submitted to Soft Matter Physics, a section of the journal Frontiers in Physics

RECEIVED 31 July 2022
ACCEPTED 05 December 2022
PUBLISHED 09 January 2023

CITATION
Oyama N, Koyama S and Kawasaki T (2023), What do deep neural networks find in disordered structures of glasses? *Front. Phys.* 10:1007861. doi: 10.3389/fphy.2022.1007861

What do deep neural networks find in disordered structures of glasses?

Norihiro Oyama[1]*, Shihori Koyama[1] and Takeshi Kawasaki[2]*

[1]Toyota Central R&D Labs, Inc., Tokyo, Japan, [2]Department of Physics, Nagoya University, Nagoya, Japan

Glass transitions are widely observed in various types of soft matter systems. However, the physical mechanism of these transitions remains elusive despite years of ambitious research. In particular, an important unanswered question is whether the glass transition is accompanied by a divergence of the correlation lengths of the characteristic static structures. In this study, we develop a deep-neural-network-based method that is used to extract the characteristic local meso-structures solely from instantaneous particle configurations without any information about the dynamics. We first train a neural network to classify configurations of liquids and glasses correctly. Then, we obtain the characteristic structures by quantifying the grounds for the decisions made by the network using Gradient-weighted Class Activation Mapping (Grad-CAM). We consider two qualitatively different glass-forming binary systems, and through comparisons with several established structural indicators, we demonstrate that our system can be used to identify characteristic structures that depend on the details of the systems. Moreover, the extracted structures are remarkably correlated with the non-equilibrium aging dynamics in thermal fluctuations.

KEYWORDS

deep neural networks, machine learning, molecular dynamics simulations, glass transition, dynamical heterogeneity of liquid state

1 Introduction

When a liquid is cooled while preventing crystallization by quenching or adding impurities, a liquid state can be maintained below melting temperature, resulting in a so-called supercooled liquid state. Further cooling of the supercooled liquid results in a dramatic increase in the viscosity of the liquid and yields a glass (more generally, an amorphous solid). In such a system, the particle motion is frozen, and the structure remains disordered. Various materials, e.g. oxides, alloys, polymers, and colloids, take on glassy states. Glassy materials are generally considered disordered and homogeneous because they basically cannot be distinguished from simple liquids that are also disordered in structure using analytical methods such as neutron, X-ray, or light scattering and other two-body correlations in the density field. However, dramatic changes to their properties can occur, for example, a 15-order-of-magnitude increase in the viscosity from a temperature change of only approximately 20% [1]. Although the glass transition

phenomenon has been studied for more than 150 years, its mechanism has not yet been clarified [2–5].

Heterogeneity in particle motion develops in supercooled liquids near the glass transition temperature, and the spatial length scale increases on such a glass transition [6–12]. This behavior is called dynamic heterogeneity and is a potential cause for the rapid increase in viscosity at the glass transition point. However, to date, the origin of this dynamic heterogeneity has not been clarified; in particular, questions remain as to whether it is formed entirely dynamically or whether a static structure exists in the background. The "dynamical facilitation theory" describes the heterogeneity associated with glass transitions as a fully dynamic phenomenon, and explains the experimental results and numerical analysis of glass transitions [13]. In contrast, "the theory of random first-order transition" (RFOT), which considers the glass transition as a thermodynamic phase transition and proposes a scenario in which a static conceptual structure called a "mosaic" develops, also explains the experimental results and numerical analysis of glass transitions [4, 14]. Thus, although these theories are contradictory in terms of whether the glass transition is a purely dynamic transition or a thermodynamic phase transition governed by a static structure, they can explain various aspects of the glass transition phenomenon. Hence, in the current state, there appears to be no definitive theory for understanding the full picture of glass transitions.

Many attempts have been made to explore the specific structures that exist in supercooled liquids. For instance, icosahedral-like structures in metallic glasses [15, 16] and medium-range crystalline order in colloidal glasses with small particle-size dispersity have been found [17–20]. Order parameters are introduced on a system-by-system basis to extract these characteristic structures, but no order parameter applicable to *all* amorphous solids has been found. It is also unclear whether such characteristic structures are universal; this is a topic of active debate. Therefore, elucidating the presence or absence of a universal structure in amorphous solids is a significant and challenging problem in fundamental physics. Tong and Tanaka recently developed a new order parameter consisting of the bond angles of particle structures and successfully extracted the characteristic structures correlated with particle dynamics for a wide range of glass-forming systems, including binary mixtures and polydisperse glassy systems with large particle size dispersions [21, 22]. However, as indicated in the corresponding literature [21, 22], this method has not been able to extract the characteristic structures in the Kob–Andersen system [23], a typical glass-forming model, and consequently, attempts to develop a universal structural analysis method for a variety of glass-like systems continues to the present day. We mention that as another branch of examples of promising static information-based approaches, a method relying on the Franz-Parisi potential has been proposed [24]. Its effectiveness was demonstrated by the quantitative correspondence with the structural relaxation time. The recently proposed microscopic version of a similar Franz-Parisi potential-based quantity would allow us to specify the local characteristic structures that govern the dynamics on the purely static basis [25].

In recent years, machine-learning approaches have been widely used to investigate the characteristic structures governing glass dynamics [26–30]. In particular, recent studies have successfully predicted the dynamics from the static structure in Kob–Andersen systems by learning from a large amount of structural data, as well as the corresponding dynamic data, using graph neural networks [28, 29]. In addition to these supervised approaches, unsupervised counterparts have also been applied to the extraction of characteristic structures from glasses, pioneered by Ronhovde and co-workers [31, 32]. Interestingly, many researchers have recently reported that the structures extracted using unsupervised methods [27, 30] exhibit correlations with the long-time dynamics, despite no information about the dynamics being provided during the training. However, although machine learning is very promising for exploring the structures of glasses, accurate learning (including preparation of the training data) is computationally expensive, and the results are difficult to interpret.

In this work, we propose a method to extract the characteristic multi-particle structures of glasses solely from the static configurations using a deep learning-based approach. To this end, we work on the classification problem for the random structures in glasses and liquids using a convolutional neural network (CNN) [33] and then identify the structures that the CNN relied on to make decisions using gradient-weighted class activation mapping (Grad-CAM) [34]. We applied our proposed method to two representative glass-forming liquid systems and compared the obtained structures with well-established structural indicators. The results demonstrate that the proposed method can extract qualitatively different characteristic structures in a system-detail-dependent manner. Surprisingly, although our method does not refer to information about the dynamics during the learning process and extracts the characteristic structure solely from the instantaneous static configurations, the obtained structures strongly correlate with the non-equilibrium aging dynamics.

The remainder of this paper is organized as follows. In Section 2, we summarize the simulation methods and protocols used for sample preparation for the deep-learning tasks. In Section 3, we introduce the CNN and Grad-CAM, and provide a brief explanation of the established structural indicators used as a reference. In Section 4, the results of the structural analyses are presented, and the correlation between distinct indicators, as well as the predictability of our method with respect to the dynamics, is discussed. Finally, in Section 5, we provide a summary of this study and an overview of future research directions.

TABLE 1 Summary of model parameters.

	m_A	m_B	σ_{AA}	σ_{AB}	σ_{BB}	ϵ_{AA}	ϵ_{AB}	ϵ_{BB}	N_A	N_B	ρ	σ^*	ϵ^*	m^*	r_{ij}^c
KAM	1.0	1.0	1.0	0.8	0.88	1.0	1.5	0.5	1300	700	1.2	σ_{AA}	ϵ_{AA}	m_A	$2.5\sigma_{ij}$
ABM	1.0	1.0	5/6	1.0	7/6	1.0	1.0	1.0	1000	1000	1.09	σ_{AB}	ϵ_{AB}	m_A	$3.0\sigma_{ij}$

2 Simulations

2.1 System setups

In this study, we consider two distinct systems: the Kob–Andersen model (KAM) [23] and the additive binary mixture (ABM) [35]. Both systems are two-dimensional (2D) and are described by the Lennard–Jones (LJ) potential with linear smoothing terms:

$$\phi_{ij}(r) = \phi_{ij}^{\star}(r) - \phi_{ij}^{\star}\left(r_{ij}^{c}\right) - \left(r - r_{ij}^{c}\right)\frac{d\phi_{ij}^{\star}}{dr}|_{r=r_{ij}^{c}}, \quad (1)$$

$$\phi_{ij}^{\star}(r) = 4\epsilon_{ij}\left[\left(\frac{\sigma_{ij}}{r}\right)^{12} - \left(\frac{\sigma_{ij}}{r}\right)^{6}\right], \quad (2)$$

where the subscript ij indicates that the variable is between particles i and j, ϵ_{ij} sets the energy scale, σ_{ij} determines the interaction range, and r_{ij}^c is the cutoff length. The dynamics of the particles obey ϕ_{ij}, whereas $\phi_{ij}^{\star}$ is the reference standard LJ potential. The smoothed LJ potential ϕ guarantees the continuity of the potential and force at cutoff distance $r = r_{ij}^c$, thus eliminating undesired artifact effects owing to the introduction of the cutoff [36].

Both systems are composed of two different types of particles (A and B) and are characterized by different parameter sets, such as ϵ_{ij} and σ_{ij}. In the case of the KAM, the LJ parameters are non-additive: $\sigma_{AA} = 1$, $\sigma_{AB} = 0.8$, $\sigma_{BB} = 0.88$, $\epsilon_{AA} = 1$, $\epsilon_{AB} = 1.5$, and $\epsilon_{BB} = 0.5$. Therefore, the concept of "particle size" is not well defined in the KAM system. For the ABM, on the other hand, the parameters are simply additive; thus, we can unambiguously say that particle A is small, and B is large (that is, $\sigma_{AA} = 5/6$, $\sigma_{AB} = 1$, $\sigma_{BB} = 7/6$, and $\epsilon_{ij} = 1$) regardless of the combination of types of particles i and j.

All observables were non-dimensionalized using characteristic length σ^*, characteristic energy ϵ^*, and particle mass m^* (the characteristic variables are listed in Table 1). The total number of particles was fixed at $N = N_A + N_B = 2000$. The number density $\rho = N/L^2$ and the number ratio of the two-particle species N_A/N_B also differ between the two systems, i.e., the KAM and ABM. With the values of ρ used here, the systems entered the glassy phase once the temperature was sufficiently low [23, 35]. Information about the parameters mentioned here is summarized in Table 1. Although we consider only 2D systems in this article for the sake of simplicity, we stress that all the analyses here can be easily extended to three-dimensional systems, which will be performed in the future.

2.2 Sample preparation protocol

We performed molecular dynamics (MD) simulations using the open-source Large-scale Atomic/Molecular Massively Parallel Simulator (LAMMPS: https://www.lammps.org/). We generated samples *via* NVT simulations using the Nosé–Hoover thermostat. Periodic boundary conditions were set in all directions. In this study, we aim to address a simple binary classification problem. For the two classes, we chose configurations at the temperature where the dynamic slowing-down starts at ($T_{\mathrm{L}} = 0.8$ for KAM and $T_{\mathrm{L}} = 2.0$ for ABM) and at a very low temperature ($T_{\mathrm{G}} = 0.05$ for both models). For both KAM and ABM, we first generated 5000 independent random configurations (4,000 were used for training, 400 for validation, and 600 for the test data) and equilibrated them at a very high temperature of $T = 4.0$. The obtained configurations were then cooled at a constant cooling rate ($\dot{T} \approx 8.33 \times 10^{-5}$), and the samples for the classification tasks were obtained at the desired temperatures T_{L} and T_{G}. The samples at T_{L} correspond to "equilibrium" supercooled liquids in the sense that their dynamics exhibit time-translational invariance, whereas those at T_{G} are regarded as "non-equilibrium" glasses in the sense that they are expected to experience aging. Note that, judging from the evolution of the potential energy of the system as a function of the temperature (Supplementary Figure S6) [37], crystallization is avoided in both systems at this cooling rate (i.e., we did not observe any discontinuous jumps in the energy). Consequently, the radial distribution function $g(r)$ of the configurations at T_{G} does not show any signs of global crystallization (Supplementary Figure S7).

3 Analytical methods

We train a neural network to distinguish two classes of systems, "glass" and "liquid," based purely on the instantaneous configurations. Then, the characteristic structures of glasses are identified by extracting the meso-scale structures that the trained network relied on to provide a correct classification. In this section, we explain the methods used to achieve these classifications and identifications of characteristic structures.

3.1 Convolutional neural network (CNN)

We first perform supervised learning to train a CNN [33, 38] to predict whether a given configuration is glass or liquid. Following Ref. [38] in which the authors tackled a similar classification task successfully, our network has no pooling layers. It is then simply composed of three convolutional layers and subsequent activations (the rectified linear units), followed by the fully connected layer, dropout layer, and final fully connected layer as the output layer. Note that, although we apply the "softmax" function subsequently to obtain the final results, the output layer of the network is the fully connected one to make it compatible with Grad-CAM, as explained in Section 3 2. The full details of the network and learning protocol, including the precise values of the hyperparameters, are summarized in the Supplementary Material. After training, the softmax layer outputs a value in the range of [0,1] which can then be interpreted as the probability for a configuration to be assigned to one of these classes.

Importantly, when we feed the particle configurations, $\rho(\boldsymbol{r}) = \sum_i^N \delta(\boldsymbol{r} - \boldsymbol{r}_i)$, obtained from the MD simulations into the CNN, they are gridized by the mapping operator $\mathcal{M}$: $\tilde{\rho} \equiv \mathcal{M}(\rho)$ (see Supplementary Material for technical details). Here, the tilde indicates that the variable is grid-based. We also mention that in the padding process at the convolutional layers, we use circular padding to properly consider the periodic boundary conditions.

3.2 Gradient-weighted class activation mapping (Grad-CAM)

Once a CNN is able to classify glasses and liquids correctly after training, we aim to extract the characteristic mesoscale structures that the CNN relies on when classifying. This identification of crucial information is called "class activation mapping" (CAM). The first-proposed simple CAM [39] assumed a global average pooling at the end of the network, and thus, cannot be utilized for networks with different types of architectures. This problem has been solved using a method called gradient-weighted class activation mapping (Grad-CAM) [34]. In Grad-CAM, CAM is calculated based on the differential of the output of the network with respect to the feature maps as

$$\alpha_m^C = \frac{1}{Z}\sum_k^u \sum_l^v \frac{\partial y^C}{\partial A_{k,l}^m}, \tag{3}$$

$$\tilde{L}^C = ReLU\left(\sum_m \alpha_m^C \tilde{A}^m\right), \tag{4}$$

where y^C is the score for class C ($C \in \{glass, liquid\}$ in the current setup) before softmax, $\tilde{A}^m$ is the m-th feature map activation of a convolutional layer, $A_{k,l}^m$ is the (k, l) component of $\tilde{A}^m$, and $Z = uv$ is the normalizing factor for the global pooling calculation. The rectified linear unit $ReLU$ simply returns x if $x > 0$ and zero otherwise. Thus, in this Grad-CAM method, the characteristic part of the input information is identified as the weighted sum of the feature maps after a specified convolution layer (usually the last layer), and the weights are obtained depending on the global average of the sensitivity (gradient) of the output with respect to each pixel of the feature maps. Importantly, this method can be applied to networks with any architecture if the backpropagation is tractable.

The results presented in this paper are all particle-based Grad-CAM scores, $\Gamma = \sum_i^N \Gamma_i \delta(\boldsymbol{r} - \boldsymbol{r}_i)$, obtained using the inverse mapping operator $\mathcal{M}^{-1}$: $\Gamma \equiv \mathcal{M}^{-1}(\tilde{L}^C)$, where Γ_i is the Grad-CAM score of particle i. We simply call Γ the Grad-CAM score. Note that, hereinafter, all particle-based variables are coarse-grained and normalized (see the Supplementary Material for technical details, including the precise definition of Γ_i).

3.3 Voronoi volume

In this study, we compared the results of the proposed method with those of handcrafted structural indicators to interpret the obtained Grad-CAM score Γ. The first reference indicator is the volume of the Voronoi cells Υ that particles reside in (here, we call them volumes, although they are in fact areas because the system is 2D). The volume of the Voronoi cell allows us to quantify the so-called free volume of each particle, which is considered a significant static characteristic that explains the divergence of the viscosity in glass transition (the free volume theory) [40]. We note that, in Refs. [41, 42], the *microscopic* correlation between the free volume and the dynamics (i.e., the dynamical propensity) was studied and concluded to be not significantly correlated. On the contrary, a strong correlation between the free volume and bond-bond breakage occurring over long periods of time in low-temperature glassy systems has been reported [43]. Despite this controversial situation, because there is no doubt that the free volume of the particles is an important interpretable static property determined geometrically from the particle structure, we will refer to it here as one of the structural indicators.

The Voronoi cell to which particle i belongs can be uniquely defined without the introduction of any additional parameters, as follows:

$$V(\boldsymbol{r}_i) = \{\boldsymbol{r} | \mathcal{D}(\boldsymbol{r}, \boldsymbol{r}_i) \le \mathcal{D}(\boldsymbol{r}, \boldsymbol{r}_j), j \ne i\}, \tag{5}$$

where $\mathcal{D}(\boldsymbol{a}, \boldsymbol{b})$ is a function that provides the 2D Euclidean distance between points $\boldsymbol{a}$ and $\boldsymbol{b}$. The point $\boldsymbol{r}$ in the equation is an arbitrary point in the system that is independent of the particle density field $\rho(\boldsymbol{r})$. The volume of the Voronoi cell for particle i can then be obtained as $\Upsilon_i \equiv \mathcal{V}(V(\boldsymbol{r}_i))$, where $\mathcal{V}(V)$ is the operator that outputs the volume of the region V. To achieve Voronoi tessellation, we used the *freud* [44, 45] Python library, which properly considers periodic boundary conditions. The Voronoi cell volumes provide a quantitative measure of the (inverse) local packing density. We call $\Upsilon = \sum_i^N \Upsilon_i \delta(\boldsymbol{r} - \boldsymbol{r}_i)$ the Voronoi volume.

3.4 Tong–Tanaka order parameter

Tong and Tanaka [21, 22] proposed an excellent order parameter that can characterize structures correlated with long-time dynamics even in glass-forming systems with large particle size dispersion, where characteristic structures are difficult to capture with bond-orientation order parameters [19]. We call this order parameter the Tong–Tanaka order parameter (TT-OP). The TT-OP has been successfully used as a structural indicator of the dynamic properties of various glasses and hence we measure it as a reference below.

To calculate the TT-OP, we first look at each particle (e.g., particle o) and its neighbors (the particles sharing the edges of the Voronoi cell with center particle o). Then, particle o's TT-OP, Θ_o, is obtained as the average difference between the angle formed by particle o and two of its neighbors that are adjacent to each other, θ^1_{ij}, and the corresponding ideal angle θ^2_{ij} (i.e., that is obtained when the distances between particles are exactly the same as the sum of their "radii"; see the Supplementary Material for more details and a schematic of the definitions of θ^1_{ij} and θ^2_{ij}):

$$\Theta_o = \frac{1}{N_o}\sum_{\langle ij\rangle} |\theta^1_{ij} - \theta^2_{ij}|, \tag{6}$$

where N_o is the number of particles neighboring particle o (this number agrees with the number of neighboring pairs of neighbors). The TT-OP $\Theta = \sum_i^N \Theta_i \delta(\boldsymbol{r} - \boldsymbol{r}_i)$ is defined as a particle-based indicator, and it has been shown that, for various systems, the spatially coarse-grained TT-OP predicts the dynamic propensity very well [22]. The results (not only of the TT-OP but also of all particle-based variables, including the Grad-CAM score Γ) presented below are all spatially coarse-grained (and further normalized to the range [0,1]). We explain the coarse-graining procedure in detail in Section 3.6.

3.5 Dynamic propensity

As a measure of the dynamic heterogeneity that appears originated from a specific configuration of particles, the so-called dynamic propensity is usually employed [46–48]. To define this variable, we introduce the isoconfigurational ensemble first: in this special ensemble, samples share an

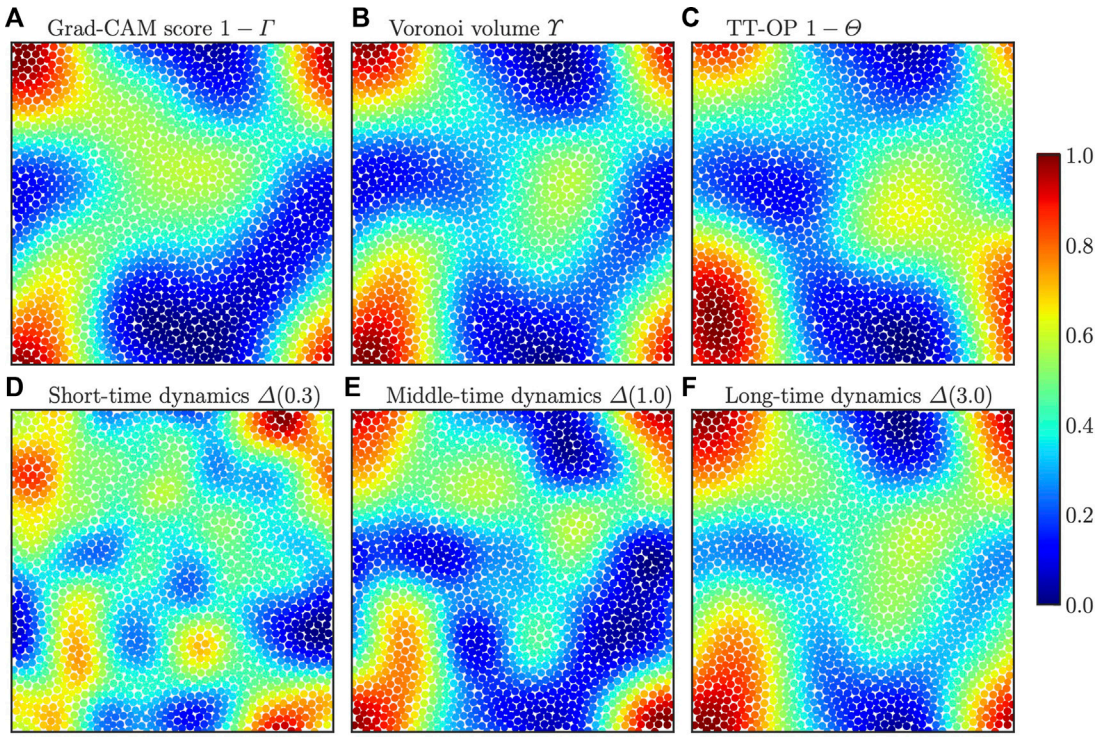

FIGURE 1
Visualization of particle-based structural indicators for a typical glass configuration of the Kob–Andersen model (KAM) system: **(A)** Grad-CAM score (Γ), **(B)** Voronoi volume (Υ), **(C)** TT-OP (Θ), and **(D–F)** Dynamic propensity (Δ) at different "time" scales. The argument of Δ stands for the mean intensity of the displacements δ at which Δ is measured: as indicated in the panel titles, $\delta \approx 0.3, 1.0, 3.0$, which roughly corresponds to $t \approx \tau_\alpha, 3\tau_\alpha, 10\tau_\alpha$, are employed. Notice that all indicators are normalized to [0,1], and the different colors distinguish the values as shown in the color bar. In addition, $1-\Gamma$ and $1-\Theta$ are shown in panels **(A)** and **(C)**, respectively, rather than Γ and Θ, for ease of comparison with the dynamic propensity. The precise values of coarse-graining length ξ_x employed here are summarized in Table 3.

TABLE 2 Classification accuracy for test data.

KAM(G)	KAM(L)	ABM(G)	ABM(L)
1.00	0.998	1.00	1.00

identical initial particle configuration, $\rho_0 = \sum_i^N \delta(\boldsymbol{r} - \mathbf{r}_i(0))$, but have different realizations of velocities with a specified temperature T (the statistics of velocities obeys the Maxwell-Boltzmann distribution with this temperature). In this study, for each initial configuration, we performed MD simulations with 30 different initial velocity distributions. For each realization, we calculated intensity of the so-called cage-relative displacement (CRD)[1], $\Delta_i^s(t)$, which is defined as $\Delta_i^s(t) = \sqrt{(\boldsymbol{d}_i^s(t) - \vec{\boldsymbol{d}}_i^s(t))^2}$, where $\boldsymbol{d}_i^s(t) \equiv \boldsymbol{r}_i^s(t) - \boldsymbol{r}_i(0)$ is the displacement vector of the particle i at time t, $\vec{\boldsymbol{d}}_i^s \equiv \frac{1}{N_i}\sum_j \boldsymbol{d}_j^s$ (the sum for j runs over the neighbors of i including i itself, and N_i stands for the number of particles involved here) is the average displacement vector of the cage to which particle i belongs, and the superscript s is the sample index (which distinguishes different realizations of the velocity distribution at $t = 0$). The dynamic propensity field Δ is then defined as the average of the sample-dependent values of the CRD field, $\Delta^s = \sum_i^N \Delta_i^s \delta(\boldsymbol{r} - \boldsymbol{r}_i(0))$, over N_s samples as $\Delta \equiv \frac{1}{N_s}\sum_s^{N_s} \Delta^s$. As the value of N_s, we basically employed $N_s = 30$ unless stated otherwise.

3.6 Coarse-graining of particle-base indicators

In References [21, 22], Tong and Tanaka showed that, when properly coarse-grained, the TT-OP introduced in Section 3.4. correlates strongly with the dynamic propensity field. In our analyses, we have coarse-grained all the particle-based indicators by a similar method to the one proposed in Ref. [22]:

$$\bar{X}_i(\xi_X) = \frac{\sum_j X_j P\left(|\boldsymbol{r}_j - \boldsymbol{r}_i|\right)}{\sum_j P\left(|\boldsymbol{r}_j - \boldsymbol{r}_i|\right)}, \tag{7}$$

where $P(r) = \exp(-(r/\xi_X)^2)$ is the coarse-graining kernel and ξ_X is the coarse-graining length for variables $X \in \{\Gamma, \Upsilon, \Theta, \Delta\}$. For the calculation of the coarse-graining of the variables X, the cutoff distance r_X^c in $P(r)$ is introduced, which is fixed as $r_X^c = 2\xi_X$ in this study. We employed this coarse-graining procedure (it is slightly different from the one employed in Ref. [22]) after comparing several options.

We stress that, in this work, we coarse-grain not only the structural indicators but also the dynamic propensity field. We explain how we determine the coarse-graining lengths ξ_X in Section 4.2. Additionally, all particle-based variables are further normalized to [0,1] by simply subtracting the minimum value and then dividing by the maximum.

4 Results and discussions

4.1 Extraction of characteristic structures using Grad-CAM

The CNN introduced in Section 3.1. was run over 250 epochs. During the training process, 4,000 training data samples (for both glasses and liquids: 8,000 samples in total) were provided with the correct labels indicating whether the samples were glasses or liquids. For both systems (KAM and ABM), the learning stage proceeded smoothly, and the classification accuracy reached almost 100% both for the training and validation data after these relatively small epochs. The same degree of accuracy was achieved for the test data (the results for the test data are summarized in Table 2). We stress here that the calculation cost for the training part is very low in our setup: the entire 250 epochs of learning only took approximately 8 h using an NVIDIA Quadro P4000 (GP104GL).

Subsequently, using Grad-CAM, we further extracted the characteristic structures that the CNN relied on when identifying glass samples as *glasses*. Notably, this calculation requires only a trivial cost (much less than a second for each sample). We present the typical results obtained for the KAM system in Figure 1A and those of ABM in Figure 2A (notice that Γ visualized here are coarse-grained with the length ξ_Γ determined in the next Section 4.2). Both these results are for the glass configurations: although we can also investigate the characteristic structures of liquids and try to extract glass-like structures from liquids (and *vice versa*) within the Grad-CAM framework, we restricted ourselves to the investigation on the characteristic structures of glasses in this study[2].

1 We employed the cage-relative displacements to exclude the undesired effects due to anomalous fluctuations that are specific to two-dimensional systems [49–52].

2 Importantly, we discarded a test sample for which the trained CNN gave the wrong classification (only 1 out of 2,400 samples: in the case of liquid in the KAM) to rule out the possible influence from such an abnormal sample, e.g., when evaluating the probability distribution function shown later in Figure 6. However, we would like to mention that the investigation of such samples is still important since they can reside in the vicinity of the "boundary" between glass and liquid classes and thus provide meaningful information about their structural differences. This investigation should be performed as future work.

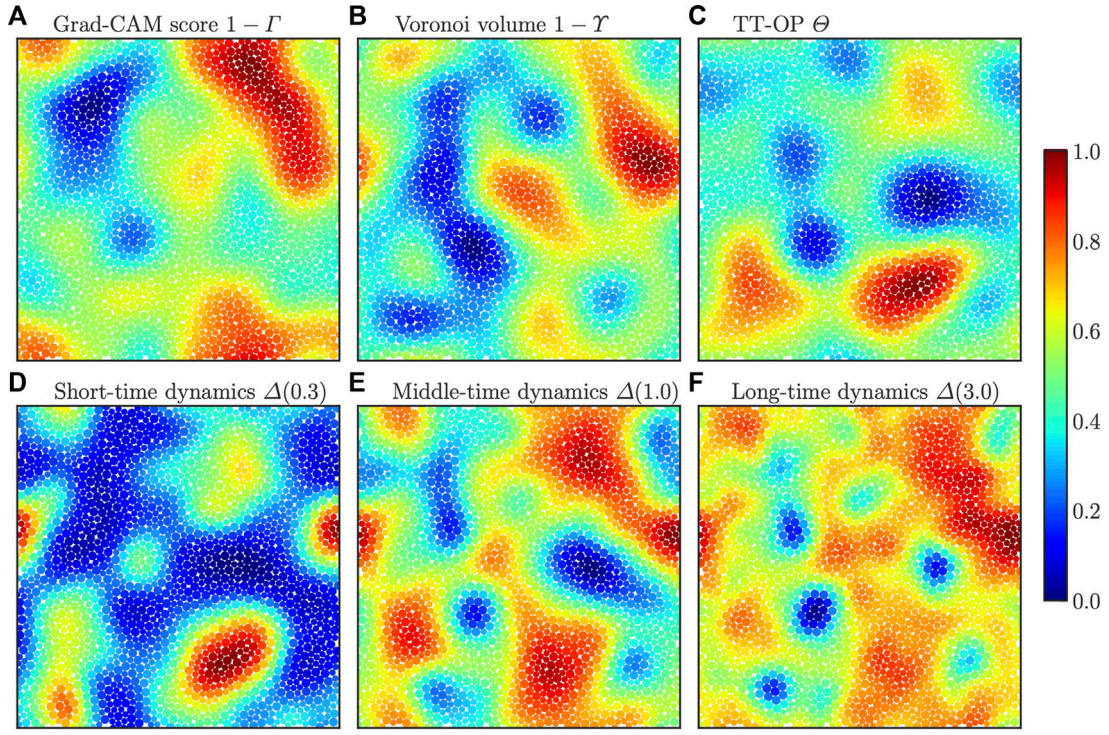

FIGURE 2
Visualization of particle-based structural indicators for a typical glass configuration in the ABM system. The meanings of the panels are basically the same as those presented in Figure 1 ((**A**) Grad-CAM score, (**B**) Voronoi volume, (**C**) TT-OP, (**D–F**) Dynamic propensity at different time scales), while $1-\Upsilon$ and Θ are shown in panels (**B**) and (**C**), rather than Υ and $1-\Theta$.

4.2 Determination of coarse-graining length

In this subsection, we explain how we determined the coarse-graining lengths ξ_X ($X \in \{\Gamma, \Upsilon, \Theta, \Delta\}$) that are used for the analyses in the following sections (or already used in Figures 1A, 2A). Since the coarse-graining lengths for the structural indicators are determined depending on the coarse-grained dynamic propensity field, we explain that for the dynamic propensity ξ_Δ, first.

Coarse-grained structural indicators exhibit spatially smooth profiles as already presented in Figures 1A, 2A. On the other hand, as shown in Supplementary Figures S4, S5, the bare dynamic propensity field without coarse-graining shows noisy profiles even within each mobile/immobile domain. When we try to quantify the dynamic heterogeneity, we are interested in the meso-scale domain exhibited by the propensity field. However, in the presence of these intra-domain noises, the estimation of correlation with structural indicators suffers from high-frequency modulations. To exclude this unintentional underestimation of the correlation, we coarse-grained the propensity field as well. To systematically determine the coarse-graining length ξ_X, we first measure the spatial correlation function of the dynamic propensity $X = \Delta$:

$$C_\Delta(r) = \langle \delta\Delta(\boldsymbol{r}_i)\delta\Delta(\boldsymbol{r}_i + \boldsymbol{r})\rangle_{|\boldsymbol{r}|=r}, \tag{8}$$

where $\delta\Delta \equiv \Delta - \bar{\Delta}$ is the deviation from the global average $\bar{\Delta}$, r is the distance from the reference particle i, and $\langle\cdot\rangle_{|\boldsymbol{r}|=r}$ stands for the spherical average over particle pairs separated by a distance r. Since we aim to smooth out the intra-domain noises here, we employ the decay length $r^\star$ defined by $C_\Delta(r^\star) \approx 1/e$ as the coarse-graining length ξ_Δ. In Figure 3, we plot the measurement results of C_Δ at three different time scales for both KAM (panel **A**) and ABM (panel **B**). For later convenience, in this study, we express the dynamic propensities at different time scales as functions of the mean intensity of the displacement (here, the displacement is cage-relative one. And the average is taken over the isoconfigurational samples and particles), $\delta(t) = \frac{1}{N}\sum_i^N \Delta_i(t)$, as $\Delta(\delta)$. In Figure 3, C_Δ at $\delta = 0.3, 1.0, 3.0$ are shown. These values of δ are expected to correspond to approximately $t \approx \tau_\alpha, 3\tau_\alpha, 10\tau_\alpha$, where τ_α is the α relaxation time [9]. We summarize the values of extracted coarse-graining length in Table 3. Below, we use these values of ξ_Δ for Δ at these three time scales.

We would like to stress that the coarse-graining of the dynamic propensity Δ introduced here seems not just an artificial operation but a physically reasonable one. To show this, we prepared 100 independent isoconfigurational samples

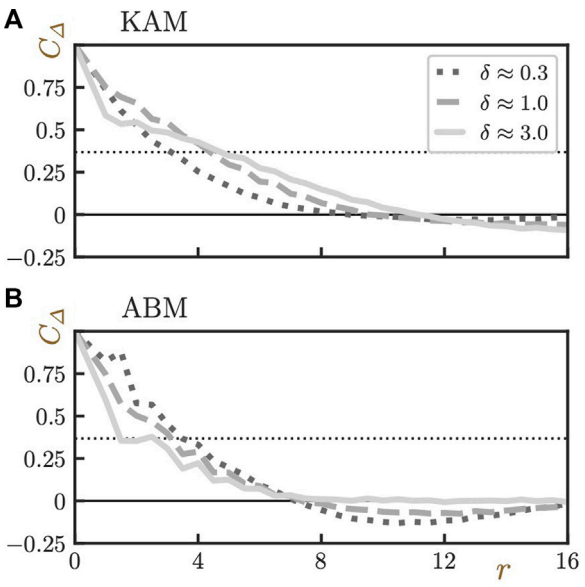

FIGURE 3
The spatial correlation function of the dynamic propensity Δ, C_Δ, as a function of the distance from the reference particle r. Results for **(A)** KAM and **(B)** ABM systems. Different line styles distinguish different time scales as shown in the legend. The horizontal dotted lines depict $C_\Delta = 1/e$.

and considered four different ensembles. For three of the ensembles, we employed $N_s = 30$, and completely different sets of samples are composed for each. We call these ensembles e^i_{30} $(i \in \{A, B, C\})$ Only in the forth ensemble, all 100 samples are used ($N_s = 100$): we call this e_{100}. Because the number of samples is different, we expect that the ensemble e_{100} should provide the statistically most reliable result. In Figure 4, we compare the bare dynamic propensity fields and the coarse-grained ones obtained from these four ensembles (only results for the KA system are shown). Although we see strong fluctuations among the bare fields of ensembles e^i_{30} (Figures 4A–C), the coarse-grained fields of these ensembles (Figures 4E–G) appear highly similar. Notably, the bare field of the ensemble e_{100} (Figure 4D) is much smoother than the ones of ensembles e^i_{30}, and rather very similar to the coarse-grained fields (Figures 4E–G) of them. These similarities can be quantitatively evaluated by measuring the Pearson's coefficient between two propensity fields of different ensembles. We summarize the results in Table 4. In this table, $C_{\Delta,\Delta}(e_\alpha, e_\beta)$, the correlations between the propensity fields of ensemble e_i and e_j, are presented. When we consider the coarse-grained field instead of the bare ones, we denote them as $\bar{e}_i$. This table shows that the coarse-grained fields obtained from ensembles of $N_s = 30$ are very close to each other $(C_{\Delta,\Delta}(\bar{e}^i_{30}, \bar{e}^j_{30}) = 0.958$. Here, regarding the correlation coefficient involving e_{30}, the average value over all combinations of i and j is shown, where $i, j \in \{A, B, C\}$ and $i \neq j$.) while the correlations between the bare fields are much smaller $(C_{\Delta,\Delta}(e^i_{30}, e^j_{30}) = 0.769)$. This indicates that the bare Δ fields contain sample-dependent large intra-domain noises and our coarse-graining procedure indeed smooth away those unintentional sample-dependent noises as we desired. Comparison between the results from ensembles with different values of N_s further provides an important insight into the meaning of the coarse-graining of Δ. As expected, the correlation between non-coarse-grained and coarse-grained fields of e_{100}, namely $C_{\Delta,\Delta}(e_{100}, \bar{e}_{100}) = 0.878$, is much larger than that of e_{30}, $C_{\Delta,\Delta}(e_{30}, \bar{e}_{30}) = 0.820$, indicating that the coarse-grained field of the ensemble with $N_s = \infty$ would be identical to its bare field. Moreover, we also mention that the correlation between coarse-grained ensembles $\bar{e}_{30}$ and $\bar{e}_{100}$ exhibits a very high value, $C_{\Delta,\Delta}(\bar{e}_{30}, \bar{e}_{100}) = 0.985$. All these results suggest that the coarse-graining of the dynamic propensity Δ is an important operation that allows to accurately estimate the "genuine" dynamic propensity field (that should be achieved in the limit of $N_s \to \infty$) from the numerical results with a finite N_s.

The coarse-graining lengths ξ_α for structural indicators $\alpha(\alpha \in \{\Gamma, \Upsilon, \Theta\})$ are then determined in the same manner as the one in Ref. [22]: the values that maximize the Pearson's correlation coefficient [27, 28, 30, 53] between structural indicators and the dynamic propensity are chosen. Here, as the dynamic propensity field, we employed the coarse-grained ones with ξ_Δ determined in the previous paragraph. The determined values of ξ_α are summarized in Table 3. See Supplementary Material for the detailed ξ_α dependence of the correlations. In Figures 1B,C, 2B,C, we show the visualization results of the coarse-grained Voronoi volume Υ and TT-OP Θ fields (the results for the same configurations as Figures 1A, 2A). We stress that all panels present much larger domains than the size simply expected from the value of ξ_α (e.g., linear spanning of $2\xi_\alpha$).

TABLE 3 Coarse-graining length for each variable.

	Figures 1, 2			Figures 5, 7	Figures 1, 2, 5, 7			Figure 6		
	$\xi_\Delta(\delta = 0.3)$	$\xi_\Delta(\delta = 1.0)$	$\xi_\Delta(\delta = 3.0)$	ξ_Δ	ξ_Γ	ξ_Υ	ξ_Θ	ξ_Γ	ξ_Υ	ξ_Θ
KAM	3.0	4.0	5.0	4.0	8.0			4.0		
ABM	3.0	3.0	2.0	3.0	5.0			3.0		

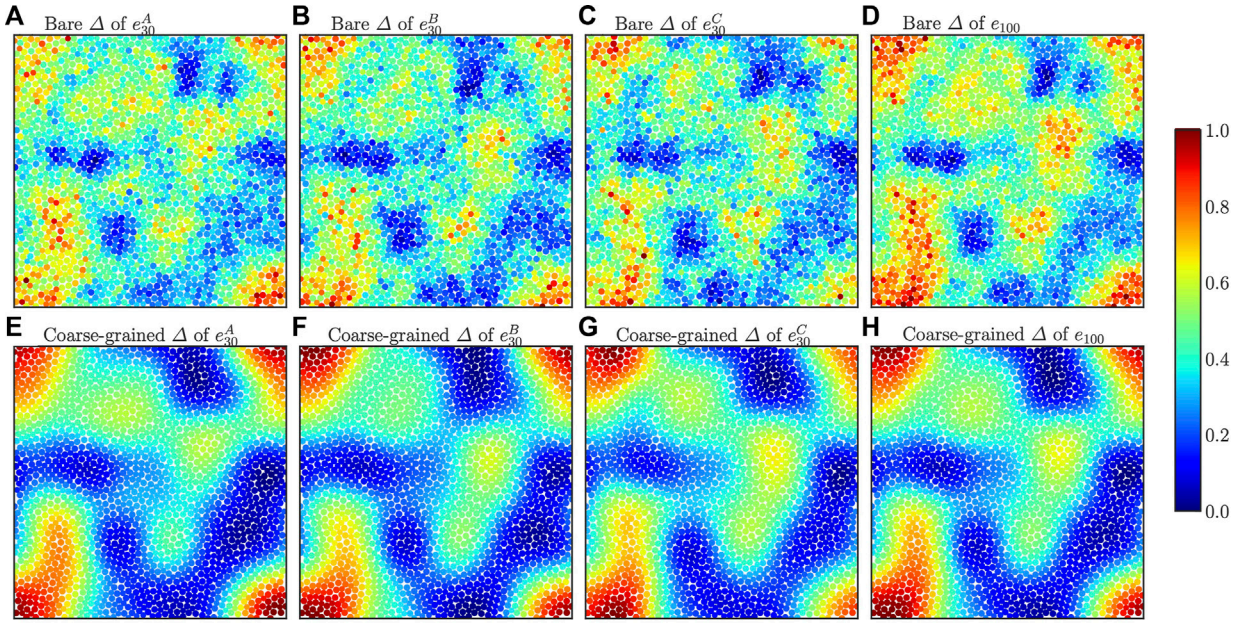

FIGURE 4
Comparisons between the bare and the coarse-grained dynamic propensity fields Δ of different ensembles. The results of Δ(1.0) of the KA system are shown. **(A–C)** The bare Δ fields of e^i_{30} ($i \in \{A, B, C\}$), **(D)** the bare Δ field of e_{100}, **(E–G)** the coarse-grained Δ of e^i_{30}, and **(H)** the coarse-grained field of e_{100}. The coarse-graining length of $\xi_\Delta = 4.0$ is employed as in Figure 1E.

TABLE 4 Pearson's coefficients between Δ of different ensembles.

$C_{\Delta,\Delta}(e^i_{30}, e^j_{30})$	$C_{\Delta,\Delta}(\bar{e}^i_{30}, \bar{e}^j_{30})$	$C_{\Delta,\Delta}(e_{30}, \bar{e}_{30})$	$C_{\Delta,\Delta}(e_{100}, \bar{e}_{100})$	$C_{\Delta,\Delta}(\bar{e}_{30}, \bar{e}_{100})$
0.769	0.958	0.820	0.878	0.985

As a reference, we also present the results without the coarse-graining of the dynamic propensity Δ (that is, results with $\xi_\Delta = 0$) in Supplementary Figures S4, S5). We note that, as shown in Supplementary Figures S4, S5, the consequences of the coarse-graining of Δ are fairly consistent with the bare Δ field.

4.3 Predictability of the dynamics

Now we ask the following question: *Are the extracted structures correlated with some material properties, for example, the dynamics?* To address this, we compared the Grad-CAM scores (Γ) with the dynamic propensity (Δ). Owing to the computational cost, we calculated the propensities only for the configurations shown in Figures 1, 2 (only one configuration for each system).

For each configuration, we performed MD simulations with 30 different initial velocity distributions and calculated the dynamic propensity field Δ following the procedure summarized in Section 3.5. Regarding the temperature during the measurement of the dynamics, we considered temperatures slightly above the glass transition point, T^*, (whose empirical definition is provided in the Supplementary Material; the obtained values are $T^* \approx 0.37$ for KAM and $T^* \approx 1.0$ for ABM) because we cannot expect any cage-breaking relaxational dynamics below T^* within the computationally accessible time window. To investigate the possible temperature dependence of the dynamics, we performed simulations at temperatures up to approximately $1.5T^*$. We stress again that although the initial velocities follow the specified temperatures (which are higher than the glass transition point T^*), the initial configurations are drawn from the sample at $T_G = 0.05$ (those shown in Figures 1, 2). In Figures 1D–F and Figures 2D–F, the propensity Δ at $\delta \approx 0.3, 1.0, 3.0$ are shown. Note again that we express the time-dependence indirectly *via* δ, the mean intensity of the cage-relative displacement, and these values of δ correspond roughly to $t \approx \tau_\alpha$, $3\tau_\alpha$, $10\tau_\alpha$ respectively. Interestingly, there is agreement between $1 - \Gamma$ and Δ at long times (Δ(1.0) and Δ(3.0)) for both systems.

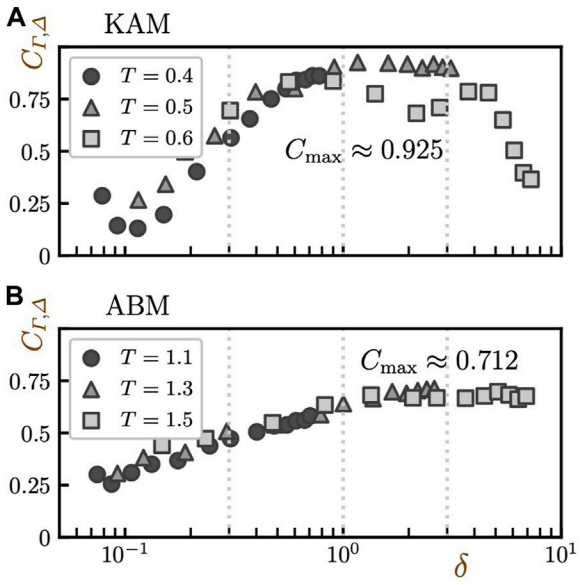

FIGURE 5
The "time" evolution of the correlation between Grad-CAM score 1 − Γ and dynamic propensity Δ as a function of the intensity of the cage-relative displacement δ. Results for **(A)** KAM and **(B)** ABM. Each simulation was performed for 3×10^8 steps, and $\delta(t)$ during those simulations is plotted on the abscissa for each plot. Different markers are used to distinguish different temperatures as shown in the legend. The vertical dotted lines indicate the delta values visualized in Figures 1, 2.

To quantify the correlation between Γ and Δ further, we calculated the Pearson's correlation coefficients, $C_{\Gamma,\Delta}$. Although the coarse-graining length of Δ is dependent on the value of δ (i.e., the time scale), for simplicity, we employed a fixed value for each system here (see Table 3). The results are presented in Figure 5. In this plot, the time dependence is indirectly reflected by the value of δ. Such a presentation allows us to compare the correlation between the dynamics (at different temperatures) and the static structure directly, thus ruling out the effect of the non-trivial dependence on time. Note that the correlation between 1 − Γ and Δ is quantified, not Γ, in agreement with the visualization. From Figure 5, we observe several striking consequences. First, $C_{\Gamma,\Delta}$ rises in accordance with the increase in δ, reaching its maximum value at $\delta \approx 1$ in both the KAM and ABM. This indicates that the structures extracted by our method are responsible for the dynamics at a longer time scale than the α relaxation (note that these are non-equilibrium aging dynamics and not intra-metabasin equilibrium relaxation). Secondly, the change in the correlation $C_{\Gamma,\Delta}$ is non-monotonic in the KAM system and starts decreasing for $\delta \geq \delta^*$, while plateauing for $\delta \geq \delta^*$ in the ABM system. These results indicate that the specified characteristic "well-ordered" clusters are transient in the KAM system, whereas they seem very stable within the time window of our calculation in the ABM system. Thirdly, the maximum correlation, $C_{\max}$, reaches very high values in both systems: 0.925 and 0.712 in the KAM and ABM, respectively. The predictability of the dynamics is surprising because our method does not require any information about the dynamics during the training process; thus, the computational cost for both the training and the sample-preparation part is low. Finally, the results of different T follow a single master curve. This result confirms the fact that the dynamics are indeed governed by the static "glass structures," at least in the temperature regime under study and concerns non-equilibrium aging dynamics.

4.4 Interpretable structural indicators

In this section, we measure two distinct local multibody structural indicators to interpret the Grad-CAM score Γ. Because these indicators are handmade, we can take advantage of their interpretable nature. In the Supplementary Material, we present the two-body correlation function $g(r)$ for reference (Supplementary Figure S7). We again stress that all the particle-based indicators, including Δ, were coarse-grained and further normalized to the interval [0,1].

4.4.1 Voronoi volume

The Voronoi volume Υ is the first interpretable local multiparticle structural indicator. In this subsection, we briefly explain the obtained Υ values for the KAM and ABM systems. A typical result for the KAM system is shown in Figure 1B in which particles with small values of Υ_i (< 0.4) appear dominant. Figure 2B presents the results for the ABM system, in which a large portion of particles exhibit relatively high values of Υ_i (> 0.4). Note that $1 - \Upsilon$ is visualized in Figure 2B.

These distinct trends are derived entirely from the difference in the set of interaction parameters (ϵ_{ij} and σ_{ij}) and the number ratio of the particle species (N_A/N_B). For instance, in the KAM system, the interaction energy is most stable when different species are in contact, and the interaction range is also the shortest in this situation (see Table 1). Therefore, small values of Υ_i are energetically favored in the KAM. In the ABM system, on the other hand, because the area occupied by particles A is almost half that of particles B (the area fraction is 1: 1.96), the region with a large Voronoi volume (corresponding to particles B) tends to be slightly dominant. Because samples with a very low temperature $T = 0.05$ are shown in Figures 1, 2, the structurally low-energy states are expected to be more probable. We also note that the small value of Υ_i does not necessarily mean that the local structure around particle i is highly ordered, as is evident in the case of the KAM.

4.4.2 Tong-Tanaka order parameter

The second interpretable structural indicator is the TT-OP Θ. As mentioned in Section 3.4, of the various locally defined structural indicators reported to date, TT-OP captures the dynamical behavior of many classes of glasses very well,

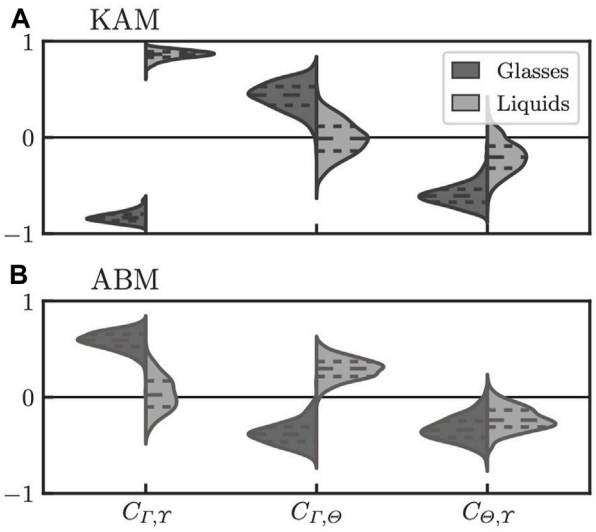

FIGURE 6
Violin plots of the Pearson's correlation coefficients between distinct structural indicators. Results for the **(A)** ABM and **(B)** KAM systems. The dark and light gray parts represent the results for glasses liquids, respectively, as shown in the legend. The dashed lines indicate the quartiles.

especially universally. The characteristic structures of glasses in terms of the TT-OP are specified by small values of Θ_i, which means that the local structure is highly ordered.

The results for the KAM system are shown in Figure 1C. We note that because of the non-additive nature of the potential parameters, defining a reference three-particle ideal configurational angle θ^{I} in the case of the KAM is non-trivial. In this study, we employed the definition using the additive assumption ($\sigma_{AA} = 1.0$, $\sigma_{BB} = 0.88$, and $\sigma_{AB} = (\sigma_{AA}+\sigma_{BB})/2 = 0.94$) rather than the parameters used in the simulations because the reference structure is easier to interpret with this additive assumption. Surprisingly, the coarse-grained Θ field looks very similar to other indicators and appears correlated to the long-time propensity field. The results for the ABM system are shown in Figure 2C. In contrast to the findings of Tong and Tanaka [21, 22], the structure is not well developed, and the spatial modulation is much smaller than that in the KAM: Intermediate values are system-spanning. This is likely because our samples were generated by quenching at a fixed cooling rate and, thus, were not well annealed. We expect these samples to exhibit aging behavior.

4.5 Correlations between different indicators

To interpret the Grad-CAM scores (Γ) obtained by our method, we further calculated the Pearson's correlation coefficients between different indicators for both the KAM and ABM. The results are summarized in Figure 6. In this figure, we show violin plots of the coefficients between different indicators (Γ, Υ and Θ) calculated using 600 samples for each case (KAM or ABM and glasses or liquids). In this subsection, for clarity, we employ different values of ξ_α from those used in other subsections as shown in Table 3. The change in the value of ξ_α does not change the qualitative discussion here, while the distributions (those are plotted in Figure 6) become broader, and thus the differences between them are less pronounced when ξ_α increases.

We call the correlation coefficients between the Grad-CAM score and the Voronoi volume $C_{\Gamma,\Upsilon}$ and define those between different pairs in a similar manner: $C_{\Gamma,\Theta}$ and $C_{\Theta,\Upsilon}$. Although the results below are mostly those for the glass configurations only, we also mention the results for the liquids when we discuss their differences from those of the glass samples. Finally, we stress that, in the main text, all correlations are based on the Pearson's definition. As presented in the Supplementary Material, however, we also obtained semi-quantitatively consistent results using Spearman's definition. Below, we explain the results for the ABM and KAM systems.

4.5.1 ABM

In the ABM system, $C_{\Gamma,\Upsilon}$ (the Grad-CAM score vs. the Voronoi volume) is the largest in terms of the intensity (Figure 6B), and its average is an intermediate positive value: $\bar{C}^{\mathrm{G}}_{\Gamma,\Upsilon} = 0.585$, where the bar represents the average over samples and the superscript G indicates that only the glass samples are considered (see Supplementary Table S2 for the summary of the average and the standard deviation of the correlation coefficients). This means that structures with large local volumes are judged to be characteristic of the glass. This behavior is consistent with the TT-OP: Both $C_{\Gamma,\Theta}$ and $C_{\Theta,\Upsilon}$ (those for the Grad-CAM score vs. the TT-OP and the TT-OP vs. the Voronoi volume, respectively) are negative, with the intensities being slightly smaller ($\bar{C}^{\mathrm{G}}_{\Gamma,\Theta} = -0.378$ and $\bar{C}^{\mathrm{G}}_{\Theta,\Upsilon} = -0.327$), meaning that structures with large values of the Voronoi volume tend to be more ordered.

However, importantly, the difference between glasses and liquids is most evidently quantified by $C_{\Gamma,\Theta}$, which becomes almost completely negative for glasses but positive for liquids. On the other hand, the probability distribution of $C_{\Gamma,\Upsilon}$ shows a large overlap between glasses and liquids; moreover, in the case of liquids, the distribution is centered around zero, indicating that the Voronoi-volume-like aspect of the Grad-CAM score is likely unable to distinguish glasses and liquids accurately. Therefore, our method seems to rely on structures that are qualitatively consistent with the TT-OP rather than on the Voronoi volume when a decision is made, although Υ is closer to Γ than Θ in terms of the correlation for glass samples, as mentioned above ($\bar{C}^{\mathrm{G}}_{\Gamma,\Upsilon} > \bar{C}^{\mathrm{G}}_{\Gamma,\Theta}$). We stress that it has been shown that the TT-OP can extract the characteristic structures associated with the dynamics in

binary additive glass formers [22], and our results seem consistent with this.

4.5.2 KAM

In the case of the KAM system, $C_{\Gamma,\Upsilon}$ and $C_{\Gamma,\Theta}$ for glasses are negative and positive, respectively, at odds with the results for the ABM (Figure 6A). Such a qualitative difference indicates that the structures extracted by our method respect the details of the systems. It should also be noted that, from the perspective of the intensity of the correlation coefficients, $C_{\Gamma,\Upsilon}$ is significantly larger than $C_{\Gamma,\Theta}$, and only $C_{\Gamma,\Upsilon}$ exhibits a clear difference in the signs between the results for glasses and liquids. This is another qualitative difference from the ABM system, where the difference in sign is evident for $C_{\Gamma,\Theta}$. However, although the TT-OP is a good descriptor for the ABM, as presented above, it is unlikely to characterize the properties of KAM systems. Thus, our method regards structures with high $C_{\Gamma,\Upsilon}$ as characteristic while $C_{\Gamma,\Theta}$ is small. In particular, the intensity of $C_{\Gamma,\Theta}$ is lower than that of $C_{\Theta,\Upsilon}$ ($\bar{C}^{\mathrm{G}}_{\Gamma,\Theta} = 0.426$, $\bar{C}^{\mathrm{G}}_{\Theta,\Upsilon} = -0.597$), suggesting that our method attempts to avoid correlation with the TT-OP selectively.

4.5.3 Summary of this subsection

Interestingly, although we could interpret the Grad-CAM scores in terms of other conventional indicators (the Voronoi volume and the TT-OP) to some extent in both the KAM and ABM, the correlations are not perfect, and Grad-CAM seems to blend different indicators in an "appropriate" manner. In particular, we emphasize that the precise recipe of such blending is obviously dependent on the system details. Therefore, it would be meaningful to regress the obtained Grad-CAM score field Γ symbolically to achieve a fuller interpretation using recently invented methods [26, 54, 55].

4.6 Dynamics vs. other indicators

In Section 4.3, we studied the predictability of the Grad-CAM score Γ with respect to the dynamics Δ by measuring the correlation coefficient between them. In this subsection, we further investigate the correlation between dynamics and other indicators, namely, the Voronoi volume Υ and the TT-OP Θ. Figure 7 presents the correlation coefficient between the dynamic propensity and the structural indicators. Note that, in this subsection, when calculating the correlation $C_{\alpha,\Delta}$, we sometimes use $1 - \alpha$ instead of α to obtain a positive value (the choices obey those in Figures 1, 2). We explain the results for Υ and Θ one by one below.

4.6.1 Voronoi volume

The time evolution of the correlation coefficient between the Voronoi volume Υ and the dynamic propensity Δ, $C_{\Upsilon,\Delta}$, is quite similar to that of $C_{\Gamma,\Delta}$: it changes non-monotonically (reaches the maximum at $\delta* > 1.0$ and then starts decreasing) in the KAM system, and grows monotonically as a function of δ and saturates at $\delta^* > 1.0$ in the ABM system. The maximum correlation $C^{\max}_{\alpha,\Delta}$ and the value of δ^* at which $C_{\alpha,\Delta}(\delta^*) = C^{\max}_{\alpha,\Delta}$ holds are summarized in Table 5. Here, the subscript $\alpha \in \{\Gamma, \Upsilon, \Theta\}$ distinguishes the indicator of interest. The maximum $C^{\max}_{\Upsilon,\Delta}$ reaches high values in both systems: 0.966 in the KAM and 0.858 in the ABM (to obtain a positive value, we employed $1-\Upsilon$ for the ABM). These values are higher than $C^{\max}_{\Gamma,\Delta}$ in both systems. This is a quite unanticipated consequence since the predictability of the free volumes with respect to the dynamic propensity has been negated previously [41, 42]. On the other hand, it has been

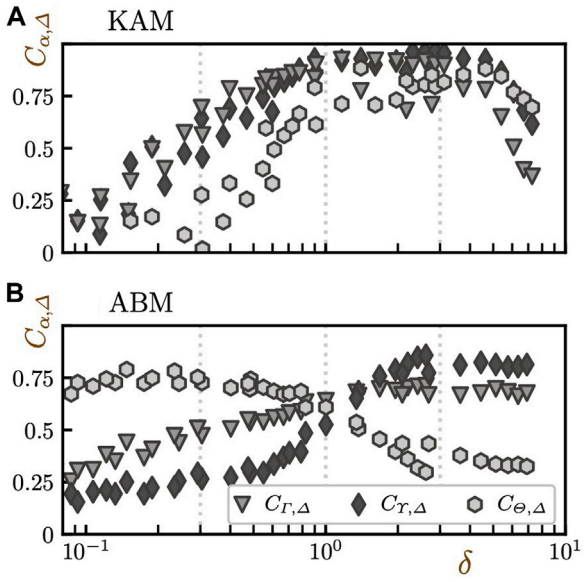

FIGURE 7
The evolution of the correlation between structural indicators (Grad-CAM score Γ, Voronoi volume Υ, and TT-OP Θ) and dynamic propensity Δ (or $1 - \Delta$ depending on the target indicator and system) as a function of the mean intensity of the cage-relative displacement δ. Results for **(A)** KAM and **(B)** ABM. The meaning of the abscissa is the same as the one in Figure 5. Different markers distinguish different indicators, as shown in the legend. Data for all temperatures are plotted without distinction. The vertical dotted lines indicate the delta values visualized in Figures 1, 2.

TABLE 5 Maximum values of correlations and their locations.

	KAM		ABM	
	$C^{\max}_{\alpha,\Delta}$	δ^*	$C^{\max}_{\alpha,\Delta}$	δ^*
$C_{\Gamma,\Delta}$	0.925	1.167	0.712	2.620
$C_{\Upsilon,\Delta}$	**0.966**	2.860	**0.858**	2.620
$C_{\Theta,\Delta}$	0.885	1.402	0.790	0.148

The best $C^{\max}_{\alpha,\Delta}$ is shown in bold letters for each system.

reported that the local potential field is strongly correlated with the dynamics when coarse-grained [48, 56, 57]. Since both the local potential and the Voronoi volume detect the metric-based information of the local packing, we expect them to possess qualitatively similar information. Therefore, it is possible that the good predictability of the Voronoi volume is a result of the coarse-graining. To draw a decisive conclusion, however, a thorough investigation using the same setup as that in [41, 42] is required.

4.6.2 Tong-Tanaka order parameter

Interestingly, the correlation between the TT-OP and the dynamic propensity, $C_{\Theta,\Delta}$, reaches high values: 0.885 and 0.790, respectively, in the KAM and ABM systems ($1-\Theta$ and Θ were employed). It is unexpected that the TT-OP provides a good predictability of the dynamics even in the KAM (the correlation is higher in the KAM than in the ABM). This good predictability is achieved maybe because we employed the additive convention of the reference angle θ_{ij}^2 or because we focused on the non-equilibrium aging dynamics. We also note that the high correlation with dynamics is observed only for long-time regimes, and the correlation is very low around the α relaxation regime ($\delta \approx 0.3$). Further comprehensive investigations are necessary to identify the cause of the unexpectedly high predictability.

In the KAM system, the qualitative trend is the same as those for correlations of other indicators ($C_{\Gamma,\Delta}$ and $C_{\Upsilon,\Delta}$): it starts from a small value and follows an upward convex curve. In the ABM system, in contrast, the time evolution of $C_{\Theta,\Delta}$ is qualitatively different from those of $C_{\Gamma,\Delta}$ or $C_{\Upsilon,\Delta}$. It is high even at the early-stage small δ regime and changes in a non-monotonic manner with the increase in δ: it increases only a little bit, reaches the maximum value at $\delta^* \approx 0.148$, remains almost at the same level, and then starts decreasing.

4.6.3 Summary of this subsection

To summarize, first, the Voronoi volume has the largest correlation with the dynamics in both KAM and ABM systems, in terms of the $C_{\alpha,\Delta}^{\max}$. Regarding the comparison between the Grad-CAM score and the TT-OP, the latter shows a stronger correlation in the ABM system (note again that the TT-OP is known to be a good descriptor of the dynamics in the ABM) while the former outperforms in the KAM.

The results presented in this article indicate that the characteristic structures extracted by the Grad-CAM capture information consistent with that of other coarse-grained structural indicators proposed in previous works [27, 30] in the sense that all structures are correlated with the dynamic propensity to some extent. However, we do observe clear differences between the correlation coefficient for the TT-OP and the other two indicators (the Voronoi volume and the Grad-CAM score), particularly in the ABM:

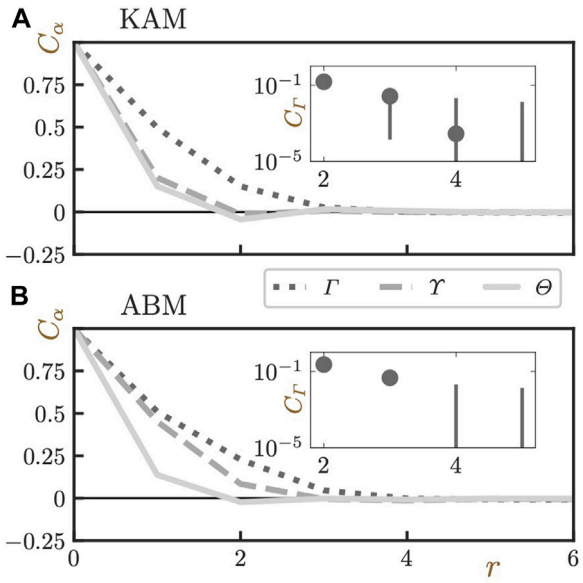

FIGURE 8
The spatial correlation functions of structural indicators $\alpha(\alpha \in \{\Gamma, \Upsilon, \Theta\})$, C_α, as a function of the distance from the reference particle r. Results for **(A)** KAM, **(B)** ABM systems. Different line styles distinguish different indicators as shown in the legend. In the insets of both panels, the magnified images of C_Γ in the vicinity of $C_\Gamma = 0$ with error bars. In these insets, the vertical axes are in the logarithmic scale. Although the values of C_Γ are negative when markers are missing, the error bars are crossing $C_\Gamma = 0$.

although $C_{\Gamma,\Delta}$ and $C_{\Upsilon,\Delta}$ reach their maximum values at $\delta > 1.0$, which corresponds to the longer time scales than α relaxation time, only $C_{\Theta,\Delta}$ exhibits clearly smaller values of δ^* (Table 5). This may suggest that the structures specified by the TT-OP and those identified by the other indicators signal qualitatively different aspects of heterogeneous dynamics. Indeed, while the TT-OP focuses on angular information, the other two indicators take into account the whole structural information.

4.7 Do the coarse-graining lengths have a structural origin?

Thus far, we have shown that, coarse-grained with proper choices of ξ_α, structural indicators show strong correlations with the dynamics Δ. In this subsection, we discuss whether we can find the structural origin of these "proper" coarse-graining lengths. To this end, we measured the same spatial correlation functions as the one in Eq. 8 for structural indicators. The results are presented in Figure 8. We can first tell, from this figure, that Υ and Θ decay very fast to $C_\alpha = 0$ (particularly in the case of KAM). In contrast, Γ decays relatively slowly in both KAM and ABM systems: C_Γ

reaches zero at $r_\Gamma \approx 3.0 - 4.0$. This indicator-dependence of the correlation length is evident in the visualizations of bare fields shown in Supplementary Figures S6, S7. Results in Figure 8 suggest that relying on Γ, and we can extract relatively long purely structurally-based correlation length. Note that, here, we define the correlation length as the one where C_Γ becomes zero, not $1/e$. We employed this choice because, unlike the case of Δ for which we introduced the coarse-graining to smooth out the intra-domain noises, we are interested in the average size of the domains as discussed below.

In both systems (KAM and ABM), the length scale r_Γ defined here as $C_\Gamma(r_\Gamma) = 0$ is roughly half of the optimal coarse-graining length ξ_α used in the aforementioned analyses (ξ_α = 8.0 for KAM and ξ_α = 5.0 for ABM). Because r_Γ is expected to correspond to the average domain size, the length scale $\xi_\alpha \approx 2r_\Gamma$ corresponds to the average distance between domains with the same sign of $\delta\Gamma \equiv \Gamma - \bar{\Gamma}$. This correspondence suggests that the dynamical domains become larger than the static ones due to collective excitations of nearby mobile domains (that are expected to be indicated by low values of Γ). This picture is consistent with a recent theoretical work [58] where the dynamic heterogeneity was explained by collective behaviors of local instabilities (that correspond to mobile domains) *via* elastic interactions.

To further give a concrete interpretation of the coarse-graining length on a purely structural basis, we must understand the interactions between domains *via* the elastic field. To provide useful data for such an exploration of new understandings, it is important to perform a comprehensive measurement of Γ for equilibrated well-annealed low-temperature samples. We leave this problem as a future work.

4.8 Relation to recent works

In the closing remarks for this section, we discuss the relation of our work to several recent works using machine learning-based methods. Recently, much effort has been dedicated to challenges in explaining the heterogeneous slow dynamics of glasses from a purely structural perspective. For instance, in Refs. [28, 29], supervised learning of graph neural networks was performed with information on dynamics as part of the training data. The trained networks succeeded in predicting the long-time glassy dynamics of the KAM system at very low temperatures (the lowest value T = 0.44 is comparable to the mode coupling transition point T_{MCT} = 0.435) solely from static structures with high precision (the correlation coefficient exceeds 0.6). As examples of unsupervised approaches, Refs. [27, 30] similarly tried to extract characteristic structures of glasses from static configurations. In these studies [27, 30], information from dynamics was not used, even in the training stage, similarly to our method. The major difference to our method was that only glass configurations were provided during the training stage [27, 30]; the liquid samples were absent. Surprisingly, the obtained structures were well-correlated with the long-time dynamics, particularly the dynamic propensity at approximately the α relaxation time. For the KAM system, the correlation coefficient reaches around 0.4 and 0.7 in Refs. [27, 30] respectively.

Because our method similarly does not require any information about the dynamics, we can say that it is also unsupervised in regard to dynamics prediction. Accordingly, it is non-trivial and interesting that the structures extracted using our method exhibit a strong correlation with the long-time heterogeneous dynamics at a longer time than the α relaxation time, as was the case for methods in Refs. [27, 30]. This implies that the characteristic structures governing the relaxational dynamics are extracted in a similar way, whether we try to identify the structural difference between glasses and liquids (our approach) or specify structurally distinct parts from the glass sample only (approaches in Refs. [27, 30]). This may support the view that the characteristic glass structures, if exist, grow gradually from completely random liquid configurations as the temperature decreases. It would be very meaningful to investigate the similarity of structures extracted by different machine learning methods.

We also note the quantitative difference in the predictability of different machine-learning methods with respect to the dynamics. Although we cannot make direct quantitative comparisons because of the varied setups in the references, our method provides the highest-level performance in terms of the simple correlation coefficient between extracted characteristic structures and long-time dynamic propensity: for our 2D ABM and KAM system, the correlation between the Grad-CAM score and dynamics reached approximately 70% and 90%, respectively.

5 Summary and overview

In this work, we proposed a method to extract the characteristic structures of amorphous systems solely from a couple of classes of static random configurations by means of classification with a CNN and quantification of the grounds for classification using Grad-CAM. We applied the proposed method to two qualitatively different binary glass-forming mixtures, *viz.* The ABM and KAM, and showed that our method could automatically extract the system-detail-dependent mesoscopic characteristic structures of glasses. The proposed method has three outstanding features. First, our method can extract characteristic structures solely from the instantaneous static structures without any information about the

dynamics. Second, the extracted characteristic structures are system-dependent; in other words, our method automatically identifies the tailor-made structural indicator suitable for each distinct system. Finally, the extracted structures are strongly correlated with the dynamic propensity. The time evolution of the correlation reveals that the characteristic structure is closely related to the dynamics at a longer time scale than that for the α relaxation, where the mean intensity of the cage-relative displacement is of the order of unity: $\delta \gtrsim 1$. Moreover, such a correlation is robust over a wide range of temperatures, at least in the range $T^* \leq T \leq 1.5T^*$. We again stress that, unlike in the previously reported studies, our dynamic propensity quantifies the non-equilibrium aging processes, not the intra-metabasin equilibrium relaxational dynamics, and is coarse-grained.

In addition, we discuss several future research directions. First, we should conduct a similar analysis using well-annealed glass configurations because the equilibrium dynamics are important to understand the properties of glasses more deeply. In particular, it is challenging to determine whether the characteristic structures that our method extracts for equilibrium glass configurations are correlated with the equilibrium dynamics. Moreover, our method can find the characteristic structures from the static configurations alone, even when the microscopic physical quantity that characterizes the two classes (e.g., the dynamic propensity) is not available, as long as the two different classes are defined, for example, by specifying macroscopic quantities such as the temperature. Therefore, it allows us to directly ask, for example, whether we observe any structural differences between normal and ultrastable glasses [59, 60], for which the dynamical properties are numerically intractable. Because Ref. [61] reported that the stability of glass samples is structurally reflected by the density of the quasi-localized vibrational (QLV) modes, it would be interesting to see if Grad-CAM also quantifies the QLV modes or highlights completely different structures. Similarly, it has been shown that the structural difference between instantaneous configurations under different external shear speeds is quantified by the density of the imaginary normal modes [62]. Our method is also applicable in these situations.

In general, we expect that the extracted structures are dependent on the precise setup of the classification problem, such as the temperature choice for each class. It would be interesting to compare the characteristic glass structures obtained from different reference high temperatures. Further, such structures could be sensitive to the details of the protocols, for example, the network architecture or the number of epochs. The investigation of the effects of these factors would be valuable.

Data availability statement

The datasets generated during the current study are available from the corresponding authors on reasonable request.

Author contributions

NO and SK performed the numerical simulations and analyzed the data. NO and TK designed the study. All authors wrote this paper.

Funding

This work was financially supported by the JST FOREST Program (Grant No. JPMJFR212T) and JSPS KAKENHI (Grant Nos. 22H04472, 20H05157, 20H00128, 19K03767, and 18H01188).

Acknowledgments

The authors thank Satoshi Koide, Takenobu Nakamura, Hayato Shiba, and Ludovic Berthier for fruitful discussions and comments.

Conflict of interest

Authors NO and SK were employed by company Toyota Central R&D Labs, Inc., Tokyo, Japan.

The remaining authors declare that the research was conducted in the absence of any commercial or financial relationships that could be construed as a potential conflict of interest.

Publisher's note

Supplementary material

The Supplementary Material for this article can be found online at: https://www.frontiersin.org/articles/10.3389/fphy.2022.1007861/full#supplementary-material

References

1. Angell CA. Formation of glasses from liquids and biopolymers. *Science* (1995) 267:1924–35. doi:10.1126/science.267.5206.1924

2. Debenedetti PG, Stillinger FH. Supercooled liquids and the glass transition. *Nature* (2001) 410:259–67. doi:10.1038/35065704

3. Dyre JC. Colloquium : The glass transition and elastic models of glass-forming liquids. *Rev Mod Phys* (2006) 78:953–72. doi:10.1103/revmodphys.78.953

4. Cavagna A. Supercooled liquids for pedestrians. *Phys Rep* (2009) 476:51–124. doi:10.1016/j.physrep.2009.03.003

5. Berthier L, Biroli G. Theoretical perspective on the glass transition and amorphous materials. *Rev Mod Phys* (2011) 83:587.

6. Kob W, Donati C, Plimpton SJ, Poole PH, Glotzer SC. Dynamical heterogeneities in a supercooled Lennard-Jones liquid. *Phys Rev Lett* (1997) 79: 2827–30. doi:10.1103/physrevlett.79.2827

7. Yamamoto R, Onuki A. Dynamics of highly supercooled liquids: Heterogeneity, rheology, and diffusion. *Phys Rev E* (1998) 58:3515–29. doi:10.1103/physreve.58.3515

8. Yamamoto R, Onuki A. Heterogeneous diffusion in highly supercooled liquids. *Phys Rev Lett* (1998) 81:4915–8. doi:10.1103/physrevlett.81.4915

9. Lačević N, Starr FW, Schrøder TB, Glotzer SC. Spatially heterogeneous dynamics investigated via a time-dependent four-point density correlation function. *J Chem Phys* (2003) 119:7372–87. doi:10.1063/1.1605094

10. Dauchot O, Marty G, Biroli G. Dynamical heterogeneity close to the jamming transition in a sheared granular material. *Phys Rev Lett* (2005) 95:265701. doi:10.1103/physrevlett.95.265701

11. Karmakar S, Dasgupta C, Sastry S. Growing length and time scales in glass-forming liquids. *Proc Natl Acad Sci U S A* (2009) 106:3675–9. doi:10.1073/pnas.0811082106

12. Keys AS, Hedges LO, Garrahan JP, Glotzer SC, Chandler D. Excitations are localized and relaxation is hierarchical in glass-forming liquids. *Phys Rev X* (2011) 1: 021013. doi:10.1103/physrevx.1.021013

13. Chandler D, Garrahan JP. Dynamics on the way to forming glass: Bubbles in space-time. *Annu Rev Phys Chem* (2010) 61:191–217. doi:10.1146/annurev.physchem.040808.090405

14. Kirkpatrick TR, Thirumalai D, Wolynes PG. Scaling concepts for the dynamics of viscous liquids near an ideal glassy state. *Phys Rev A* (1989) 40: 1045–54. doi:10.1103/physreva.40.1045

15. Hirata A, Guan P, Fujita T, Hirotsu Y, Inoue A, Yavari AR, et al. Direct observation of local atomic order in a metallic glass. *Nat Mater* (2011) 10:28–33. doi:10.1038/nmat2897

16. Hirata A, Kang LJ, Fujita T, Klumov B, Matsue K, Kotani M, et al. Geometric frustration of icosahedron in metallic glasses. *Science* (2013) 341:376–9. doi:10.1126/science.1232450

17. Kawasaki T, Araki T, Tanaka H. Correlation between dynamic heterogeneity and medium-range order in two-dimensional glass-forming liquids. *Phys Rev Lett* (2007) 99:215701. doi:10.1103/physrevlett.99.215701

18. Tanaka H, Kawasaki T, Shintani H, Watanabe K. Critical-like behaviour of glass-forming liquids. *Nat Mater* (2010) 9:324–31. doi:10.1038/nmat2634

19. Kawasaki T, Tanaka H. Structural signature of slow dynamics and dynamic heterogeneity in two-dimensional colloidal liquids: glassy structural order. *J Phys : Condens Matter* (2011) 23:194121. doi:10.1088/0953-8984/23/19/194121

20. Leocmach M, Tanaka H. Roles of icosahedral and crystal-like order in the hard spheres glass transition. *Nat Commun* (2012) 3:974. doi:10.1038/ncomms1974

21. Tong H, Tanaka H. Revealing hidden structural order controlling both fast and slow glassy dynamics in supercooled liquids. *Phys Rev X* (2018) 8:011041. doi:10.1103/physrevx.8.011041

22. Tong H, Tanaka H. Structural order as a genuine control parameter of dynamics in simple glass formers. *Nat Commun* (2019) 10:5596. doi:10.1038/s41467-019-13606-3

23. Kob W, Andersen HC. Testing mode-coupling theory for a supercooled binary Lennard-Jones mixture. II. Intermediate scattering function and dynamic susceptibility. *Phys Rev E* (1995) 52:4134–53. doi:10.1103/physreve.52.4134

24. Berthier L. Self-Induced heterogeneity in deeply supercooled liquids. *Phys Rev Lett* (2021) 127:088002. doi:10.1103/physrevlett.127.088002

25. Guiselin B, Tarjus G, Berthier L. Static self-induced heterogeneity in glass-forming liquids: Overlap as a microscope. *J Chem Phys* (2022) 156:194503. doi:10.1063/5.0086517

26. Schoenholz SS, Cubuk ED, Kaxiras E, Liu AJ. Relationship between local structure and relaxation in out-of-equilibrium glassy systems. *Proc Natl Acad Sci U S A* (2017) 114:263–7. doi:10.1073/pnas.1610204114

27. Boattini E, Marín-Aguilar S, Mitra S, Foffi G, Smallenburg F, Filion L. Autonomously revealing hidden local structures in supercooled liquids. *Nat Commun* (2020) 11:5479. doi:10.1038/s41467-020-19286-8

28. Bapst V, Keck T, Grabska-Barwińska A, Donner C, Cubuk ED, Schoenholz SS, et al. Unveiling the predictive power of static structure in glassy systems. *Nat Phys* (2020) 16:448–54. doi:10.1038/s41567-020-0842-8

29. Shiba H, Hanai M, Suzumura T, Shimokawabe T. Unraveling intricate processes of glassy dynamics from static structure by machine learning relative motion. *arxiv* [Preprint] (2022). doi:10.48550/arXiv.2206.14024

30. Paret J, Jack RL, Coslovich D. Assessing the structural heterogeneity of supercooled liquids through community inference. *J Chem Phys* (2020) 152:144502. doi:10.1063/5.0004732

31. Ronhovde P, Chakrabarty S, Hu D, Sahu M, Sahu KK, Kelton KF, et al. Detecting hidden spatial and spatio-temporal structures in glasses and complex physical systems by multiresolution network clustering. *Eur Phys J E* (2011) 34:105. doi:10.1140/epje/i2011-11105-9

32. Ronhovde P, Chakrabarty S, Hu D, Sahu M, Sahu KK, Kelton KF, et al. Detection of hidden structures for arbitrary scales in complex physical systems. *Sci Rep* (2012) 2:329. doi:10.1038/srep00329

33. Valueva M, Nagornov N, Lyakhov P, Valuev G, Chervyakov N. Application of the residue number system to reduce hardware costs of the convolutional neural network implementation. *Mathematics Comput Simulation* (2020) 177:232–43. doi:10.1016/j.matcom.2020.04.031

34. Selvaraju RR, Cogswell M, Das A, Vedantam R, Parikh D, Batra D. Grad-CAM: Visual explanations from deep networks via gradient-based localization. *Int J Comput Vis* (2020) 128:336–59. doi:10.1007/s11263-019-01228-7

35. Oyama N, Mizuno H, Ikeda A. Unified view of avalanche criticality in sheared glasses. *Phys Rev E* (2021) 104:015002. doi:10.1103/physreve.104.015002

36. Shimada M, Mizuno H, Ikeda A. Anomalous vibrational properties in the continuum limit of glasses. *Phys Rev E* (2018) 97:022609. doi:10.1103/physreve.97.022609

37. Sastry S, Debenedetti PG, Stillinger FH. Signatures of distinct dynamical regimes in the energy landscape of a glass-forming liquid. *Nature* (1998) 393:554–7. doi:10.1038/31189

38. Swanson K, Trivedi S, Lequieu J, Swanson K, Kondor R. Deep learning for automated classification and characterization of amorphous materials. *Soft Matter* (2020) 16:435–46. doi:10.1039/c9sm01903k

39. Zhou B, Khosla A, Lapedriza A, Oliva A, Torralba A. Learning deep features for discriminative localization. In: 2016 IEEE Conference on Computer Vision and Pattern Recognition (CVPR); 2016 Jun 27–30; Las Vegas, NV. IEEE (2016). p. 2921–9.

40. Cohen MH, Turnbull D. Molecular transport in liquids and glasses. *J Chem Phys* (1959) 31:1164–9. doi:10.1063/1.1730566

41. Widmer-Cooper A, Harrowell P. On the relationship between structure and dynamics in a supercooled liquid. *J Phys : Condens Matter* (2005) 17:S4025–34. doi:10.1088/0953-8984/17/49/001

42. Widmer-Cooper A, Harrowell P. Free volume cannot explain the spatial heterogeneity of Debye–Waller factors in a glass-forming binary alloy. *J Non-Crystalline Sol* (2006) 352:5098–102. doi:10.1016/j.jnoncrysol.2006.01.136

43. Shiba H, Kawasaki T. Spatiotemporal heterogeneity of local free volumes in highly supercooled liquid. *J Chem Phys* (2013) 139:184502. doi:10.1063/1.4829442

44. Ramasubramani V, Dice BD, Harper ES, Spellings MP, Anderson JA, Glotzer SC. freud: A software suite for high throughput analysis of particle simulation data. *Comput Phys Commun* (2020) 254:107275. doi:10.1016/j.cpc.2020.107275

45. Dice B, Ramasubramani V, Harper E, Spellings M, Anderson J, Glotzer S. Analyzing particle systems for machine learning and data visualization with freud. In: Proceedings of the 18th Python in Science Conference (SciPy 2019); 2019 Jul 8–14; Austin, TX (2019). p. 27–33.

46. Widmer-Cooper A, Harrowell P, Fynewever H. How reproducible are dynamic heterogeneities in a supercooled liquid? *Phys Rev Lett* (2004) 93: 135701. doi:10.1103/physrevlett.93.135701

47. Widmer-Cooper A, Harrowell P. On the study of collective dynamics in supercooled liquids through the statistics of the isoconfigurational ensemble. *J Chem Phys* (2007) 126:154503. doi:10.1063/1.2719192

48. Berthier L, Jack RL. Structure and dynamics of glass formers: Predictability at large length scales. *Phys Rev E* (2007) 76:041509. doi:10.1103/physreve.76.041509

49. Shiba H, Yamada Y, Kawasaki T, Kim K. Unveiling dimensionality dependence of glassy dynamics: 2D infinite fluctuation eclipses inherent structural relaxation. *Phys Rev Lett* (2016) 117:245701. doi:10.1103/physrevlett.117.245701

50. Illing B, Fritschi S, Kaiser H, Klix CL, Maret G, Keim P. Mermin–Wagner fluctuations in 2D amorphous solids. *Proc Natl Acad Sci U S A* (2017) 114:1856–61. doi:10.1073/pnas.1612964114

51. Shiba H, Keim P, Kawasaki T. Isolating long-wavelength fluctuation from structural relaxation in two-dimensional glass: cage-relative displacement. *J Phys : Condens Matter* (2018) 30:094004. doi:10.1088/1361-648x/aaa8b8

52. Shiba H, Kawasaki T, Kim K. Local density fluctuation governs the divergence of viscosity underlying elastic and hydrodynamic anomalies in a 2D glass-forming liquid. *Phys Rev Lett* (2019) 123:265501. doi:10.1103/physrevlett.123.265501

53. Coslovich D, Ikeda A. Revisiting the single-saddle model for the β -relaxation of supercooled liquids. *J Chem Phys* (2022) 156:094503. doi:10.1063/5.0083173

54. Brunton SL, Proctor JL, Kutz JN. Discovering governing equations from data by sparse identification of nonlinear dynamical systems. *Proc Natl Acad Sci U S A* (2016) 113:3932–7. doi:10.1073/pnas.1517384113

55. Rudy SH, Brunton SL, Proctor JL, Kutz JN. Data-driven discovery of partial differential equations. *Sci Adv* (2017) 3:e1602614. doi:10.1126/sciadv.1602614

56. Donati C, Glotzer SC, Poole PH, Kob W, Plimpton SJ. Spatial correlations of mobility and immobility in a glass-forming Lennard-Jones liquid. *Phys Rev E* (1999) 60:3107–19. doi:10.1103/physreve.60.3107

57. Matharoo GS, Razul MSG, Poole PH. Structural and dynamical heterogeneity in a glass-forming liquid. *Phys Rev E* (2006) 74:050502. doi:10.1103/physreve.74.050502

58. Ozawa M, Biroli G. Elasticity, facilitation and dynamic heterogeneity in glass-forming liquids. *arxiv* [Preprint] (2022). doi:10.48550/arXiv.2209.08861

59. Berthier L, Charbonneau P, Flenner E, Zamponi F. Origin of ultrastability in vapor-deposited glasses. *Phys Rev Lett* (2017) 119:188002. doi:10.1103/physrevlett.119.188002

60. Khomenko D, Scalliet C, Berthier L, Reichman DR, Zamponi F. Depletion of two-level systems in ultrastable computer-generated glasses. *Phys Rev Lett* (2020) 124:225901. doi:10.1103/physrevlett.124.225901

61. Wang L, Ninarello A, Guan P, Berthier L, Szamel G, Flenner E. Low-frequency vibrational modes of stable glasses. *Nat Commun* (2019) 10:26. doi:10.1038/s41467-018-07978-1

62. Oyama N, Mizuno H, Ikeda A. Instantaneous normal modes reveal structural signatures for the herschel-bulkley rheology in sheared glasses. *Phys Rev Lett* (2021) 127:108003. doi:10.1103/physrevlett.127.108003

Frontiers in Physics

Investigates complex questions in physics to understand the nature of the physical world

Addresses the biggest questions in physics, from macro to micro, and from theoretical to experimental and applied physics.

Discover the latest Research Topics

See more →

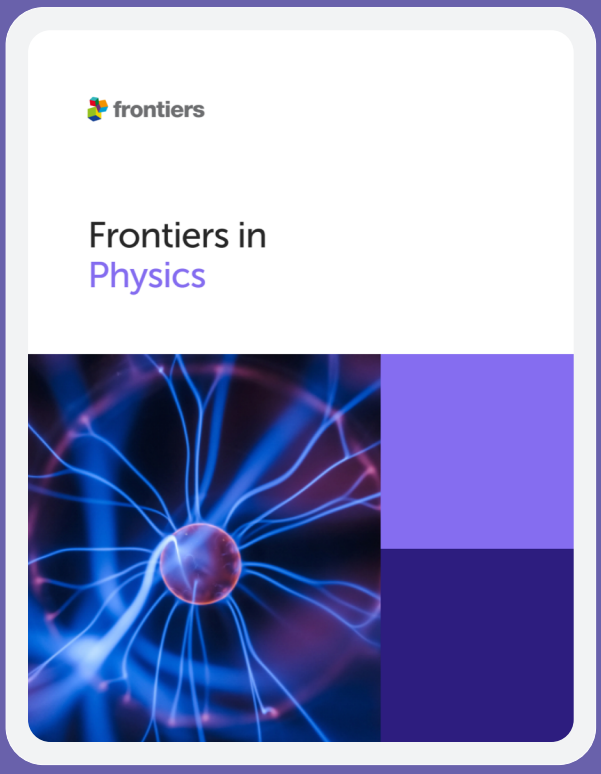

Frontiers

Avenue du Tribunal-Fédéral 34
1005 Lausanne, Switzerland
frontiersin.org

Contact us

+41 (0)21 510 17 00
frontiersin.org/about/contact